SAPIENZA
UNIVERSITÀ DI ROMA

Neutrino Oscillations within the Induced Gravitational Collapse Paradigm of Long Gamma-Ray Bursts

IRAP Ph.D.

Dottorato di Ricerca in Fisica – XXXI Ciclo

Candidate

Juan David Uribe Suárez
ID number 1727981

Thesis Advisor

Prof. Jorge Armando
Rueda Hernandez

A thesis submitted in partial fulfillment of the requirements
for the degree of Doctor of Philosophy in Physics

September 2019

Thesis defended on September 2019
in front of a Board of Examiners composed by:

Prof. Dr. Paolo De Bernardis (chairman)

Prof. Dr. Christopher Lee Fryer

Prof. Dr. Shun Zhou

Neutrino Oscillations within the Induced Gravitational Collapse Paradigm of Long Gamma-Ray Bursts

Ph.D. thesis. Sapienza – University of Rome

ISBN: 000000000-0

This thesis has been typeset by LaTeX and the Sapthesis class.

Version: October 18, 2019

Author's email: jd.uribe242@uniandes.edu.co

Dedicated to
Aaron, Saffo, Pascual, Gauguin, Noche and Joaquín

Abstract

The specific class of binary-driven hypernovae within the induced gravitational collapse scenario for the explanation of the long Gamma-Ray Bursts indicates as progenitor a binary system composed of a carbon-oxygen core and a neutron star in a tight orbit. The supernova explosion of the core triggers a hypercritical (highly super-Eddington) accretion process onto the NS companion, making it reach the critical mass with consequent formation of a Kerr black hole. Recent numerical simulations of the above system show that a part of the ejecta keeps bound to the newborn Kerr black hole with enough angular momentum to generate a new process of hypercritical accretion, i.e. an accretion disk. Throughout this entire process, we focus on two contexts of neutrino emission leading to two different systems in which an analysis of neutrino flavour oscillations (or flavour transformations) not only constitutes a novel extension of the induced gravitational collapse paradigm literature but also can have an impact on a wide range of astrophysical phenomena: from e^-e^+ plasma production in the vicinity of neutron stars or black holes in GRB models, to r-process nucleosynthesis in disk winds and characterization of astrophysical MeV neutrino sources. In particular, we study neutrino oscillations in:

1. *Spherical accretion onto a neutron star:* During this process, copious amounts of neutrino–anti-neutrino pairs ($\nu\bar{\nu}$) are emitted at the neutron star surface. The neutrino emission can reach luminosities of up to 10^{57} MeV s^{-1}, mean neutrino energies 20 MeV, and neutrino densities 10^{31} cm^{-3}. Along their path from the vicinity of the NS surface outward, such neutrinos experience flavour transformations dictated by the neutrino to electron density ratio. We determine the neutrino and electron on the accretion zone and use them to compute the neutrino flavour evolution. For normal and inverted neutrino-mass hierarchies and within the two-flavour formalism ($\nu_e\nu_x$), we estimate the final electronic and non-electronic neutrino content after two oscillation processes: (1) neutrino collective effects due to neutrino self-interactions where the neutrino density dominates and, (2) the Mikheyev-Smirnov-Wolfenstein effect, where the electron density dominates. We find that the final neutrino content is composed by ∼55% (∼62%) of electronic neutrinos, i.e. $\nu_e + \bar{\nu}_e$, for the normal (inverted) neutrino-mass hierarchy.

2. *Neutrino-cooled disks around a Kerr black hole:* In this phase of the binary-driven hypernovae, given the extreme conditions of high density (up to 10^{12} g cm^{-3}) and temperatures (up to tens of MeV) inside this disk, neutrinos can reach densities of 10^{33} cm^{-3} and energies of 50 MeV. Although the geometry of the disk is significantly different from that of spherical accretion, these conditions provide an environment that allows neutrino flavour transformations. We estimate the evolution of the electronic and non-electronic neutrino content within the two-flavour formalism ($\nu_e\nu_x$) under the action of neutrino collective effects by neutrino self-interactions. We find that neutrino oscillations inside the disk can have frequencies between $\sim$ (10^5–10^9) s^{-1}, leading the disk to achieve flavour equipartition. This implies that the energy deposition rate by neutrino annihilation ($\nu + \bar{\nu} \rightarrow e^- + e^+$) in the vicinity

of the Kerr black hole is smaller than previous estimates in the literature not accounting by flavour oscillations inside the disk. The exact value of the reduction factor depends on the ν_e and ν_x optical depths but it can be as high as ~ 5.

This work has allowed us to identify key theoretical and numerical features involved in the study of neutrino oscillations and our results are a first step toward the analysis of neutrino oscillations in unique astrophysical settings other than core-collapse supernovae. As such, they deserve further attention.

Contents

List of Figures

List of Tables

Units, Symbols and Acronyms

Throughout this text, all equation are written in Planck units $c = G = \hbar = k_B = k_e = 1$. However, we will report any calculated quantity with restored units in a system appropriate for the context. For example, distance can be reported in cm or in Schwarzschild radius units. We also insert here a summary of acronyms and symbols used throughout to improve readability[1] (Table 0.1).

Table 0.1. Acronyms and symbols used in this work in alphabetical order.

Extended Wording	**Acronym/Symbol**
Binary-driven hypernova	BdHN
Black hole	BH
Carbon-oxygen core	$\mathrm{CO_{core}}$
Electron (anti)-neutrino	$(\bar{\nu}_e)\nu_e$
Gamma-ray burst	GRB
Gamma-ray flash	GRF
Induced gravitational collapse	IGC
Massive neutron star	MNS
Mikheyev-Smirnov-Wolfenstein	MSW
Neutrino-cooled acrretion disk	NCAD
Neutron star	NS
New neutron star created in the SN explosion	νNS
Non-electron (anti)-neutrino	$(\bar{\nu}_x)\nu_x$
Self-interaction potential	SIP
Short Gamma-ray burst	S-GRB
Short Gamma-ray flash	S-GRF
Smooth particle hydrodynamics	SPH
Standard Model	SM
Supernova	SN
Ultrashort Gamma-ray burst	U-GRB
Ultra high-energy cosmic ray	UHECR
White dwarf	WD
X-ray flash	XRF

[1] When neutrino flavour is not an issue, we suppress the subscripts e and x to refer to (anti)-neutrinos $(\bar{\nu})\nu$.

List of Publications

- Becerra, L., Guzzo, M. M., Rossi-Torres, F., Rueda, J. A., Ruffini, R., and **Uribe, J. D.** Neutrino Oscillations within the Induced Gravitational Collapse Paradigm of Long Gamma-Ray Bursts. ApJ, **852** (2018), 120. arXiv:1712.07210. doi:10.3847/1538-4357/aaa296.

- **Uribe Suárez, J. D.** and Rueda Hernandez, J. A. Neutrino oscillations in a neutrino-dominated accretion disk around a Kerr BH. arXiv e-prints, (2019), arXiv:1909.01841. Submitted to Phys. Rev. D.

Chapter 1

Introduction

The first ideas of neutrino mixing were advanced by Bruno Pontecorvo in [224, 225] soon after the discovery of the electron anti-neutrino by Cowan *et al.* [57]. Motivated by the Kaon mixing $K^0 \rightleftharpoons \bar{K}^0$ proposed by Gell-Mann and Pais in [115], Pontecorvo postulated that there might exist the phenomenon of neutrino-antineutrino mixing.After the discovery of muon neutrinos [58], Maki *et al.* introduced a model of two-flavour mixing [174] within the Nagoya model of particles [139]. Their ideas lead to the core concept of neutrino oscillations: a neutrino created at a source in a particular flavour state may be detected in a different flavour state at a certain distance from the source. In 1967, motivated by the deficit reported by Davis on the measurement of solar neutrinos at the Homestake experiment [62], Pontecorvo published two articles [226, 122], establishing the phenomenological theory of two-neutrino mixing. He suggested that the deficit can be explained if electron neutrinos emitted from the sun are transformed during their travel to earth into a different flavour, to which the Homestake experiment was insensitive. This is the core concept behind the mechanism of neutrino oscillation.

Between 1975 and 1976 the standard theory of neutrino oscillations in vacuum was developed in [86, 98, 34]. To these results, Wolfenstein, Mikheyev and Smirnov added the insight that the medium induced modification of the neutrino dispersion relations is critical to understand the solar neutrino problem and showed that oscillations can be amplified when a neutrino beam travels through an adiabatic density gradient [308, 192]. Concurrently, the efforts of Nötzold Dolgov, Rudzsky, Stodolsky, Sigl and Raffelt helped develop the general kinetic equation for mixed neutrinos that allows calculating the refraction index of neutrinos due to self-interactions (ν–ν) [206, 74, 245, 235, 284].

The theory of neutrino mixing is now supported by the measurements in the Super-Kamiokande experiment [110], the SNO experiment [9] and reactor KamLAND experiment [84], and elevated by the 2015 Nobel Prize award. Accordingly, over the last years, the aims of the neutrino community turned into analysing the consequences of neutrino oscillations in different physical contexts, with a unique emphasis on the study of SN neutrinos (see, e.g., [234, 216, 81, 279, 112, 78, 90, 82, 237, 88, 89, 50, 80, 77, 60, 59, 280, 83, 312, 33, 152, 305, 194, 131, 321]). However, core-collapse SN is not the only astrophysical system with an immense emission of neutrinos or in which neutrinos play an important role.

Recently, Ruffini *et al.* [266] suggested a binary nature for the progenitors of both long and short GRBs. For such systems, the IGC paradigm offers as progenitor a binary system comprised of a CO_{core} and a NS in a tight orbit. The core-collapse of the CO_{core} produces a supernova SN explosion ejecting material that triggers an accretion process onto the binary NS companion. It was shown in [24] that in spherical accretion onto a NS a large number of neutrinos are emitted from the NS surface. Moreover, it was shown in [25] that the angular momentum of the SN ejecta is high enough to circularize around the NS forming an accretion disk. For high enough accretion rates, the physical behaviour of this disk is that of the *neutrino-cooled accretion disk* (NCAD). Is in these two distinct accretion systems in which we are interested in evaluating the possible outcomes of neutrino oscillations.

This thesis is based on research that, so far, produced two articles [27, 302] and we believe that the best way to present this text is by keeping the structure of these articles as constant as possible. With this in mind, this thesis is organized as follows. This chapter is divided in two main sections. Sec. 1.1 reviews the essential equations of neutrino oscillations in vacuum and matter (including neutrinos themselves). We follow the standard derivation found in [212, 236, 315]. Although these derivations are based on the paradoxical *same momentum* assumption, the method is easy to understand and, it reproduces the correct equations. For a comment on the proper interpretation of this scheme, we refer the reader to [11]. In Sec. 1.2, we present a summary of the physics involved in GRB emission. We mention the role of neutrinos in the production of the energetic plasma e^-e^+ that explains the GRB prompt emission in gamma-rays. This summary frames and describes the astrophysical systems where we applied the concepts of neutrino oscillations. A more extensive review, including some of the results contained in this text, can be found in [248].

In Chapter 2 we describe the hydrodynamics of hypercritical spherical accretion on a NS within the IGC scenario. For accretion rates between $(10^{-2}$–$10^{-5})M_\odot$ s^{-1}, the range of temperature and density developed on the NS surface ensure that the dominant channel of neutrino emission is electron-positron pair annihilation. This emission reaches luminosities up to 10^{52} erg s^{-1} with average neutrino energies of the order of 20 MeV. Such conditions make the XRFs and the BdHNe astrophysical laboratories for MeV-neutrino physics. In particular, using the characterization of the neutrino content at the surface, we follow the neutrino flavour transformations from the bottom of the accretion zone, where neutrinos are created, until their escape outside the Bondi-Hoyle region. This allows us to calculate the neutrino spectrum emerging from the accreting system.

Finally, in recent SPH simulations it is confirmed that the accretion onto the NS companion in a CO_{core} occurs from a disk-like structure formed by the particles that circularize before being accreted [26]. Additionally, in a NS-NS merger, matter can remain bound to the newborn central object (NS or BH) and form an accreting disk. NCADs (neutrino-cooled accretion disks) are of special interest for GRB physics since their main cooling mechanism is the emission of copious amounts of (anti)-neutrinos. These $\nu\bar{\nu}$ pairs can be the source of the e^-e^+ plasma through the $\nu + \bar{\nu} \to e^- + e^+$ process, but the efficiency of this process depends on the emitted neutrino flavour content which is affected by neutrino mixing. In that context, and as a generalization of the system considered in Chapter 2, Chapter 3 focuses in disk accretion onto BHs. In particular, we describe the hydrodynamic properties of

NCADs and build a simplified model to add the dynamics of neutrino oscillations to the already established equations of thin disk accretion. Under this model, the disk reaches flavour equipartition. We evaluate how this fact influences the disk's behaviour and how the flavour emission changes.

1.1 Fundamentals of Neutrino Oscillations

1.1.1 Oscillations in Vacuum

Within the SM of particles, neutrinos are defined in terms of flavours $(\nu_e, \nu_\mu, \nu_\tau)$ related to the three charged leptons (e, μ, τ) involved in their production processes via the weak charged-current interactions (flavour states). However, we now know that neutrinos are massive particles and when we think of a freely propagating massive particle we usually think of a mass eigenstate ν_n of the Klein-Gordon equation[1] $(\Box + m_n^2)\nu_n = 0$ with eigenvalue m_n. If the mass states are non-degenerate, the collection $(\nu_n,\, n \in \{1,2,3\})$ does constitute a basis in which the mass matrix is diagonal $\mathbf{M} = \mathrm{diag}(m_1, m_2, m_3)$. In general, the mass basis and the flavour basis $(\nu_\alpha,\, \alpha \in \{e, \mu, \tau\})$ do not need to coincide[2]. Hence, the fields describing the massive neutrinos ν_n and flavour-eigenstate neutrinos ν_α and the corresponding states $|\nu_n\rangle$ and $|\nu_\alpha\rangle$ are related by an unitary transformation $\mathbf{U}$ such that[3]

$$\nu_\alpha = \sum_i (\mathbf{U})_{\alpha i}\, \nu_i, \quad |\nu_\alpha\rangle = \sum_i (\mathbf{U}^*)_{\alpha i}\, |\nu_i\rangle. \tag{1.1}$$

$\mathbf{U}$ is known as the lepton mixing matrix or the Maki-Nakagawa-Sakata-Pontecorvo matrix (MNSP), and is parametrized by three rotations angles $\theta_{12}, \theta_{13}, \theta_{23}$ and a CP-violating phase δ_{cp}

$$\mathbf{U} = \begin{pmatrix} c_{12}c_{13} & s c_{13} & s_{13}\mathrm{e}^{-\mathrm{i}\delta_{\mathrm{cp}}} \\ -s_{12}c_{23} - c_{12}s_{13}s_{23}\mathrm{e}^{\mathrm{i}\delta_{\mathrm{cp}}} & c_{12}c_{23} - s_{12}s_{13}s_{23}\mathrm{e}^{\mathrm{i}\delta_{\mathrm{cp}}} & s_{23}c_{13} \\ s_{12}s_{23} - c_{12}c_{23}s_{13}\mathrm{e}^{\mathrm{i}\delta_{\mathrm{cp}}} & -c_{12}s_{23} - c_{23}s_{12}s_{13}\mathrm{e}^{\mathrm{i}\delta_{\mathrm{cp}}} & c_{13}c_{23} \end{pmatrix}, \tag{1.2}$$

where $c_{ij} = \cos\theta_{ij}$ and $s_{ij} = \sin\theta_{ij}$. These angles are measured parameters in the SM [120, 292] and represent an extension of it. Consider a stationary source of neutrinos of a definite flavour state propagating in the x direction. This flavour state is a linear combination of mass eigenstates by Eq. (1.1). If we assume that the mass eigenstates all have the same momentum p and expand the ν_n fields in plane waves form $\nu_n(x,t) = \nu_n(t)\exp(\mathrm{i}px)$, we obtain the temporal evolution of the Klein-Gordon equation as $[(p + \mathrm{i}\partial_t)(p - \mathrm{i}\partial_t) - m_n^2]\nu_n(t) = 0$. In the astrophysical contexts we are interested in, neutrino energies are of the order ~ 10 MeV, while constraints on the neutrino masses require $\sum_i m_i \lesssim 1$ eV [185]. This means that we can linearize the Klein-Gordon equation using the mass energy relation for ultra-relativistic neutrinos $E_i = \sqrt{p^2 + m_i^2} \approx p + m_i^2/2p$ and to a first order approximation

[1] Technically, an eigenstate of Dirac's equation but the neutrino spinor structure is not important to describe neutrino oscillations.

[2] During this section we reserve Greek indices for flavour states and Latin indices for mass states.

[3] Remember that the one-particle states $|\nu\rangle$ are obtained by the Hermitian-conjugate field operator $\nu^\dagger$ acting on the vacuum state $|0\rangle$. For this reason the appearance of the complex conjugate in the second equation.

we get the Schrödinger-type equation

$$\mathrm{i}\partial_t \nu_n = \left(p + \frac{m_n^2}{2p}\right)\nu_n. \tag{1.3}$$

In terms of the state vectors, if the source emits a fixed flavour $|\nu(0)\rangle = |\nu_\alpha\rangle$, then after a time t, the nth mass eigenstate will picks up a phase factor $\exp(-\mathrm{i}E_n t)$ such that

$$|\nu_\alpha(t)\rangle = \sum_n (\mathbf{U})_{\alpha n} \exp\left(-\mathrm{i}\left[p + \frac{m_n^2}{2p}\right]\right)|\nu_n\rangle. \tag{1.4}$$

and the probability of measuring a state ν_β (transition probability) is

$$\begin{aligned} P_{\nu_\alpha\to\nu_\beta}(t) &= |\langle\nu_\beta|\nu_\alpha(t)\rangle|^2 = \sum_{i,j}(\mathbf{U})_{\alpha i}(\mathbf{U})_{\beta j}(\mathbf{U}^*)_{\alpha j}(\mathbf{U}^*)_{\beta i}\exp\left(-\mathrm{i}\frac{\Delta m_{ji}^2}{2p}t\right) \\ &= \sum_i |(\mathbf{U})_{\alpha i}|^2|(\mathbf{U})_{\alpha i}|^2 + 2\,\mathrm{Re}\left[\sum_{i<j}(\mathbf{U})_{\alpha i}(\mathbf{U})_{\beta j}(\mathbf{U}^*)_{\alpha j}(\mathbf{U}^*)_{\beta i}\exp\left(-\mathrm{i}\frac{\Delta m_{ji}^2}{2p}t\right)\right] \end{aligned} \tag{1.5}$$

where $\Delta m_{ji}^2 = m_j^2 - m_i^2$ is the mass-squared difference. Through the unitary property of the mixing matrix we can to prove that the $P_{\nu_\alpha\to\nu_\beta}$ is a probability measure over the set $\{\nu_\alpha, \,|\, \alpha = e,\mu,\tau\}$, so that $\sum_\alpha P_{\nu_\alpha\to\nu_\beta} = \sum_\beta P_{\nu_\alpha\to\nu_\beta} = 1$. Then, it is possible to define the survival probability as

$$P_{\nu_\alpha\to\nu_\alpha}(t) = 1 - \sum_{\beta\neq\alpha} P_{\nu_\alpha\to\nu_\beta}(t) = 1 - 4\sum_{i<j}|(\mathbf{U})_{\alpha i}|^2|(\mathbf{U})_{\alpha j}|^2\sin^2\left(\frac{\Delta m_{ji}^2}{2p}t\right). \tag{1.6}$$

Is at this point that the concept of *hierarchy* becomes important. The neutrino masses are characterized by two independent differences [92]

$$\Delta m_{21}^2 = m_2^2 - m_1^2, \quad \Delta m^2 = m_3^2 - \frac{m_2^2 + m_1^2}{2}. \tag{1.7}$$

Δm_{21}^2 is often referred as the "solar" mass difference, while Δm^2 as the "atmospheric" mass difference. Depending on the sign of Δm^2, there are two possible mass hierarchies: normal (NH) and inverted (IH) (Table 1.1). The first corresponds to the positive sign of Δm^2 ($m_1 < m_2 < m_3$), whereas the latter refers to the negative sign of Δm^2 ($m_3 < m_1 < m_2$). The diagonal squared mass matrix $\mathbf{M}^2$ can be written as

$$\mathbf{M}^2 = (m_3^2 - \Delta m^2)\mathbb{1} + \mathrm{diag}(-\Delta m_{21}^2, \Delta m_{21}^2, \pm\Delta m^2). \tag{1.8}$$

where the upper (lower) sign refers to NH (IH). The transition probabilities for anti-neutrinos $P_{\bar\nu_\alpha\to\bar\nu_\beta}$ can be found analogously, by recalling that the one-particle states $|\nu\rangle$ are obtained by the neutrino field operator ν rather than its Hermitian-conjugate.

As can be seen from Eq. (1.5) and Eq. (1.6), oscillations are only sensitive to the squared-mass difference, making it extremely difficult to measure the individual neutrino masses directly [129]. For this reason, the information about the neutrino masses is usually given in terms of inequalities. Neutrinos and anti-neutrinos are

Table 1.1. Mixing and squared mass differences as they appear in [292]. Error values in parenthesis are shown in 3σ interval. The squared mass difference is defined as $\Delta m^2 = m_3^2 - \left(m_2^2 + m_1^2\right)/2$ and its sign depends on the hierarchy $m_1 < m_2 < m_3$ or $m_3 < m_1 < m_2$.

$\Delta m^2_{21} = 7.37\,(6.93 - 7.96) \times 10^{-5}$ eV^2
$\lvert\Delta m^2\rvert = 2.56\,(2.45 - 2.69) \times 10^{-3}$ eV^2 Normal Hierarchy
$\lvert\Delta m^2\rvert = 2.54\,(2.42 - 2.66) \times 10^{-3}$ eV^2 Inverted Hierarchy
$\sin^2\theta_{12} = 0.297\,(0.250 - 0.354)$
$\sin^2\theta_{23}(\Delta m^2 > 0) = 0.425\,(0.381 - 0.615)$
$\sin^2\theta_{23}(\Delta m^2 < 0) = 0.589\,(0.383 - 0.637)$
$\sin^2\theta_{13}(\Delta m^2 > 0) = 0.0215\,(0.0190 - 0.0240)$
$\sin^2\theta_{13}(\Delta m^2 < 0) = 0.0216\,(0.0190 - 0.0242)$

related by a CP transformation which interchanges ν with $\bar{\nu}$ and reverses the helicity. Additionally, a T transformation interchanges the initial and final states. From this we can deduce the relations [118]

$$P_{\nu_\alpha\to\nu_\beta} \overset{\mathrm{T}}{\longleftrightarrow} P_{\nu_\beta\to\nu_\alpha}, \tag{1.9a}$$

$$P_{\nu_\alpha\to\nu_\beta} \overset{\mathrm{CP}}{\longleftrightarrow} P_{\bar{\nu}_\alpha\to\bar{\nu}_\beta}, \tag{1.9b}$$

$$P_{\nu_\alpha\to\nu_\beta} \overset{\mathrm{CPT}}{\longleftrightarrow} P_{\bar{\nu}_\beta\to\bar{\nu}_\alpha}. \tag{1.9c}$$

Under the CPT invariance we are guaranteed the relations $P_{\nu_\alpha\to\nu_\beta} = P_{\bar{\nu}_\beta\to\bar{\nu}_\alpha}$ and $P_{\nu_\alpha\to\nu_\alpha} = P_{\bar{\nu}_\alpha\to\bar{\nu}_\alpha}$. Hence, it is possible to discover CP or T violation in oscillation experiments by measuring only transition probabilities (*appearance* experiments)[4]. Oscillation of the kind $P_{\nu_\alpha\to\bar{\nu}_\beta}$ have been shown to be modulated by an extra factor m_i/p [281, 63], rendering them irrelevant for our purpose. Since in some astrophysical applications we deal with a statistical mixture of neutrinos and not independent single particle states, it is often useful to cast the equations of oscillations terms of the density matrix ($\rho = \sum_\alpha \mathsf{p}_\alpha |\nu_\alpha\rangle\langle\nu_\alpha|$ and $\bar{\rho} = \sum_\alpha \mathsf{p}_\alpha |\bar{\nu}_\alpha\rangle\langle\bar{\nu}_\alpha|$ with the statistical weights p_α and the normalization condition $\sum_\alpha \mathsf{p}_\alpha = 1$).

$$\dot{\rho}_p = [\mathsf{H}_{\mathrm{vac}}, \rho]\,, \qquad \dot{\bar{\rho}}_p = -\,[\mathsf{H}_{\mathrm{vac}}, \bar{\rho}]\,. \tag{1.10}$$

where the dot represents a time derivative and $\mathsf{H}_{\mathrm{vac}}$ is the vacuum Hamiltonian

$$\mathsf{H}_{\mathrm{vac}} = \frac{1}{2p}\mathbf{M}^2. \tag{1.11}$$

[4]Neutrino oscillation experiments are divided in two categories. Appearance experiments: These experiments measure transitions probabilities between different neutrino flavours by counting in the detector the number of events due to flavours not emitted by the source. Disappearance experiments: These experiments measure the survival probability of a neutrino flavour by counting in the detector the number of events due to the same flavour emitted by the source.

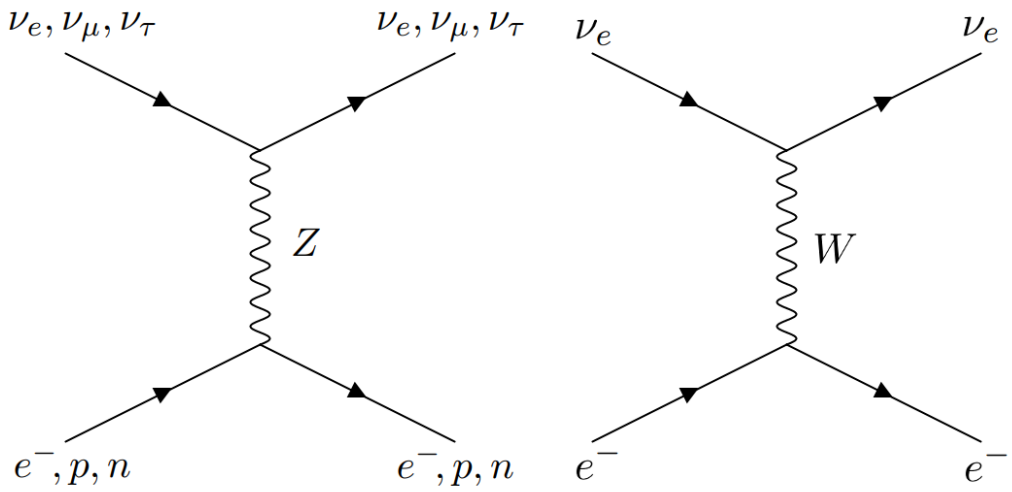

Figure 1.1. Feynman diagrams of the coherent forward elastic scattering processes (not counting automorphisms of the diagram) that generate the charged-current potential and the neutral-current potential.

To finish the discussion of the quantum mechanical picture of mixing, it should be noted that, as we mentioned at the beginning of this chapter, the derivation of Eq. (1.10) assumes that neutrinos of a definite flavour have a well-defined momentum p, i.e. all the mass eigenstates involved in its linear decomposition have the same momentum. However, in [144] it is remarked that although technically incorrect, it is a harmless error since it can be proved that it leads to the right oscillation probabilities by a significantly easier path [119, 11].

1.1.2 Oscillations in Matter

As neutrinos travel through ordinary matter (e.g. in the Sun, a SN or an accretion disk), the weak interaction couples the neutrinos to matter and, as long as the density is not high enough to trap them, besides few momenta changing scattering events, they also experience elastic coherent forward scattering. This effect can modify the oscillation behaviour significantly. The reason for this being that interactions with a medium changes the dispersion relation particles travelling through it [308]. Is in this aspect that equivalence can be drawn between this phenomenon and photons propagating through glass. Now, when we say "ordinary matter" we refer to electron, positrons, protons and neutrons. This induces an asymmetry between the scattering events of electron neutrinos and non-electron neutrinos since ν_e can interact have charged- and neutral-current interactions while ν_μ and ν_τ can have only neutral-current interactions (Fig. 1.1). The essential point to be noted is that the refractive index is different for different flavours so that the medium is flavour birefringent and neutrinos of different flavours acquire different phases. Since the contribution to the phase change due to neutral-current interactions is identical for all neutrino flavours, only charged-current interactions affect the oscillation evolution.

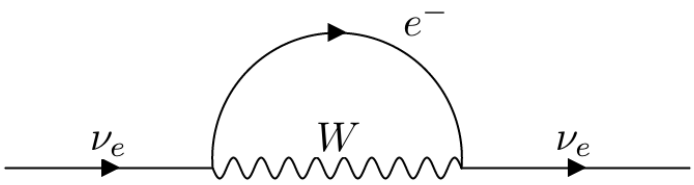

Figure 1.2. The Feynman diagram for charged-current contributions to self-energy of neutrinos in the presence of background electrons.

To calculate the dispersion relation of a particle travelling through media we need to calculate the pole of its propagator. This is done by calculating the neutrino self-energy in the thermal bath of the medium [206]. The propagator is [68]

$$\frac{1}{\not{p} - m - \Sigma(p)} \tag{1.12}$$

In the lowest order, the contribution to $\Sigma(p)$ comes from the 1-loop self-energy correction in Fig. 1.2

$$\mathrm{i}\Sigma(p) = \mathrm{i}\left(\frac{g_w}{2\sqrt{2}}\right)^2 \int \frac{dk^4}{(2\pi)^4}\gamma_\alpha(1-\gamma_5)\mathrm{i}S_e(k)\gamma_\beta(1-\gamma_5)\frac{\mathrm{i}g^{\alpha\beta}}{M_w^2} \tag{1.13}$$

where S_e is the electron propagator, k is the electron four-momentum and the momentum dependence of the W-propagator is ignored [315]. The electron propagator can be written as

$$\mathrm{i}S_e(k) = [\not{k} + m_e]\left(\frac{\mathrm{i}}{k^2 - m_e^2} - 2\pi\delta(k^2 - m_e^2)\eta(k\cdot u)\right) \tag{1.14}$$

where u is the four-velocity of the medium and $\eta(k\cdot u)$ is defined in terms of Fermi-Dirac distributions and the step function $\boldsymbol{\Theta}$ (see also Appx. D for a list of constants)

$$\eta(k\cdot u) = \frac{\boldsymbol{\Theta}(x)}{\exp(E_k - \mu) + 1} - \frac{\boldsymbol{\Theta}(-x)}{\exp(E_k + \mu) + 1} \tag{1.15}$$

integration over the final-state phase space yields

$$\Sigma(k) = \sqrt{2}G_F(n_{e^-} - n_{e^+})\gamma_0 \tag{1.16}$$

where $n_{e^\pm}$ are the respective integrals of the electron (positron) Fermi-Dirac distributions in Eq. (1.16).

It is important to note that the similarity between the behaviours of ν_μ and ν_τ allows us to make a useful approximation. It is possible to consider both flavours of non-electronic neutrinos as a single flavour $\nu_x = \nu_\mu + \nu_\tau$. Hence, Three-flavour oscillations can be approximated by two-flavour oscillations. This approximation is stressed by the strong hierarchy of the squared-mass differences $|\Delta m^2_{13}| \approx |\Delta m^2_{23}| \gg |\Delta m^2_{12}|$ and the smallness of the θ_{13} mixing angle (Table 1.1). In this case, the mixing matrix is a 2×2 Hermitian matrix parametrized by the single mixing angle

θ_{13} and in the vacuum potential only one squared-mass difference appears (we will drop the suffix in the mixing angle)

$$\mathsf{H}_{\text{vac}} = \frac{\Delta m^2}{4p}\begin{pmatrix} -\cos 2\theta & \sin 2\theta \\ \sin 2\theta & \cos 2\theta \end{pmatrix} \tag{1.17}$$

The Hamiltonian now includes an extra term H_{m} of the form

$$\mathsf{H}_{\text{m}} = \frac{1}{2}\begin{pmatrix} \sqrt{2}G_F(n_{e^-} - n_{e^+}) & 0 \\ 0 & -\sqrt{2}G_F(n_{e^-} - n_{e^+}) \end{pmatrix} \tag{1.18}$$

where G_f is the Fermi coupling constant. It is not difficult to see that the new Hamiltonian can be written in a "vacuum-equivalent" form by redefining the mixing angle and the squared-mass difference

$$\tan 2\theta_{\text{m}} = \frac{\tan 2\theta}{1 - \frac{2\sqrt{2}G_F(n_{e^-} - n_{e^+})}{\Delta m^2 \cos 2\theta}}, \tag{1.19a}$$

$$\Delta m^2_{\text{m}} = \sqrt{\left(\Delta m^2 \cos 2\theta - 2\sqrt{2}G_F(n_{e^-} - n_{e^+})\right)^2 + (\Delta m^2 \sin 2\theta)^2} \tag{1.19b}$$

These equations exhibit an interesting feature. If the we have $2\sqrt{2}G_F(n_{e^-} - n_{e^+}) = \Delta m^2 \cos 2\theta$, then the mixing angle is $\theta = \pi/4$, i.e. the mixing is maximal and is possible to observe a total transition between two neutrino flavours. Note, however that this transition separates the behaviour of ν and $\bar{\nu}$. Since in ordinary matter, the density of free electrons is positive, the total transition can only exist if $\theta < \pi/4$. If $\theta > \pi/4$ the transition cannot be reached. On the other hand, due to the -1 factor in the equation of oscillations for anti-neutrinos (see Eq. (1.10), there is a total transition between two anti-neutrino flavors only if $\theta > \pi/4$. Therefore, the dynamics of neutrino oscillations in matter is different from that of neutrino oscillations in vacuum. This phenomenon is called the MSW effect after Mikheyev, Smirnov, and Wolfenstein [192, 31, 308].

It is a well known fact that in SN, around 99% of the energy released comes from neutrino emission. This emission lasts about 10 s, and releases about 10^{58} MeV of energy. Therefore, the number of neutrinos emitted is $\sim 10^{58}$. An incredibly large number[5]. Meaning that in the analysis of the accretion systems we are interested, our definition of ordinary matter should include neutrinos themselves, i.e. we must consider the effects of coherent forward scattering of the form $\nu_\alpha + \nu_\beta \to \nu_\alpha + \nu_\beta$. If we examine the diagrams in Fig. 1.3, we can see that the first diagram does not contribute to neutrino oscillations since it affects the neutrino refractive index identically for all flavours (it is flavour blind). In the second diagram, the background $\nu_{p,e}$ shifts the refractive index of the $\nu_{q,e}$ we observing via a interchange of momentum. The same occurs in the third but instead of momentum, the particles interchange flavours.

The derivation of the dispersion relation of neutrino self-interactions follows in the same way as we did for the electron background. But there is a caveat. In deriving Eq. (1.16) it is assumed that the background electrons are a isotropic gas.

[5]Compare with Avogadro's number $\sim 10^{23}$.

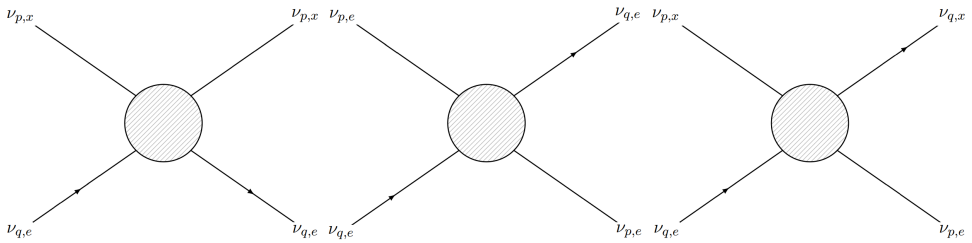

Figure 1.3. Possible diagrams representing ν-ν interactions with momenta p, q. The lines without arrows represent the background or "medium neutrinos" and lines with arrows represent the neutrinos we are following. In all cases the particles come from the left and exit through the right of the diagram. The first diagram is does not contribute to neutrino oscillations. The next two do contribute to neutrino oscillations [111, 213, 214].

If neutrinos can be considered an isotropic gas, then we get a similar term of the form $\sqrt{2}G_F(n_\nu - n_{\bar{\nu}})$. However, if neutrinos constitute an anisotropic gas, the new term in the Hamiltonian takes the form

$$\mathsf{H}_{\nu\nu} = \sqrt{2}G_F \int (\rho_{\mathbf{q},t} - \bar{\rho}_{\mathbf{q},t}) \, (1 - \mathbf{v}_{\mathbf{q},t} \cdot \mathbf{v}_{\mathbf{p},t}) \, \frac{d^3\mathbf{q}}{(2\pi)^3} \tag{1.20}$$

where $\rho_{\mathbf{p},t}$ ($\bar{\rho}_{\mathbf{p},t}$) is the matrix of occupation numbers: $(\rho_{\mathbf{p},t})_{ij} = \langle a_j^\dagger a_i \rangle_{\mathbf{p},t}$ for neutrinos and $((\bar{\rho}_{\mathbf{p},t})_{ij} = \langle \bar{a}_i^\dagger \bar{a}_j \rangle_{\mathbf{p},t}$ for anti-neutrinos, for each momentum $\mathbf{p}$ and flavours i, j, and $(\bar{a}^\dagger)a^\dagger$ and $(\bar{a})a$ are the (anti)-neutrino creation and annihilation operators respectively. The diagonal elements are the distribution functions $f_{\nu_i(\bar{\nu}_i)}(\mathbf{p})$ such that their integration over the momentum space gives the neutrino number density n_{ν_i} of a determined flavour i at time t. The off-diagonal elements provide information about the *overlapping* between the two neutrino flavours. Collecting all the terms an allowing for an isotropic background of ordinary matter, we write the full oscillations Hamiltonian as [74, 284, 125]

$$\begin{aligned} \mathsf{H}_{\mathbf{p},t} = \Omega_{\mathbf{p},t} &+ \sqrt{2}G_F \int \left(l_{\mathbf{q},t} - \bar{l}_{\mathbf{q},t}\right) (1 - \mathbf{v}_{\mathbf{q},t} \cdot \mathbf{v}_{\mathbf{p},t}) \, \frac{d^3\mathbf{q}}{(2\pi)^3} \\ &+ \sqrt{2}G_F \int (\rho_{\mathbf{q},t} - \bar{\rho}_{\mathbf{q},t}) \, (1 - \mathbf{v}_{\mathbf{q},t} \cdot \mathbf{v}_{\mathbf{p},t}) \, \frac{d^3\mathbf{q}}{(2\pi)^3} \end{aligned} \tag{1.21a}$$

$$\begin{aligned} \bar{\mathsf{H}}_{\mathbf{p},t} = -\Omega_{\mathbf{p},t} &+ \sqrt{2}G_F \int \left(l_{\mathbf{q},t} - \bar{l}_{\mathbf{q},t}\right) (1 - \mathbf{v}_{\mathbf{q},t} \cdot \mathbf{v}_{\mathbf{p},t}) \, \frac{d^3\mathbf{q}}{(2\pi)^3} \\ &+ \sqrt{2}G_F \int (\rho_{\mathbf{q},t} - \bar{\rho}_{\mathbf{q},t}) \, (1 - \mathbf{v}_{\mathbf{q},t} \cdot \mathbf{v}_{\mathbf{p},t}) \, \frac{d^3\mathbf{q}}{(2\pi)^3} \end{aligned} \tag{1.21b}$$

where $\Omega_{\mathbf{p},t} = \mathsf{H}_{\text{vac}}$ is the matrix of vacuum oscillation frequencies, $l_{\mathbf{p},t}$ and $\bar{l}_{\mathbf{p},t}$ are matrices of occupation numbers for charged leptons built in a similar way to the neutrino matrices, and $\mathbf{v}_{\mathbf{p},t} = \mathbf{p}/p$ is the velocity of a particle with momentum $\mathbf{p}$ (either neutrino or charged lepton). Also, $\mathsf{H}_{\mathbf{p},t}$ ($\bar{\mathsf{H}}_{\mathbf{p},t}$) is the full oscillation Hamiltonian for (anti)-neutrinos.

The evolution of the oscillations of an ensemble of mixed neutrinos is governed

by the Liouville equations

$$i\dot{\rho}_{\mathbf{p},t} = [\mathsf{H}_{\mathbf{p},t}, \rho_{\mathbf{p},t}]\,, \tag{1.22a}$$

$$i\dot{\bar{\rho}}_{\mathbf{p},t} = \left[\bar{\mathsf{H}}_{\mathbf{p},t}, \bar{\rho}_{\mathbf{p},t}\right]. \tag{1.22b}$$

This will be the starting point for our analysis of neutrino oscillations. Eq. (1.22) can be simplified to a more tractable form when applied to a specific system, but this process depends on its geometry and the matter conditions. So we will stop the analysis of oscillations here and retake it in both Chapter 2 and Chapter 3 after we describe the IGC paradigm of GRBs. For an extensive review in the techniques and phenomenology involved in the physics if neutrino oscillations we refer the reader to [236, 118, 315] and references therein.

1.2 Induced Gravitational Collapse, Binary-Driven Hypernovae and Long Gamma-ray Bursts

1.2.1 The Binary Nature of GRB Progenitors

We first recall that GRBs have been traditionally classified by a phenomenological division based on the duration of the time-interval in which the 90% of the total isotropic energy in gamma-rays is emitted, the t_{90}. Long GRBs are those with $t_{90} > 2$ s and short GRBs the sources with $t_{90} < 2$ s [183, 149, 69, 160, 297].

In the case of short bursts, rapid consensus was reached in the scientific community that they could be the product of mergers of NS-NS and/or NS-BH binaries (see, e.g., the pioneering works [121, 209, 85, 204]). We shall return on this issue below by entering into the description of their properties and also to introduce additional mergers of compact-star object binaries leading to short bursts.

For long bursts, possibly the most compelling evidence of the necessity of a binary progenitor comes from the systematic and spectroscopic analysis of the GRBs associated with SNe, the so-called GRB-SNe, started with the pioneering discovery of the spatial and temporal concomitance of GRB 980425 [220] and SN 1998bw [113]. Soon after, many associations of other nearby GRBs with type Ib/c SNe were evidenced (see, e.g., [66, 48]).

There are models in the literature attempting an explanation of both the SN and the GRB within the same astrophysical system. For instance, GRBs have been assumed to originate from a violent SN from the collapse of a massive and fast rotating star, a “collapsar” [311]. A very high rotating rate of the star is needed to produce a collimated, jet emission. This traditional picture adopts for the GRB dynamics the “fireball” model based on the existence of a single ultra-relativistic collimated jet [38, 283, 188, 223, 179]. There is a vast literature devoted to this “traditional" approach and we refer the reader to it for additional details (see, e.g., [221, 222, 186, 187, 29, 162], and references therein).

Nevertheless, it is worth to mention here some of the most important drawbacks of the aforementioned “traditional” approach and which has motivated the introduction of an alternative model, based on a binary progenitor, for the explanation of long GRBs:

- SNe Ic as the ones associated with GRBs lack hydrogen and helium in their spectra. It has been recognized that they most likely originate in helium stars, CO_{core}, or Wolf-Rayet stars, that have lost their outermost layers (see, e.g., [288], and references therein). The pre-SN star, very likely, does not follow a single-star evolution but it belongs to a tight binary with a compact star companion (e.g., a NS). The compact star strips off the pre-SN star outermost layers via binary interactions such as mass-transfer and tidal effects (see, e.g., [205, 132, 109, 318, 288]).

- Denoting the beaming angle by θ_j, to an observed isotropic energy $E_{\rm iso}$ it would correspond to a reduced intrinsic source energy released $E_s = f_b E_{\rm iso} < E_{\rm iso}$, where $f_b = (1 - \cos\theta_j) \sim \theta_j^2/2 < 1$. Extremely small beaming factors $f_b \sim 1/500$ (i.e., $\theta_j \sim 1^\circ$) are inferred to reduce the observed energetics of $E_{\rm iso} \sim 10^{54}$ erg to the expected energy release by such a scenario $\sim 10^{51}$ erg [95]. However, the existence of such extremely narrow beaming angles have never been observationally corroborated [56, 277, 43].

- An additional drawback of this scenario is that it implies a dense and strong wind-like circumburst medium (CBM) in contrast with the one observed in most GRBs (see, e.g., [134]). Indeed, the average CBM density inferred from GRB afterglows is of the order of 1 baryon per cubic centimeter [254]. The baryonic matter component in the GRB process is represented by the so-called baryon load [260]. The GRB e^+e^- plasma should engulf a limited amount of baryons in order to be able to expand at ultra-relativistic velocities with Lorentz factors $\Gamma \gtrsim 100$ as requested by the observed non-thermal component in the prompt Gamma-ray emission spectrum [283, 223, 188]. The amount of baryonic mass M_B is thus limited by the prompt emission to a maximum value of the baryon-load parameter, $B = M_B/E_{e^+e^-} \lesssim 10^{-2}$, where $E_{e^+e^-}$ is the total energy of the e^+e- plasma [260].

- GRBs and SNe have markedly different energetics. SNe emit energies in the range 10^{49}–10^{51} erg, while GRBs emit in the range 10^{49}–10^{54} erg. Thus, the origin of GRB energetics point to the gravitational collapse to a stellar-mass BH. The SN origin points to evolutionary stages of a massive star leading to a NS or to a complete disrupting explosion, but not to a BH. The direct formation of a BH in a core-collapse SN is currently ruled out by the observed masses of pre-SN progenitors, $\lesssim 18\ M_\odot$ [286]. It is theoretically known that massive stars with such a relatively low mass do not lead to a direct collapse to a BH (see [285, 286] for details) .

- It was recently shown in [267] that the observed thermal emission in the X-ray flares present in the early (rest-frame time $t \sim 10^2$ s) afterglow implies an emitter of size $\sim 10^{12}$ cm expanding at mildly-relativistic velocity, e.g., $\Gamma \lesssim 4$. This is clearly in contrast with the "collapsar-fireball" scenario in which there is an ultra-relativistic emitter (the jet) with $\Gamma \sim 10^2$–10^3 extending from the prompt emission all the way to the afterglow.

Therefore, it seems most unlikely that the GRB and the SN can originate from the same single-star progenitor. Following this order of ideas, it was introduced for

the explanation of the spatial and temporal coincidence of the two phenomena the concept of IGC [256, 263]. Two scenarios for the GRB-SN connection have been addressed: [256] considered that the GRB was the trigger of the SN. However, for this scenario to happen it was shown that the companion star had to be in a very fine-tuned phase of its stellar evolution [256]. [263] proposed an alternative scenario in a compact binary: the explosion of a Ib/c SN triggering an accretion process onto a NS companion. The NS, reaching the critical mass value, gravitationally collapses leading to the formation of a BH. The formation of the BH consequently leads to the emission of the GRB. Much more about this binary scenario has been discovered since its initial proposal; its theoretical studies and the search for its observational verification have led to the formulation of a much rich phenomenology which will be the main subject of this section.

Therefore, both short and long GRBs appear to be produced by binary systems, well in line with the expectation that most massive stars belong to binary systems (see, e.g., [276, 287], and references therein). The increasing amount and quality of the multiwavelength data of GRBs have revealed the richness of the GRB phenomenon which, in a few seconds, spans different regimes from X-ray precursors to the gamma-rays of the prompt emission, to the optical and X-rays of the early and late afterglow, to the optical emission of the associated SNe and, last but not least, the presence or absence of high-energy GeV emission. This, in addition to the multiyear effort of reaching a comprehensive theoretical interpretation of such regimes, have lead to the conclusion that GRBs separate into subclasses, each with specific energy release, spectra, duration, among other properties and, indeed, all with binary progenitors [266, 250, 269, 271, 307].

1.2.2 GRB Subclasses

Up to 2017 we had introduced seven GRB subclasses summarized in Table 1.2. In addition, we have recently introduced in [251, 249] the possibility of a further GRB subclass produced by WD-WD mergers. We now give a brief description of all the GRB subclasses identified. In [307] we have renominated the GRB subclasses introduced in [266] and in [251, 249], and inserted them into two groups: BdHNe and compact-object binary mergers. Below we report both the old and the new names to facilitate the reader when consulting our works prior to [307].

i. **X-ray flashes (XRFs)**. These systems have CO_{core}-NS binary progenitors in which the NS companion does not reach the critical mass for gravitational collapse [24, 25]. In the SN explosion, the binary might or might not be disrupted depending on the mass loss and/or the kick imparted [229]. Thus XRFs lead either to two NSs ejected by the disruption, or to binaries composed of a newly-formed ~ 1.4–$1.5\ M_\odot$ NS (hereafter νNS) born at the center of the SN, and a massive NS (MNS) which accreted matter from the SN ejecta. Some observational properties are: Gamma-ray isotropic energy $E_{\rm iso} \lesssim 10^{52}$ erg, rest-frame spectral peak energy $E_{p,i} \lesssim 200$ keV and a local observed rate of $\rho_{\rm XRF} = 100^{+45}_{-34}$ Gpc^{-3} yr^{-1} [266]. We refer the reader to Table 1.2 and [266, 269] for further details on this class. In [307], this class has been divided into BdHN type II, the sources with $10^{50} \lesssim E_{\rm iso} \lesssim 10^{52}$ erg, and BdHN type III, the

sources with $10^{48} \lesssim E_{\rm iso} \lesssim 10^{50}$ erg.

ii. **Binary-driven hypernovae**. Originate in compact $\rm CO_{core}$-NS binaries where the accretion onto the NS becomes high enough to bring it to the point of gravitational collapse, hence forming a BH. We showed that most of these binaries survive to the SN explosion owing to the short orbital periods ($P \sim$ 5 min) for which the mass loss cannot be considered as instantaneous, allowing the binary to keep bound even if more than half of the total binary mass is lost [103]. Therefore, BdHNe produce νNS-BH binaries. Some observational properties are: $E_{\rm iso} \gtrsim 10^{52}$ erg, $E_{p,i} \gtrsim 200$ keV and a local observed rate of $\rho_{\rm BdHN} = 0.77^{+0.09}_{-0.08}$ Gpc^{-3} yr^{-1} [266]. We refer the reader to Table 1.2 and [266, 269] for further details on this class. In [307] this class has been renominated as BdHN type I.

iii. **BH-SN**. These systems originate in $\rm CO_{core}$ (or Helium or Wolf-Rayet star)-BH binaries, hence the hypercritical accretion of the SN explosion of the $\rm CO_{core}$ occurs onto a BH previously formed in the evolution path of the binary. They might be the late evolutionary stages of X-ray binaries such as Cyg X-1 [116, 28], or microquasars [193]. Alternatively, they can form following the evolutionary scenario XI in [107]. If the binary survives to the SN explosion BH-SNe produce νNS-BH, or BH-BH binaries when the central remnant of the SN explosion collapses directly to a BH (see, although, [285, 286]). Some observational properties are: $E_{\rm iso} \gtrsim 10^{54}$ erg, $E_{p,i} \gtrsim 2$ MeV and an upper limit to their rate is $\rho_{\rm BH-SN} \lesssim \rho_{\rm BdHN} = 0.77^{+0.09}_{-0.08}$ Gpc^{-3} yr^{-1}, namely the estimated observed rate of BdHNe type I which by definition covers systems with the above $E_{\rm iso}$ and $E_{p,i}$ range [266]. We refer the reader to Table 1.2 and [266, 269] for further details on this class. In [307] this class has been renominated as BdHN type IV.

Table 1.2. Table summarizing the GRB subclasses, extending and updating previous versions in [307, 266, 269]. We here unify the subclasses under two general names, BdHNe and BMs. Two new GRB subclasses are introduced; BdHN Type III and BM Type IV. In addition to the subclass name in "Class" column and "Type" column, as well as the previous names in "Previous Alias" column, we report the number of GRBs with known redshift identified in each subclass updated by the end of 2016 in "number" column (the value in a bracket indicates the lower limit). We recall as well the "in-state" representing the progenitors and the "out-state" representing the outcomes, as well as the the peak energy of the prompt emission, $E_{\rm p,i}$, the isotropic gamma-ray energy, $E_{\rm iso}$ defined in the 1 keV to 10 MeV energy range, the isotropic emission of ultra-high energy photons, $E_{\rm iso,Gev}$, defined in the 0.1–100 GeV energy range, and the local observed rate $\rho_{\rm GRB}$ [266]. We adopt as definition of kilonova a phenomenon more energetic than a nova (about 1000 times). A kilonova can be an infrared-optical counterpart of a NS-NS merger. In that case the transient is powered by the energy release from the decay of r-process heavy nuclei processed in the merger ejecta [168, 190, 293, 30]. FB-KN stands for fallback-powered kilonova [251, 249]: a WD-WD merger can emit an infrared-optical transient, peaking at ~ 5 day post-merger, with the ejecta powered by accretion of fallback matter onto the newborn WD formed in the merger. The density rate of the GRB subclasses BdHN III (HN) and BM IV (FB-KN) have not yet been estimated.

Class	**Type**	**Previous Alias**	**Number**	***In-State***	***Out-State***	$\boldsymbol{E_{\rm p,i}}$ **(MeV)**	$\boldsymbol{E_{\rm iso}}$ **(erg)**	$\boldsymbol{E_{\rm iso,Gev}}$ **(erg)**	$\boldsymbol{\rho_{\rm GRB}}$ **(Gpc^{-3} yr^{-1})**
Binary-driven	I	BdHN	329	CO_{core}-NS	νNS-BH	~ 0.2–2	$\sim 10^{52}$–10^{54}	$\gtrsim 10^{52}$	$0.77^{+0.09}_{-0.08}$
hypernova	II	XRF	(30)	CO_{core}-NS	νNS-NS	~ 0.01–0.2	$\sim 10^{50}$–10^{52}	–	100^{+45}_{-34}
(BdHN)	III	HN	(19)	CO_{core}-NS	νNS-NS	~ 0.01	$\sim 10^{48}$–10^{50}	–	–
	IV	BH-SN	5	CO_{core}-BH	νNS-BH	$\gtrsim 2$	$> 10^{54}$	$\gtrsim 10^{53}$	$\lesssim 0.77^{+0.09}_{-0.08}$
	I	S-GRF	18	NS-NS	MNS	~ 0.2–2	$\sim 10^{49}$–10^{52}	–	$3.6^{+1.4}_{-1.0}$
Binary	II	S-GRB	6	NS-NS	BH	~ 2–8	$\sim 10^{52}$–10^{53}	$\gtrsim 10^{52}$	$\left(1.9^{+1.8}_{-1.1}\right) \times 10^{-3}$
Merger	III	GRF	(1)	NS-WD	MNS	~ 0.2–2	$\sim 10^{49}$–10^{52}	–	$1.02^{+0.71}_{-0.46}$
(BM)	IV	FB-KN*	(1)	WD-WD	NS/MWD	< 0.2	$< 10^{51}$	–	–
	V	U-GRB	(0)	NS-BH	BH	$\gtrsim 2$	$> 10^{52}$	–	$\approx 0.77^{+0.09}_{-0.08}$

We proceed with the short bursts which are amply thought to originate from compact-object binary mergers. First, we discuss the traditionally proposed binary mergers namely NS-NS and/or NS-BH mergers [121, 209, 85, 204, 189, 244, 166, 29]. These binary mergers can be separated into three subclasses [103, 264, 266]:

iv. **Short Gamma-ray flashes**. They are produced by NS-NS mergers leading to a MNS, namely when the merged core does not reach the critical mass of a NS. Some observational properties are: $E_{\rm iso} \lesssim 10^{52}$ erg, $E_{p,i} \lesssim 2$ MeV and a local observed rate of $\rho_{\rm S-GRF} = 3.6^{+1.4}_{-1.0}$ Gpc^{-3} yr^{-1} [266]. We refer the reader to Table 1.2 and [266, 269] for further details on this class. In [307] this class has been renominated as BM type I.

v. **Authentic short GRBs**. They are produced by NS-NS mergers leading to a BH, namely when the merged core reaches the critical mass of a NS, hence it forms a BH as a central remnant [265, 264, 200]. Some observational properties are: $E_{\rm iso} \gtrsim 10^{52}$ erg, $E_{p,i} \gtrsim 2$ MeV and a local observed rate of $\rho_{\rm S-GRB} = \left(1.9^{+1.8}_{-1.1}\right) \times 10^{-3}$ Gpc^{-3} yr^{-1} [266]. We refer the reader to Table 1.2 and [266, 269] for further details on this class. In [307] this class has been renominated as BM type II.

vi. **Ultra-short GRBs**. This is a theoretical GRB subclass subjected for observational verification. U-GRBs are expected to be produced by νNS-BH mergers whose binary progenitors can be the outcome of BdHNe type I (see II above) or of BdHNe type IV (BH-SN; see III above). The following observational properties are expected: $E_{\rm iso} \gtrsim 10^{52}$ erg, $E_{p,i} \gtrsim 2$ MeV and a local observed rate similar to the one of BdHNe type I since we have shown that most of them are expected to remain bound [103], i.e., $\rho_{\rm U-GRB} \approx \rho_{\rm BdHN} = 0.77^{+0.09}_{-0.08}$ Gpc^{-3} yr^{-1} [266]. We refer the reader to Table 1.2 and [266, 269] for further details on this class. In [307] this class has been renominated as BM type V.

Besides the existence of the above three subclasses of long bursts and three subclasses of short bursts in which the presence of NSs plays a fundamental role, there are two subclasses of bursts in which there is at least a WD component.

vii. **Gamma-ray flashes**. These sources show an extended and softer emission, i.e., they have hybrid properties between long and short bursts and have no associated SNe [67]. It has been proposed that they are produced by NS-WD mergers [266]. These binaries are expected to be very numerous [45] and a variety of evolutionary scenarios for their formation have been proposed [32, 108, 296, 165]. GRFs form a MNS and not a BH [266]. Some observational properties are: $10^{51} \lesssim E_{\rm iso} \lesssim 10^{52}$ erg, $0.2 \lesssim E_{p,i} \lesssim 2$ MeV and a local observed rate of $\rho_{\rm GRF} = 1.02^{+0.71}_{-0.46}$ Gpc^{-3} yr^{-1} [266]. It is worth noting that this rate is low with respect to the one expected from the current number of known NS-WD in the Galaxy [45]. From the GRB observations only one NS-WD merger has been identified (GRB 060614 [46]). This implies that most NS-WD mergers are probably under the threshold of current X and Gamma-ray instruments. We refer the reader to Table 1.2 and [266, 269] for

further details on this class. In [307] this class has been renominated as BM type III.

viii. **Fallback kilonovae**. This is a recently introduced GRB subclass having as progenitors WD-WD mergers [251, 249]. The WD-WD mergers of interest are those that do not produce type Ia SNe but that lead to a massive ($M \sim 1\ M_\odot$), fast rotating ($P \sim 1$–10 s), highly-magnetized ($B \sim 10^9$–10^{10} G) WD. Some observational properties are: $E_{\rm iso} \lesssim 10^{51}$ erg, $E_{p,i} \lesssim 2$ MeV and a local observed rate $\rho_{\rm FB-KN} = (3.7\text{–}6.7) \times 10^5$ Gpc^{-3} yr^{-1} [251, 249, 180, 181]. The coined name FB-KN is due to the fact that they are expected to produce an infrared-optical transient by the cooling of the ejecta expelled in the dynamical phase of the merger and heated up by fallback accretion onto the newly-formed massive WD.

The density rates for all GRB subclasses have been estimated assuming no beaming [266, 269, 251, 249]. The GRB density rates have been analysed in [266] following the method suggested in [291].

The Specific Case of BdHNe

We review in this section the specific case of BdHNe type I and II. As we have mentioned, the progenitor system is an exploding $\rm CO_{core}$ as a type Ic SN in presence of a NS companion [266, 307]. Fig. 1.4 shows a comprehensive summary of the binary path leading to this variety of compact binaries that are progenitors of the above subclasses of long GRBs and that, at the same time, have an intimate connection with the short GRBs.

We emphasize on the theoretical framework concerning the $\rm CO_{core}$-NS binaries which have been extensively studied by our group in a series of publications [246, 133, 105, 103, 25, 24]. The $\rm CO_{core}$ explodes as SN producing an accretion process onto the NS. For sufficiently compact binaries, e.g., orbital periods of the order of few minutes, the accretion is highly super-Eddington (hypercritical) leading to the possibility of the IGC of the NS once it reaches the critical mass, and forms a BH (see Fig. 1.5).

If the binary is not disrupted by the explosion, BdHNe produces new binaries composed of a new NS (νNS) formed at the center of the SN, and a more massive NS or a BH companion (see Fig. 1.4).

In the case of BH formation, the rotation of the BH together with the presence of the magnetic field inherited from the NS and the surrounding matter conform to what we have called the *inner engine* of the high-energy emission [272, 268, 273, 258]. The electromagnetic field of the engine is mathematically described by the Wald solution [306]. The above ingredients induce an electric field around the BH which under the BdHN conditions is initially overcritical, creating electron-positron (e^+e^-) pair plasma which self-accelerates to ultra-relativistic velocities and whose transparency explains to the GRB prompt emission in gamma-rays. The electric field is also able to accelerate protons which along the rotation axis lead to ultra high-energy cosmic rays (UHECRs) of up to 10^{21} eV. In the other directions the acceleration process lead to proton-synchrotron radiation which explains the GeV emission [272, 268]. The interaction/feedback of the GRB into the SN makes it

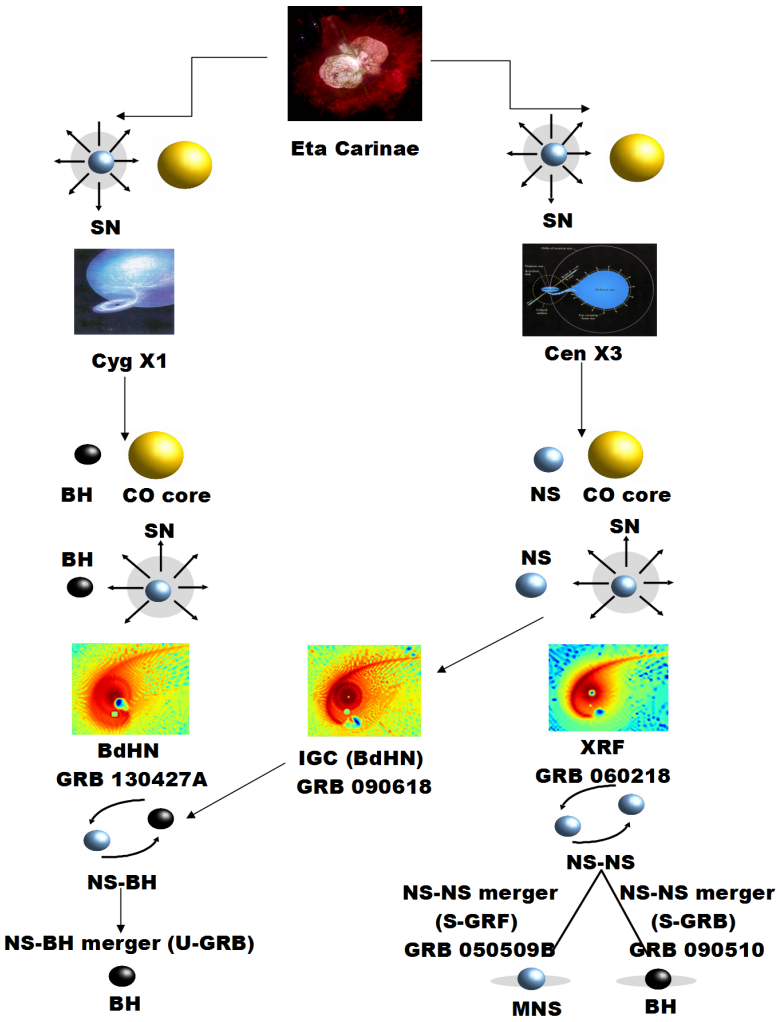

Figure 1.4. Taken from Fig. 1 in [247]. Binary evolutionary paths leading to BdHNe I (previously named BdHNe) and II (previously named XRFs) and whose out-states, in due time, evolve into progenitors of short GRBs. The massive binary has to survive two core-collapse SN events. The first event forms a NS (right-side path) or BH (left-side path). The massive companion continues its evolution until it forms a CO_{core}. This simplified evolution diagram which does not show intermediate stages such as common-envelope phases (see, e.g., [103, 25], and references therein). At this stage the binary is a CO_{core}-NS (right-side path) or a CO_{core}-BH (left-side path). Then, it occurs the second SN event which forms what we call the νNS at its center. We focus in this here to review the theoretical and observational aspects of interaction of this SN event with the NS companion (BdHNe I and II). We do not treat here the case of a SN exploding in an already formed BH companion (BdHNe IV). At this point the system can form a νNS-BH/NS (BdHN I/II) binary (right-side path), or a νNS-BH (BdHN IV) in the (left-side path). The emission of gravitational waves will make this compact-object binaries to merge, becoming progenitors of short GRBs [103]. We recall to the reader that S-GRBs and S-GRFs stand for, respectively, authentic short GRBs and short Gamma-ray flashes, the two subclasses of short bursts from NS-NS mergers, the former produced when the merger leads to a more massive NS and the latter when a BH is formed [266].

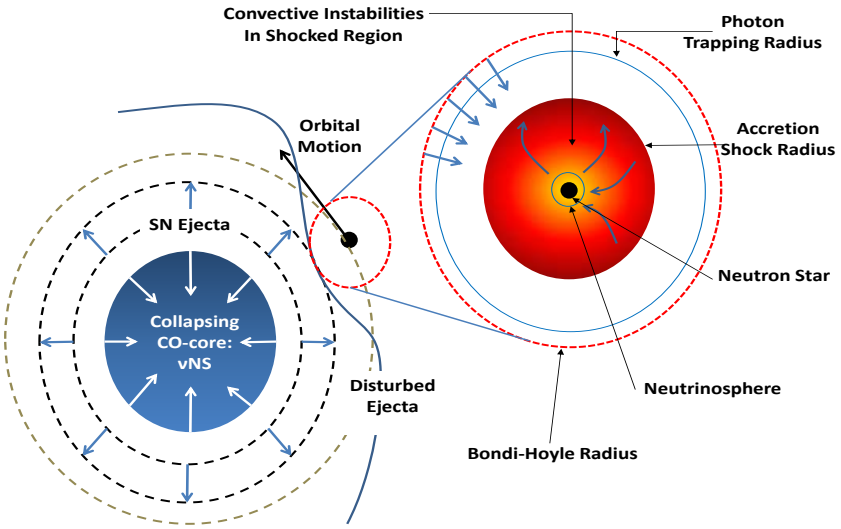

Figure 1.5. Scheme of the IGC scenario (taken from Fig. 1 in [105]). The CO_{core} undergoes SN explosion, NS accretes part of the SN ejecta and then reaches the critical mass for gravitational collapse to a BH, with consequent emission of a GRB. The SN ejecta reach the NS Bondi-Hoyle radius and fall toward the NS surface. The material shocks and decelerates while it piles over the NS surface. At the neutrino emission zone, neutrinos take away most of the gravitational energy gained by the matter infall. The neutrinos are emitted above the NS surface that allow the material to reduce its entropy to be finally incorporated to the NS. For further details and numerical simulations of the above process see [105, 25, 24].

become the hypernova (HN) [270, 26] observed in the optical, powered by nickel decay, a few days after the GRB trigger. The SN shock breakout and the hypercritical accretion can be observed as X-ray precursors [24]. The e^+e^- feedback onto the SN ejecta also produces gamma- and X-ray flares observed in the early afterglow [267]. The synchrotron emission by relativistic electrons from the νNS in the expanding magnetized HN ejecta and the νNS pulsar emission explain the early and late X-ray afterglow [257].

1.2.3 Simulations of the IGC process and BdHNe

Preamble: First Analytic Estimates

The IGC scenario was formulated in 2012 [246] presenting a comprehensive astrophysical picture supporting this idea as well as a possible evolutionary scenario leading to the progenitor CO_{core}-NS binaries. It was also there presented an analytic formula for the accretion rate onto the NS companion on the basis of the following simplified assumptions: (1) a uniform density profile of the pre-SN CO_{core}; (2) the ejecta was evolved following an homologous expansion; (3) the mass of the NS (assumed to be initially 1.4 $M_\odot$) and the CO_{core} (in the range 4–8 $M_\odot$) were assumed nearly constant. So, it was shown that the accretion rate onto the NS is highly super-Eddington, namely it is hypercritical, reaching values of up to 0.1 $M_\odot$ s^{-1} for compact binaries with orbital periods of the order of a few minutes. This estimate implied that the hypercritical accretion could induce the gravitational collapse of

the NS which, in a few seconds, would reach the critical mass with consequence formation of a BH. A first test of this IGC first model in real data was soon presented in the case of GRB 090618 [133].

First Numerical Simulations: 1D Approximation

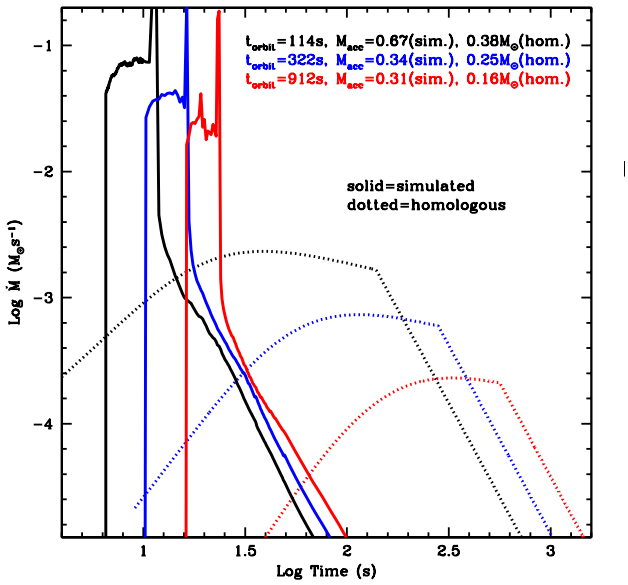

Figure 1.6. Hypercritical accretion rate onto the NS companion for selected separation distances. The CO_{core} is obtained with a progenitor star of zero-age main-sequence (ZAMS) mass of 20 $M_\odot$, calculated in [105]. The numerical calculation leads to a sharper accretion profile with respect to the one obtained assuming homologous expansion of the SN ejecta. Taken from Fig. 3 in [105].

The first numerical simulations were implemented in 2014 in [105] via a 1D code including (see Fig. 1.6): (1) the modeling of the SN via the 1D core-collapse SN code of Los Alamos [99]; (2) the micro-physics experienced by the inflow within the accretion region including the neutrino (ν) emission and hydrodynamics processes such as shock formation; (3) with the above it was followed by the evolution of the material reaching the Bondi-Hoyle capture region and the subsequent in-fall up to the NS surface. Hypercritical accretion rates in the range 10^{-3}–10^{-1} $M_\odot$ s^{-1} were inferred, confirming the first analytic estimates and the IGC of the NS companion for binary component masses similar to the previous ones and for orbital periods of the order of 5 min.

The above simulations were relevant in determining that the fate of the system is mainly determined by the binary period (P); the SN ejecta velocity (v_{ej}) and the NS initial mass. P and v_{ej} enter explicitly in the Bondi-Hoyle accretion rate formula through the capture radius expression, and implicitly via the ejecta density since they influence the decompression state of the SN material at the NS position.

2D Simulations Including Angular Momentum Transfer

Soon after, in 2015, we implemented in [25] a series of improvements to the above calculations by relaxing some of the aforementioned assumptions (see Fig. 1.7). We adopted for the ejecta a density profile following a power-law with the radial distance and evolved it with an homologous expansion. The angular momentum transport, not included in the previous estimates, was included. With this addition it was possible to estimate the spin-up of the NS companion by the transfer of angular momentum from the in-falling matter which was shown to circularize around the NS before being accreted. General relativistic effects were also introduced, when calculating the evolution of the structure parameters (mass, radius, spin, etc) of the accreting NS, in the NS gravitational binding energy, and in the angular momentum transfer by the circularized particles being accreted from the innermost circular orbit.

One of the most important results of [25] was that, taking into account that the longer the orbital P the lower the accretion rate, it was there computed the maximum orbital period ($P_{\rm max}$) for which the NS reaches the critical mass for gravitational collapse, so for BH formation. The dependence of $P_{\rm max}$ on the initial mass of the NS was also there explored. The orbital period $P_{\rm max}$ was then presented as the separatrix of two families of long GRBs associated with these binaries: at the time we called them *Family-1*, the systems in which the NS does not reach the critical mass, and *Family-2* the ones in which it reaches the critical mass and forms a BH. It can be seen that the Family-1 and Family-2 long GRBs evolve subsequently into the concepts of *XRFs* and *BdHNe*, respectively.

First 3D Simulations

A great step toward the most recent simulations was achieved in 2016 in [24] where an SPH-like simulation was implemented in which the SN ejecta was emulated by "point-like" particles. The mass and number of the particles populating each layer were assigned, for self-consistency, according to the power-law density profile. The initial velocity of the particles of each layer was set, in agreement with the chosen power-law density profile, following a radial velocity distribution; i.e., $v \propto r$.

The evolution of the SN particles was followed by Newtonian equations of motion in the gravitational field of the NS companion, also taking into account the orbital motion which was included under the assumption that the NS performs a circular orbit around the $\rm CO_{core}$ center that acts as the common center-of-mass, namely assuming that the mass of the pre-SN core is much larger than the NS mass.

The accretion rate onto the NS was computed, as in [25], using the Bondi-Hoyle accretion formula and, every particle reaching the Bondi-Hoyle surface, was removed from the system. The maximum orbital period $P_{\rm max}$ in which the NS collapses by accretion could be further explored including the dependence on the mass of the pre-SN $\rm CO_{core}$, in addition to the dependence on the NS mass.

A detailed study of the hydrodynamics and the neutrino emission in the accretion region on top the NS surface was performed. Concerning the neutrino emission, ν and $\bar{\nu}$ production processes were considered and showed that electron-positron annihilation ($e^+e^- \rightarrow \nu\bar{\nu}$) overcomes by orders of magnitude any other mechanism

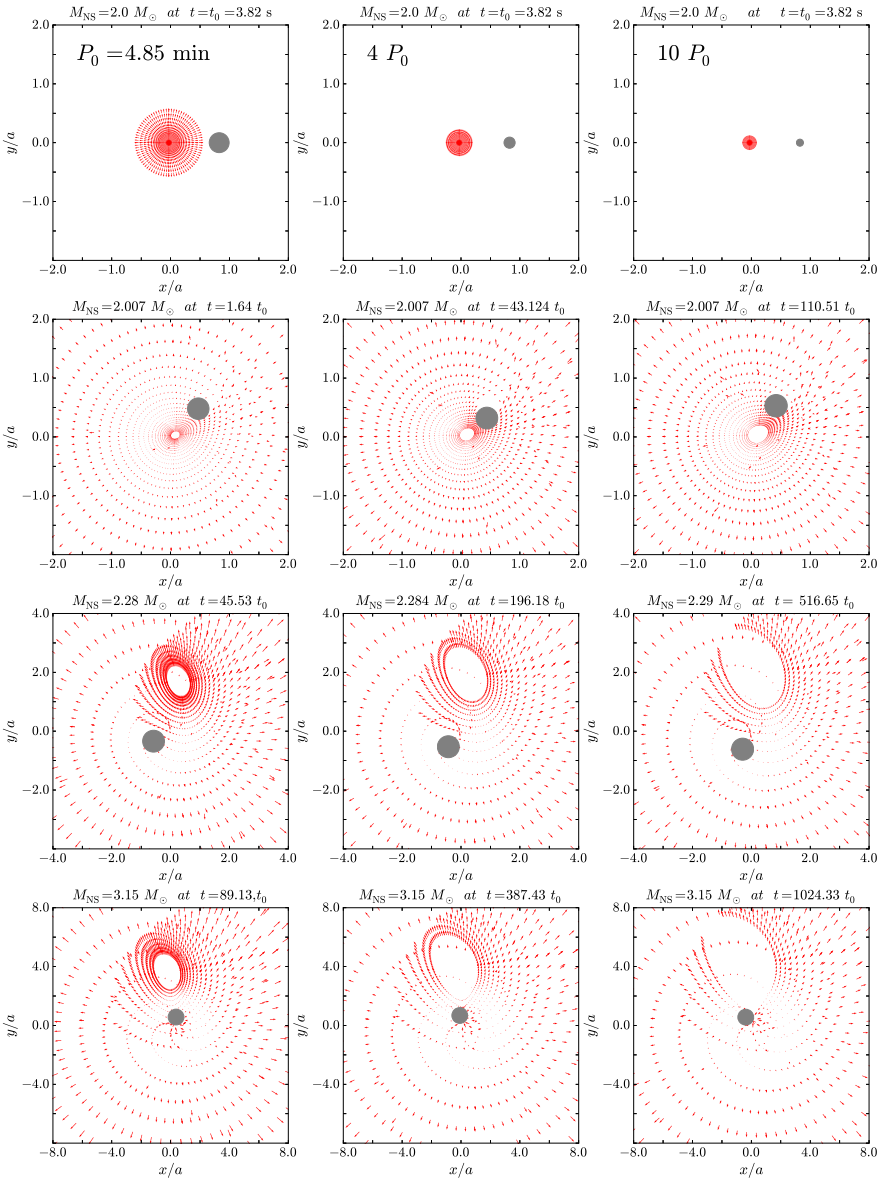

Figure 1.7. Numerical simulations of the SN ejecta velocity field (red arrows) at selected times of the accretion process onto the NS (taken from Fig. 3 in [25]). In these snapshots we have adopted the CO_{core} obtained from a $M_{ZAMS} = 30\ M_\odot$ progenitor; an ejecta outermost layer velocity $v_{0_{star}} = 2 \times 10^9$ cm s^{-1}, an initial NS mass, $M_{NS}(t = t_0) = 2.0\ M_\odot$. The minimum orbital period to have no Roche-lobe overflow is $P_0 = 4.85$ min. In the left, central and right columns of snapshots we show the results for binary periods $P = P_0$, $4P_0$, and $10P_0$, respectively. The Bondi-Hoyle surface, the filled gray circle, increases as the evolution continues mainly due to the increase of the NS mass (the decrease of the lower panels is only apparent due to the enlargement of the x-y scales). The x-y positions refer to the center-of-mass reference frame. The last image in each column corresponds to the instant when the NS reaches the critical mass value. For the initial conditions of these simulations, the NS ends its evolution at the mass-shedding limit with a maximum value of the angular momentum $J = 6.14 \times 10^{49}$ g cm^2 s^{-1} and a corresponding critical mass of 3.15 $M_\odot$.

of neutrino emission in the range of accretion rates 10^{-8}–10^{-2} $M_\odot$ s^{-1}, relevant for XRFs and BdHNe. The neutrino luminosity can reach values of up to 10^{52} erg s^{-1} and the neutrino mean energy of 20 MeV for the above upper value of the accretion rate. For the reader interested in the neutrino emission, we refer to [27] for a detailed analysis of the neutrino production in XRFs and BdHNe including flavour oscillations experienced by the neutrinos before abandoning the system.

Concerning the hydrodynamics, the evolution of the temperature and density of outflows occurring during the accretion process owing to convective instabilities was estimated. It was there shown the interesting result that the temperature of this outflow and its evolution can explain the early (i.e., precursors) X-ray emission that has been observed in some BdHNe and in XRFs, exemplified there analyzing the early X-ray emission observed in GRB 090618, a BdHN I, and in GRB 060218, a BdHN II (an XRF).

A most important result of these simulations was the possibility of having a first glance of the morphology acquired by the SN ejecta: the matter density, initially spherically symmetric, becomes highly asymmetric due to the accretion process and the action of the gravitational field of the NS companion (see Fig. 1.8).

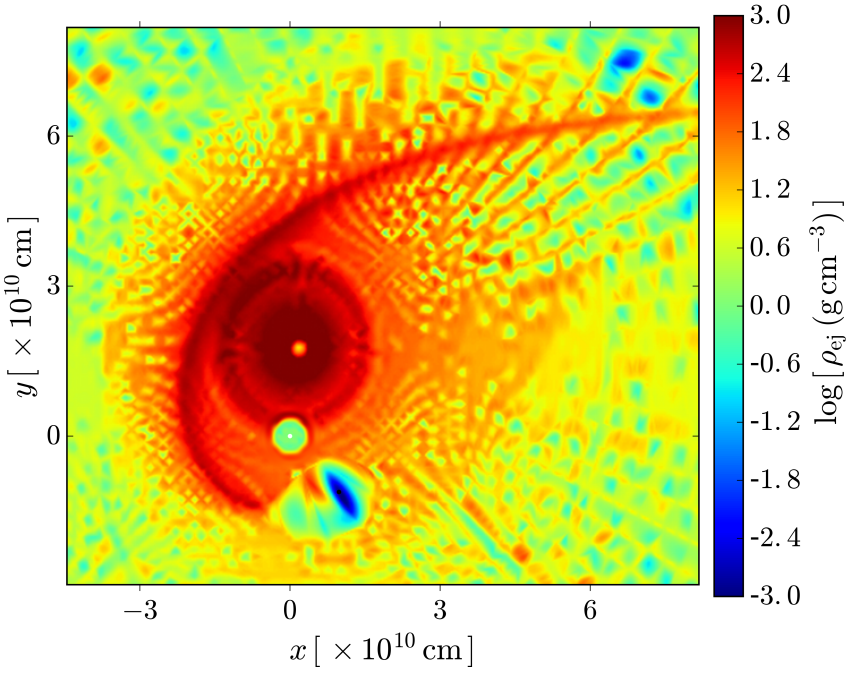

Figure 1.8. Snapshot of the SN ejecta density in the orbital plane of the $\mathrm{CO_{core}}$-NS binary. Numerical simulation taken from Fig. 6 in [24]. The plot corresponds to the instant when the NS reaches the critical mass and forms the BH (black dot at $(1,-1)$), approximately 250 s from the SN explosion. The νNS is represented by the white dot at the origin $(0,0)$. The binary parameters are: the initial mass of the NS companion is 2.0 $M_\odot$; the $\mathrm{CO_{core}}$ leading to an ejecta mass of 7.94 $M_\odot$, and the orbital period is $P \approx 5$ min, namely a binary separation $a \approx 1.5 \times 10^{10}$ cm.

Most Recent 3D SPH Simulations

We have recently presented in [26] new, 3D hydrodynamic simulations of the IGC scenario by adapting the SPH code developed at Los Alamos, *SNSPH* [104], which has been tested and applied in a variety of astrophysical situations [106, 319, 72, 22].

The time $t = 0$ of the simulation is set as the time at which the SN shock breaks out the CO_{core} external radius. We calculate the accretion rate both onto the NS companion and onto the νNS (via fallback), and calculate the evolution of other binary parameters such as the orbital separation, eccentricity, etc. Fig. 1.9 shows an example of simulation for a binary system composed of a CO_{core} of mass $\approx 6.85\ M_\odot$, the end stage of a ZAMS progenitor star of $M_{zams} = 25\ M_\odot$, and a $2\ M_\odot$ NS companion. The initial orbital period is ≈ 5 min.

The accretion rate onto both stars was estimated from the flux of SPH particles falling, per unit time, into the Bondi-Hoyle accretion region of the NS (see Fig. 1.10). It is confirmed that the accretion onto the NS companion occurs from a disk-like structure formed by the particles that circularize before being accreted; see vortexes in the upper panel of Fig. 1.9 and the disk structure is clearly seen in the lower panel.

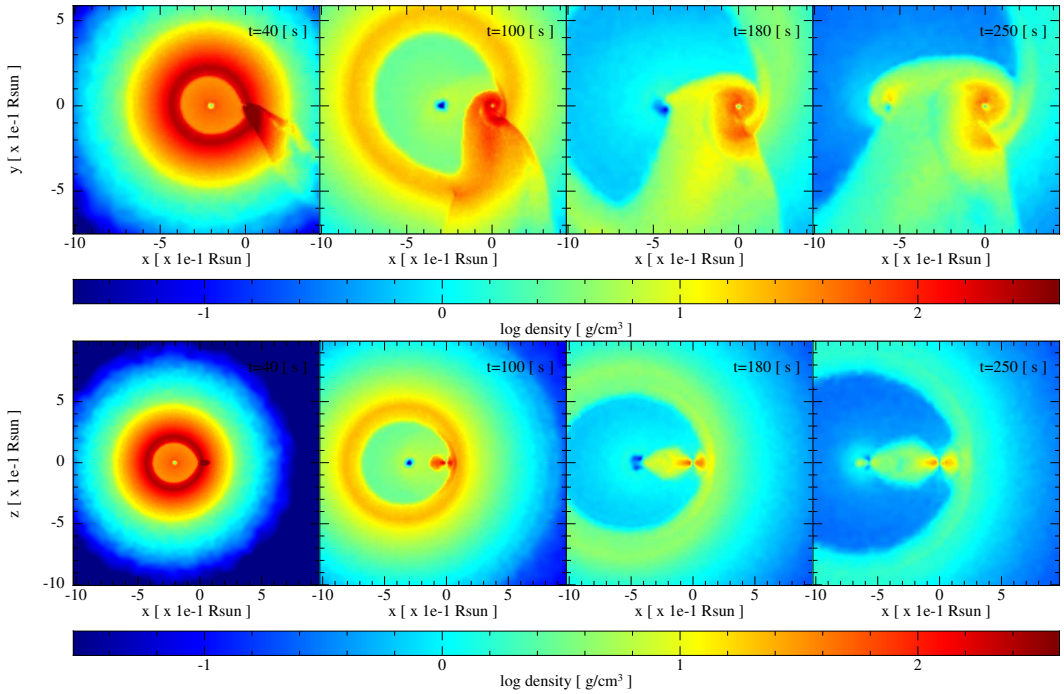

Figure 1.9. Snapshots of the 3D SPH simulations of the IGC scenario (taken from Fig. 2 in [26]). The initial binary system is formed by a CO_{core} of mass $\approx 6.85\ M_\odot$, from a ZAMS progenitor star of $25\ M_\odot$, and a $2\ M_\odot$ NS with an initial orbital period of approximately 5 min. The upper panel shows the mass density on the equatorial (orbital) plane, at different times of the simulation. The time $t = 0$ is set in our simulations at the moment of the SN shock breakout. The lower panel shows the plane orthogonal to the orbital one. The reference system has been rotated and translated for the x-axis to be along the line joining the νNS and the NS centers, and its origin is at the NS position.

Several binary parameters were explored thanks to the new code. We performed

simulations changing the CO_{core} mass, the NS companion mass, the orbital period, the SN explosion energy (so the SN kinetic energy or velocity). We also explored intrinsically asymmetric SN explosion. We checked if the νNS and/or the NS companion reach the mass-shedding (Keplerian) limit or the secular axisymmetric instability, i.e., the critical mass. The NS can also become just a more massive, fast rotating, stable NS when the accretion is moderate. All this was done for various NS nuclear equations of state (NL3, TM1 and GM1).

We followed the orbital evolution up to the instant when most of the ejecta has abandoned the system to determine if the system remains bound or becomes unbound by the explosion. We thus assessed the CO_{core}-NS parameters leading to the formation of νNS-NS (from XRFs) or νNS-BH (from BdHNe) binaries. The first proof that BdHNe remain bound leading to νNS-BH binaries was presented in [103] (see next section).

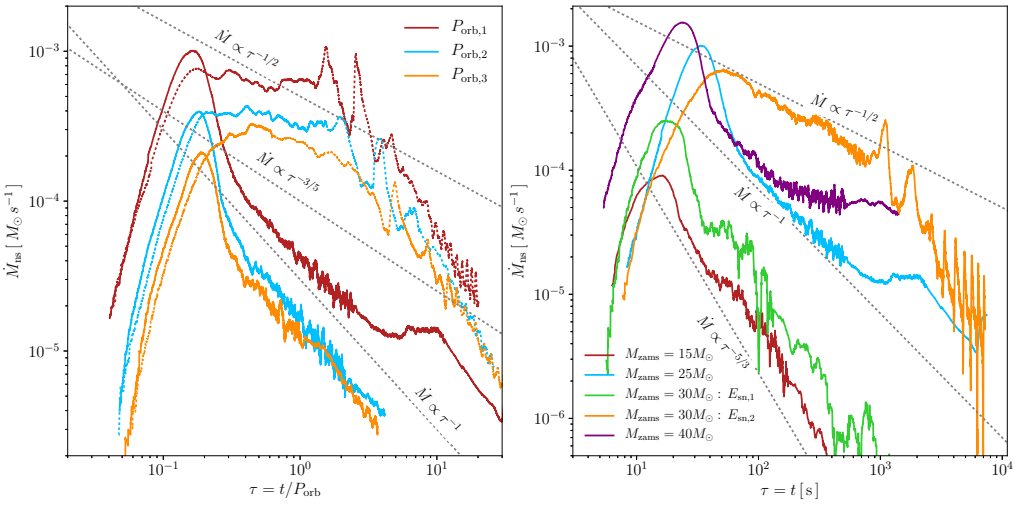

Figure 1.10. (**a**) Mass-accretion rate onto the NS companion in the IGC scenario (taken from Fig. 9 in [26]). Different colors correspond to different initial orbital periods: $P_{orb,1} = 4.8$ min (red line), $P_{orb,1} = 8.1$ min (blue line), $P_{orb,1} = 11.8$ min (orange line). The other parameters that characterize the initial binary system are the same as in Fig. 1.9. The solid lines correspond to a SN energy of 1.57×10^{51} erg, while the dotted ones correspond to a lower SN energy of 6.5×10^{50} erg. It can be seen that the mass-accretion rate scales with the binary orbital period. (**b**) Mass-accretion rate on the NS companion for all the CO_{core} progenitors (see Table 1 and Fig. 13 in [26]). The NS companion has an initial mass of $2\,M_\odot$ and the orbital period is close to the minimum period that the system can have in order that there is no Roche-lobe overflow before the collapse of the CO_{core}: 6.5 min, 4.8 min, 6.0 min and 4.4 min for the $M_{zams} = 15M_\odot$, $25M_\odot$, $30M_\odot$ and $40M_\odot$ progenitors, respectively.

1.2.4 Hypercritical Accretion: Rate and Hydrodynamics

We now give details of the accretion process within the IGC scenario following [105, 25, 103, 24]. There are two main physical conditions for which hypercritical (i.e., highly super-Eddington) accretion onto the NS occurs in XRFs and BdHNe. The first is that the photons are trapped within the inflowing material and the second is that

the shocked atmosphere on top of the NS becomes sufficiently hot ($T \sim 10^{10}$ K) and dense ($\rho \gtrsim 10^6$ g cm^{-3}) to produce a very efficient neutrino–anti-neutrino cooling emission. In this way the neutrinos become mainly responsible for releasing the energy gained by accretion, allowing hypercritical accretion to continue.

Accretion Rate and NS Evolution

The first numerical simulations of the IGC were performed in [105], including: (1) realistic SN explosions of the CO_{core}; (2) the hydrodynamics within the accretion region; (3) the simulated evolution of the SN ejecta up to their accretion onto the NS. [25] then estimated the amount of angular momentum carried by the SN ejecta and how much is transferred to the NS companion by accretion. They showed that the SN ejecta can circularize for a short time and form a disc-like structure surrounding the NS before being accreted. The evolution of the NS central density and rotation angular velocity (the NS is spun up by accretion) was computed from full numerical solutions of the axisymmetric Einstein equations. The unstable limits of the NS are set by the mass-shedding (or Keplerian) limit and the critical point of gravitational collapse given by the secular axisymmetric instability [25]. The accretion rate of the SN ejecta onto the NS is given by:

$$\dot{M}_B(t) = \pi \rho_{ej} R_{cap}^2 \sqrt{v_{rel}^2 + c_{s,ej}^2}, \qquad R_{cap}(t) = \frac{2M_{NS}(t)}{v_{rel}^2 + c_{s,ej}^2}, \tag{1.23}$$

where ρ_{ej} and $c_{s,ej}$ are the density and sound speed of the ejecta, R_{cap} and M_{NS} are the NS gravitational capture radius (Bondi-Hoyle radius) and gravitational mass, and v_{rel} the ejecta velocity relative to the NS: $\vec{v}_{rel} = \vec{v}_{orb} - \vec{v}_{ej}$; $|\vec{v}_{orb}| = \sqrt{(M_{core} + M_{NS})/a}$, and $\vec{v}_{ej}$ is the velocity of the supernova ejecta (see Fig. 1.5).

Numerical simulations of the SN explosions suggest the adopted homologous expansion of the SN, i.e., $v_{ej}(r,t) = nr/t$, where r is the position of each layer from the SN center and n is the expansion parameter. The density evolves as

$$\rho_{ej}(r,t) = \rho_{ej}^0(r/R_{star}(t), t_0) \frac{M_{env}(t)}{M_{env}(0)} \left(\frac{R_{star}(0)}{R_{star}(t)}\right)^3, \tag{1.24}$$

where $M_{env}(t)$ the mass of the CO_{core} envelope, $R_{star}(t)$ is the radius of the outermost layer, and ρ_{ej}^0 is the pre-SN CO_{core} density profile; $\rho_{ej}(r,t_0) = \rho_{core}(R_{core}/r)^m$, where ρ_{core}, R_{core} and m are the profile parameters obtained from numerical simulations. Typical parameters of the CO_{core} mass are (3.5–9.5) $M_\odot$ corresponding to (15–30) $M_\odot$ zero-age-main-sequence (ZAMS) progenitors (see [105, 25] for details). The binary period is limited from below by the request of having no Roche lobe overflow by the CO_{core} before the SN explosion [105]. For instance, for a CO_{core} of 9.5 $M_\odot$ forming a binary system with a 2 $M_\odot$ NS, the minimum orbital period allowed by this condition is $P_{min} \approx 5$ min. For these typical binary and pre-SN parameters, Equation (1.23) gives accretion rates 10^{-4}–$10^{-2} M_\odot$ s^{-1}.

We adopt an initially non-rotating NS companion so its exterior spacetime at time $t = 0$ is described by the Schwarzschild metric. The SN ejecta approach the NS with specific angular momentum, $l_{acc} = \dot{L}_{cap}/\dot{M}_B$, circularizing at a radius $r_{circ} \geq r_{lco}$ if $l_{acc} \geq l_{lso}$ with r_{lco} the radius of the last circular orbit (LCO). For a non-rotating NS $r_{lco} = 6M_{NS}$ and $l_{lco} = 2\sqrt{3}M_{NS}$. For typical parameters, $r_{circ}/r_{lco} \sim 10$–10^3.

The accretion onto the NS proceeds from the radius $r_{\rm in}$. The NS mass and angular angular momentum evolve as [25, 54]:

$$\dot{M}_{\rm NS} = \left(\frac{\partial M_{\rm NS}}{\partial M_b}\right)_{J_{\rm NS}} \dot{M}_b + \left(\frac{\partial M_{\rm NS}}{\partial J_{\rm NS}}\right)_{M_b} \dot{J}_{\rm NS}, \qquad \dot{J}_{\rm NS} = \xi\, l(r_{\rm in}) \dot{M}_{\rm B}, \tag{1.25}$$

where M_b is the NS baryonic mass, $l(r_{\rm in})$ is the specific angular momentum of the accreted material at $r_{\rm in}$, which corresponds to the angular momentum of the LCO, and $\xi \leq 1$ is a parameter that measures the efficiency of angular momentum transfer. In this picture we have $\dot{M}_b = \dot{M}_B$.

For the integration of Equations (1.23) and (1.25) we have to supply the values of the two partial derivatives in Equation (1.25). They are obtained from the relation of the NS gravitational mass, $M_{\rm NS}$, with M_b and $J_{\rm NS}$, namely from the knowledge of the NS binding energy. For this we use the general relativistic calculations of rotating NSs presented in [53]. They show that, independent on the nuclear EOS, the following analytical formula represents the numerical results with sufficient accuracy (error $< 2\%$):

$$\frac{M_b}{M_\odot} = \frac{M_{\rm NS}}{M_\odot} + \frac{13}{200}\left(\frac{M_{\rm NS}}{M_\odot}\right)^2 \left(1 - \frac{1}{137} j_{\rm NS}^{1.7}\right), \tag{1.26}$$

where $j_{\rm NS} \equiv J_{\rm NS}/(M_\odot^2)$.

In the accretion process, the NS gains angular momentum and therefore spins up. To evaluate the amount of angular momentum transferred to the NS at any time we include the dependence of the LCO specific angular momentum as a function of $M_{\rm NS}$ and $J_{\rm NS}$. For corotating orbits, the following relation is valid for the NL3, TM1 and GM1 EOS [54, 25]:

$$l_{\rm lco} = M_{\rm NS}\left[2\sqrt{3} - 0.37\left(\frac{j_{\rm NS}}{M_{\rm NS}/M_\odot}\right)^{0.85}\right]. \tag{1.27}$$

The NS continues the accretion until it reaches an instability limit or up to when all the SN ejecta overcomes the NS Bondi-Hoyle region. We take into account the two main instability limits for rotating NSs: the mass-shedding or Keplerian limit and the secular axisymmetric instability limit. The latter defines critical NS mass. For the aforementioned nuclear EOS, the critical mass can be approximately written as [53]:

$$M_{\rm NS}^{\rm crit} = M_{\rm NS}^{J=0}(1 + k j_{\rm NS}^p), \tag{1.28}$$

where k and p are EOS-dependent parameters (see Table 1.3). These formulas fit the numerical results with a maximum error of 0.45%.

Additional details and improvements of the hypercritical accretion process leading to XRFs and BdHNe were presented in [24]. Specifically:

1. The density profile included finite size/thickness effects and additional $\rm CO_{core}$ progenitors, leading to different SN ejecta masses being considered.

2. In [25] the maximum orbital period, $P_{\rm max}$, over which the accretion onto NS companion is not sufficient to bring it to the critical mass, was inferred. Thus, binaries with $P > P_{\rm max}$ lead to XRFs while the ones with $P \lesssim P_{\rm max}$ lead to BdHNe. Becerra et al. [24] extended the determination of $P_{\rm max}$ for all the

Table 1.3. Critical NS mass in the non-rotating case and constants k and p needed to compute the NS critical mass in the non-rotating case given by Equation (1.28). The values are for the NL3, GM1 and TM1 EOS.

EOS	$M_{\rm crit}^{J=0}$ $(M_\odot)$	p	k
NL3	2.81	1.68	0.006
GM1	2.39	1.69	0.011
TM1	2.20	1.61	0.017

possible initial values of the NS mass. They also examined the outcomes for different values of the angular momentum transfer efficiency parameter.

3. The expected luminosity during the process of hypercritical accretion for a wide range of binary periods covering both XRFs and BdHNe was estimated.

4. It was shown that the presence of the NS companion originates asymmetries in the SN ejecta (see, e.g., Fig. 6 in [24]). The signatures of such asymmetries in the X-ray emission was there shown in the specific example of XRF 060218.

Hydrodynamics in the Accretion Region

The accretion rate onto the NS can be as high as $\sim 10^{-2}$–10^{-1} $M_\odot$ s^{-1}. For such accretion rates:

1. The magnetic pressure is much smaller than the random pressure of the infalling material, therefore the magnetic-field effects on the accretion process are negligible [101, 246].

2. The photons are trapped within the infalling matter, hence the Eddington limit does not apply and hypercritical accretion occurs. The trapping radius is defined as [52]:

$$r_{\rm trapping} = \min\{\dot{M}_B\kappa/(4\pi), R_{\rm cap}\}, \tag{1.29}$$

where κ is the opacity. [105] estimated a Rosseland mean opacity of $\approx 5 \times 10^3$ cm^2 g^{-1} for the CO$_{\rm cores}$. This, together with our typical accretion rates, lead to $\dot{M}_B\kappa/(4\pi) \sim 10^{13}$–$10^{19}$ cm. This radius is much bigger than the Bondi-Hoyle radius.

3. The above condition, and the temperature-density values reached on top of the NS surface, lead to an efficient neutrino cooling which radiates away the gain of gravitational energy of the infalling material [322, 262, 101, 246, 105].

The accretion shock moves outward as the material piles onto the NS. Since the post-shock entropy is inversely proportional to the shock radius position, the NS atmosphere is unstable with respect to Rayleigh-Taylor convection at the beginning

of the accretion process. Such instabilities might drive high-velocity outflows from the accreting NS [102, 100]. The entropy at the base of the atmosphere is [101]:

$$S_{\rm bubble} \approx 16 \left(\frac{1.4\,M_\odot}{M_{\rm NS}}\right)^{-7/8} \left(\frac{M_\odot\,{\rm s}^{-1}}{\dot{M}_{\rm B}}\right)^{1/4} \left(\frac{10^6\,{\rm cm}}{r}\right)^{3/8} /{\rm nucleon}, \qquad (1.30)$$

The material expands and cools down adiabatically, i.e., $T^3/\rho =$ constant. In the case of a spherically symmetric expansion, $\rho \propto 1/r^3$ and

$$T_{\rm bubble} = 195\, S_{\rm bubble}^{-1} \left(\frac{10^6\,{\rm cm}}{r}\right) \quad {\rm MeV}. \qquad (1.31)$$

In the more likely case that the material expand laterally we have [100]: $\rho \propto 1/r^2$, i.e., $T_{\rm bubble} = T_0(S_{\rm bubble})\,(r_0/r)^{2/3}$, where $T_0(S_{\rm bubble})$ is obtained from the above equation at $r = r_0 \approx R_{\rm NS}$. This implies a bolometric blackbody flux at the source from the rising bubbles:

$$F_{\rm bubble} \approx 2\times 10^{40} \left(\frac{M_{\rm NS}}{1.4\,M_\odot}\right)^{-7/2} \left(\frac{\dot{M}_{\rm B}}{M_\odot\,{\rm s}^{-1}}\right) \left(\frac{R_{\rm NS}}{10^6\,{\rm cm}}\right)^{3/2} \left(\frac{r_0}{r}\right)^{8/3} {\rm erg\,s^{-1}cm^{-2}}. \qquad (1.32)$$

The above thermal emission has been shown [105] to be a plausible explanation of the early X-ray (precursor) emission observed in some GRBs. The X-ray precursor observed in GRB 090618 [134, 133] is explained adopting an accretion rate of $10^{-2}\ M_\odot\ {\rm s}^{-1}$, the bubble temperature drops from 50 keV to 15 keV while expanding from $r \approx 10^9$ cm to 6×10^9 cm (see Fig. 1.11). More recently, the X-ray precursor has been observed in GRB 180728A and it is well explained by a bubble of $\sim$7 keV at $\sim 10^{10}$ cm and an accretion rate of $10^{-3}\ M_\odot\ {\rm s}^{-1}$ (see [307] for details).

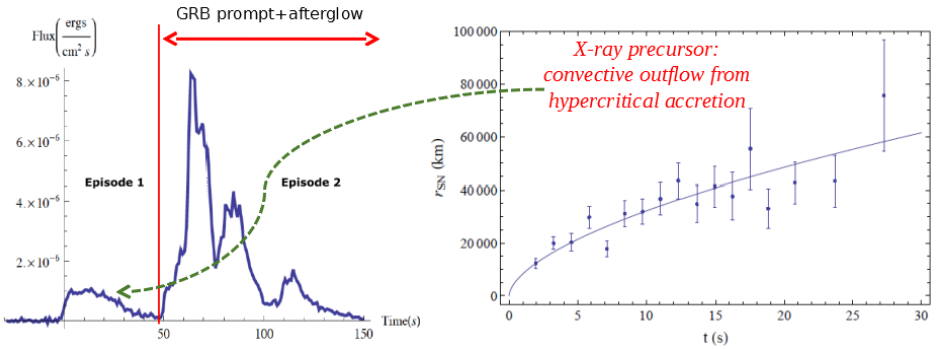

Figure 1.11. (**a**) Fermi-GBM (NaI 8–440 keV) light-curve of GRB 090618 (adapted from Fig. 1 in [134]). (**b**) Expanding radius of the thermal blackbody emission observed in the "Episode 1" of GRB 090618 (adapted from Fig. 2 in [134]). The interpretation of such an X-ray precursor as being due to the emission of the convective bubbles during the process of hypercritical accretion onto the NS was proposed for the first time in [105].

Accretion Luminosity

The energy release in a time-interval dt, when an amount of mass dM_b with angular momentum $l\dot{M}_b$ is accreted, is [24]:

$$L_{\rm acc} = \dot{M}_b - \dot{M}_{\rm NS} = \dot{M}_b \left[1 - \left(\frac{\partial M_{\rm NS}}{\partial J_{\rm NS}}\right)_{M_b} l - \left(\frac{\partial M_{\rm NS}}{\partial M_b}\right)_{J_{\rm NS}}\right]. \tag{1.33}$$

This is the amount of gravitational energy gained by the matter by infalling to the NS surface that is not spent in NS gravitational binding energy. The total energy release in the time interval from t to $t + dt$,

$$\Delta E_{\rm acc} \equiv \int L_{\rm acc} dt, \tag{1.34}$$

is given by the NS binding energy difference between its initial and final state. The typical luminosity is $L_{\rm acc} \approx \Delta E_{\rm acc}/\Delta t_{\rm acc}$, where $\Delta t_{\rm acc}$ is the duration of the accretion process.

The value of $\Delta t_{\rm acc}$ is approximately given by the flow time of the slowest layers of the SN ejecta to the NS companion position. If we denote the velocity of these layers by $v_{\rm inner}$, we have $\Delta t_{\rm acc} \sim a/v_{\rm inner}$, where a is the binary separation. For $a \sim 10^{11}$ cm and $v_{\rm inner} \sim 10^8$ cm s^{-1}, $\Delta t_{\rm acc} \sim 10^3$ s. For shorter separations, e.g., $a \sim 10^{10}$ cm ($P \sim 5$ min), $\Delta t_{\rm acc} \sim 10^2$ s. For a binary with $P = 5$ min, the NS accretes $\approx 1\ M_\odot$ in $\Delta t_{\rm acc} \approx 100$ s. From Equation (1.26) one obtains that the binding energy difference of a 2 $M_\odot$ and a 3 $M_\odot$ NS, is $\Delta E_{\rm acc} \approx 13/200(3^2 - 2^2)\ M_\odot \approx 0.32\ M_\odot$. This leads to $L_{\rm acc} \approx 3 \times 10^{-3}\ M_\odot \approx 0.1\dot{M}_b$. The accretion power can be as high as $L_{\rm acc} \sim 0.1\dot{M}_b \sim 10^{47}$–$10^{51}$ erg s^{-1} for accretion rates in the range $\dot{M}_b \sim 10^{-6}$–$10^{-2}\ M_\odot$ s^{-1}.

1.2.5 Post-Explosion Orbits and Formation of NS-BH Binaries

The SN explosion leaves as a central remnant a νNS and the induced gravitational collapse of the NS companion leads to BH formation. Therefore, BdHNe potentially leads to νNS-BH binaries, providing the binary keeps bound. This question was analysed via numerical simulations in [103].

Typical binaries become unbound during an SN explosion because of mass loss and the momentum imparted (kick) to the νNS by the explosion. A classical astrophysical result shows that, assuming the explosion as instantaneous (sudden mass loss approximation), disruption occurs if half of the binary mass is lost. For this reason the fraction of massive binaries that can produce double compact-object binaries is usually found to be very low (e.g., ∼0.001–1%) [107, 76, 229].

Assuming instantaneous mass loss, the post-explosion semi-major axis is [130]:

$$\frac{a}{a_0} = \frac{M_0 - \Delta M}{M_0 - 2a_0 \Delta M/r}, \tag{1.35}$$

where a_0 and a are the initial and final semi-major axes respectively, M_0 is the (initial) binary mass, ΔM is the change of mass (in this case the amount of mass loss), and r is the orbital separation before the explosion. For circular orbits, the

system is unbound if it loses half of its mass. For the very tight BdHNe, however, additional effects have to be taken into account to determine the fate of the binary.

The shock front in an SN moves at roughly 10^4 km s^{-1}, but the denser, lower-velocity ejecta, can move at velocities as low as 10^2–10^3 km s^{-1} [105]. This implies that the SN ejecta overcomes an NS companion in a time 10–1000 s. For wide binaries this time is a small fraction of the orbital period and the "instantaneous" mass-loss assumption is perfectly valid. BdHNe have instead orbital periods as short as 100–1000 s, hence the instantaneous mass-loss approximation breaks down.

We recall the specific examples studied in [103]: close binaries in an initial circular orbit of radius 7×10^9 cm, CO_{core} radii of $(1–4) \times 10^9$ cm with a 2.0 $M_\odot$ NS companion. The CO_{core} leaves a central 1.5 $M_\odot$ NS, ejecting the rest of the core. The NS leads to a BH with a mass equal to the NS critical mass. For these parameters it was there obtained that even if 70% of the mass is lost the binary remains bound, providing the explosion time is of the order of the orbital period ($P = 180$ s) with semi-major axes of less than 10^{11} cm (see Fig. 1.12).

The tight νNS-BH binaries produced by BdHNe will, in due time, merge owing to the emission of gravitational waves. For the above typical parameters the merger time is of the order of 10^4 year, or even less (see Fig. 1.12). We expect little baryonic contamination around such merger site since this region has been cleaned-up by the BdHN. These conditions lead to a new family of sources which we have called ultrashort GRBs, U-GRBs.

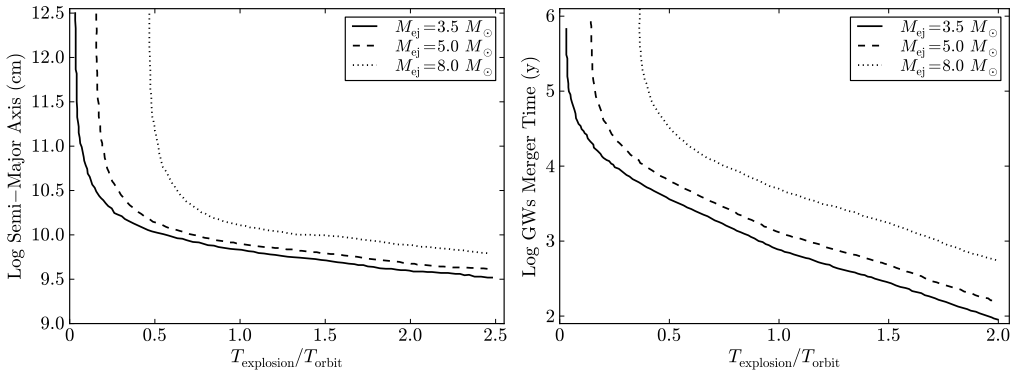

Figure 1.12. (**a**) Semi-major axis versus explosion time for three different mass ejecta scenarios: 3.5 $M_\odot$ (solid), 5.0 $M_\odot$ (dotted), 8.0 $M_\odot$ (dashed), including mass accretion and momentum effects (taken from Fig. 2 in [103]). Including these effects, all systems with explosion times above 0.7 times the orbital time are bound and the final separations are on par with the initial separations. (**b**) Merger time due to gravitational wave emission as a function of explosion time for the same three binaries of the left panel (taken from Fig. 3 in [103]). Note that systems with explosion times 0.1–0.6 T_{orbit} have merger times less than roughly 10^4 y. For most of our systems, the explosion time is above this limit and we expect most of these systems to merge quickly.

1.2.6 BdHN Formation, Occurrence Rate and Connection with Short GRBs

An Evolutionary Scenario

The X-ray binary and SN communities have introduced a new evolutionary scenario for the formation of compact-object binaries (NS-NS or NS-BH). After the collapse of the primary star forming a NS, the binary undergoes mass-transfer episodes finally leading to the ejection of both the hydrogen and helium shells of the secondary star. These processes lead naturally to a binary composed of a CO_{core} and an NS companion (see Fig. 1.4). In the X-ray binary and SN communities these systems are called "ultra-stripped" binaries [295]. These systems are expected to comprise 0.1–1% of the total SNe [294].

The existence of ultra-stripped binaries supports our scenario from the stellar evolution side. In the above studies most of the binaries have orbital periods in the range 3×10^3–3×10^5 s which are longer with respect to the short periods expected in the BdHN scenario. Clearly, XRF and BdHN progenitors should be only a small subset that result from the binaries with initial orbital separation and component masses leading to CO_{core}-NS binaries with short orbital periods, e.g., 100–1000 s for the occurrence of BdHNe. This requires fine-tuning both of the CO_{core} mass and the binary orbit. From an astrophysical point of view the IGC scenario is characterized by the BH formation induced by the hypercritical accretion onto the NS companion and the associated GRB emission. Indeed, GRBs are a rare phenomenon and the number of systems approaching the conditions for their occurrence must be low (see [103] for details).

Occurrence Rate

If we assume that XRFs and BdHNe can be final stages of ultra-stripped binaries, then the percentage of the ultra-stripped population leading to these long GRBs must be very small. The observed occurrence rate of XRFs and BdHNe has been estimated to be ~ 100 Gpc^{-3} yr^{-1} and ~ 1 Gpc^{-3} yr^{-1}, respectively [266], namely the 0.5% and 0.005% of the Ibc SNe rate, 2×10^4 Gpc^{-3} yr^{-1} [124]. It has been estimated that (0.1–1%) of the SN Ibc could originate from ultra-stripped binaries [294], which would lead to an approximate density rate of (20–200) Gpc^{-3} yr^{-1}. This would imply that a small fraction ($\lesssim$5%) of the ultra-stripped population would be needed to explain the BdHNe while, roughly speaking, almost the whole population would be needed to explain the XRFs (see Table 1.2). These numbers, while waiting for a confirmation by further population synthesis analyses, would suggest that most SNe originated from ultra-stripped binaries should be accompanied by an XRF. It is interesting that the above estimates are consistent with traditional estimates that only $\sim$0.001–1% of massive binaries lead to double compact-object binaries [107, 76, 229].

Connection with Short GRBs

It is then clear that XRFs and BdHNe lead to νNS-NS and νNS-BH binaries. In due time, the emission of gravitational waves shrink their orbit leading to mergers potentially detectable as short GRBs. This implies a connection between the rate of

long and short GRBs. It is clear from the derived rates (see Table 1.2 and [266, 269]) that the short GRB population is dominated by the low-luminosity class of short Gamma-ray flashes (S-GRFs), double NS mergers that do not lead to BH formation. It can be seen that it is sufficient $\lesssim 4\%$ of XRFs to explain the S-GRFs population, which would be consistent with the fact that many XRF progenitor binaries will get disrupted by the SN explosion. Therefore, by now, the observed rates of the GRB subclasses are consistent with the interesting possibility of a connection between the progenitors of the long and the ones of the short GRBs.

In this line, it is important to mention that, for instance, in a NS-NS merger, matter can remain bound to the newborn central object (a massive NS or a BH) and form a disk of high-density matter accreting at high rates onto the central object. The results of this thesis are also relevant for the analysis of the neutrino emission and their subsequent annihilation into e^+e^- pairs in the vicinity of the newborn NS or BH.

Chapter 2

Neutrino Oscillations in Spherical Accretion onto a NS

2.1 Introduction

The emergent picture of gamma-ray burst is that both, short-duration and long-duration GRBs, originate from binary systems [266].

Short bursts originate from NS-NS or NS-BH mergers [121, 209, 85, 204, see, e.g.,]. For this case [202] introduced the role of neutrino-anti-neutrino ($\nu\bar{\nu}$) annihilation leading to the formation of an electron-positron plasma (e^-e^+) in NS-NS and NS-BH mergers. Such a result triggered many theoretical works, including the general relativistic treatment by [275] of the $\nu\bar{\nu}$ annihilation process giving rise to the e^-e^+ plasma in a NS-NS system.

For long bursts we stand on the IGC paradigm [255, 263, 133, 246, 105, 261], based on the hypercritical accretion process of the SN ejecta of the explosion of a CO_{core} onto a NS binary companion. In the above processes, the emission of neutrinos is a key ingredient.

We focus hereafter on the neutrino emission of long bursts within the IGC scenario. The role of neutrinos in this paradigm has been recently addressed [105, 103, 25, 24]. The hypercritical accretion of the SN ejecta onto the NS companion can reach very high rates of up to $10^{-2}\ M_\odot\ s^{-1}$ and its duration can be of the order of 10–10^4 s depending on the binary parameters. The photons become trapped within the accretion flow and thus do not serve as an energy sink. The high temperature developed on the NS surface leads to e^-e^+ pairs that, via weak interactions, annihilate into $\nu\bar{\nu}$ pairs with neutrino luminosities of up to 10^{52} erg s^{-1} for the highest accretion rates. Thus, this process dominates the cooling and give rise to a very efficient conversion of the gravitational energy gained by accretion into radiation. We refer to [24] for further details on this process.

The above hypercritical accretion process can lead the NS to two alternative fates, leading to the existence of two long GRB sub-classes [105, 103, 25, 24, 266]:

I. The hypercritical accretion leads to a more massive NS companion but not to a BH. These binaries explain the XRFs; long bursts with isotropic energy $E_{\rm iso} \lesssim 10^{52}$ erg and rest-frame spectral peak energy $E_{p,i} \lesssim 200$ keV (see [266]

for further details). The local observed number density rate of this GRB sub-class is [266]: $\rho_{\rm GRB} = 100^{+45}_{-34}$ Gpc^{-3}yr^{-1}.

II. The hypercritical accretion is high enough to make the NS reach its critical mass triggering its gravitational collapse with consequent BH formation. These binaries explain the BdHNe; long bursts with $E_{\rm iso} \gtrsim 10^{52}$ erg and $E_{p,i} \gtrsim$ 200 keV (see [266] for further details). The local observed number density rate of this GRB sub-class is [266]: $\rho_{\rm GRB} = 0.77^{+0.09}_{-0.08}$ Gpc^{-3}yr^{-1}.

Simulations of the hypercritical accretion process in the above binaries have been presented in [105, 103, 25, 24]. It has been shown how, thanks to the development of a copious neutrino emission near the NS surface, the NS is allowed to accrete matter from the SN at very high rates. The specific conditions leading to XRFs and BdHNe as well as a detailed analysis of the neutrino production in these systems have been presented in [24]. Neutrino emission can reach luminosities of 10^{52} erg s^{-1} and the mean neutrino energy of the order of 20 MeV. Under these conditions, XRFs and BdHNe become astrophysical laboratories for MeV-neutrino physics additional to core-collapse SNe.

On the other hand, the emission of TeV-PeV neutrinos is relevant for the observations of detectors such as the IceCube [1]. High-energy neutrino emission mechanisms have been proposed within the context of the traditional model of long GRBs. In the traditional "collapsar" scenario [310, 210, 173] the gravitational collapse of a single, fast rotating, massive star originates a BH surrounded by a massive accretion disk (see [222] for a review), and the GRB dynamics follows the "fireball" model that assumes the existence of an ultra-relativistic collimated jet with Lorentz factor $\Gamma \sim 10^2$–10^3 (see, e.g., [283, 223, 188, 179]). This scenario has been adopted for the explanation of the prompt emission, as well as both the afterglow and the GeV emission of long GRBs. The GRB light-curve structures are there described by (internal or external) shocks (see, e.g., [242, 243]). The high-energy neutrinos in this context are produced from the interaction of shock-accelerated cosmic-rays (e.g. protons) with the interstellar medium (see [8, 162] and references therein). A recent analysis of the thermal emission of the X-ray flares observed in the early afterglow of long GRBs (at source rest-frame times $t \sim 10^2$ s) show that it occurs at radii $\sim 10^{12}$ cm and expands with a mildly-relativistic $\Gamma \lesssim 4$ (see [267] for further details). This rules out the ultra-relativistic expansion in the GRB afterglow traditionally adopted in the literature. Interestingly, the aforementioned mechanisms of high-energy neutrino production conceived in the collapsar-fireball model can still be relevant in the context of BdHNe and authentic short GRBs (S-GRBs, NS-NS mergers with $E_{\rm iso} \gtrsim 10^{52}$ erg leading to BH formation; see [266], for the classification of long and short bursts in seven different sub-classes). The emission in the 0.1–100 GeV energy band observed in these two GRB sub-classes has been shown to be well explained by a subsequent accretion process onto the newly-born BH [261, 264, 265, 266, 10]. Such GeV emission is not causally connected either with the prompt emission or with the afterglow emission comprising the flaring activity [267]. An ultra-relativistic expanding component is therefore expected to occur in BdHNe and S-GRBs which deserves to be explored in forthcoming studies as a possible source of high-energy neutrinos. Specifically, this motivates the to identify the possible additional channels to be explored in the hypercritical accretion

not around a NS but around a BH. The aim of this work is to extend the analysis of the MeV-neutrino emission in the hypercritical accretion process around a NS in the XRFs and BdHNe to assess the possible occurrence of neutrino flavour oscillations.

We shall show in this chapter that, before escaping to the outer space, i.e. outside the Bondi-Hoyle accretion region, the neutrinos experience an interesting phenomenology. The neutrino density near the NS surface is so high that the neutrino SIP, usually negligible in other very well-known scenarios like the Sun, the upper layers of Earth's atmosphere and terrestrial reactor and accelerator experiments, becomes more relevant than the matter potential responsible for the famous MSW effect [308, 192]. A number of papers have been dedicated to the consequences of the neutrino self-interaction dominance [206, 215, 234, 216, 81, 279, 112, 90, 82, 237, 88, 89, 50, 77, 80, 60, 59, 280, 83, 312], most of them focused on SN neutrinos. In these cases, the SN induces the appearance of collective effects such as synchronized and bipolar oscillations leading to an entirely new flavour content of emitted neutrinos when compared with the spectrum created deep inside the star. The density of neutrinos produced in the hypercritical accretion process of XRFs and BdHNe is such that the neutrino self-interactions, as in the case of SNe, dominate the neutrino flavour evolution, giving rise to the aforementioned collective effects. The main neutrino source, in this case, is the $\nu\bar{\nu}$ pair production from e^-e^+ annihilation [24] which leads to an equal number of neutrinos and anti-neutrinos of each type. This equality does not happen in the SN standard scenario. We will show that bipolar oscillations, inducing very quick flavour pair conversions $\nu_e\bar{\nu}_e \leftrightarrow \nu_\mu\bar{\nu}_\mu \leftrightarrow \nu_\tau\bar{\nu}_\tau$, can occur with oscillation length as small as $O(0.05\text{–}1)$ kilometers. However, the ν–$\bar{\nu}$ symmetry characterizing our system leads to the occurrence of kinematic decoherence making the neutrino flavour content to reach equipartition deep inside the accretion zone. In the regions far from the NS surface where the neutrino density is not so high, the matter potential turns to dominate and MSW resonances can take place. As a result, an entirely different neutrino flavour content emerges from the Bondi-Hoyle surface when compared with what was originally created in the bottom of the accretion zone.

This chapter is organized as follows. In Sec. 2.2 we outline the general features of the accretion process onto the NS within the IGC paradigm and present the processes responsible for the neutrino creation. From these features, we obtain the distribution functions that describe the neutrino spectrum near the NS surface. Sec. 2.3 shows a derivation of the equations that drive the evolution of neutrino oscillations closely related to the geometrical and physical characteristics of our system. In Sec. 2.4 we discuss some details on the neutrino oscillation phenomenology. Since we have to face a non-linear integro-differential system of equations of motion, we introduce the single-angle approximation to later recover the full realistic phenomenology after generalizing our results to the multi-angle approach and, consequently, decoherent picture. In Sec. 2.5 the final neutrino emission spectra are presented and compared with those ones in which neutrinos are created in the accretion zone. Finally, we present in Sec. 2.6 the conclusions and some perspectives for future research on this subject.

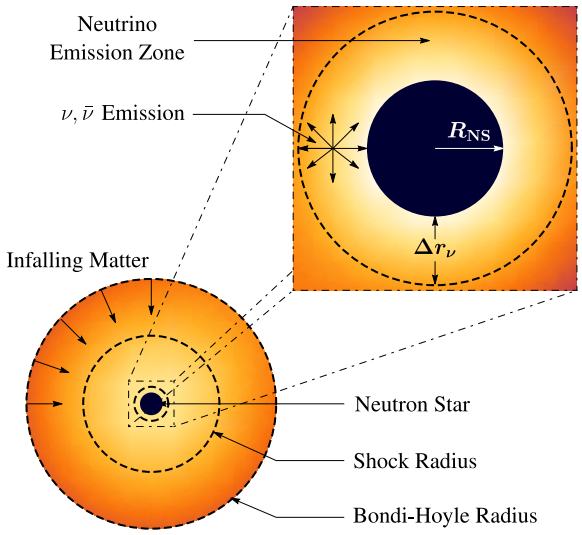

Figure 2.1. Schematic representation of the accretion process onto the NS and the neutrino emission. The supernova ejected material reaches the NS Bondi-Hoyle radius and falls onto the NS surface. The material shocks and decelerates as it piles over the NS surface. At the neutrino emission zone, neutrinos take away most of the infalling matter's energy. The neutrino emission allows the material to reduce its entropy to be incorporated to the NS. The image is not to scale. For binary system with $M_{\rm NS} = 2M_\odot$ and $R_{\rm NS} = 10$ km, and a $M_{\rm ZAMS} = 20M_\odot$ progenitor, at $\dot{M} = 10^{-2}M_\odot$/s, the position of the Bondi-Hoyle and Shock radii are 2.3×10^5 km and 31 km, respectively. The neutrino emission zone's thickness is $\Delta r_\nu = 0.8$ km.

2.2 Neutrino Creation During Hypercritical Accretion

The SN material first reaches the gravitational capture region of the NS companion, namely the Bondi-Hoyle region. The infalling material shocks as it piles up onto the NS surface forming an accretion zone where it compresses and eventually becomes sufficiently hot to trigger a highly efficient neutrino emission process. Neutrinos take away most of the infalling matter's gravitational energy gain, letting it reduce its entropy and be incorporated into the NS. Fig. 2.1 shows a sketch of this entire hypercritical accretion process.

It was shown in [24] that the matter in the accretion zone near the NS surface develops conditions of temperature and density such that it is in a non-degenerate, relativistic, hot plasma state. The most efficient neutrino emission channel under those conditions becomes the electron positron pair annihilation process:

$$e^- e^+ \rightarrow \nu\, \bar{\nu}. \tag{2.1}$$

The neutrino emissivity produced by this process is proportional to the accretion rate to the 9/4 power (see below). This implies that the higher the accretion rate the higher the neutrino flux, hence the largest neutrino flux occurs at the largest accretion rate. We turn now to estimate the accretion rate and thus the neutrino emissivity we expect in our systems.

2.2.1 Accretion Rate in XRFs and BdHNe

We first discuss the amount of SN matter per unit time reaching the gravitational capture region of the NS companion, namely the Bondi-Hoyle accretion rate. It has been shown in [23, 24] that the shorter (smaller) the orbital period (separation) the higher the peak accretion rate $\dot{M}_{\rm peak}$ and the shorter the time at which it peaks, $t_{\rm peak}$. The Bondi-Hoyle accretion rate is proportional to the density of the accreted matter and inversely proportional to its velocity. Thus, we expect the accretion rate to increase as the denser and slower inner layers of the SN reach the accretion region. Based on these arguments, [24] derived simple, analytic formulas for $\dot{M}_{\rm peak}$ and $t_{\rm peak}$ as a function of the orbital period (given all the other binary parameters) that catch both the qualitatively and quantitatively behaviors of these two quantities obtained from full numerical integration. We refer the reader to the Appx. A of that article for further details. For the scope of this work these analytic expressions are sufficient to give us an estimate of the hypercritical accretion rates and related time scale developed in these systems:

$$t_{\rm peak} \approx \left(1-\frac{2M_{\rm NS}}{M}\right)\left(\frac{M}{4\pi^2}\right)^{1/3}\left(\frac{R^0_{\rm star}}{\eta R_{\rm core}}\right)\frac{P^{2/3}}{v_{\rm star,0}}, \tag{2.2a}$$

$$\dot{M}_{\rm peak} \approx 2\pi^2\frac{(2M_{\rm NS}/M)^{5/2}}{(1-2M_{\rm NS}/M)^3}\eta^{3-m}\frac{\rho_{\rm core}R^3_{\rm core}}{P}, \tag{2.2b}$$

where P is the orbital period, m is the index of the power-law density profile of the pre-SN envelope, $v_{\rm star,0}$ is the velocity of the outermost layer of the SN ejecta, $M = M_{\rm CO} + M_{\rm NS}$ is the total binary mass, $M_{\rm CO} = M_{\rm env} + M_{\nu\rm NS}$ is the total mass of the $\rm CO_{core}$ given by the envelope mass and the mass of the central remnant, i.e. the new NS (hereafter νNS) formed from the region of the $\rm CO_{core}$ which undergoes core-collapse (i.e. roughly speaking the iron core of density $\rho_{\rm core}$ and radius $R_{\rm core}$). We here adopt $M_{\nu\rm NS} = 1.5\ M_\odot$. The parameter η is given by

$$\eta \equiv \frac{R^0_{\rm star}}{R_{\rm core}}\frac{1+m}{1+m(R^0_{\rm star}/\hat{R}_{\rm core})}, \tag{2.3}$$

where $R^0_{\rm star}$ is the total radius of the pre-SN $\rm CO_{core}$; $\hat{\rho}_{\rm core}$ and $\hat{R}_{\rm core}$ are parameters of the pre-SN density profile introduced to account of the finite size of the envelope, and m is the power-law index followed by the density profile at radii $r > R_{\rm core}$ (see [24] for further details).

Fig. 2.2 shows the peak accretion rate in Eq. (2.2) as a function of the orbital period. In this example, we consider the following binary parameters [24]: a $\rm CO_{core}$ produced by a zero-age main-sequence (ZAMS) progenitor with $M_{\rm ZAMS} = 20\ M_\odot$, i.e. $M_{\rm CO} = 5.4\ M_\odot$, an initial NS mass 2.0 $M_\odot$, and a velocity of the outermost ejecta layer $v_{\rm star,0} = 2\times10^9$ cm s^{-1}. For these parameters, $\eta \approx 0.41$.

It was shown in [25, 24] the existence of a maximum orbital period, $P_{\rm max}$, over which the accretion onto NS companion is not high enough to bring it to the critical mass for gravitational collapse to a BH. As we have recalled in the Introduction, $\rm CO_{core}$-NS binaries with $P > P_{\rm max}$ lead to XRFs while the ones with $P \lesssim P_{\rm max}$ lead to BdHNe. For the binary parameters of the example in Fig. 2.2, $P_{\rm max} \approx 127$ min (vertical dashed line). We can therefore conclude that BdHNe can

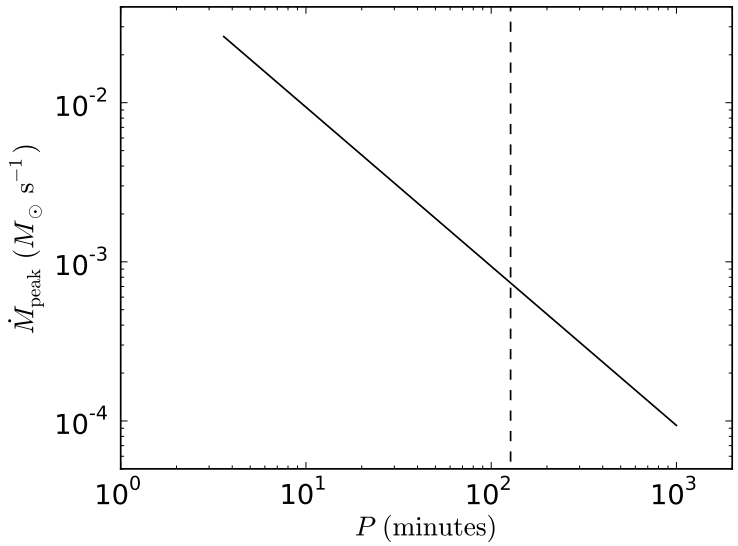

Figure 2.2. Peak accretion rate, $\dot{M}_{\rm peak}$, as a function of the binary orbital period, as given by Eq. (2.2). This example corresponds to the following binary parameters: a $\rm CO_{core}$ formed by a $M_{\rm ZAMS} = 20\ M_\odot$ progenitor, i.e. $M_{\rm CO} = 5.4\ M_\odot$, an initial NS mass $2.0\ M_\odot$, $v_{\rm star,0} = 2 \times 10^9$ cm s^{-1}, $\eta \approx 0.41$ and index $m = 2.946$ (see [24] for further details). For these parameters the largest orbital period for the induced collapse of the NS to a BH by accretion is $P_{\rm max} \approx 127$ min which is represented by the vertical dashed line.

have peak accretion rates in the range $\dot{M}_{\rm peak} \sim 10^{-3}$– few $10^{-2}\ M_\odot\ {\rm s}^{-1}$ while XRFs would have $\dot{M}_{\rm peak} \sim 10^{-4}$–$10^{-3}\ M_\odot\ {\rm s}^{-1}$.

2.2.2 Neutrino Emission at Maximum Accretion

For the accretion rate conditions characteristic of our models at peak $\sim 10^{-4}$–$10^{-2}\ M_\odot\ {\rm s}^{-1}$, pair annihilation dominates the neutrino emission and electron neutrinos remove the bulk of the energy [24]. The e^+e^- pairs producing the neutrinos are thermalized at the matter temperature. This temperature is approximately given by:

$$T_{\rm acc} \approx \left(\frac{3P_{\rm shock}}{4\sigma}\right)^{1/4} = \left(\frac{7}{8}\frac{\dot{M}_{\rm acc}v_{\rm acc}}{4\pi R_{\rm NS}^2\sigma}\right)^{1/4}, \tag{2.4}$$

where $P_{\rm shock}$ is the pressure of the shock developed on the accretion zone above the NS surface, $\dot{M}_{\rm acc}$ is the accretion rate, $v_{\rm acc}$ is the velocity of the infalling material and σ is the Stefan-Boltzmann constant. It can be checked that, for the above accretion rates, the system develops temperatures and densities ($T \gtrsim 10^{10}$ K and $\rho \gtrsim 10^6$ g cm^{-3}; see, e.g., Fig. 16 in [24]) for which the neutrino emissivity of the e^+e^- annhiliation process can be estimated by the simple formula [317]:

$$\epsilon_{e^-e^+} \approx 8.69 \times 10^{30} \left(\frac{T}{1\,{\rm MeV}}\right)^9\ {\rm MeV\,cm^{-3}\,s^{-1}}, \tag{2.5}$$

The accretion zone is characterized by a temperature gradient with a typical scale height $\Delta r_{\rm ER} = T/\nabla T \approx 0.7\ R_{\rm NS}$. Owing to the strong dependence of the

neutrino emission on temperature, most of the neutrinos are emitted from a spherical shell around the NS of thickness (see Fig. 2.1)

$$\Delta r_\nu = \frac{\epsilon_{e^-e^+}}{\nabla \epsilon_{e^-e^+}} = \frac{\Delta r_{\rm ER}}{9} \approx 0.08 R_{\rm NS}. \tag{2.6}$$

Eqs. (2.4) and (2.5) imply the neutrino emissivity satisfies $\epsilon_{e^-e^+} \propto \dot{M}_{\rm acc}^{9/4}$ as we had anticipated. These conditions lead to the neutrinos to be efficient in balancing the gravitational potential energy gain, allowing the hypercritical accretion rates. The effective accretion onto the NS can be estimated as

$$\dot{M}_{\rm eff} \approx \Delta M_\nu \frac{L_\nu}{E_g}, \tag{2.7}$$

where ΔM_ν, L_ν are, respectively, the mass and neutrino luminosity in the emission region, and $E_g = (1/2) M_{\rm NS} \Delta M_\nu / (R_\nu + \Delta r_\nu)$ is half the gravitational potential energy gained by the material falling from infinity to the $R_{\rm NS} + \Delta r_\nu$. The neutrino luminosity is

$$L_\nu \approx 4\pi R_{\rm NS}^2 \Delta r_\nu \epsilon_{e^-e^+}. \tag{2.8}$$

with $\epsilon_{e^-e^+}$ being the neutrino emissivity in Eq. (2.5). For $M_{\rm NS} = 2\ M_\odot$ and temperatures 1–10 MeV, the Eqs. (2.7) and (2.8) result $\dot{M}_{\rm eff} \approx 10^{-10}$–$10^{-1}\ M_\odot\ {\rm s}^{-1}$ and $L_\nu \approx 10^{48}$–10^{57} MeV s^{-1}.

Table 2.1. Characteristics inside the neutrino emission zone and the neutrino spectrum for selected values of the accretion rate $\dot{M}$. The electron fraction is $Y_e = 0.5$, the pinching parameter for the neutrino spectrum is $\eta_{\nu\bar{\nu}} = 2.0376$.

$\dot{M}$ ($M_\odot$ s^{-1})	ρ (g cm^{-3})	T (MeV)	$\eta_{e^\mp}$	$n_{e^-} - n_{e^+}$ (cm^{-3})	$T_{\nu\bar{\nu}}$ (MeV)	$\langle E_\nu \rangle$ (MeV)	$F^C_{\nu_e,\bar{\nu}_e}$ (cm^{-2}s^{-1})	$F^C_{\nu_x,\bar{\nu}_x}$ (cm^{-2}s^{-1})	$n^C_{\nu_e\bar{\nu}_e}$ (cm^{-3})	$n^C_{\nu_x\bar{\nu}_x}$ (cm^{-3})	$\sum_i n^C_{\nu_i\bar{\nu}_i}$ (cm^{-3})
10^{-8}	1.46×10^6	1.56	∓ 0.325	4.41×10^{29}	1.78	6.39	4.17×10^{36}	1.79×10^{36}	2.78×10^{26}	1.19×10^{26}	3.97×10^{26}
10^{-7}	3.90×10^6	2.01	∓ 0.251	1.25×10^{30}	2.28	8.24	3.16×10^{37}	1.36×10^{37}	2.11×10^{27}	9.00×10^{26}	3.01×10^{27}
10^{-6}	1.12×10^7	2.59	∓ 0.193	3.38×10^{30}	2.93	10.61	2.40×10^{38}	1.03×10^{38}	1.60×10^{28}	6.90×10^{27}	2.29×10^{28}
10^{-5}	3.10×10^7	3.34	∓ 0.147	9.56×10^{30}	3.78	13.69	1.84×10^{39}	7.87×10^{38}	1.23×10^{29}	5.20×10^{28}	1.75×10^{29}
10^{-4}	8.66×10^7	4.30	∓ 0.111	2.61×10^{31}	4.87	17.62	1.39×10^{40}	5.94×10^{39}	9.24×10^{29}	3.96×10^{29}	1.32×10^{30}
10^{-3}	2.48×10^8	5.54	∓ 0.082	7.65×10^{31}	6.28	22.70	1.04×10^{41}	4.51×10^{40}	7.00×10^{30}	3.00×10^{30}	1.00×10^{31}
10^{-2}	7.54×10^8	7.13	∓ 0.057	2.27×10^{32}	8.08	29.22	7.92×10^{41}	3.39×10^{41}	5.28×10^{31}	2.26×10^{31}	7.54×10^{31}

2.2.3 Neutrino Spectrum at the NS Surface

After discussing the general features of neutrino emission during the accretion process, it is necessary for our analysis of the neutrino oscillations to determine the neutrino spectrum at the NS surface using the technical details in Appx. D. Specifically, we need to determine the ratios at which the neutrinos of each flavour are created and their average energy so that we can find a fitting distribution function f_ν with these characteristics, as it is usually done in supernovae neutrino emission [137, 138]. That is, a Fermi-Dirac distribution in terms of two parameters: the effective neutrino temperature $T_{\nu\bar{\nu}}$ and the effective neutrino degeneracy parameter $\eta_{\nu\bar{\nu}}$ otherwise known as the *pinching* parameter [236, 145]. To that end, it is enough to calculate the first two moments. In particular, for a relativistic non-degenerate plasma ($k_B T > 2m_e c^2$ and $1 > \eta_{e^\mp}$, see Table 2.1) Eq. (D.7) can be approximated with a very good accuracy by [317].

$$\varepsilon_i^m \approx \frac{2G_F^2 (T)^{8+m}}{9\pi^5} C_{+,i}^2 \left[\mathcal{F}_{m+1,0}(\eta_{e^+})\mathcal{F}_{1,0}(\eta_{e^-}) + \mathcal{F}_{m+1,0}(\eta_{e^-})\mathcal{F}_{1,0}(\eta_{e^+})\right] \tag{2.9}$$

where $\mathcal{F}_{k,\ell}(\eta) = \mathcal{F}_{k,\ell}(y=0,\eta)$. Since the main source of neutrinos is the $e^- e^+$ pair annihilation process we can conclude that neutrinos and anti-neutrinos are created in equal number. For $m = 1$, $\eta_{e^\pm} = 0$ and adding over every flavour this expression reduces to Eq. (2.5). With Eqs. (D.8) and (2.9) we find

$$\langle E_\nu \rangle = \langle E_{\bar{\nu}} \rangle \approx 4.1\, T \tag{2.10a}$$

$$\langle E_\nu^2 \rangle = \langle E_{\bar{\nu}}^2 \rangle \approx 20.8 T^2, \tag{2.10b}$$

regardless of the neutrino flavour. Furthermore, we can calculate the ratio of emission rates between electronic and nonelectronic neutrino flavours in terms of the weak interaction constants

$$\frac{\varepsilon_e^0}{\varepsilon_x^0} = \frac{\varepsilon_e^0}{\varepsilon_\mu^0 + \varepsilon_\tau^0} = \frac{C_{+,e}^2}{C_{+,\mu}^2 + C_{+,\tau}^2} \approx \frac{7}{3}. \tag{2.11}$$

Some comments must be made about the results we have obtained:

- It is well known that, within the Standard Model of Particles, there are three neutrino flavours $\nu_e, \bar{\nu}_e$, $\nu_\mu, \bar{\nu}_\mu$ and $\nu_\tau, \bar{\nu}_\tau$. However, as in Eq. (2.11), we will simplify our description using only two flavours: the electronic neutrinos and anti-neutrinos $\nu_e, \bar{\nu}_e$, and a superposition of the other flavours $\nu_x, \bar{\nu}_x$ ($x = \mu + \tau$). This can be understood as follows. Since the matter in the accretion zone is composed by protons, neutrons, electrons and positrons, ν_e and $\bar{\nu}_e$ interact with matter by both charged and neutral currents, while ν_μ, ν_τ, $\bar{\nu}_\mu$ and $\bar{\nu}_\tau$ interact only by neutral currents. Therefore, the behavior of these states can be clearly divided into electronic and non-electronic. This distinction will come in handy when studying neutrino oscillations.

- Representing the neutrino (anti-neutrino) density and flux in the moment of their creation with $n^c_{\nu_i(\bar{\nu}_i)}$ and $F^c_{\nu_i(\bar{\nu}_i)}$ respectively and using Eq. (2.11) we can

recollect two important facts:

$$n^C_{\nu_i} = n^C_{\bar{\nu}_i},\ \ F^C_{\nu_i} = F^C_{\bar{\nu}_i}\ \ \forall i \in \{e, \mu, \tau\} \tag{2.12a}$$

$$\frac{n^C_{\nu_e}}{n^C_{\nu_x}} = \frac{n^C_{\bar{\nu}_e}}{n^C_{\bar{\nu}_x}} = \frac{F^C_{\nu_e}}{F^C_{\nu_x}} = \frac{F^C_{\bar{\nu}_e}}{F^C_{\bar{\nu}_x}} \approx \frac{7}{3}. \tag{2.12b}$$

Eqs. (2.12) imply that, in the specific environment of our system, of the total number of neutrinos+anti-neutrinos emitted, $N_\nu + N_{\bar{\nu}}$, 70% are electronic neutrinos ($N_{\nu_e} + N_{\bar{\nu}_e}$), 30% are non-electronic ($N_{\nu_x} + N_{\bar{\nu}_x}$), while the total number of neutrinos is equal to the total number of anti-neutrinos, i.e. $N_\nu = N_{\bar{\nu}}$, where $N_\nu = N_{\nu_e} + N_{\nu_x}$ and $N_{\bar{\nu}} = N_{\bar{\nu}_e} + N_{\bar{\nu}_x}$.

- Bearing in mind such high neutrino energies as the ones suggested by Eqs. (2.10) , from here on out we will use the approximation

$$E_\nu \approx |\mathbf{p}| \gg m_\nu, \tag{2.13}$$

where $\mathbf{p}$ is the neutrino momentum.

- From Eq. (D.8) we obtain the same energy moments for both neutrinos and anti-neutrinos but, as [195] points out, these energies should be different since, in reality, this expression returns the arithmetic mean of the particle and antiparticle energy moments, that is $\left(\langle E^m_\nu\rangle + \langle E^m_{\bar{\nu}}\rangle\right)/2$. However, if we calculate the differences between the energy moments with equations (41) and (46) in [195] for the values of T and $\eta_{e^\pm}$ we are considering, we get $\Delta\langle E\rangle \sim 10^{-2}$–$10^{-3}$ MeV and $\Delta\langle E^2\rangle \sim 10^{-3}$–$10^{-4}$ MeV^2. These differences are small enough that we can use the same effective temperature and pinching parameter for both neutrinos and anti-neutrinos.

Solving the equations

$$4.1T = T_{\nu\bar{\nu}}\frac{\mathcal{F}_{3,0}\left(\eta_{\nu\bar{\nu}}\right)}{\mathcal{F}_{2,0}\left(\eta_{\nu\bar{\nu}}\right)} \tag{2.14a}$$

$$20.8T^2 = T^2_{\nu\bar{\nu}}\frac{\mathcal{F}_{4,0}\left(\eta_{\nu\bar{\nu}}\right)}{\mathcal{F}_{2,0}\left(\eta_{\nu\bar{\nu}}\right)} \tag{2.14b}$$

for any value of T in Table (2.1) we find $T_{\nu\bar{\nu}} = 1.1331T$ and $\eta_{\nu\bar{\nu}} = 2.0376$. Integrating a Fermi-Dirac distribution over the neutrino momentum space using these values should give the neutrino number density. To achieve this we normalize it with the factor $1/\left(2\pi^2 T^3_{\nu\bar{\nu}}\mathcal{F}_{2,0}\left(\eta_{\nu\bar{\nu}}\right)\right)$ and then we multiply by

$$n^C_{\nu_i(\bar{\nu}_i)} = w_{\nu_i(\bar{\nu}_i)}\frac{L_\nu}{4\pi R^2_{\rm NS}\langle E_\nu\rangle\langle v\rangle} = 2w_{\nu_i(\bar{\nu}_i)}\varepsilon^0_i\Delta r_\nu, \tag{2.15}$$

where the neutrino's average radial velocity at $r = R_{\rm NS}$ is $\langle v\rangle = 1/2$ [61] and $w_{\nu_e} = w_{\bar{\nu}_e} = 0.35$ and $w_{\nu_x} = w_{\bar{\nu}_x} = 0.15$. To calculate the neutrino fluxes we simply set $F^C_{\nu(\bar{\nu}_i)} = \langle v\rangle n^C_{\nu_i(\bar{\nu}_i)}$. Gathering our results we can finally write the distribution functions as

$$f_{\nu_e} = f_{\bar{\nu}_e} = \frac{2\pi^2 n^C_{\nu_e}}{T^3_{\nu\bar{\nu}}\mathcal{F}_{2,0}\left(\eta_{\nu\bar{\nu}}\right)}\frac{1}{1+\exp\left(E/T_{\nu\bar{\nu}} - \eta_{\nu\bar{\nu}}\right)} \tag{2.16a}$$

$$f_{\nu_x} = f_{\bar{\nu}_x} = \frac{2\pi^2 n^C_{\nu_x}}{T^3_{\nu\bar{\nu}}\mathcal{F}_{2,0}\left(\eta_{\nu\bar{\nu}}\right)}\frac{1}{1+\exp\left(E/T_{\nu\bar{\nu}} - \eta_{\nu\bar{\nu}}\right)} \tag{2.16b}$$

It can be checked that these distributions obey

$$\int f_{\nu_i} \frac{d^3\mathbf{p}}{(2\pi)^3} = n^C_{\nu_i} \tag{2.17a}$$

$$\int E f_{\nu_i} \frac{d^3\mathbf{p}}{(2\pi)^3} = \langle E_\nu \rangle n^C_{\nu_i} = \varepsilon^1_i \tag{2.17b}$$

and with these conditions satisfied we can conclude that Eqs. (2.16) are precisely the ones that emulate the neutrino spectrum at the NS surface. In Table 2.1 we have collected the values of every important quantity used in the calculations within this section for the range of accretion rates in which we are interested.

Considering that the problem we attacked in this section reduces to finding a normalized distribution whose first two moments are fixed, the choice we have made with Eqs. (2.16) is not unique. The solution depends on how many moments are used to fit the distribution and what kind of function is used as an ansatz. A different solution based on a Maxwell-Boltzmann distribution can be found in [145, 93, 195].

At this stage, we can identify two main differences between neutrino emission in SNe and in the IGC process of XRFs and BdHNe, within the context of neutrino oscillations. The significance of these differences will become clearer in next sections but we mention them here to establish a point of comparison between the two systems since SN neutrino oscillations have been extensively studied.

- Neutrinos of all flavours in XRFs and BdHNe have the same temperature, which leads to equal average energy. The neutrinos produced in SNe are trapped and kept in thermal equilibrium within their respective neutrino-sphere. The neutrino-spheres have different radii, causing different flavours to have different average energies. This energy difference leads to a phenomenon called *spectral stepwise swap* which, as we will show below, is not present in our systems (see [236, 90, 59] and references therein).

- As we have discussed above, in XRFs and BdHNe neutrinos and anti-neutrinos are emitted in equal number. Due to this fact, kinematical decoherence occurs (up to a number difference of 30% this statement is valid; see Sec. 2.4 for further details). Instead, SN neutrino and anti-neutrino fluxes differ such that $F_{\nu_e} > F_{\bar{\nu}_e} > F_{\nu_x} = F_{\bar{\nu}_x}$. It has been argued that this difference between neutrinos and anti-neutrinos is enough to dampen kinematical decoherence, so that bipolar oscillations are a feature present in SN neutrinos (see, e.g., [88]).

In the next section, we will use the results presented here to determine the neutrino flavour evolution in the accretion zone.

2.3 Neutrino Oscillations

In recent years the picture of neutrino oscillations in dense media, based only on MSW effects, has undergone a change of paradigm by the insight that the refractive effects of neutrinos on themselves due to the neutrino SIP are crucial [206, 215, 234, 216, 81, 279, 112, 90, 82, 237, 88, 89, 50, 77, 80, 60, 59, 280, 83, 312].

As we discussed in Sec. 2.2, in our physical system of interest neutrinos are mainly created by electron-positron pair annihilation and so the number of neutrinos is equal to the number of anti-neutrinos. Such a fact creates an interesting and unique physical situation, different from, for example, SN neutrinos for which traditional models predict a predominance of electron neutrinos mainly due to the deleptonization caused by the URCA process [88].

The neutrino SIP decays with the radial distance from the neutron star faster than the matter potential. This is a direct consequence of the usual $1/r^2$ flux dilution and the collinearity effects due to the neutrino velocity dependence of the potential. Consequently, we identify three different regions along the neutrino trajectory in which the oscillations are dominated by intrinsically different neutrino phenomenology. Fig. 2.3 illustrates the typical situation of the physical system we are analyzing. Just after the neutrino creation in the regions of the accretion zone very close to the surface of the NS, neutrinos undergo kinematic decoherence along the same length scale of a single cycle of the so-called bipolar oscillations. Bipolar oscillations imply very fast flavour conversion between neutrino pairs $\nu_e\bar{\nu}_e \leftrightarrow \nu_\mu\bar{\nu}_\mu \leftrightarrow \nu_\tau\bar{\nu}_\tau$ and, amazingly, the oscillation length in this region can be so small as of the order tens of meters.

Note that kinematic decoherence is just the averaging over flavour neutrino states process resulting from quick flavour conversion which oscillation length depends on the neutrino energy. It does not imply quantum decoherence and, thus, neutrinos are yet able to quantum oscillate if appropriate conditions are satisfied. In fact, as it can be observed from Figs. 2.4 and 2.5 below, bipolar oscillations preserve the characteristic oscillation pattern, differently from quantum decoherence which would lead to a monotonous dumping figure.

Kinematic decoherence is relevant when three conditions are met: (i) The SIP dominates over the vacuum potential. (ii) The matter potential does not fulfill the MSW condition. (iii) There is a low asymmetry between the neutrino and anti-neutrino fluxes. We will see that our system satisfies all three conditions.

As the SIP becomes small and the matter potential becomes important, oscillations are suppressed and we do not expect significant changes in the neutrino flavour content along this region. This situation changes radically when the matter potential is so small that it is comparable with neutrino vacuum frequencies $\Delta m^2/2p$, where Δm^2 is the neutrino squared mass difference and p is the norm of the neutrino momentum $\mathbf{p}$. In this region, the neutrino SIP is negligible and the usual MSW resonances can occur. Therefore, we can expect a change in the neutrino spectrum.

2.3.1 Equations of Oscillation

To derive the equation of neutrino oscillations we take Eq. (1.22) as a starting point. Let us first present the relevant equations for neutrinos. Due to the similarity between $H_{\mathbf{p}}$ and $\bar{H}_{\mathbf{p}}$, the corresponding equations for anti-neutrinos can be obtained in an analogous manner. In the two-flavour approximation, ρ in Eq. (1.22) can be written in terms of Pauli matrices and the polarization vector $\mathsf{P}_{\mathbf{p}}$ as:

$$\rho_{\mathbf{p}} = \begin{pmatrix} \rho_{ee} & \rho_{ex} \\ \rho_{xe} & \rho_{xx} \end{pmatrix}_{\mathbf{p}} = \frac{1}{2}\left(f_{\mathbf{p}}\mathbb{1} + \mathsf{P}_{\mathbf{p}} \cdot \vec{\sigma}\right), \tag{2.18}$$

where $f_{\mathbf{p}} = \mathrm{Tr}[\rho_{\mathbf{p}}] = f_{\nu_e}(\mathbf{p}) + f_{\nu_x}(\mathbf{p})$ is the sum of the distribution functions for ν_e and ν_x. Note that the z component of the polarization vector obeys

$$\mathsf{P}^z_{\mathbf{p}} = f_{\nu_e}(\mathbf{p}) - f_{\nu_x}(\mathbf{p}). \tag{2.19}$$

Hence, this component tracks the fractional flavour composition of the system and appropriately normalizing $\rho_{\mathbf{p}}$ allows to define a survival and mixing probability

$$P_{\nu_e \leftrightarrow \nu_e} = \frac{1}{2}\left(1 + \mathsf{P}^z_{\mathbf{p}}\right), \tag{2.20a}$$

$$P_{\nu_e \leftrightarrow \nu_x} = \frac{1}{2}\left(1 - \mathsf{P}^z_{\mathbf{p}}\right). \tag{2.20b}$$

On the other hand, the Hamiltonian can be written as a sum of three interaction terms:

$$\mathsf{H} = \mathsf{H}_{\mathrm{vac}} + \mathsf{H}_{\mathrm{m}} + \mathsf{H}_{\nu\nu}. \tag{2.21}$$

where H is the two-flavour Hamiltonian. The first term is the Hamiltonian in vacuum [234]:

$$\mathsf{H}_{\mathrm{vac}} = \frac{\omega_{\mathbf{p}}}{2}\begin{pmatrix} -\cos 2\theta & \sin 2\theta \\ \sin 2\theta & \cos 2\theta \end{pmatrix} = \frac{\omega_{\mathbf{p}}}{2}\mathbf{B}\cdot\vec{\sigma} \tag{2.22}$$

where $\omega_{\mathbf{p}} = \Delta m^2/2p$, $\mathbf{B} = (\sin 2\theta, 0, -\cos 2\theta)$ and θ is the smallest neutrino mixing angle in vacuum.

The other two terms in Eqs. (1.21) are special since they make the evolution equations non-linear. Even though they are very similar, we are considering that the electrons during the accretion form an isotropic gas; hence, the vector $\mathbf{v_q}$ in the first integral is distributed uniformly on the unit sphere and the factor $\mathbf{v_q}\cdot\mathbf{v_p}$ averages to zero. After integrating the matter Hamiltonian is given by:

$$\mathsf{H}_{\mathrm{m}} = \frac{\lambda}{2}\begin{pmatrix} 1 & 0 \\ 0 & -1 \end{pmatrix} = \frac{\lambda}{2}\mathbf{L}\cdot\vec{\sigma} \tag{2.23}$$

where $\lambda = \sqrt{2}G_F\left(n_{e^-} - n_{e^+}\right)$ is the charged current matter potential and $\mathbf{L} = (0, 0, 1)$.

Such simplification cannot be made with the final term. Since neutrinos are responsible for the energy loss of the infalling material during accretion, they must be escaping the accretion zone and the net neutrino and anti-neutrino flux is non-zero.In this case the factor $\mathbf{v_q}\cdot\mathbf{v_p}$ cannot be averaged to zero. At any rate, we can still use Eq. (2.18) and obtain [215, 326, 176]:

$$\mathsf{H}_{\nu\nu} = \sqrt{2}G_F\left[\int(1 - \mathbf{v_q}\cdot\mathbf{v_p})\left(\mathsf{P_q} - \bar{\mathsf{P}}_{\mathbf{q}}\right)\frac{d^3\mathbf{q}}{(2\pi)^3}\right]\cdot\vec{\sigma} \tag{2.24}$$

Introducing every Hamiltonian term in Eqs. (1.22), and using the commutation relations of the Pauli matrices, we find the equations of oscillation for neutrinos and

anti-neutrinos for each momentum mode $\mathbf{p}$:

$$\dot{\mathsf{P}}_{\mathbf{p}} = \left[\omega_{\mathbf{p}}\mathbf{B} + \lambda\mathbf{L} + \sqrt{2}G_F\int(1 - \mathbf{v}_{\mathbf{q}}\cdot\mathbf{v}_{\mathbf{p}})\left(\mathsf{P}_{\mathbf{q}} - \bar{\mathsf{P}}_{\mathbf{q}}\right)\frac{d^3\mathbf{q}}{(2\pi)^3}\right]\times\mathsf{P}_{\mathbf{p}} \tag{2.25a}$$

$$\dot{\bar{\mathsf{P}}}_{\mathbf{p}} = \left[-\omega_{\mathbf{p}}\mathbf{B} + \lambda\mathbf{L} + \sqrt{2}G_F\int(1 - \mathbf{v}_{\mathbf{q}}\cdot\mathbf{v}_{\mathbf{p}})\left(\mathsf{P}_{\mathbf{q}} - \bar{\mathsf{P}}_{\mathbf{q}}\right)\frac{d^3\mathbf{q}}{(2\pi)^3}\right]\times\bar{\mathsf{P}}_{\mathbf{p}}. \tag{2.25b}$$

Solving the above equations would yield the polarization vectors as a function of time. However, in our specific physical system, both the matter potential λ and the neutrino potential vary with the radial distance from the NS surface as well as the instant t of the physical process which can be characterized by the accretion rate $\dot{M}$. As we will see later, the time dependence can be ignored. This means that Eqs. (2.25) must be written in a way that makes explicit the spatial dependence, i.e. in terms of the vector $\mathbf{r}$. For an isotropic and homogeneous neutrino gas or a collimated ray of neutrinos the expression $dt = dr$ would be good enough, but for radiating extended sources the situation is more complicated. In Eqs. (1.22) we must replace the matrices of occupation numbers by the space dependent Wigner functions $\rho_{\mathbf{p},\mathbf{r},t}$ (and $\bar{\rho}_{\mathbf{p},\mathbf{r},t}$) and the total time derivative by the Liouville operator [49, 290]

$$\dot{\rho}_{\mathbf{p},\mathbf{r},t} = \overbrace{\frac{\partial\rho_{\mathbf{p},\mathbf{r},t}}{\partial t}}^{\text{Explicit Time}} + \overbrace{\mathbf{v}_{\mathbf{p}}\cdot\nabla_{\mathbf{r}}\,\rho_{\mathbf{p},\mathbf{r},t}}^{\text{Drift}} + \overbrace{\dot{\mathbf{p}}\cdot\nabla_{\mathbf{p}}\,\rho_{\mathbf{p},\mathbf{r},t}}^{\text{External Forces}} \tag{2.26}$$

We will ignore the third term of the Liouville operator since we won't consider the gravitational deflection of neutrinos. For peak accretion rates $\dot{M} \approx 10^{-8}$–$10^{-2}\ M_\odot$/s the characteristic accretion time is $\Delta t_{acc} = M/\dot{M} \approx M_\odot/\dot{M} \approx 10^8$–$10^2$ s. The distances traveled by a neutrino in these times are $r \approx 3\times10^{12}$–3×10^{18} cm. These distances are much larger than the typical binary separation a. As a consequence, we can consider the neutrino evolution to be a stationary process. This fact allows us to neglect the first term in Eq. (2.26). Putting together these results, the equations become:

$$i\mathbf{v}_{\mathbf{p}}\cdot\nabla_{\mathbf{r}}\,\rho_{\mathbf{p},\mathbf{r}} = [H_{\mathbf{p},\mathbf{r}}, \rho_{\mathbf{p},\mathbf{r}}] \tag{2.27a}$$

$$i\mathbf{v}_{\mathbf{p}}\cdot\nabla_{\mathbf{r}}\,\bar{\rho}_{\mathbf{p},\mathbf{r}} = [\bar{H}_{\mathbf{p},\mathbf{r}}, \bar{\rho}_{\mathbf{p},\mathbf{r}}], \tag{2.27b}$$

where $H_{\mathbf{p},\mathbf{r}}$ and $\bar{H}_{\mathbf{p},\mathbf{r}}$ are the same as (1.21) but the matrices of densities (as well as the polarization vectors) depend on the position $\mathbf{r}$. Note, however, that the electrons in the accretion zone still form an isotropic gas and Eq. (2.23) is still valid and the matter Hamiltonian depends on $\mathbf{r}$ through $n_{e^-}(\mathbf{r}) - n_{e^+}(\mathbf{r})$. The first two terms in the Hamiltonian remain virtually unchanged. On the other hand, projecting the eqautions of oscillation onto the radial distance from the NS and using the axial symmetry of the system, the integral in the neutrino-neutrino interaction term can be written as

$$\frac{\sqrt{2}G_F}{(2\pi)^2}\int(1 - v_{\vartheta'_r}v_{\vartheta_r})\,(\rho_{q,\vartheta',r} - \bar{\rho}_{q,\vartheta',r})\,q^2dq|d\cos\vartheta'_r|. \tag{2.28}$$

Since the farther from the NS the interacting neutrinos approach a perfect collinearity, the projected velocities v_{ϑ_r} become decreasing functions of the position. In this particular geometry the diagonal elements of the matrix of densities are written as a product of independent distributions over each variable p, ϑ, ϕ, where the ϕ dependence has been integrated out. The one over p is the normalized Fermi-Dirac distribution and the one over ϑ is assumed uniform due to symmetry. The r dependence is obtained through the geometrical flux dilution. Knowing this, the diagonal elements of matrices of densities at the NS surface are

$$(\rho_{\mathbf{p},\mathbf{R}_{\rm NS}})_{ee} = (\bar{\rho}_{\mathbf{p},\mathbf{R}_{\rm NS}})_{ee} = f_{\nu_e}(\mathbf{p}) \tag{2.29a}$$

$$(\rho_{\mathbf{p},\mathbf{R}_{\rm NS}})_{xx} = (\bar{\rho}_{\mathbf{p},\mathbf{R}_{\rm NS}})_{xx} = f_{\nu_x}(\mathbf{p}) \tag{2.29b}$$

where the functions f_{ν_i} are given by Eqs. (2.16).

2.3.2 Single-Angle Approximation

The integro-differential Eqs. (2.25) and (2.27) are usually numerically solved for the momentum $\mathbf{p}$ and the scalar $\mathbf{v_q} \cdot \mathbf{v_p}$. Such simulation are quite time-consuming and the result is frequently too complicated to allow for a clear interpretation of the underlying physics. For this reason, the analytic approximation called the *single-angle limit* is made. Such approximation consists in *imposing* a self-maintained coherence in the neutrino system, i.e. it is assumed that the flavour evolution of all neutrinos emitted from an extended source is the same as the flavour evolution of the neutrinos emitted from the source along a particular path. Under this premise, the propagation angle between the test neutrino and the background neutrinos is fixed. In expression (2.28) this is equivalent to dropping the ϑ' dependence of ρ and replacing the projected velocity v_{ϑ_r} either by an appropriate average at each r as in [59] or by a representative angle (usually 0 or $\pi/4$). We will follow the former approach and apply the *bulb model* described in [79]. Within this model it is shown that the projected velocity at a distance r from the neutrino emission zone is

$$v_r = \sqrt{1 - \left(\frac{R_{\rm NS}}{r}\right)^2 \left(1 - v_{R_{\rm NS}}^2\right)}. \tag{2.30}$$

where $v_{R_{\rm NS}}$ is the projected velocity at the NS surface. By redefining the matrices of density with a change of variable $u = 1 - v_{R_{\rm NS}}^2$ in the integral (2.28)

$$\rho_{p,u,r} \frac{p^2}{2\,(2\pi)^2} \to \rho_{p,u,r}, \tag{2.31}$$

and using Eq. (2.18), we can write the full equations of motion

$$\frac{\partial}{\partial r}\mathsf{P}_{p,r} = \left[\omega_{p,r}\mathbf{B} + \lambda_r\mathbf{L} + \mu_r\int_0^\infty \left(\mathsf{P}_{q,r} - \bar{\mathsf{P}}_{q,r}\right) dq\right] \times \mathsf{P}_{p,r} \tag{2.32a}$$

$$\frac{\partial}{\partial r}\bar{\mathsf{P}}_{p,r} = \left[-\omega_{p,r}\mathbf{B} + \lambda_r\mathbf{L} + \mu_r\int_0^\infty \left(\mathsf{P}_{q,r} - \bar{\mathsf{P}}_{q,r}\right) dq\right] \times \bar{\mathsf{P}}_{p,r} \tag{2.32b}$$

where we have replaced v_r by it's average value

$$\langle v_r \rangle = \frac{1}{2}\left[1 + \sqrt{1 - \left(\frac{R_{\rm NS}}{r}\right)^2}\right]. \tag{2.33}$$

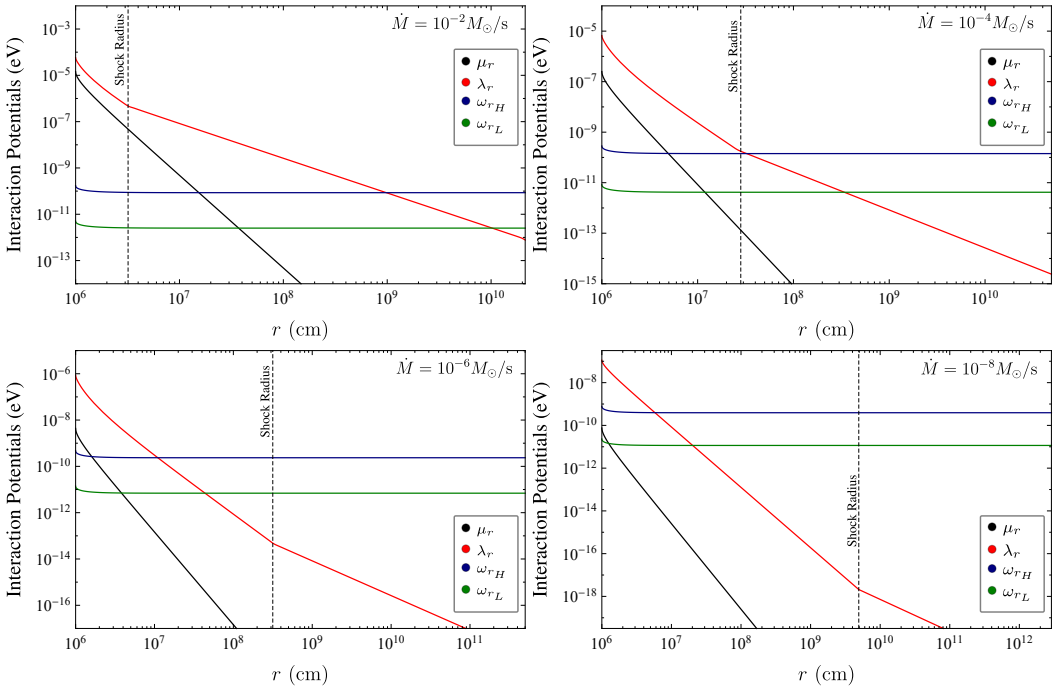

Figure 2.3. Interaction potentials as functions of the radial distance from the NS center for selected accretion rates $\dot{M}$ (see Table 2.1). Each plot runs from the NS surface to the Bondi-Hoyle surface. μ_r stands for the self-interaction neutrino potential, λ_r is the matter potential and ω_H and ω_L are the higher and lower resonances corresponding to the atmospheric and solar neutrino scales, respectively, defined in Eq. (2.52). Outside the Bondi-Hoyle region the neutrino and electron densities depend on the direction of their path relative to the SN and the particular ejecta density profile.

All the interaction potentials now depend on r and each effective potential strength is parametrized as follows [59]

$$\omega_{p,r} = \frac{\Delta m^2}{2p\langle v_r\rangle}, \tag{2.34}$$

$$\lambda_r = \sqrt{2} G_F \left(n_{e^-}(r) - n_{e^+}(r)\right) \frac{1}{\langle v_r\rangle}, \tag{2.35}$$

$$\mu_r = \frac{\sqrt{2} G_F}{2} \left(\sum_{i\in\{e,x\}} n^C_{\nu_i\bar{\nu}_i}\right) \left(\frac{R_{\mathrm{NS}}}{r}\right)^2 \left(\frac{1-\langle v_r\rangle^2}{\langle v_r\rangle}\right). \tag{2.36}$$

It is worth mentioning that all the effective potential strengths are affected by the geometry of the extended source through the projected velocity on the right side of Eqs. (2.27). For the neutrino-neutrino interaction potential, we have chosen the total neutrino number density as parametrization. This factor comes from the freedom to re-normalize the polarization vectors in the EoM. A different choice has been made in [88]. Of the other two r dependent factors, one comes from the geometrical flux dilution and the other accounts for collinearity in the single-angle approximation. Over all μ_r decays as $1/r^4$.

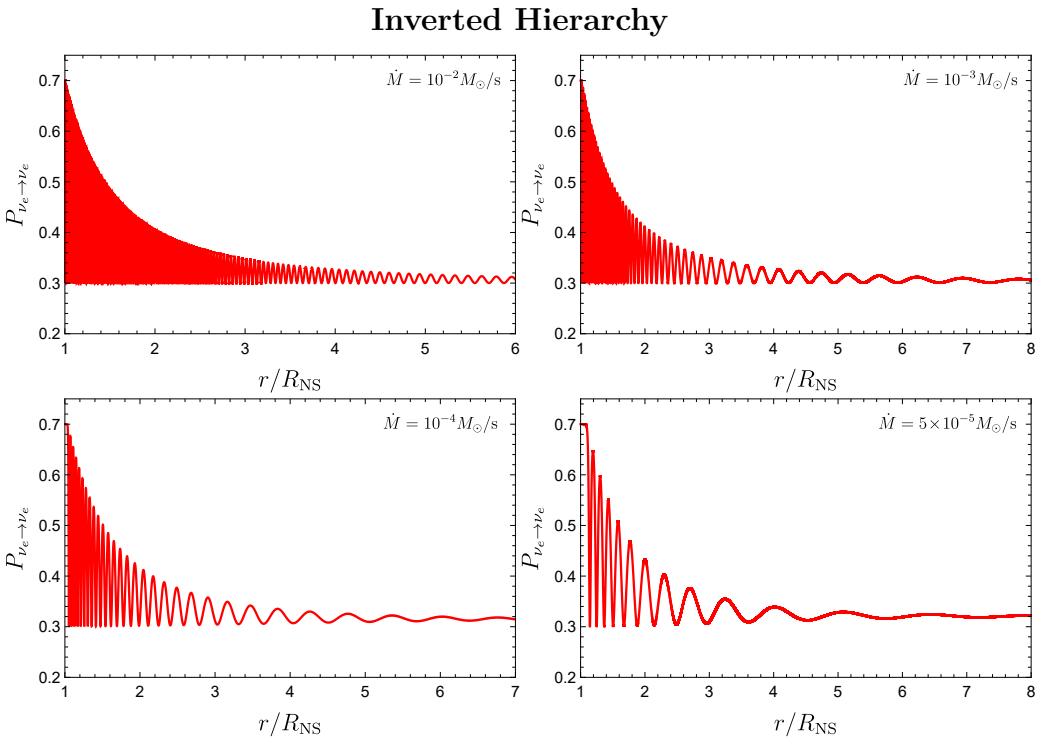

Figure 2.4. Neutrino flavour evolution for inverted hierarchy. Electron neutrino survival probability is shown as a function of the radial distance from the NS surface. The curves for the electron anti-neutrino match the ones for electron neutrinos.

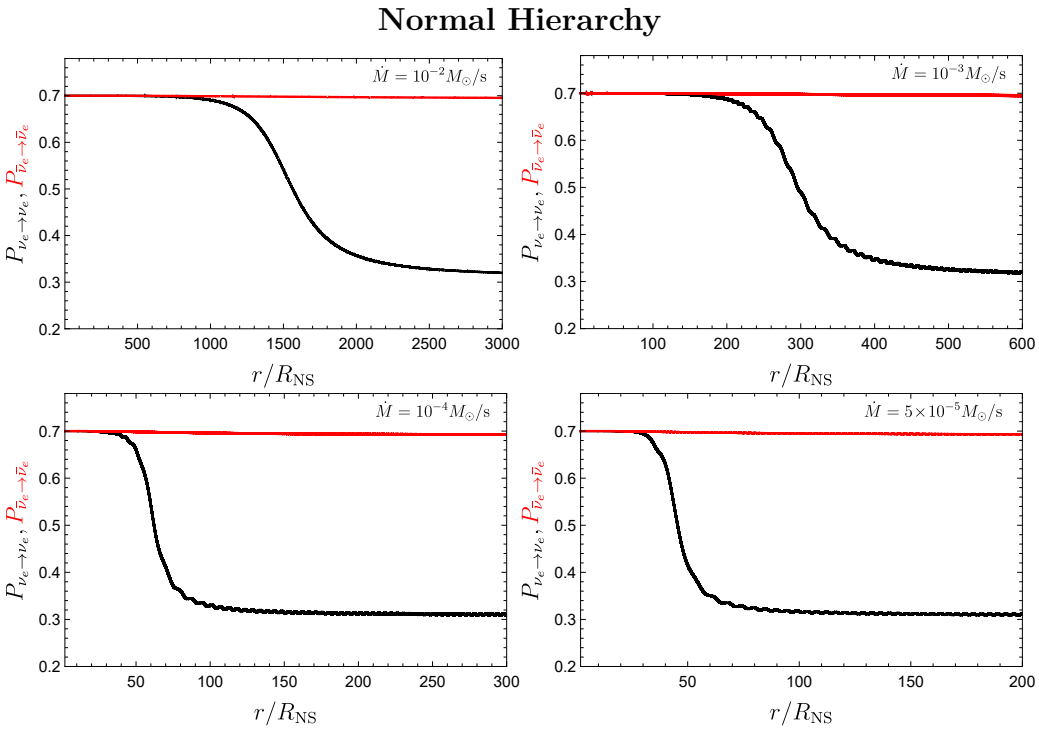

Figure 2.5. Electron neutrino and anti-neutrino flavour evolution for normal hierarchy.The survival probability is shown as a function of the radial distance from the NS surface.

In Fig. 2.3 the behavior of the effective potentials within the single-angle formalism is shown for $\dot{M} = 10^{-2} M_\odot$ s^{-1}, $10^{-4} M_\odot$ s^{-1}, $10^{-6} M_\odot$ s^{-1} and $10^{-8} M_\odot$ s^{-1}. In all cases, the neutrino energy is the corresponding average reported in Table 2.1. Since the oscillatory dynamics of the neutrino flavours are determined by the value of the potentials, and the value of the potentials depends on the data in Table 2.1, it is important to establish how sensible is this information to the model we have adopted. In particular, to the pre-SN envelope density profile index m. The reported accretion rates can be seen as different states in the evolution of a binary system or as peak accretion rates of different binary systems. For a given accretion rate, the temperature and density conditions on the neutron star surface are fixed. This, in turn, fixes the potentials involved in the equations of flavour evolution and the initial neutrino and anti-neutrino flavour content. To see the consequences of changing the index m we can estimate the peak accretion rates for new values using Eqs. (2.2). Since we are only interested in type Ic supernovae, we shall restrict these values to the ones reported in Table 1 of [24] (that is $m = 2.771$, 2.946 and 2.801), and in each case, we consider the smallest binary separation such that there is no Roche-Lobe overflow. For these parameters, we find peak accretion rates $\dot{M}_{\rm peak} \sim 10^{-2}$–$10^{-4} M_\odot$ s^{-1} with peak times at $t_{\rm peak} \approx$ 7–35 min. Because these accretion rates are still within the range in Table 2.1, the results contained in Sec. 2.4 apply also to these cases with different value of the m-index.

The profiles for the electron and positron number densities were adopted from the simulations presented in [24]. Due to the dynamics of the infalling matter, close to the NS, the behavior of $n_{e^-}(r) - n_{e^+}(r)$ is similar to μ_r. At the shock radius, the electron density's derivative presents a discontinuity and its behavior changes allowing for three distinct regions inside the Bondi-Hoyle radius. The matter potential is always higher than the neutrino potential yet, in most cases, both are higher than the vacuum potential, so we expect neutrino collective effects (neutrino oscillations) and MSW resonances to play a role in the neutrino flavour evolution inside the Bondi-Hoyle radius. Outside the capture region, as long as the neutrinos are not directed towards the SN, they will be subjected to vacuum oscillations.

2.4 Single-Angle Solutions and Multi-Angle Effects

The full dynamics of neutrino oscillations is a rather complex interplay between the three potentials discussed in Sec. 2.3.1, yet the neutrino-anti-neutrino symmetry allows us to generalize our single-angle calculations for certain accretion rates using some numerical and algebraic results obtained in [125, 90, 88] and references therein. Specifically, we know that if $\mu_r \gg \omega_r$, as long as the MSW condition $\lambda_r \simeq \omega_r$ is not met, collective effects should dominate the neutrino evolution even if $\lambda_r \gg \mu_r$. On the other hand, if $\mu_r \lesssim \omega_r$, the neutrino evolution is driven by the relative values between the matter and vacuum potentials. With this in mind, we identify two different ranges of values for the accretion rate: $\dot{M} \gtrsim 5 \times 10^{-5} M_\odot$ s^{-1} and $\dot{M} \lesssim 5 \times 10^{-5} M_\odot$ s^{-1}.

2.4.1 High Accretion Rates

For accretion rates $\dot{M} \gtrsim 5 \times 10^{-5} M_\odot \text{ s}^{-1}$ the potentials obey the following hierarchy

$$\lambda_r \gtrsim \mu_r \gg \omega_r, \tag{2.37}$$

hence, we expect strong effects of neutrino self-interactions. In order to appreciate the interesting physical processes which happen with the neutrinos along their trajectory in the accretion zone, we begin this analysis with a simplified approach, using a monochromatic spectrum with the same energy for both neutrinos and anti-neutrinos. Let us introduce the following definitions

$$\mathbf{D} = \mathsf{P}_r - \bar{\mathsf{P}}_r \tag{2.38}$$

$$\mathbf{Q} = \mathsf{P}_r + \bar{\mathsf{P}}_r - \frac{\omega_r}{\mu_r}\mathbf{B}. \tag{2.39}$$

The role of the matter potential is to logarithmically extend the period of the bipolar oscillations so we can ignore it for now. Also, we will restrict our analysis to a small enough region at $R_{\text{NS}} + \Delta r_\nu$ so that we can consider $\frac{d}{dr}(\omega_r/\mu_r) \approx 0$ (adiabatic approximation). Then, By summing and subtracting Eqs. (2.32) and using definitions (2.38) and (2.39), we obtain

$$\frac{d}{dr}\mathbf{Q} = \mu \mathbf{D} \times \mathbf{Q} \tag{2.40}$$

$$\frac{d}{dr}\mathbf{D} = \omega \mathbf{B} \times \mathbf{Q}. \tag{2.41}$$

We are now able to build a very useful analogy. The equations above are analogous to the equations of motion of a simple mechanical pendulum with a vector position given by $\mathbf{Q}$, precessing around an angular momentum $\mathbf{D}$, subjected to a force $\omega\mu\mathbf{B}$ with a moment of inertia proportional to the inverse of μ. With Eqs. (2.12) and (2.19) the initial conditions for the polarization vectors are

$$\mathsf{P}(R_{\text{NS}}) = \bar{\mathsf{P}}(R_{\text{NS}}) = (0, 0, 0.4) \tag{2.42}$$

We can easily show that $|\mathbf{Q}(R_{\text{NS}})| = |\mathsf{P}(R_{\text{NS}}) + \bar{\mathsf{P}}(R_{\text{NS}})| + O(\omega/\mu) \approx 0.8$. Calculating $\frac{d}{dr}(\mathbf{Q} \cdot \mathbf{Q})$ it can be checked that this value is conserved.

The analogous angular momentum is $\mathbf{D}(R_{\text{NS}}) = \mathsf{P}(R_{\text{NS}}) - \bar{\mathsf{P}}(R_{\text{NS}}) = 0$. Thus, the pendulum moves initially in a plane defined by $\mathbf{B}$ and the z-axis, i.e., the plane xz. Then, it is possible to define an angle φ between $\mathbf{Q}$ and the z-axis such that

$$\mathbf{Q} = |\mathbf{Q}| \left(\sin\varphi, 0, \cos\varphi\right). \tag{2.43}$$

Note that the only non-zero component of $\mathbf{D}$ is y-component and from (2.40) and (2.41) we find

$$\frac{d\varphi}{dr} = \mu |\mathbf{D}| \tag{2.44}$$

and

$$\frac{d|\mathbf{D}|}{dr} = -\omega |\mathbf{Q}| \cos(2\theta + \varphi). \tag{2.45}$$

The above equations can be equivalently written as

$$\frac{d^2\varphi}{dr^2} = -k^2 \sin(2\theta + \varphi), \tag{2.46}$$

where we have introduced the inverse characteristic distance k by

$$k^2 = \omega\mu|\mathbf{Q}|, \tag{2.47}$$

which is related to the anharmonic oscillations described by the non-linear Eq. (2.44) and Eq. (2.45). The logarithmic correction to the oscillation length due to matter effects is [125]

$$\tau_{\dot{M}} = -k^{-1} \ln\left[\theta \frac{k}{(k^2+\lambda^2)^{1/2}}\left(1 + \frac{\omega}{|\mathbf{Q}|\mu}\right)\right]. \tag{2.48}$$

The initial conditions (2.42) imply

$$\varphi\left(R_{\rm NS}\right) = \arcsin\left(\frac{\omega}{|\mathbf{Q}|\mu}\sin 2\theta\right). \tag{2.49}$$

To investigate the physical meaning of the above equation, let us assume for a moment that 2θ is a small angle. In this case $\varphi\left(R_{\rm NS}\right)$ is also a small angle. If $k^2 > 0$, which is true for the normal hierarchy $\Delta m^2 > 0$, we expect small oscillations around the initial position since the system begins in a stable position of the potential associated with Eqs. (2.44) and (2.45). No strong flavour oscillations are expected. On the contrary, for the inverted hierarchy $\Delta m^2 < 0$, $k^2 < 0$ and the initial $\varphi(R_{\rm NS})$ indicates that the system begins in an unstable position and we expect very large anharmonic oscillations. P^z (as well as $\bar{\mathsf{P}}^z$) oscillates between two different maxima passing through a minimum $-\mathsf{P}^z$ ($-\bar{\mathsf{P}}^z$) several times. This behavior implies total flavour conversion: all electronic neutrinos (anti-neutrinos) are converted into non-electronic neutrinos (anti-neutrinos) and vice-versa. This has been called bipolar oscillations in the literature [83].

We solved numerically Eqs. (2.32) for both normal and inverted hierarchies using a monochromatic spectrum dominated by the average neutrino energy for $\dot{M} = 10^{-2}, 10^{-3}, 10^{-4}$ and $5\times10^{-5} M_\odot$ s^{-1}, and the respective values reported in Table 2.1 with the initial conditions given by Eqs. (2.12) and (2.29). The behavior of the electronic neutrino survival probability inside the accretion zone is shown in Figs. 2.4 and 2.5 for inverted hierarchy and normal hierarchy, respectively. For the inverted hierarchy, there is no difference between the neutrino and anti-neutrino survival probabilities. This should be expected since for these values of r the matter and self-interaction potentials are much larger than the vacuum potential, and there is virtually no difference between Eqs. (2.32). Also, note that the anti-neutrino flavour proportions discussed in Sec. 2.2.3 remain virtually unchanged for normal hierarchy while the neutrino flavour proportions change drastically around the point $\lambda_r \sim \omega_r$. The characteristic oscillation length of the survival probability found on these plots is

$$\tau \approx (0.05 - 1) \text{ km} \tag{2.50}$$

which agree with the ones given by Eq. (2.48) calculated at the NS surface up to a factor of order one. Such a small value of τ suggests extremely quick $\nu_e\bar{\nu}_e \leftrightarrow \nu_x\bar{\nu}_x$ oscillations.

Clearly, the full equations of oscillation are highly non-linear so the solution may not reflect the real neutrino flavour evolution. Concerning the single-angle approximation, it is discussed in [125, 237, 90] that in the more realistic multi-angle approach, kinematic decoherence happens. And in [88] the conditions for decoherence as a function of the neutrino flavour asymmetry have been discussed. It is concluded that if the symmetry of neutrinos and anti-neutrinos is broken beyond the limit of $O(25\%)$, i.e., if the difference between emitted neutrinos and anti-neutrinos is roughly larger than 25% of the total number of neutrinos in the medium, decoherence becomes a sub-dominant effect.

As a direct consequence of the peculiar symmetric situation we are dealing with, in which neutrinos and anti-neutrinos are produced in similar numbers, bipolar oscillations happen and, as we have already discussed, they present very small oscillation length as shown in Eq. (2.50). Note also that the bipolar oscillation length depends on the neutrino energy. Therefore, the resulting process is equivalent to an averaging over the neutrino energy spectrum and an equipartition among different neutrino flavours is expected [237]. Although, for simplicity, we are dealing with the two neutrino hypothesis, this behavior is easily extended to the more realistic three neutrino situation. We assume, therefore, that at few kilometers from the emission region neutrino flavour equipartition is a reality:

$$\nu_e : \nu_\mu : \nu_\tau = 1 : 1 : 1. \tag{2.51}$$

Note that the multi-angle approach keeps the order of the characteristic length τ of Eq. (2.48) unchanged and kinematics decoherence happens within a few oscillation cycles [279, 125, 237]. Therefore, we expect that neutrinos created in regions close to the emission zone will be equally distributed among different flavours in less than few kilometers after their creation. Once the neutrinos reach this maximally mixed state, no further changes are expected up until the matter potential enters the MSW resonance region. We emphasize that kinematics decoherence does not mean quantum decoherence. Figs. 2.4 and 2.5 clearly show the typical oscillation pattern which happens only if quantum coherence is still acting on the neutrino system. Differently from quantum decoherence, which would reveals itself by a monotonous dumping in the oscillation pattern, kinematics decoherence is just the result of averaging over the neutrino energy spectrum resulting from quick flavour conversion which oscillation length depends on the neutrino energy. Therefore, neutrinos are yet able to quantum oscillate if appropriate conditions are satisfied. We discuss now the consequences of the matter potential.

Matter Effects

After leaving the emisison region, beyond $r \approx R_{\rm NS} + \Delta r_\nu$, where Δr_ν is the width defined in Eq. (2.6), the effective neutrino density quickly falls in a asymptotic behavior $\mu_r \approx 1/r^4$. The decay of λ_r is slower. Hence, very soon the neutrino flavour evolution is determined by the matter potential. Matter suppresses neutrino oscillations and we do not expect significant changes in the neutrino flavour content along a large region. Nevertheless, the matter potential can be so small that there will be a region along the neutrino trajectory in which it can be compared with the

neutrino vacuum frequencies and the higher and lower resonant density conditions will be satisfied, i.e.:

$$\lambda(r_H) = \omega_H = \frac{\Delta m^2}{2\langle E_\nu \rangle} \text{ and } \lambda(r_L) = \omega_L = \frac{\Delta m^2_{21}}{2\langle E_\nu \rangle}, \tag{2.52}$$

where Δm^2 and Δm^2_{21} are, respectively, the squared-mass differences found in atmospheric and solar neutrino observations. Table 1.1 shows the experimental values of mixing angles and mass-squared differences taken from [217]. The definition of Δm^2 used is: $\Delta m^2 = m_3^2 - (m_2^2 + m_1^2)/2$. Thus, $\Delta m^2 = \Delta m^2_{31} - \Delta m^2_{21}/2 > 0$, if $m_1 < m_2 < m_3$, and $\Delta m^2 = \Delta m^2_{32} + \Delta m^2_{21}/2 < 0$ for $m_3 < m_1 < m_2$. When the above resonance conditions are satisfied the MSW effects happen and the flavour content of the flux of electronic neutrinos and anti-neutrinos will be again modified. The final fluxes can be written as

$$F_{\nu_e}(E) = P_{\nu_e \to \nu_e}(E) F^0_{\nu_e}(E) + [1 - P_{\nu_e \to \nu_e}(E)]\, F^0_{\nu_x}(E) \tag{2.53a}$$

$$F_{\bar{\nu}_e}(E) = P_{\bar{\nu}_e \to \bar{\nu}_e}(E) F^0_{\bar{\nu}_e}(E) + [1 - P_{\bar{\nu}_e \to \bar{\nu}_e}(E)]\, F^0_{\bar{\nu}_x}(E) \tag{2.53b}$$

where $F^0_{\nu_e}(E)$, $F^0_{\nu_x}(E)$, $F^0_{\bar{\nu}_e}(E)$ and $F^0_{\bar{\nu}_x}(E)$ are the fluxes of electronic and non-electronic neutrinos and anti-neutrinos after the bipolar oscillations of the emission zone and $P_{\nu_e \to \nu_e}(E)$ and $P_{\bar{\nu}_e \to \bar{\nu}_e}(E)$ are the survival probability of electronic neutrinos and anti-neutrinos during the resonant regions.

In order to evaluate $F_{\nu_e}(E)$ and $F_{\bar{\nu}_e}(E)$ after matter effects, we have to estimate the survival probability at the resonant regions. There are several articles devoted to this issue; for instance we can adopt the result in [94], namely, for normal hierarchy

$$P_{\nu_e \to \nu_e}(E) = X \sin^2 \theta_{12} \tag{2.54a}$$

$$P_{\bar{\nu}_e \to \bar{\nu}_e}(E) = \cos^2 \theta_{12} \tag{2.54b}$$

and, for inverted hierarchy

$$P_{\nu_e \to \nu_e}(E) = \sin^2 \theta_{12} \tag{2.55a}$$

$$P_{\bar{\nu}_e \to \bar{\nu}_e}(E) = X \cos^2 \theta_{12} \tag{2.55b}$$

The factor X, the conversion probability between neutrino physical eigenstates, is given by [219, 94, 153]

$$X = \frac{\exp(2 r_{\rm res} k_{\rm res} \cos 2\theta_{13}) - 1}{\exp(2 r_{\rm res} k_{\rm res}) - 1}, \tag{2.56}$$

where $r_{\rm res} = r_L$ or $r_{\rm res} = r_H$, defined according to Eq. (2.52) and

$$\frac{1}{k_{\rm res}} = \left| \frac{d \ln \lambda_r}{dx} \right|_{r = r_{\rm res}}. \tag{2.57}$$

The factor X is related to how fast physical environment features relevant for neutrino oscillations change, such as neutrino and matter densities.

For slow and adiabatic changes $X \to 0$ while for fast and non-adiabatic, $X \to 1$. In our specific cases, the MSW resonances occur very far from the accretion zone where the matter density varies very slow and therefore $X \to 0$, as can be explicitly calculated from Eq. (2.56). Consequently, it is straightforward to estimate the final fluxes of electronic and non-electronic neutrinos and anti-neutrinos.

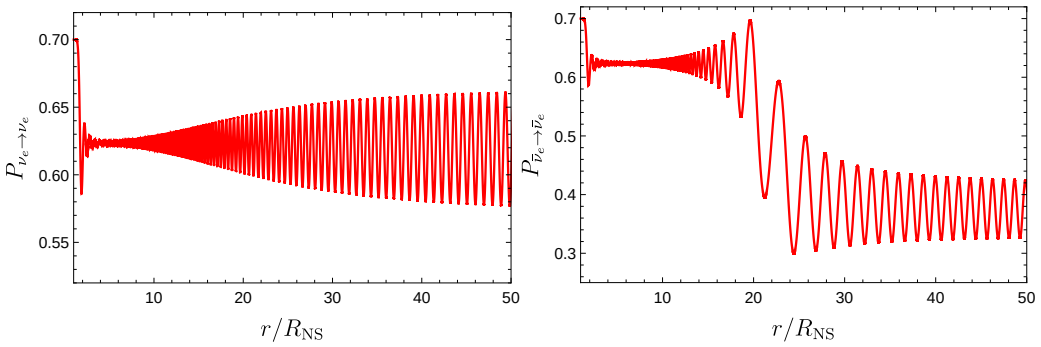

Figure 2.6. Electron neutrino and anti-neutrino flavour evolution for inverted hierarchy and $\dot{M} = 10^{-6} M_\odot$ s^{-1}. The survival probability is shown as a function of the radial distance from the NS surface.

2.4.2 Low Accretion Rates

For accretion rates $\dot{M} < 5 \times 10^{-5} M_\odot$ s^{-1}, either the matter potential is close enough to the vacuum potential and the MSW condition is satisfied, or both the self-interaction and matter potentials are so low that the flavour oscillations are only due to the vacuum potential. In both cases, bipolar oscillations are not present. In Fig. (2.6) we show the survival probability for $\dot{M} = 10^{-6} M_\odot$ s^{-1} as an example. We can see that neutrinos and anti-neutrinos follow different dynamics. In particular, for anti-neutrinos there are two decreases. The first one, around $r \approx (1\text{–}2) R_{\rm NS}$, is due to bipolar oscillations which are rapidly damped by the matter potential as discussed in Sec. 2.4.1. The second one happens around $r \approx (10\text{–}20) R_{\rm NS}$. It can be seen from the bottom left panel of Fig. 2.3 (that one for $\dot{M} = 10^{-6} M_\odot$ s^{-1}), that around $r \approx (1\text{–}2) \times 10^7$ cm (or, equivalently, $r \approx (10\text{–}20)\, R_{\rm NS}$) the higher MSW resonance occurs ($\lambda_r \sim \omega_{r_H}$). For inverted hierarchy, such resonance will affect anti-neutrinos depleting its number, as can be seen from Eq. (2.53). Without bipolar oscillations, it is not possible to guarantee that decoherence will be complete and Eq. (2.51) is no longer valid. The only way to know the exact flavour proportions is to solve the full Eqs. (2.25).

Table 2.2. Fraction of neutrinos and anti-neutrinos for each flavour after decoherence and matter effects. $n = 2\sum_i n_{\nu_i}$.

	$n^0_{\nu_e}/n$	$n^0_{\bar{\nu}_e}/n$	$n^0_{\nu_x}/n$	$n^0_{\bar{\nu}_x}/n$	n_{ν_e}/n	$n_{\bar{\nu}_e}/n$	n_{ν_x}/n	$n_{\bar{\nu}_x}/n$
Normal Hierarchy	$\frac{1}{6}$	$\frac{1}{6}$	$\frac{1}{3}$	$\frac{1}{3}$	$\frac{1}{3}$	$\frac{1}{6}+\frac{1}{6}\sin^2\theta_{12}$	$\frac{1}{6}$	$\frac{1}{3}-\frac{1}{6}\sin^2\theta_{12}$
Inverted Hierarchy	$\frac{1}{6}$	$\frac{1}{6}$	$\frac{1}{3}$	$\frac{1}{3}$	$\frac{1}{6}+\frac{1}{6}\cos^2\theta_{12}$	$\frac{1}{3}$	$\frac{1}{3}-\frac{1}{6}\cos^2\theta_{12}$	$\frac{1}{6}$

2.5 Neutrino Emission Spectra

Using the the calculations of last section we can draw a comparison between the creation spectra of neutrinos and anti-neutrinos at the NS surface (F_ν^c, n_ν^c), initial spectra after kinematic decoherence (F_ν^0, n_ν^0) and emission spectra after the MSW resonances (F_ν, n_ν). Table 2.2 contains a summary of the flavour content inside the Bondi-Hoyle radius. With these fractions and Eqs. (2.16) it is possible to reproduce the spectrum for each flavour and for accretion rates $M \geq 5\times10^{-5} M_\odot$ s^{-1}.

The specific cases for $\dot{M} = 10^{-2} M_\odot$ s^{-1} are shown in Fig. 2.7. In such figures, the left column corresponds to normal hierarchy and the right corresponds to inverted hierarchy. The first two rows show the number fluxes after each process studied. The last row shows the relative fluxes F_ν/F_ν^C between the creation and emission fluxes. For the sake of clarity, we have normalized the curves to the total neutrino number at the NS surface

$$n = 2 \sum_{i\in\{e,x\}} n_{\nu_i}. \tag{2.58}$$

so that each one is a normalized Fermi-Dirac distribution multiplied by the appropriate flavour content fraction. To reproduce any other case, it is enough to use Eqs. (2.16) with the appropriate temperature.

At this point two comments have to be made about our results:

- As we mentioned before, the fractions in Table 2.2 were obtained by assuming a monochromatic spectrum and using the single-angle approximation. This would imply that the spectrum dependent phenomenon called the *spectral stepwise swap* of flavours is not present in our analysis even though it has been shown that it can also appear in multi-angle simulations [90]. Nevertheless, we know from our calculations in Sec. 2.2.3 that neutrinos and anti-neutrinos of all flavours are created with the exact same spectrum up to a multiplicative constant. Hence, following [238, 239], by solving the equation

$$\int_{E_c}^{\infty} (n_{\nu_e} - n_{\nu_x})\, dE = \int_0^{\infty} (n_{\bar{\nu}_e} - n_{\bar{\nu}_x})\, dE, \tag{2.59}$$

  we find that the critical (split) energy is $E_c = 0$. This means that the resulting spectrum should still be unimodal and the spectral swap in our system could be approximated by a multiplicative constant that is taken into account in the decoherence analysis of Sec. 2.4.

- The fluxes of electronic neutrinos and anti-neutrinos shown in these figures and in Eqs. (2.53) represent fluxes at different positions up to a geometrical $1/r^2$ factor, r being the distance from the NS radius. Also, since we are considering the fluxes before and after each oscillatory process, the values of r are restricted to $r = R_{\rm NS}$ for F_ν^C, $\tau_{\dot{M}} < r < r_H$ for F_ν^0, and $r > r_L$ for F_ν. To calculate the number flux at a detector, for example, much higher values of r have to be considered and it is necessary to study vacuum oscillations in more detail. Such calculations will be presented elsewhere.

From Fig. 2.7 one can observe that the dominance of electronic neutrinos and anti-neutrinos found at their creation at the bottom of the accretion zone is promptly

erased by kinematic decoherence in such a way that the content of the neutrinos and anti-neutrinos entering the MSW resonant region is dominated by non-electronic flavours. After the adiabatic transitions provoked by MSW transitions, electronic neutrinos and anti-neutrinos dominate again the emission spectrum except for non-electronic anti-neutrinos in the normal hierarchy. Although no energy spectrum distortion is expected, the flavour content of neutrinos and anti-neutrinos produced near the NS surface escape to the outer space in completely different spectra when compared with the ones in which they were created, as shown in the last row of Fig. 2.7.

2.6 Concluding Remarks and Perspectives

We can now proceed to draw the conclusions and some astrophysical consequences of this work:

1. The main neutrino production channel in XRFs and BdHNe in the hypercritical accretion process is pair annihilation: $e^{-}e^{+} \rightarrow \nu\bar{\nu}$. This mechanism produces an initial equal number of neutrino and anti-neutrino and an initial 7/3 relative fraction between electronic and other flavours. These features lead to a different neutrino phenomenology with respect to the typical core-collapse SN neutrinos produced via the URCA process.

2. The neutrino density is higher than both the electron density and the vacuum oscillation frequencies for the inner layers of the accretion zone and the SIP dictates the flavour evolution along this region, as it is illustrated by Fig. 2.3. This particular system leads to very fast pair conversions $\nu_e\bar{\nu}_e \leftrightarrow \nu_{\mu,\tau}\bar{\nu}_{\mu,\tau}$ induced by bipolar oscillations with oscillation length as small as $O(0.05\text{–}1)$ km. However, due to the characteristics of the main neutrino production process, neutrinos and anti-neutrinos have very similar fluxes inside the neutrino emission zone and kinematic decoherence dominates the evolution of the polarization vectors.

3. The kinematic decoherence induces a fast flux equipartition among the different flavours that then enters the matter dominated regions in which MSW resonances take place.

4. Therefore, the neutrino flavour content emerging from the Bondi-Hoyle surface to the outer space is different from the original one at the bottom of the accretion zone. As shown in Table 2.2, The initial 70% and 30% distribution of electronic and non-electronic neutrinos becomes 55% and 45% or 62% and 38% for normal or inverted hierarchy, respectively. Since the $\nu \leftrightarrow \bar{\nu}$ oscillations are negligible [224, 227, 314] the total neutrino to anti-neutrino ratio is kept constant.

We have shown that such a rich neutrino phenomenology is uniquely present in the hypercritical accretion process in XRFs and BdHNe. This deserves the appropriate attention since it paves the way for a new arena of neutrino astrophysics besides SN neutrinos. There are a number of issues which have still to be investigated:

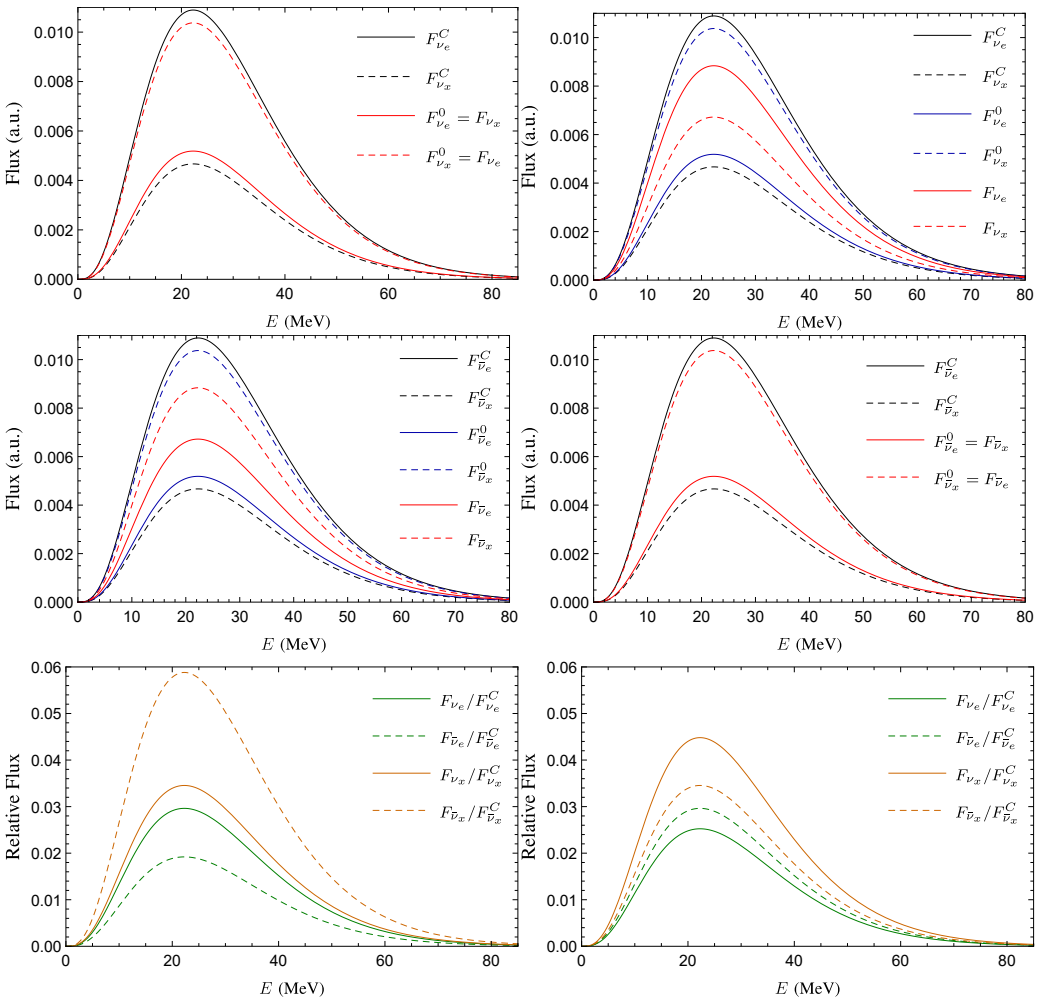

Figure 2.7. Several neutrino and anti-neutrino number fluxes for different neutrino flavours are presented for $\dot{M} = 10^{-2} M_\odot/\mathrm{s}$. Each column corresponds to a neutrino mass hierarchy: normal hierarchy on the left and inverted hierarchy on the right. The first two rows show the number fluxes after each process studied. F^C_ν, F^0_ν and F_ν are the creation flux at the bottom accretion zone due to e^+e^- pair annihilation, the flux after the region with dominant neutrino-neutrino potential and the final emission flux after the region with dominant neutrino-matter potential, respectively. The last row shows the relative fluxes F_ν/F^C_ν between the creation and emission fluxes.

1. We have made some assumptions which, albeit being a first approximation to a more detailed picture, have allowed us to set the main framework to analyse the neutrino oscillations phenomenology in these systems. We have shown in [25] that the SN ejecta carry enough angular momentum to form a disk-like structure around the NS before being accreted. However, the knowledge of the specific properties of such possible disk-like structure surrounding the neutron star is still pending of more accurate numerical simulations at such distance scales. For instance, it is not clear yet if such a structure could be modeled via thin-disk or thick-disk models. We have adopted a simplified model assuming isotropic accretion and the structure of the NS accretion region used in [24] which accounts for the general physical properties of the system. In order to solve the hydrodynamic equations, the neutrino-emission region features, and the neutrino flavour-oscillation equations, we have assumed: spherically symmetric accretion onto a non-rotating NS, a quasi-steady-state evolution parametrized by the mass accretion rate, a polytropic equation of state, and subsonic velocities inside the shock radius. The matter is described by a perfect gas made of ions, electrons, positrons and radiation with electron and positron obeying a Fermi-Dirac distribution. The electron fraction was fixed and equal to 0.5. We considered pair annihilation, photo-neutrino process, plasmon decay and bremsstrahlung to calculate neutrino emissivities. Under the above conditions we have found that the pair annihilation dominates the neutrino emission for the accretion rates involved in XRFs and BdHNe (see [24] for further details). The photons are trapped within the infalling material and the neutrinos are transparent, taking away most of the energy from the accretion. We are currently working on the relaxation of some of the above assumptions, e.g. the assumption of spherical symmetry to introduce a disk-like accretion picture, and the results will be presented elsewhere. In this line it is worth mentioning that some works have been done in this direction (see, e.g., [324, 325]), although in a Newtonian framework, for complete dissociated matter, and within the thin-disk approximation. In these models, disk heights H are found to obey the relation $H/r \sim 0.1$ near the neutron star surface which suggests that the results might be similar to the ones of a spherical accretion as the ones we have adopted. We are currently working on a generalization including general relativistic effects in axial symmetry to account for the fast rotation that the NS acquires during the accretion process. This was already implemented for the computation of the accretion rates at the Bondi-Hoyle radius position in [24], but it still needs to be implemented in the computation of the matter and neutrino density-temperature structure near the NS surface. In addition, the description of the equation of state of the infalling matter can be further improved by taking into account beta and nuclear statistical equilibrium.

   In forthcoming works we will relax the assumptions made not only on the binary system parameters but also make more detailed calculations on the neutrino oscillations including general relativistic and multi-angle effects. This paper, besides presenting a comprehensive non-relativistic account of flavour transformations in spherical accretion, serves as a primer that has allowed

us to identify key theoretical and numerical features involved in the study of neutrino oscillations in the IGC scenario of GRBs. From this understanding, we can infer that neutrino oscillations might be markedly different in a disk-like accretion process. First, depending on the value of the neutron-star mass, the inner disk radius may be located at an $r_{\rm inner} > R_{\rm NS}$ beyond the NS surface (see, e.g., [266, 54]), hence the neutrino emission must be located at a distance $r \geq r_{\rm inner}$. On the other hand, depending on the accretion rate, the density near the inner radius can be higher than in the present case and move the condition for neutrino cooling farther from the inner disk radius, at $r > r_{\rm inner}$. Both of these conditions would change the geometric set up of the neutrino emission. Furthermore, possible larger values of T and ρ may change the mechanisms involved in neutrino production. For example, electron-positron pair capture, namely $p + e^- \to n + \nu_e$, $n + e^+ \to p + \bar{\nu}_e$ and $n \to p + e^- + \bar{\nu}_e$, may become as efficient as the electron-positron pair annihilation. This, besides changing the intensity of the neutrino emission, would change the initial neutrino-flavour configuration.

2. Having obtained the flux as well as the total number of neutrinos and anti-neutrinos of each flavour that leave the binary system during the hypercritical accretion process in XRFs and BdHNe, it raises naturally the question of the possibility for such neutrinos to be detected in current neutrino observatories. For instance, detectors such as Hyper-Kamiokande are more sensitive to the inverse beta decay events produced in the detector, i.e. $\bar{\nu}_e + p \to e^+ + n$ (see [3] for more details), consequently, the $\bar{\nu}_e$ are the most plausible neutrinos to be detected. [170] have pointed out that for a total energy in $\bar{\nu}_e$ of 10^{52} erg and $\langle E_{\bar{\nu}_e} \rangle \sim 20$ MeV, the Hyper-Kamiokande neutrino-horizon is of the order of 1 Mpc. In the more energetic case of BdHNe we have typically $\langle E_{\nu,\bar{\nu}} \rangle \sim 20$ MeV (see Table 2.1) and a total energy carried out $\bar{\nu}_e$ of the order of the gravitational energy gain by accretion, i.e. $E_g \sim 10^{52}$–10^{53} erg. Therefore we expect the BdHN neutrino-horizon distance to be also of the order of 1 Mpc. These order-of-magnitude estimates need to be confirmed by detailed calculations, including the vacuum oscillations experienced by the neutrinos during their travel to the detector, which we are going to present elsewhere.

3. If we adopt the local BdHNe rate ~ 1 Gpc^{-3} yr^{-1} [266] and the data reported above at face value, it seems that the direct detection of this neutrino signal is very unlikely. However, the physics of neutrino oscillations may have consequences on the powering mechanisms of GRBs such as the electron-positron pair production by neutrino-pair annihilation. The energy deposition rate of this process depends on the local energy-momentum distribution of (anti)neutrinos which, as we have discussed, is affected by the flavour oscillation dynamics. This phenomenon may lead to measurable effects on the GRB emission.

4. An IGC binary leading either to an XRF or to a BdHN is a unique neutrino-physics laboratory in which there are at least three neutrino emission channels at the early stages of the GRB-emission process: i) the neutrinos emitted in the explosion of the $\rm CO_{core}$ as SN; ii) the neutrinos studied in this work

created in the hypercritical accretion process triggered by the above SN onto the NS companion, and iii) the neutrinos from fallback accretion onto the νNS created at the center of the SN explosion. It remains to establish the precise neutrino time sequence as well as the precise relative neutrino emissivities from all these events. This is relevant to establish both the time delays in the neutrino signals as well as their fluxes which will become a unique signature of GRB neutrinos following the IGC paradigm.

5. As discussed in [266], there are two cases in which there is the possibility to have hypercritical accretion onto a BH. First, in BdHNe there could be still some SN material around the newly-born BH which can create a new hypercritical accretion process [24]. Second, a $\sim 10\ M_\odot$ BH could be already formed before the SN explosion, namely the GRB could be produced in a $\mathrm{CO_{core}}$-BH binary progenitor. The conditions of temperature and density in the vicinity of these BHs might be very different to the ones analysed here and, therefore, the neutrino emission and its associated phenomenology. We have recalled in the introduction that such an accretion process onto the BH can explain the observed 0.1–100 GeV emission in BdHNe [261, 264, 265, 266, 10]. The interaction of such an ultra-relativistic expanding emitter with the interstellar medium could be a possible source of high-energy (e.g. TeV-PeV) neutrinos, following a mechanisms similar to the one introduced in the traditional collapsar-fireball model of long GRBs (see [8, 162] and references therein).

6. Although the symmetry between the neutrino and anti-neutrino number densities has allowed us to generalize the results obtained within the single-angle and monochromatic spectrum approximations, to successfully answer the question of detectability, full-scale numerical solutions will be considered in the future to obtain a precise picture of the neutrino-emission spectrum. In particular, it would be possible to obtain an r-dependent neutrino spectrum without the restrictions discussed in Sec. 2.5.

7. For low accretion rates ($\dot{M} \lesssim 5 \times 10^{-5}\ M_\odot\ \mathrm{s}^{-1}$) the matter and self-interaction potentials in Eqs. (2.32) decrease and the general picture described in Fig. 2.3 changes. The resonance region could be located around closer to the NS surface, anticipating the MSW condition $\lambda_r \sim \omega_r$ and interfering with the kinematic decoherence. This changes the neutrino flavour evolution and, of course, the emission spectrum. Hence, the signature neutrino-emission spectrum associated with the least luminous XRFs might be different from the ones reported here.

Chapter 3

Neutrino Oscillations in NCADs around Kerr BHs

3.1 Introduction

Neutrino flavour oscillations are now an experimental fact [65] and, in recent years, its study based only on MSW effects [308, 192] has been transformed by the insight that refractive effects of neutrinos on themselves due to the neutrino SIP are essential. Their behaviour in vacuum, matter or by neutrino self-interactions have been studied in the context of early universe evolution [18, 87, 278, 157, 158, 156, 184, 171, 75, 309, 2, 148], solar and atmospheric neutrino anomalies [13, 14, 91, 64, 117, 177, 73, 128, 304], and core-collapse SN [234, 216, 81, 279, 112, 78, 90, 82, 237, 88, 89, 50, 80, 77, 60, 59, 280, 83, 312, 33, 152, 305, 194, 131, 321] and references therein. We are here interested in astrophysical situations when neutrino self-interactions becomes more relevant than the matter potential. This implies systems in which a high density of neutrinos is present and in fact most of the literature on neutrino self-interaction dominance are concentrated on supernova neutrinos. It has been there shown how collective effects, such as synchronized and bipolar oscillations, change the flavour content of the emitted neutrinos when compared with the original content deep inside the exploding star.

This chapter aims to explore the problem of neutrino flavour oscillations in the case of long GRBs within the BdHN scenario. The GRB progenitor is a binary system composed of a CO_{core} and a companion neutron star (NS) [255, 263, 133, 246, 105, 261]. The CO_{core} explodes as SN ejecting matter that produces a hypercritical accretion (i.e. highly super-Eddington) process onto the NS companion. The NS reaches the critical mass for gravitational collapse, hence forming a rotating BH. The emission of neutrinos is a crucial ingredient since they act as the main cooling process that allows the accretion onto the NS to proceed at very high rates of up to $1\ M_\odot\ \mathrm{s}^{-1}$ [105, 103, 25, 24, 26].

In [27] and Chapter 2, we studied the neutrino flavour oscillations in the aforementioned hypercritical accretion process onto the NS, all the way to BH formation. We showed that, the density of neutrinos on top the NS, in the accreting "atmosphere", is such that neutrino self-interactions dominate the flavour evolution leading to collective effects. The latter induce in this system quick flavour conversions with a

short oscillation length as small as (0.05–1) km. Far from the NS surface the neutrino density decrease and so the matter potential and MSW resonances dominate the flavour oscillations. The main result has been that the neutrino flavour content emerging on top of the accretion zone was completely different compared to the one created at the bottom of it.

In the BdHN scenario, part of the SN ejecta keeps bound to the newborn Kerr BH, forming an accretion disk onto it. In this context, the study of accretion disks and their nuances related to neutrinos is of paramount importance to shed light on this aspect of the GRB central engine. In most cases, the mass that is exchanged in close binaries has enough angular momentum so that it cannot fall radially. As a consequence, the gas will start rotating around the star or BH forming a disk. However, the magneto-hydrodynamics that describe the behaviour of accretion disks are too complex to be solved analytically and full numerical analysis are time-consuming and costly. To bypass this difficulty, different models make approximations that allow casting the physics of an accretion disk as a two- or even one-dimensional problem. These approximations can be pigeonholed into four categories: *symmetry*, *temporal evolution*, *viscosity* and *dynamics*. Almost all analytic models are axially symmetric. This is a sensible assumption for any physical systems that rotates. Similarly, most models are time-independent although this is a more complicated matter. A disk can evolve in time in several ways. For example, the accretion rate $\dot{M}$ depends on the external source of material which need not be constant and, at the same time, the infalling material increases the mass and angular momentum of the central object, constantly changing the gravitational potential. Additionally, strong winds and outflows can continually change the mass of the disk. Nonetheless, $\dot{M}(\boldsymbol{x}, t) = \dot{M} = \text{constant}$ is assumed. Viscosity is another problematic approximation. For the gas to spiral down, its angular momentum needs to be reduced by shear stresses. These come from the turbulence driven by differential rotation and the electromagnetic properties of the disk [16, 127, 17, 15] but, again, to avoid magneto-hydrodynamical calculations, the turbulence accounted for using a phenomenological viscosity $\alpha = \text{constant}$, such that the kinematical viscosity takes the form $\nu \approx \alpha H c_s$, where c_s is the local isothermal sound speed of the gas and H is the height of the disk measured from the plane of rotation (or half-thickness). This idea was first put forward by [282] and even though there is disagreement about the value and behaviour of the viscosity constant, and it has been criticized as inadequate [147, 218, 146, 159], several thriving models use this prescription. Finally, the assumptions concerning the dynamics of the disk are related to what terms are dominant in the energy conservation equation and the Navier-Stokes equation that describe the fluid (apart from the ones related to symmetry and time independence). In particular, it amounts to deciding what cooling mechanisms are important, what external potentials should be considered and what are the characteristics of the internal forces in the fluid. The specific tuning of these terms breeds one of the known models: *thin disks*, *slim disks*, *advection-dominated accretion flows* (ADAFs), *thick disks*, *neutrino-cooled accretion disks* (also called neutrino-dominated accretion flows NDAFs), *convection-dominated accretion flows* (CDAFs), *luminous hot accretion flows* (LHAFs), *advection-dominated inflow-outflow solutions* (ADIOS) and *magnetized tori*. The options are numerous and each model is full of subtleties making accretion flows around a given object an extremely rich area of research.

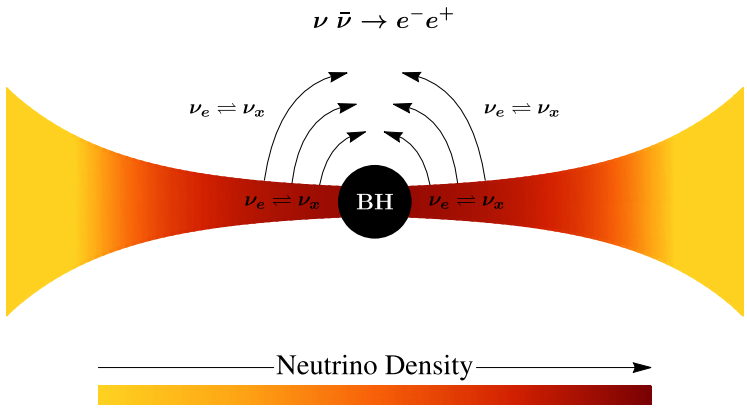

Figure 3.1. Schematic representation of the physical system. Due to conditions of high temperature and density, neutrinos are produced in copious amounts inside the disk. Since they have a very low cross-section, neutrinos are free to escape but not before experiencing collective effects due to the several oscillation potentials. The energy deposition rate of the process $\nu + \bar{\nu} \to e^- + e^+$ depends on the local distribution of electronic and non-electronic (anti)-neutrinos which is affected by the flavour oscillation dynamics.

For useful reviews and important articles with a wide range of subjects related to accretion disks see [232, 161, 4, 178, 96, 37, 201, 140, 233, 199, 6, 320, 36, 164, 169] and references therein.

NCADs are of special interest for GRBs. They are hyperaccreting slim disks, optically thick to radiation that can reach high densities $\rho \approx 10^{10}$–10^{13} g cm^{-3} and high temperatures $T \approx 10^{10}$–10^{11} K around the inner edge. Under these conditions, the main cooling mechanism is neutrino emission since copious amounts of (mainly electron) neutrinos and anti-neutrinos are created by electron-positron pair annihilation, URCA and nucleon-nucleon bremsstrahlung processes, and later emitted from the disk surface. These $\nu\bar{\nu}$ pairs might then annihilate above the disk producing an $e^- e^+$ dominated outflow. NCADs were proposed as a feasible central engine for GRBs in [228] and have been studied extensively since [203, 154, 70, 155, 167, 123, 51, 142, 135, 143, 172, 316]. In [70] and later in [51], it was found that the inner regions of the disk can be optically thick to $\nu_e\bar{\nu}_e$ trapping them inside the disk, hinting that NCADs may be unable to power GRBs. Yet, the system involves neutrinos propagating through dense media and, consequently, an analysis of neutrino oscillations, missing in the above literature, must be performed. Fig. 3.1 represents the standard situation of the physical system of interest. The dominance of the SIP induces collective effects or decoherence. In either case, the neutrino flavour content of the disk changes. Some recent articles are starting to recognize their role in accretion disks and spherical accretion [175, 97, 299, 27, 313]. The energy deposition rate above and accretion disk by neutrino-pair annihilation as a powering mechanism of GRBs in NCADs can be affected by neutrino oscillation in

two ways. The neutrino spectrum emitted at the disk surface depends not only on the disk temperature and density but also the neutrino flavour transformations inside the disk. Also, once the neutrinos are emitted they undergo flavour transformations before being annihilated. Our main objective is to analyse the consequences of neutrino flavour oscillations in NCADs.

The chapter is organized as follows. In Sec. 3.2 we outline the features of NCADs making emphasis on the assumptions needed to derive the equations. In Sec. 3.3 we discuss the general details of the equation that drive the evolution of neutrino oscillations and use the information of the previous section to build a simple model that adds this dynamic to NCADs. In Sec. 3.4 we give some details on the initial conditions needed to solve the equations of accretion disks and neutrino oscillations. In Sec. 3.5 we discuss the main results of our calculations and analyse in detail the neutrino oscillation phenomenology in accretion disks. Finally, we present in Sec. 3.6 the conclusions of this work.

3.2 Hydrodynamics

3.2.1 Velocities and Averaging

To describe the spacetime around a Kerr BH of mass M we use the metric $g_{\mu\nu}$ in Boyer-Lindquist coordinates, with spacelike signature, and with a dimensionless spin parameter $a = J/M^2$ so that the line element is

$$\begin{aligned} ds^2 = &\left(g_{tt} - \omega^2 g_{\phi\phi}\right) dt^2 + g_{\phi\phi}\left(d\phi - \omega\, dt\right)^2 \\ &+ g_{rr}\, dr^2 + g_{\theta\theta}\, d\theta^2, \end{aligned} \tag{3.1}$$

in coordinates (t, r, θ, ϕ). The covariant components $(\boldsymbol{g})_{\mu\nu}$ of the metric are

$$\begin{aligned} g_{tt} &= -\left(1 - \frac{2\,M\,r}{\Sigma}\right),\ g_{rr} = \frac{\Sigma}{\Delta},\ g_{\theta\theta} = \Sigma, \\ g_{\phi\phi} &= \left(r^2 + M^2 a^2 + \frac{2\,M^3 a^2 r}{\Sigma}\sin^2\theta\right)\sin^2\theta, \\ g_{t\phi} &= -\frac{2\,M^2\,a\,r}{\Sigma}\sin^2\theta, \end{aligned} \tag{3.2}$$

and its determinant is

$$g = -\Sigma^2 \sin^2\theta, \tag{3.3}$$

with the well known functions $\Sigma = r^2 + M^2 a^2 \cos^2\theta$ and $\Delta = r^2 - 2Mr + M^2 a^2$. We denote the coordinate frame by CF. Note that these coordinates can be used by an observer on an asymptotic rest frame. The angular velocity of the locally non-rotating frame (LNRF) is

$$\omega = -\frac{g_{t\phi}}{g_{\phi\phi}} = \frac{2\,a\,M^2}{(r^3 + M^2 a^2 r + 2M^3 a^2)}, \tag{3.4}$$

and in Eq. (3.2) it can be seen explicitly that if an observer has a an angular velocity $d\phi/dt = \omega$ it would not measure any differences between the $\pm\phi$ directions. The

LNRF is defined by orthonormality and the coordinate change $\phi_{\rm LNRF} = \tilde{\phi} = \phi - \omega\, t$ [19, 21]. We assume that the disk lies on the equatorial plane of the BH ($\theta = \pi/2$) . This way we represent the average movement of the fluid by geodesic circular orbits with angular velocity $\Omega = d\phi/dt = u^\phi/u^t$ plus a radial velocity so that the local rest frame (LRF) of the fluid is obtained by performing, first, an azimuthal Lorentz boost with velocity $\beta^{\hat{\phi}}$ to a corotating frame (CRF) [114], and then a radial Lorentz boost with velocity $\beta^{\tilde{r}}$. Clearly, the metric on the LNRF, CRF and LRF is diag$(-1, 1, 1, 1)$. The expression for the angular velocity of circular orbits is obtained by setting $\dot{r} = \ddot{r} = 0$ in the r-component of the geodesic equation

$$\Omega^{\pm} = \pm \frac{\sqrt{M}}{(r^{3/2} \pm M^{3/2} a)}, \tag{3.5}$$

where $(+)$ is for prograde orbits and $(-)$ is for retrograde orbits. We will limit our calculations to prograde movement with $0 \leq a \leq 1$ but extension to retrograde orbits is straightforward. Finally, we can get the components of the 4-velocity of the fluid by transforming $\boldsymbol{u}_{\rm LRF} = (1, 0, 0, 0)$ back to the CF

$$u^\mu = \left(\frac{\gamma_{\tilde{r}} \gamma_{\hat{\phi}}}{\sqrt{\omega^2 g_{\phi\phi} - g_{tt}}}, \frac{\gamma_{\tilde{r}} \beta^{\tilde{r}}}{\sqrt{g_{rr}}}, 0, \frac{\gamma_{\tilde{r}} \gamma_{\hat{\phi}} \Omega}{\sqrt{\omega^2 g_{\phi\phi} - g_{tt}}} \right), \tag{3.6}$$

leaving $\beta^{\tilde{r}}$ to be determined by the conservation laws. In Eq. (3.6) we have replaced $\beta^{\hat{\phi}}$ with Eq. (A.3). A discussion on the explicit form of the transformations and some miscellaneous results are given in Appendix A. We will also assume that the disk is in a steady-state. This statement requires some analysis. There are two main ways in which it can be false:

I. As matter falls into the BH, its values M and a change [20, 298], effectively changing the spacetime around it. For the spacetime to remain the same we require $\Omega^{-1} \ll t_{\rm acc} = \Delta M_0 / \dot{M}_{\rm acc}$, where ΔM_0 is the total mass of the disk and $\dot{M}_{\rm acc}$ is the accretion rate. The characteristic accretion time must be bigger than the dynamical time of the disk so that flow changes due to flow dynamics are more important than flow changes due to spacetime changes. Equivalent versions of this condition that appear throughout disk accretion articles are $t_{\rm dym} \ll t_{\rm visc}$ and

$$\beta^r \ll \beta^\phi < 1, \tag{3.7}$$

where it is understood that the accretion rate obeys $\dot{M}_{\rm acc} \approx \Delta M_0 / t_{\rm acc}$. To put this numbers into perspective, consider a solar mass BH ($M = 1 M_\odot$) and a disk with mass between $\Delta M_0 = (1 - 10) M_\odot$. For accretion rates up to $\dot{M}_{\rm acc} = 1 M_\odot/{\rm s}$ the characteristic accretion time is $t_{\rm acc} \lesssim (1 - 10)$ s, while $\Omega^{-1} \sim (10^{-5} - 10^{-1})$ s between $r = r_{\rm ISCO}$ and $r = 2000 M_\odot$. Consequently, a wide range of astrophysical system satisfy this condition and it is equivalent to claiming that both $\boldsymbol{\partial}_t$ and $\boldsymbol{\partial}_\phi$ are Killing fields.

II. At any point inside the disk, any field $\psi(t, r, \theta, \phi)$ that reports a property of the gas may variate in time due to the turbulent motion of the flow. So, to

assume that any field is time-independent and smooth enough in r for its flow to be described by Eq. (3.6) means replacing such field by its average over an *appropriate* spacetime volume. The same process allows to choose a *natural* set of variables that split the hydrodynamics into r-component equations and θ-component equations. The averaging process has been explained in [207, 211, 114]. We include the analysis here and try to explain it in a self-consistent manner. The turbulent motion is characterized by the eddies. The azimuthal extension of the largest eddies can be 2π, like waves crashing around an island, but their linear measure cannot be larger than the thickness of the disk, and, as measured by an observer on the CRF, their velocity is of the order of $\beta^{\tilde{r}}$ so that their period along the r component is $\Delta\tilde{t} \approx (\text{Thickness})/\beta^{\tilde{r}}$, e.g. [163, §33]. If we denote by H the average half-thickness of the disk as measured by this observer at r over the time $\Delta\tilde{t}$, then the appropriate volume $\mathcal{V}$ is composed by the points (t, r, θ, ϕ) such that $t \in [t^* - \Delta t/2, t^* + \Delta t/2]$, $\theta \in [\theta_{\min}, \theta_{\max}]$ and $\phi \in [0, 2\pi)$, where we have transformed $\Delta\tilde{t}$ and $\Delta\tilde{r}$ back to the CF using Eqs. (A.4) as approximations. The values $\theta_{\min}$ and $\theta_{\max}$ correspond to the upper and lower faces of the disk, respectively. Then, the average takes the form

$$\psi(t, r, \theta, \phi) \mapsto \psi(r, \theta) = \langle \psi(t, r, \theta, \phi) \rangle = \frac{\int_{t^*-\Delta t/2}^{t^*+\Delta t/2} \int_0^{2\pi} \psi(r, t, \theta, \phi) \sqrt{\frac{-g}{g_{rr} g_{\theta\theta}}} dt d\phi}{\int_{t^*-\Delta t/2}^{t^*+\Delta t/2} \int_0^{2\pi} \sqrt{\frac{-g}{g_{rr} g_{\theta\theta}}} dt d\phi}. \tag{3.8}$$

The steady-state condition is achieved by requiring that the Lie derivative of the averaged quantity along the Killing field $\boldsymbol{\partial}_t$ vanishes: $\mathcal{L}_{\boldsymbol{\partial}_t} \langle \psi \rangle = 0$. Note that the thickness measurement performed by the observer already has an error $\sim M^2 a^2 H^3 / 6 r^4$ since it extends the Lorentz frame beyond the local neighbourhood but, if we assume that the disk is thin ($H/r \ll 1$), and we do, this error remains small. At the same time, we can take all metric components evaluated at the equator and use Eq. (3.6) as the representative average velocity. Under these conditions, we have $\theta_{\max} - \theta_{\min} \approx 2H/r$ and the term $\sqrt{-g/g_{rr}}$ in Eq. (3.8) cancels out. It becomes clear that an extra θ integral is what separates the radial and polar variables. In other words, the r-component variables are the *vertically integrated* fields

$$\psi(r, \theta) \mapsto \psi(r) = \int_{\theta_{\min}}^{\theta_{\max}} \psi(r, \theta) \sqrt{g_{\theta\theta}} d\theta. \tag{3.9}$$

The vertical equations of motion can be obtained by setting up Newtonian (with relativistic corrections) equations for the field $\psi(r, \theta)$ at each value of r (see, e.g., [207, 5, 7, 169]).

3.2.2 Conservation Laws

The equations of evolution of the fluid are contained in the conservation laws $\nabla_\mu T^{\mu\nu} = 0$ and $\nabla_\mu (\rho u^\mu) = 0$. The most general stress-energy tensor for a Navier-

Stokes viscous fluid with heat transfer is [196, 191]

$$\boldsymbol{T} = \overbrace{(\rho + U + P)\,\boldsymbol{u}\otimes\boldsymbol{u} + P\boldsymbol{g}}^{\text{Ideal Fluid}} + \overbrace{(-2\eta\boldsymbol{\sigma} - \zeta\,(\boldsymbol{\nabla}\cdot\boldsymbol{u})\,\boldsymbol{P})}^{\text{Viscous Stress}} + \overbrace{\boldsymbol{q}\otimes\boldsymbol{u} + \boldsymbol{u}\otimes\boldsymbol{q}}^{\text{Heat flux}}, \tag{3.10}$$

where ρ, P, U, ζ, η, $\boldsymbol{q}$, $\boldsymbol{P}$ and $\boldsymbol{\sigma}$ are the rest-mass energy density, pressure, internal energy density, dynamic viscosity, bulk viscosity, heat-flux 4-vector, projection tensor and shear tensor, respectively, and thermodynamic quantities are measured on the LRF. We do not consider electromagnetic contributions and ignore the causality problems associated with the equations derived from this stress-energy tensor since we are not interested in phenomena close to the horizon [114]. Before deriving the equations of motion and to add a simple model of neutrino oscillations to the dynamics of disk accretion we must make some extra assumption. We will assume that the θ integral in Eq. (3.8) can be approximated by

$$\int_{\theta_{\min}}^{\theta_{\max}} \psi\sqrt{g_{\theta\theta}}d\theta \approx \psi r\,(\theta_{\max} - \theta_{\min}) \approx 2H\psi, \tag{3.11}$$

for any field ψ. Also, we use Stokes' hypothesis ($\zeta = 0$). Since we are treating the disk as a thin differentially rotating fluid, we will assume that, on average, the only non-zero component of the shearing stress on the CRF is $\sigma_{\tilde{r}\tilde{\phi}}$ (there are torques only on the ϕ direction), and $q_{\tilde{\theta}}$ is the only non-zero component of the energy flux (on average the flux is vertical). By $u^\mu\sigma_{\mu\nu} = 0$ and Eq. (A.7) we have

$$\sigma_{r\phi} = \frac{\gamma_{\hat{\phi}}^3}{2}\frac{g_{\phi\phi}}{\sqrt{\omega^2 g_{\phi\phi} - g_{tt}}}\partial_r\Omega\,, \quad \sigma_{rt} = -\Omega\sigma_{r\phi}. \tag{3.12}$$

Finally, the turbulent viscosity is estimated to be $\sim l\Delta u$ where l is the size of the turbulent eddies and Δu is the average velocity difference between points in the disk separated by a distance l. By the same arguments in [163, §33] and in Sec. 3.2.2, l can be at most equal to $2H$ and Δu can be at most equal to the isothermal sound speed $c_s = \sqrt{\partial P/\partial\rho}$ or else the flow would develop shocks [96]. The particular form of c_s can be calculated from Eq. (3.16). This way we get

$$\eta = \Pi\nu_{\text{turb}} = 2\alpha\Pi H c_s, \tag{3.13}$$

with $\alpha \leq 1$ and $\Pi = \rho + U + P$. In a nutshell, this is the popular α-prescription put forward by [282]. As we mentioned at the end of Sec. 3.2.1, on the CRF for a fixed value of r, the polar equation takes the form of Euler's equation for a fluid at rest where the acceleration is given by the tidal gravitational acceleration, that is, the θ component of the fluid's path-lines relative acceleration in the θ direction.

$$\frac{1}{r}\partial_\theta P \approx \rho r\cos\theta\left[\boldsymbol{R}\left(\boldsymbol{u}, \boldsymbol{\partial}_{\tilde{\theta}}, \boldsymbol{u}\right)\cdot\boldsymbol{\partial}_{\tilde{\theta}}\right]_{\theta=\pi/2}, \tag{3.14}$$

with $\boldsymbol{R}$ the Riemann curvature tensor. With $u^{\tilde{\mu}} \approx (1,0,0,0)$, Eq. (3.11), Eq. (A.8) and assuming that there is no significant compression of the fluid under the action

of the tidal force, integration of this equation yields the relation up to second order in $\pi/2-\theta$

$$P=\frac{1}{2}\rho R^{\tilde{\theta}}{}_{\tilde{t}\tilde{\theta}\tilde{t}}\Big|_{\theta=\pi/2}\left(H^2-r^2\left(\frac{\pi}{2}-\theta\right)^2\right), \tag{3.15}$$

where we used the condition $P=0$ at the disk's surface. Hence, the average pressure inside the disk is (cf. [7, 169, 51])

$$P=\frac{1}{3}\rho H^2 R^{\tilde{\theta}}{}_{\tilde{t}\tilde{\theta}\tilde{t}}\Big|_{\theta=\pi/2}. \tag{3.16}$$

The equation of mass conservation is obtained by directly inserting into Eq. (B.5) the averaged density and integrating vertically

$$\begin{aligned}0&=\partial_r\left(2rH\rho u^r\right)\\&\Rightarrow 2Hr\rho u^r=\text{constant}\\&\Rightarrow 2Hr\rho u^r=-\frac{\dot{M}}{2\pi},\end{aligned} \tag{3.17}$$

where the term $2Hr\rho u^r$ is identified as the average inward mass flux through a cylindrical surface of radius r per unit azimuthal angle and thus must be equal to the accretion rate divided by 2π. The same process applied to Eq. (B.4) yields the energy conservation equation

$$u^r\left[\partial_r\left(HU\right)-\frac{U+P}{\rho}\partial_r\left(H\rho\right)\right]=2\eta H\sigma^{r\phi}\sigma_{r\phi}-H\epsilon, \tag{3.18}$$

where factors proportional to H/r were ignored and we assume $\Pi\approx\rho$ to integrate the second term on the left hand side. ϵ is the average energy density measured on the LRF (see the discussion around Eq. (B.7)). The first term on the right hand side is the viscous heating rate F_{heat} and the second term is the cooling rate F_{cool}. The last constitutive equation is obtained by replacing the density in Eq. (3.17) using Eq. (B.12)

$$u^r=-\frac{4\alpha Hc_s\sigma^r_\phi}{Mf\left(x,x^*\right)}. \tag{3.19}$$

3.2.3 Equations of State

We consider that the main contribution to the rest-mass energy density of the disk is made up of neutrons, protons and ions. This way $\rho=\rho_{\text{B}}=n_Bm_B$ with baryon number density n_B and baryon mass m_B equal to the atomic unit mass. The disk's baryonic mass obeys Maxwell-Boltzmann statistics and its precise composition is determined by the Nuclear Statistical Equilibrium (NSE). We denote the mass fraction of an ion i by $X_i=\rho_i/\rho_B$ (if $i=p$ or n then we are referring to proton or neutrons) and it can be calculated by the Saha equation [55, 47]

$$X_i=\frac{A_im_B}{\rho}G_i\left(\frac{TA_im_B}{2\pi}\right)^{3/2}\exp\left(\frac{Z_i\left(\mu_p+\mu_p^C\right)+N_i\mu_n-\mu_i^C+B_i}{T}\right). \tag{3.20a}$$

$$\text{With constraints} \quad \sum_i X_i = 1, \quad \sum_i Z_i Y_i = Y_e. \tag{3.20b}$$

In these equations T, A_i, N_i, Z_i, Y_e, Y_i, G_i, μ_i and B_i are the temperature, atomic number, neutron number, proton number, electron fraction (electron abundance per baryon), ion abundance per baryon, nuclear partition function, chemical potential (including the nuclear rest-mass energy) and ion binding energy. The μ_i^C are the Coulomb corrections for the NSE state in a dense plasma (see Appendix C). The binding energy data for a large collection of nuclei can be found in [182] and the temperature-dependent partition functions are found in [241, 240]. Even though we take into account Coulomb corrections in NSE we assume that the baryonic mass can be described by an ideal gas[1] and

$$P_B = \sum_i P_i = n_B T \sum_i \frac{X_i}{A_i}, \quad U_B = \frac{3}{2} P_B. \tag{3.21}$$

The disk also contains photons, electrons, positrons, neutrinos and anti-neutrinos. As it is usual in neutrino oscillations analysis, we distinguish only between electron (anti)-neutrinos $\nu_e, (\bar{\nu}_e)$ and x (anti)-neutrinos $\nu_x(\bar{\nu}_x)$, where $x = \mu + \tau$ is the superposition of muon neutrinos and tau neutrinos. Photons obey the usual relations

$$P_\gamma = \frac{\pi^2 T^4}{45}, \quad U_\gamma = 3P_\gamma, \tag{3.22}$$

while, for electrons and positrons we have

$$n_{e^\pm} = \frac{\sqrt{2}}{\pi^2}\xi^{3/2}\left[\mathcal{F}_{1/2,0}\left(\xi, \eta_{e^\pm}\right) + \xi \mathcal{F}_{3/2,0}\left(\xi, \eta_{e^\pm}\right)\right], \tag{3.23a}$$

$$U_{e^\pm} = \frac{\sqrt{2}}{\pi^2}\xi^{5/2}\left[\mathcal{F}_{3/2,0}\left(\xi, \eta_{e^\pm}\right) + \xi \mathcal{F}_{5/2,0}\left(\xi, \eta_{e^\pm}\right)\right], \tag{3.23b}$$

$$P_{e^\pm} = \frac{2\sqrt{2}}{3\pi^2}\xi^{5/2}\left[\mathcal{F}_{3/2,0}\left(\xi, \eta_{e^\pm}\right) + \frac{\xi}{2}\mathcal{F}_{5/2,0}\left(\xi, \eta_{e^\pm}\right)\right], \tag{3.23c}$$

with $\xi = T/m_e$ and written in terms of the generalized Fermi functions (see Appx. D.1). In these equations $\eta_{e^\pm} = \left(\mu_{e^\pm} - m_e\right)/T$ is the electron (positron) degeneracy parameter without rest-mass contributions (not to be confused with η in Sec. (3.2.2)). Since electrons and positrons are in equilibrium with photons due to the pair creation and annihilation processes ($e^- + e^+ \to 2\gamma$) we know that their chemical potentials are related by $\mu_{e^+} = -\mu_{e^-}$, which implies $\eta_{e^+} = -\eta_{e^-} - 2/\xi$. From the charge neutrality condition and we obtain

$$n_B Y_e = n_{e^-} - n_{e^+}. \tag{3.24}$$

For neutrinos, the story is more complicated. In the absence of oscillations and if the disk is hot and dense enough for neutrinos to be trapped within it and in

[1] Since bulk viscosity effects appear as a consequence of correlations between ion velocities due to Coulomb interactions and of large relaxation times to reach local equilibrium, the NSE and ideal gas assumptions imply that imposing Stokes' hypothesis becomes de rigueur [303, 191, 40]

thermal equilibrium, n_ν, U_ν, P_ν can be calculated with Fermi-Dirac statistics using the same temperature T

$$n^{\text{trapped}}_{\nu(\bar{\nu})} = \frac{T^3}{\pi^2}\mathcal{F}_{2,0}\left(\eta_{\nu(\bar{\nu})}\right), \tag{3.25a}$$

$$U^{\text{trapped}}_{\nu(\bar{\nu})} = \frac{T^4}{\pi^2}\mathcal{F}_{3,0}\left(\eta_{\nu(\bar{\nu})}\right), \tag{3.25b}$$

$$P^{\text{trapped}}_{\nu(\bar{\nu})} = \frac{U^{\text{trapped}}_{\nu(\bar{\nu})}}{3}, \tag{3.25c}$$

where it is understood that $\mathcal{F}(\eta) = \mathcal{F}(y{=}0, \eta)$ with $\eta_{\nu(\bar{\nu})} = \mu_{\nu(\bar{\nu})}/T$ and the ultra-relativistic approximation $m_\nu \ll 1$ for any neutrino flavour is used. If thermal equilibrium is has not been achieved, Eq. (3.25) cannot be used. Nevertheless, at any point in the disk and for a given value of T and ρ, (anti)-neutrinos are being created through several processes. The processes we take into account are *pair annihilation* $e^- + e^+ \to \nu + \bar{\nu}$, *electron or positron capture by nucleons* $p + e^- \to n + \nu_e$ or $n + e^+ \to p + \bar{\nu}_e$, *electron capture by ions* $A + e^- \to A' + \nu_e$, plasmon decay $\tilde{\gamma} \to \nu + \bar{\nu}$ and *nucleon-nucleon bremsstrahlung* $n_1 + n_2 \to n_3 + n_4 + \nu + \bar{\nu}$. The emission rates can be found in Appendix D. The chemical equilibrium for these processes determines the values of $\eta_{\nu(\bar{\nu})}$. In particular,

$$\eta_{\nu_e} = \eta_{e^-} + \ln\left(\frac{X_p}{X_n}\right) + \frac{1-\mathbb{Q}}{\xi}, \tag{3.26a}$$

$$\eta_{\bar{\nu}_e} = -\eta_{\nu_e}, \tag{3.26b}$$

$$\eta_{\nu_x} = \eta_{\bar{\nu}_x} = 0, \tag{3.26c}$$

satisfy all equations. Here, $\mathbb{Q} = (m_n - m_p)/m_e \approx 2.531$. Once the (anti)-neutrino number and energy emission rates (R_i, Q_i) are calculated for each process i, the (anti)-neutrino thermodynamic quantities are given by

$$n^{\text{free}}_{\nu(\bar{\nu})} = H\sum_i N_{i,\nu(\bar{\nu})}, \tag{3.27a}$$

$$U^{\text{free}}_{\nu(\bar{\nu})} = H\sum_i Q_{i,\nu(\bar{\nu})}, \tag{3.27b}$$

$$P^{\text{free}}_{\nu(\bar{\nu})} = \frac{U^{\text{free}}_{\nu(\bar{\nu})}}{3}, \tag{3.27c}$$

Remember we are using Planck units so in these expressions there should be an H/c instead of just an H. The transition for each (anti)-neutrino flavour between both regimes occurs when Eq. (3.25b) and Eq. (3.27b) are equal and it can be simulated by defining the parameter

$$w_{\nu(\bar{\nu})} = \frac{U^{\text{free}}_{\nu(\bar{\nu})}}{U^{\text{free}}_{\nu(\bar{\nu})} + U^{\text{trapped}}_{\nu(\bar{\nu})}}. \tag{3.28}$$

With this equation, the (anti)-neutrino average energy can be defined as

$$\langle E_{\nu(\bar{\nu})}\rangle = \left(1 - w_{\nu(\bar{\nu})}\right)\frac{U^{\text{free}}_{\nu(\bar{\nu})}}{n^{\text{free}}_{\nu(\bar{\nu})}} + w_{\nu(\bar{\nu})}\frac{U^{\text{trapped}}_{\nu(\bar{\nu})}}{n^{\text{trapped}}_{\nu(\bar{\nu})}}. \tag{3.29}$$

and the approximated number and energy density are

$$n_{\nu(\bar{\nu})} = \begin{cases} n^{\text{free}}_{\nu(\bar{\nu})}, & \text{if } w_{\nu(\bar{\nu})} < 1/2. \\ n^{\text{trapped}}_{\nu(\bar{\nu})}, & \text{if } w_{\nu(\bar{\nu})} \geq 1/2. \end{cases} \tag{3.30a}$$

$$U_{\nu(\bar{\nu})} = \begin{cases} U^{\text{free}}_{\nu(\bar{\nu})}, & \text{if } w_{\nu(\bar{\nu})} < 1/2. \\ U^{\text{trapped}}_{\nu(\bar{\nu})}, & \text{if } w_{\nu(\bar{\nu})} \geq 1/2. \end{cases} \tag{3.30b}$$

$$P_{\nu(\bar{\nu})} = \frac{U_{\nu(\bar{\nu})}}{3}. \tag{3.30c}$$

Note that both Eq. (3.27c) and (3.30c) are approximations since they are derived from equilibrium distributions, but they help make the transition smooth. Besides, the neutrino pressure before thermal equilibrium is negligible. This method was presented in [51] where it was used only for electron (anti)-neutrinos. The total (anti)-neutrino number and energy flux through one the disk's faces can be approximated with

$$\dot{n}_{\nu_j(\bar{\nu}_j)} = \sum_{j\in\{e,x\}} \frac{n_{\nu_j(\bar{\nu}_j)}}{1+\tau_{\nu_j(\bar{\nu}_j)}}, \tag{3.31a}$$

$$F_{\nu_j(\bar{\nu}_j)} = \sum_{j\in\{e,x\}} \frac{U_{\nu_j(\bar{\nu}_j)}}{1+\tau_{\nu_j(\bar{\nu}_j)}}. \tag{3.31b}$$

Here, τ_{ν_i} is the total optical depth for the (anti)-neutrino $\nu_i\,(\bar{\nu}_i)$. Collecting all the expressions we write the total internal energy and total pressure

$$U = \sum_{j\in\{e,x\}} \left(U_{\nu_j} + U_{\bar{\nu}_j}\right) + U_B + U_{e^-} + U_{e^+} + U_\gamma \ , \tag{3.32a}$$

$$P = \sum_{j\in\{e,x\}} \left(P_{\nu_j} + P_{\bar{\nu}_j}\right) + P_B + P_{e^-} + P_{e^+} + P_\gamma \ . \tag{3.32b}$$

The (anti)-neutrino energy flux through the disk faces contributes to the cooling term in the energy conservation equation but it is not the only one. Another important energy sink is *photodisintegration* of ions. To calculate it we proceed as follows. The energy spent to knocking off a nucleon of an ion i is equal to the binding energy per nucleon B_i/A_i. Now, consider a fluid element of volume V whose moving walls are attached to the fluid so that no baryons flow in or out. The total energy of photodisintegration contained within this volume is the sum over i of (energy per nucleon of ion i)$\times$(# of freed nucleons of ion i inside V). This can be written as $\sum_i (B_i/A_i) n_{f,i} V$, or, alternatively, $n_B V \sum_i (B_i/A_i) X_{f,i}$. If we approximate B_i/A_i by the average binding energy per nucleon $\bar{B}$ (which is a good approximation save for a couple of light ions) the expression becomes $n_B V \bar{B} \sum_i X_{f,i} = n_B V \bar{B} X_f = n_B V \bar{B}(X_p + X_n)$. The rate of change of this energy as measured by an observer on the LRF with proper time λ is

$$\frac{d}{d\lambda}\left[n_B V \bar{B}\,(X_p + X_n)\right] = n_B V \bar{B} \frac{d}{d\lambda}\,(X_p + X_n)\,. \tag{3.33}$$

The derivative of $n_B V$ vanishes by baryon conservation. Transforming back to CF and taking the average we find the energy density per unit time used in disintegration of ions

$$\epsilon_{\text{ions}} = n_B \bar{B} u^r H \partial_r \left(X_p + X_n\right). \tag{3.34}$$

The average energy density measured on the LRF ϵ appearing in Eq. (3.18) is

$$\epsilon = \epsilon_{\text{ions}} + \frac{1}{H} \sum_{i \in \{e,x\}} \left(F_{\nu_i} + F_{\bar{\nu}_i}\right). \tag{3.35}$$

Finally, a similar argument allows us to obtain the equation of lepton number conservation. For any lepton ℓ, the total lepton number density is $\sum_{\ell \in \{e,\mu,\tau\}} \left(n_\ell - n_{\bar{\ell}} + n_{\nu_\ell} - n_{\bar{\nu}_\ell}\right)$. So, with Eq. (3.24), calculating the rate of change as before, using Gauss' theorem and taking the average we get

$$u^r H \left[n_B \partial_r Y_e + \partial_r \sum_{\ell \in \{e,x\}} \left(n_{\nu_\ell} - n_{\bar{\nu}_\ell}\right) \right] = \sum_{\ell \in \{e,x\}} \left(\dot{n}_{\bar{\nu}_\ell} - \dot{n}_{\nu_\ell}\right), \tag{3.36}$$

where the right hand side represents the flux of lepton number through the disk's surface.

3.3 Neutrino Oscillations

To study the flavour evolution of neutrinos within a particular system, a Hamiltonian governing neutrino oscillation must be set up. The relative strength of the potentials appearing in such Hamiltonian depends on four elements: geometry, mass content, neutrino content and neutrino mass hierarchy. Geometry refers to the nature of net neutrino fluxes and possible gravitational effects. Mass and neutrino content refers to the distribution of leptons of each flavour (e, μ, τ) present in the medium. Finally, mass hierarchy refers to the relative values of the masses m_1, m_2, m_3 for each neutrino mass eigenstates (see Table 1.1). We dedicate this section to a detailed derivation of the equations of flavour evolution for a neutrino dominated accretion disk. To maintain consistency with traditional literature of neutrino oscillations we will reuse some symbols appearing in previews sections. To avoid confusion we point out that the symbols in this section are independent of previews sections unless we explicitly draw a comparison.

3.3.1 Equations of Oscillation

To derive the equations of oscillations we repeat the procedure used in Sec. 2.3.1. However, since the system studied here has a different geometry from spherical accretion, the arguments and the resulting equations will be different. Consider an observer on the LRF (which is almost identical to the CRF due to Eq. (3.7) at a point r. In its spatial local frame, the unit vectors $\hat{x}, \hat{y}, \hat{z}$ are parallel to the unit vectors $\hat{r}, \hat{\theta}, \hat{\phi}$ of the CF, respectively. Solving Eq. (1.22) in this coordinate system would yield matrices $\rho, \bar{\rho}$ as functions of time t. However, in our specific physical system, both the matter density and the neutrino density vary with the radial distance from the BH. This means that the equations of oscillations must be

written in a way that makes explicit the spatial dependence, i.e. in terms of the coordinates x, y, z. For a collimated ray of neutrinos, the expression $dt = dr$ would be good enough, but for radiating extended sources or neutrino gases the situation is more complicated.

In Eq. (1.22) we must replace the matrices of occupation numbers by the space-dependent Wigner functions $\rho_{\mathbf{p},\mathbf{x},t}$ (and $\bar{\rho}_{\mathbf{p},\mathbf{x},t}$) and the total time derivative by the Liouville operator [49, 290]

$$\dot{\rho}_{\mathbf{p},\mathbf{x},t} = \overbrace{\frac{\partial \rho_{\mathbf{p},\mathbf{x},t}}{\partial t}}^{\text{Explicit Time}} + \overbrace{\mathbf{v}_{\mathbf{p}} \cdot \nabla_{\mathbf{x}} \rho_{\mathbf{p},\mathbf{x},t}}^{\text{Drift}} + \overbrace{\dot{\mathbf{p}} \cdot \nabla_{\mathbf{p}} \rho_{\mathbf{p},\mathbf{x},t}}^{\text{External Forces}} \tag{3.37}$$

In this context, $\mathbf{x}$ represents a vector in the LRF. In the most general case, finding $\rho_{\mathbf{p},\mathbf{x},t}$ and $\bar{\rho}_{\mathbf{p},\mathbf{x},t}$ means solving a 7D neutrino transport problem in the variables $x, y, z, p_x, p_y, p_z, t$. Since our objective is to construct a simple model of neutrino oscillations inside the disk, to obtain the specific form of Eq. (1.22) we must simplify the equations by imposing on it conditions that are consistent with the assumptions made in Sec. 3.2.

- Due to axial symmetry, the neutrino density is constant along the $\mathbf{z}$ direction. Moreover, since neutrinos follow geodesics, we can set $\dot{p}_z \approx \dot{p}_\phi = 0$.
- Within the thin disk approximation (as represented by Eq. (3.11)) the neutrino and matter densities are constant along the $\mathbf{y}$ direction and the momentum change due to curvature along this direction can be neglected, that is, $\dot{p}_y \approx 0$.
- In the LRF, the normalized radial momentum of a neutrino can be written as $p_x = \pm \frac{r}{\sqrt{r^2 - 2Mr + M^2a^2}}$. Hence, the typical scale of the change of momentum with radius is $\Delta r_{p_x,\text{eff}} = \left| \frac{d \ln p_x}{dr} \right|^{-1} = \frac{r\left(r^2 - 2Mr + M^2a^2\right)}{M(Ma^2 - r)}$, which obeys $\Delta r_{p_x,\text{eff}} > r_s$ for $r > 2r_{\text{in}}$. This means that we can assume $\dot{p}_x \approx 0$ up to regions very close to the inner edge of the disk.
- We define an effective distance $\Delta r_{\rho,\text{eff}} = \left| \frac{d \ln(Y_e n_B)}{dr} \right|^{-1}$. For all the systems we evaluated we found that is comparable to the height of the disk ($\Delta r_{\rho,\text{eff}} \sim 2 - 5) r_s$. This means that at any point of the disk we can calculate neutrino oscillations in a small regions assuming that both the electron density and neutrino densities are constant.
- We neglect energy and momentum transport between different regions of the disk by neutrinos that are recaptured by the disk due to curvature. This assumption is reasonable except for regions very close to the BH but is consistent with the thin disk model (see, e.g., [211]). We also assume that the neutrino content of neighbouring regions of the disk (different values of r) do not affect each other. As a consequence of the results discussed above, we assume that at any point inside the disk and at any instant of time an observer can describe both the charged leptons and neutrinos as isotropic gases around small enough regions of the disk. This assumption is considerably restrictive but we will generalize it in Sec. 3.5.

The purpose of these approximations is twofold. (1) We can reduce the problem considerably since they allow us to add the neutrino oscillations dynamics of the disk by simply studying the behaviour of neutrinos at each point of the disk using the constant values of density and temperature at that point. As we will see in Sec. 3.5, this corresponds to a transient state of the disk since, very fast, neighbouring regions of the disk start interacting. (2) Also, the approximations allow us to simplify the equations of oscillation considering that all but the first term in Eq. (3.37) vanish, leaving only a time derivative. In addition, both terms of the form $\mathbf{v}_{\mathbf{q},t} \cdot \mathbf{v}_{\mathbf{p},t}$ in Eq. (1.21) average to zero so that $\rho_{\mathbf{p},\mathbf{x},t} = \rho_{p,t}$ and $\bar{\rho}_{\mathbf{p},\mathbf{x},t} = \bar{\rho}_{p,t}$.

We are now in a position to derive the simplified equations of oscillation for this particular model. Let us first present the relevant equations for neutrinos. Due to the similarity between $\mathsf{H}_{p,t}$ and $\bar{\mathsf{H}}_{p,t}$, the corresponding equations for anti-neutrinos can be obtained analogously. For simplicity, we will drop the suffix t since the time dependence is now obvious. In the two-flavour approximation, ρ_p is a 2×2 Hermitian matrix and can be expanded in terms of the Pauli matrices σ_i and a polarization vector $\mathsf{P}_p = (\mathsf{P}^x, \mathsf{P}^y, \mathsf{P}^z)$ in the neutrino flavour space, such that

$$\rho_p = \begin{pmatrix} \rho_{ee} & \rho_{ex} \\ \rho_{xe} & \rho_{xx} \end{pmatrix} = \frac{1}{2} \left(f_p \mathbb{1} + \mathsf{P}_p \cdot \vec{\sigma} \right), \tag{3.38}$$

where $f_p = \mathrm{Tr}[\rho_p] = f_{\nu_e}(p) + f_{\nu_x}(p)$ is the sum of the distribution functions for ν_e and ν_x. Note that the z component of the polarization vector obeys

$$\mathsf{P}^z_p = f_{\nu_e}(p) - f_{\nu_x}(p). \tag{3.39}$$

Hence, this component tracks the fractional flavour composition of the system. Appropriately normalizing ρ_p allows to define a survival and mixing probability

$$P_{p,\nu_e \to \nu_e} = \frac{1}{2} \left(1 + \mathsf{P}^z_p \right), \tag{3.40a}$$

$$P_{p,\nu_e \to \nu_x} = \frac{1}{2} \left(1 - \mathsf{P}^z_p \right). \tag{3.40b}$$

The Hamiltonian can be written as a sum of three interaction terms:

$$\mathsf{H} = \mathsf{H}_{\mathrm{vac}} + \mathsf{H}_{\mathrm{m}} + \mathsf{H}_{\nu\nu}. \tag{3.41}$$

The first term is the Hamiltonian in vacuum [234]:

$$\mathsf{H}_{\mathrm{vac}} = \frac{\omega_p}{2} \begin{pmatrix} -\cos 2\theta & \sin 2\theta \\ \sin 2\theta & \cos 2\theta \end{pmatrix} = \frac{\omega_p}{2} \mathbf{B} \cdot \vec{\sigma}, \tag{3.42}$$

where $\omega_p = \Delta m^2 / 2p$, $\mathbf{B} = (\sin 2\theta, 0, -\cos 2\theta)$ and θ is the smallest neutrino mixing angle in vacuum. The other two terms in Eqs. (1.21) are special since they make the evolution equations non-linear. Since we are considering that the electrons inside the form an isotropic gas, the vector $\mathbf{v}_\mathbf{q}$ in the first integral is distributed uniformly on the unit sphere and the factor $\mathbf{v}_\mathbf{q} \cdot \mathbf{v}_p$ averages to zero. After integrating the matter Hamiltonian is given by

$$\mathsf{H}_{\mathrm{m}} = \frac{\lambda}{2} \begin{pmatrix} 1 & 0 \\ 0 & -1 \end{pmatrix} = \frac{\lambda}{2} \mathbf{L} \cdot \vec{\sigma}, \tag{3.43}$$

where $\lambda = \sqrt{2}G_F\left(n_{e^-} - n_{e^+}\right)$ is the charged current matter potential and $\mathbf{L} = (0, 0, 1)$. Similarly, the same product disappears in the last term and after integrating we get

$$\mathsf{H}_{\nu\nu} = \sqrt{2}G_F\left[\mathsf{P} - \bar{\mathsf{P}}\right] \cdot \vec{\sigma}. \tag{3.44}$$

Clearly, $\mathsf{P} = \int \mathsf{P}_p \, d\mathbf{p}/(2\pi)^3$. Introducing every Hamiltonian term in Eqs. (1.22), and using the commutation relations of the Pauli matrices, we find the equations of oscillation for neutrinos and anti-neutrinos for each momentum mode p

$$\dot{\mathsf{P}}_p = \left[\omega_p\mathbf{B} + \lambda\mathbf{L} + \sqrt{2}G_F\left(\mathsf{P} - \bar{\mathsf{P}}\right)\right] \times \mathsf{P}_p, \tag{3.45a}$$

$$\dot{\bar{\mathsf{P}}}_p = \left[-\omega_p\mathbf{B} + \lambda\mathbf{L} + \sqrt{2}G_F\left(\mathsf{P} - \bar{\mathsf{P}}\right)\right] \times \bar{\mathsf{P}}_p, \tag{3.45b}$$

where we have assumed that the total neutrino distribution remains constant $\dot{f}_p = 0$. In this form, it is clear how the polarization vectors can be normalized. Performing the transformation $\mathsf{P}_p/f_p \mapsto \mathsf{P}_p$ and $\bar{\mathsf{P}}_p/\bar{f}_p \mapsto \bar{\mathsf{P}}_p$ and, multiplying and dividing the last term by the total neutrino density Eqs. (3.45) can be written as

$$\dot{\mathsf{P}}_p = \left[\omega_p\mathbf{B} + \lambda\mathbf{L} + \mu\mathbf{D}\right] \times \mathsf{P}_p, \tag{3.46a}$$

$$\dot{\bar{\mathsf{P}}}_p = \left[-\omega_p\mathbf{B} + \lambda\mathbf{L} + \mu\mathbf{D}\right] \times \bar{\mathsf{P}}_p \tag{3.46b}$$

$$\mathbf{D} = \frac{1}{n_{\nu_e} + n_{\nu_x}} \int \left(f_q\mathsf{P}_q - \bar{f}_q\bar{\mathsf{P}}_q\right) \frac{d\mathbf{q}}{(2\pi)^3}. \tag{3.46c}$$

This is the traditional form of the equations in terms of the vacuum, matter and self-interaction potentials ω_p, λ and μ with

$$\mu = \sqrt{2}G_F \sum_{i\in\{e,x\}} n_{\nu_i}. \tag{3.47}$$

Different normalization schemes are possible (see, e.g., [125, 88, 61, 194]). By assuming that we can solve the equations of oscillation with constant potentials λ and μ simplifies the problem even further. Following [81], with the vector transformation (a rotation around the z axis of flavour space)

$$R_z = \begin{pmatrix} \cos(\lambda t) & \sin(\lambda t) & 0 \\ -\sin(\lambda t) & \cos(\lambda t) & 0 \\ 0 & 0 & 1 \end{pmatrix} \tag{3.48}$$

Eq. (3.46) become

$$\dot{\mathsf{P}}_p = \left[\omega_p\mathbf{B} + \mu\mathbf{D}\right] \times \mathsf{P}_p, \tag{3.49a}$$

$$\dot{\bar{\mathsf{P}}}_p = \left[-\omega_p\mathbf{B} + \mu\mathbf{D}\right] \times \bar{\mathsf{P}}_p, \tag{3.49b}$$

eliminating the λ potential but making $\mathbf{B}$ time dependent. Defining the vector $\mathbf{S}_p = \mathsf{P}_p + \bar{\mathsf{P}}_p$ and, adding and subtracting Eq. (3.49a) and Eq. (3.49b) we get

$$\dot{\mathbf{S}}_p = \omega_p\mathbf{B} \times \mathbf{D}_p + \mu\mathbf{D} \times \mathbf{S}_p \approx \mu\mathbf{D} \times \mathbf{S}_p, \tag{3.50a}$$

$$\dot{\mathbf{D}}_p = \omega_p\mathbf{B} \times \mathbf{S}_p + \mu\mathbf{D} \times \mathbf{D}_p \approx \mu\mathbf{D} \times \mathbf{D}_p \tag{3.50b}$$

The last approximation is true if we assume that the SIP is larger than the vacuum potential $\omega_p/\mu \ll 1$. We will show later that this is the case for thin disks (see Fig. 3.5). The first equation implies that all the vectors $\mathbf{S}_p$ and their integral $\mathbf{S}$ evolve in the same way, suggesting the relation $\mathbf{S}_p = \left(f_p + \bar{f}_p\right)\mathbf{S}$. By replacing in Eq. (3.50b) and integrating

$$\dot{\mathbf{S}} = \mu \mathbf{D} \times \mathbf{S} \tag{3.51a}$$

$$\dot{\mathbf{D}} = \langle\omega\rangle \mathbf{B} \times \mathbf{S}. \tag{3.51b}$$

where $\langle\omega\rangle = \int \omega_p \left(f_p + \bar{f}_p\right) d\mathbf{p}/(2\pi)^3$ is the average vacuum oscillation potential. The fact that in our model the equations of oscillations can be written in this way has an important consequence. Usually, as it is done in supernovae neutrino oscillations, to solve Eq. (3.46) we would need the neutrino distributions throughout the disk. If neutrinos are trapped, their distribution is given by Eq. (3.25). If neutrinos are free, their temperature is not the same as the disk's temperature. Nonetheless, we can approximate the neutrino distribution in this regime by a Fermi-Dirac distribution with the same chemical potential as defined by Eq. (3.26) but with an effective temperature T_ν^{eff}. This temperature can be obtained by solving the equation $\langle E_\nu \rangle = U\left(T_\nu^{\text{eff}}, \eta_\nu\right)/n\left(T_\nu^{\text{eff}}, \eta_\nu\right)$ which gives

$$T^{\text{eff}}_{\nu_x,\bar{\nu}_x} = \langle E_{\nu_x,\bar{\nu}_x} \rangle \frac{180\,\zeta(3)}{7\pi^4} \tag{3.52a}$$

$$T^{\text{eff}}_{\nu_e,\bar{\nu}_e} = \frac{\langle E_{\nu_e,\bar{\nu}_e} \rangle}{3} \frac{\text{Li}_3\left(-\exp\left(\eta_{\nu_e,\bar{\nu}_e}\right)\right)}{\text{Li}_4\left(-\exp\left(\eta_{\nu_e,\bar{\nu}_e}\right)\right)} \tag{3.52b}$$

where $\zeta(3)$ is Apéry's constant (ζ is the Riemann zeta function) and $\text{Li}_s(z)$ is Jonquière's function. For convenience and considering the range of values that the degeneracy parameter reaches (see Sec. 3.6), we approximate the effective temperature of electron neutrinos and anti-neutrinos with the expressions

$$T^{\text{eff}}_{\nu_e} = \frac{\langle E_{\nu_e} \rangle}{3}\left(a\eta^2_{\nu_e} + b\eta_{\nu_e} + c\right) \tag{3.53a}$$

$$T^{\text{eff}}_{\bar{\nu}_e} = \frac{\langle E_{\bar{\nu}_e} \rangle}{3}. \tag{3.53b}$$

with constants $a = 0.0024$, $b = -0.085$, $c = 0.97$. However, Eq. (3.51) allow us to consider just one momentum mode, and the rest of the spectrum behaves in the same way.

3.4 Initial Conditions and Integration

In the absence of oscillations, we can use Eqs. (3.18), (3.16) and (3.36) to solve for the set of functions $\eta_{e^-}(r)$, $\xi(r)$, $Y_e(r)$ using as input parameters the accretion rate $\dot{M}$, the dimensionless spin parameter a, the viscosity parameter α and the BH mass M. From [51, 169] we learn that neutrino dominated disks require accretion between 0.01 $M_\odot$ s^{-1} and 1 $M_\odot$ s^{-1} (this accretion rate range vary depending on the value

of α). For accretion rates smaller than the above lower value the neutrino cooling is not efficient and, for rates larger than the upper value, the neutrinos are trapped within the flow. We also limit ourselves to the above accretion rate range since it is consistent with the one expected to occur in a BdHN (see, e.g., [105, 24, 26]).

We also know that high spin parameter, high accretion rate and low viscosity parameter produces disks with higher density and higher temperature. This can be explained using the fact that several variables of the disk, like pressure, density and height are proportional to a positive power of the quotient $\dot{M}/\alpha$. To avoid this semi-degeneracy in the system, reduce the parameter space and considering that we want to study the dynamics of neutrino oscillations inside the disk, we fix the BH mass at $M = 3M_{\odot}$, the viscosity parameter at $\alpha = 0.01$ and the spin parameter at $a = 0.95$ while changing the accretion rate.

Eqs. (3.18) and (3.36) are first order ordinary differential equations and since we perform the integration from an external (far away) radius $r_{\rm out}$ up to the innermost stable circular orbit $r_{\rm in}$ we must provide two boundary conditions at $r_{\rm out}$. Following the induced gravitational collapse (IGC) paradigm of gamma-ray bursts (GRBs) associated with type Ib/c supernovae we assume that at the external edge of the disk, the infalling matter is composed mainly by the ions present in the material ejected from an explosion of a carbon-oxygen core, that is, mainly oxygen and electrons. This fixes the electron fraction $Y_e\left(r_{\rm out}\right) = 0.5$. The second boundary condition can be obtained by the relation $\left(T\eta + m_B\right)\sqrt{g_{tt}} =$ constant [300, 150, 151], with η the degeneracy parameter of the fluid. If we require the potentials to vanishes at infinity and invoking Euler's theorem we arrive at the relation in the weak field limit

$$\frac{M}{r_{\rm out}} = \left.\frac{\rho + U + P - TS}{\rho}\right|_{r=r_{\rm out}}. \tag{3.54}$$

For a classical gas composed of ions and electrons this relation becomes

$$\frac{M}{r_{\rm out}} \lesssim \left.\frac{U}{\rho}\right|_{r=r_{\rm out}}. \tag{3.55}$$

Eq. (3.55) can be used with Eq. (3.16) and Eq. (3.32) to solve for $\eta_{e^-}(r_{\rm out})$, $\xi\left(r_{\rm out}\right)$. The value of $r_{\rm out}$ is chosen to be at most the circularization radius of the accreting material as described in [25, 24]. We can estimate this radius by solving for r in the expression of the angular momentum per unit mass for a equatorial circular orbits. So using Eq. (3.6) we need to solve

$$u_\phi = M\frac{x^2 - 2x + a^2}{x^{3/2}\sqrt{x^3 - 3x + 2a}} \sim 9 \times 10^{13}\,{\rm cm}^2\,{\rm s}^{-1}, \tag{3.56}$$

where $x = \sqrt{r/M}$ which yields $r_{\rm out} \sim 1800 r_s$. Finally, for the initial conditions to be accepted, they are evaluated by the gravitational instability condition [208]

$$\sqrt{\left.R^{\tilde{\theta}}{}_{\tilde{t}\tilde{\theta}\tilde{t}}\right|_{\theta=\pi/2}}\,\Omega \geq 2\sqrt{3}\pi\rho \tag{3.57}$$

Integration of the equations proceeds as follows, with the initial conditions we solve Eq. (3.36) to obtain the electron fraction in the next integration point. With the new value of the electron fraction we solve the differential-algebraic system of

Eqs. (3.18) and (3.16) at this new point. This process continues until the innermost stable circular orbit $r_{\rm in}$ is reached.

To add the dynamics of neutrino oscillations we proceed same as before but at each point of integration, once the values of Y_e, η and ξ are found, we solve Eq. (3.46) for the average momentum mode to obtain the survival probabilities as a function of time. We then calculate the new neutrino and anti-neutrino distributions with the conservation of total number density and the relations

$$n^{\rm new}_{\nu_e}(t) = P_{\nu_e\to\nu_e}(t)\, n_{\nu_e} + [1 - P_{\nu_e\to\nu_e}(t)]\, n_{\nu_x} \tag{3.58a}$$

$$n^{\rm new}_{\nu_x}(t) = P_{\nu_x\to\nu_x}(t)\, n_{\nu_x} + [1 - P_{\nu_x\to\nu_x}(t)]\, n_{\nu_e}. \tag{3.58b}$$

Since the disk is assumed to be in a steady-state, we then perform a time average of Eq. (3.58) as discussed in Sec. 3.2. With the new distributions, we can calculate the new neutrino and anti-neutrino average energies and use them to re-integrate the disk equations.

Neutrino emission within neutrino-cooled disks is dominated by electron and positron capture which only produces electron (anti)-neutrinos. The second most important process is electron-positron annihilation but it is several orders of magnitude smaller. In Fig. 3.2 we show the total number emissivity for these two processes for an accretion rate of $\dot{M} = 0.1 M_\odot$ s $^{-1}$. Other cases behave similarly. Moreover, although the degeneracy parameter suppresses the positron density, a high degeneracy limit does not occur in the disk and the degeneracy is kept low at values between $\sim$ (0.2–3), as shown in Fig. 3.3. The reason for this is the effect of high degeneracy on neutrino cooling. Higher degeneracy leads to a lower density of positrons which suppresses the neutrino production and emission, which in turn leads to a lower cooling rate, higher temperature, lower degeneracy and higher positron density. This equilibrium leads, via the lepton number conservation Eq. (3.36), to a balance between electronic and non-electronic neutrino densities within the inner regions of the disk. Given this fact, to solve the equations of oscillations, we can approximate the initial conditions of the polarization vectors with

$$\mathsf{P} = \bar{\mathsf{P}} \approx (0, 0, 1). \tag{3.59}$$

3.5 Results and Analysis

In Fig. 3.3 and Fig. 3.4 we present the main features of accretion disks for the parameters $M = 3M_\odot$, $\alpha = 0.01$, $a = 0.95$, and three different accretion rates $\dot{M} = 1 M_\odot$ s^{-1}, $\dot{M} = 0.1 M_\odot$ s^{-1} and $\dot{M} = 0.01 M_\odot$ s^{-1}. It exhibits the usual characteristics of thin accretions disks. High accretion rate disks have higher density, temperature and electron degeneracy. Also, for high accretion rates, the cooling due to photodisintegration and neutrino emission kicks in at larger radii. For all cases, as the disk heats up, the number of free nucleons starts to increase enabling the photodisintegration cooling at $r \sim$ (100–300)r_s. Only the disintegration of alpha particles is important and the nucleon content of the infalling matter is of little

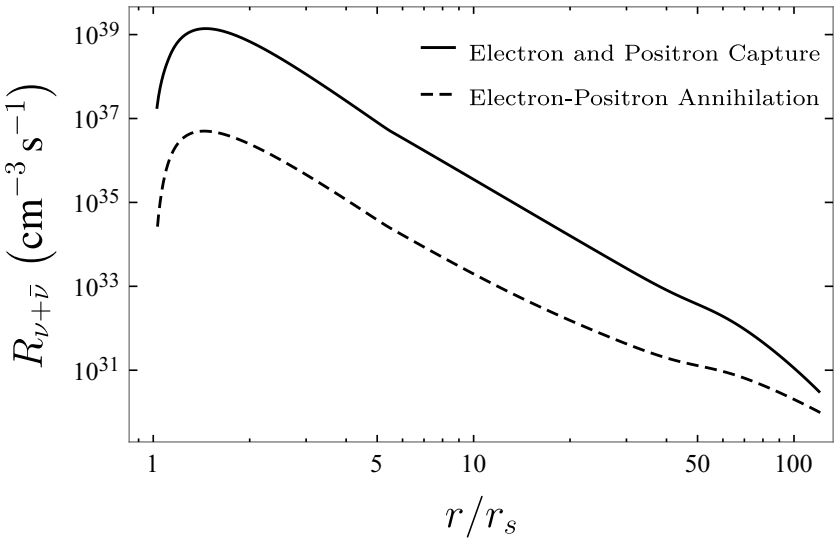

Figure 3.2. Total number emissivity for electron and positron capture ($p + e^- \to n + \nu_e$, $n + e^+ \to p + \bar{\nu}_e$) and electron-positron annihilation ($e^- + e^+ \to \nu + \bar{\nu}$) for accretion disks with $\dot{M} = 0.1 M_\odot$ s^{-1} between the inner radius and the ignition radius.

consequence for the dynamics of the disk. When the disk reaches temperatures ~ 1.3 MeV, the electron capture switches on, the neutrino emission becomes significant and the physics of the disk is dictated by the energy equilibrium between F_{heat} and F_ν. The radius at which neutrino cooling becomes significant (called ignition radius r_{ing}) is defined by the condition $F_\nu \sim F_{\text{heat}}/2$. For the low accretion rate $\dot{M} = 0.01 M_\odot$ s^{-1}, the photodisintegration cooling finishes before the neutrino cooling becomes significant, this leads to fast heating of the disk. Then the increase in temperature triggers a strong neutrino emission that carries away the excess heat generating a sharp spike in F_ν surpassing F_{heat} by a factor of ~ 3.5. This behaviour is also present in the systems studied in [51], but there it appears for fixed accretion rates and high viscosity ($\alpha = 0.1$). This demonstrates the semi-degeneracy mentioned in Sec. 3.5. The evolution of the fluid can be tracked accurately through the degeneracy parameter. At the outer radius, η_{e^-} starts to decrease as the temperature of the fluid rises. Once neutrino cooling becomes significant, it starts to increase until the disk reaches the local balance between heating and cooling. At this point, η_{e^-} stops rising and is maintained (approximately) at a constant value. Very close to r_{in}, the zero torque condition of the disk becomes important and the viscous heating is reduced drastically. This is reflected in a sharp decrease in the fluid's temperature and increase in the degeneracy parameter. For the high accretion rate and additional effect has to be taken into account. Due to high ν_e optical depth, neutrino cooling is less efficient, leading to an increase in temperature and a second dip in the degeneracy parameter. This dip is not observed in low accretion rates because τ_{ν_e} does not reach significant values.

With the information in Fig. 3.3 we can obtain the oscillation potentials which we plot in Fig. 3.5. Since the physics of the disk for $r < r_{\text{ign}}$ is independent of the initial conditions at the external radius and for $r > r_{\text{ign}}$ the neutrino emission is negligible, the impact of neutrino oscillations is important only inside r_{ign}. We can

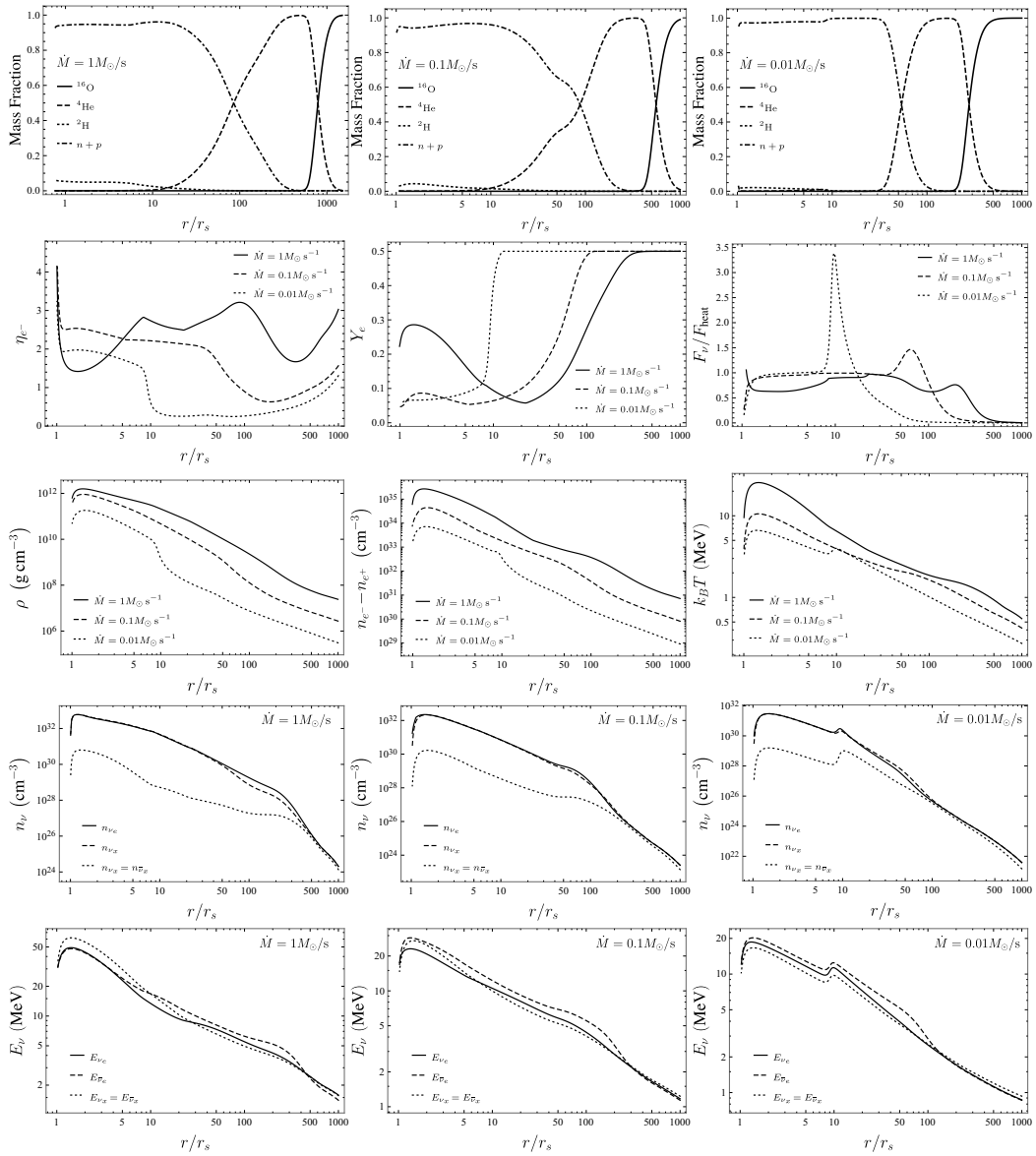

Figure 3.3. Properties of accretion disks in the absence of oscillations with $M = 3M_\odot$, $\alpha = 0.01$, $a = 0.95$ for accretion rates $\dot{M} = 1M_\odot$ s^{-1}, $\dot{M} = 0.1M_\odot$ s^{-1} and $\dot{M} = 0.01M_\odot$ s^{-1}, respectively.

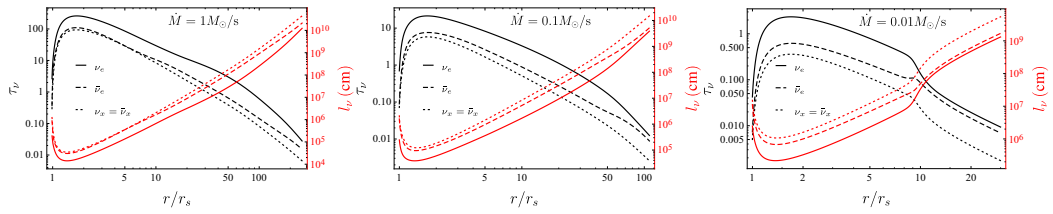

Figure 3.4. Total optical depth (*left scale*) and mean free path (*right scale*) for neutrinos and anti-neutrinos of both flavours for accretion disks with $\dot{M} = 1M_\odot$ s^{-1}, $0.1M_\odot$ s^{-1}, $0.01M_\odot$ s^{-1} between the inner radius and the ignition radius.

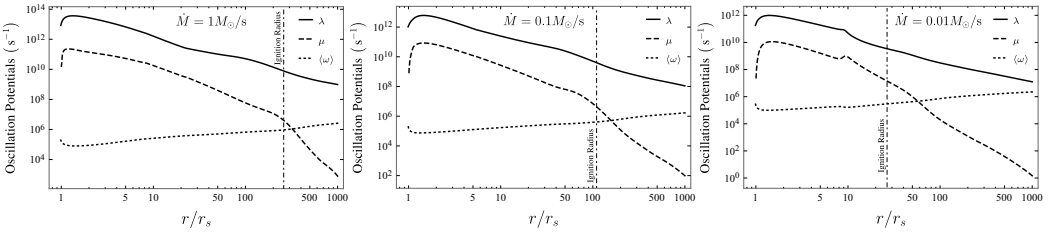

Figure 3.5. Oscillation potentials as functions of r with $M = 3M_\odot$, $\alpha = 0.01$, $a = 0.95$ for accretion rates $\dot{M} = 1M_\odot$ s^{-1}, $\dot{M} = 0.1M_\odot$ s^{-1} and $\dot{M} = 0.01M_\odot$ s^{-1}, respectively. The vertical line represents the position of the ignition radius.

see that the discussion at the end of Sec. 3.3.1 is justified since for $r_{\rm in} < r < r_{\rm ign}$ the potentials obey the relation

$$\langle\omega\rangle \ll \mu \ll \lambda. \tag{3.60}$$

Generally, the full dynamics of neutrino oscillations is a rather complex interplay between the three potentials, yet it is possible to understand the neutrino response in the disk using some numerical and algebraic results obtained in [125, 90, 88] and references therein. Specifically, we know that if $\mu \gg \langle\omega\rangle$, as long as the MSW condition $\lambda \simeq \langle\omega\rangle$ is not met (precisely our case), collective effects should dominate the neutrino evolution even if $\lambda \gg \mu$. On the other hand, if $\mu \lesssim \langle\omega\rangle$, the neutrino evolution is driven by the relative values between the matter and vacuum potentials (not our case). With Eq. (3.51) we can build a very useful analogy. These equations are analogous to the equations of motion of a simple mechanical pendulum with a vector position given by $\mathbf{S}$, precessing around with angular momentum $\mathbf{D}$, subjected to a gravitational force $\langle\omega\rangle\mu\mathbf{B}$ with mass μ^{-1}. Using Eq. (3.59) obtains the expression $|\mathbf{S}| = S \approx 2 + O(\langle\omega\rangle/\mu)$. Calculating $\partial_t(\mathbf{S}\cdot\mathbf{S})$ it can be checked that this value is conserved up to fluctuations of order $\langle\omega\rangle/\mu$. The analogous angular momentum is $\mathbf{D} = \mathsf{P} - \bar{\mathsf{P}} = 0$. Thus, the pendulum moves initially in a plane defined by $\mathbf{B}$ and the z-axis, i.e., the plane xz. Then, it is possible to define an angle φ between $\mathbf{S}$ and the z-axis such that

$$\mathbf{S} = S\left(\sin\varphi, 0, \cos\varphi\right). \tag{3.61}$$

Note that the only non-zero component of $\mathbf{D}$ is y-component. From Eq. (3.51) we find

$$\dot{\varphi} = \mu D \tag{3.62a}$$

$$\dot{D} = -\langle\omega\rangle S\cos(\varphi + 2\theta). \tag{3.62b}$$

The above equations can be equivalently written as

$$\ddot{\varphi} = -k^2\sin(2\theta + \varphi), \tag{3.63}$$

where we have introduced the inverse characteristic time k by

$$k^2 = \langle\omega\rangle\mu S, \tag{3.64}$$

which is related to the anharmonic oscillations of the pendulum. The role of the matter potential λ is to logarithmically extend the oscillation length by the relation [125]

$$\tau = -k^{-1} \ln \left[\frac{k}{\theta \left(k^2 + \lambda^2\right)^{1/2}} \left(1 + \frac{\langle \omega \rangle}{S\mu}\right) \right]. \tag{3.65}$$

The total oscillation time can then be approximated by the period of an harmonic pendulum plus the logarithmic extension

$$t_{\rm osc} = \frac{2\pi}{k} + \tau. \tag{3.66}$$

The initial conditions of Eq. (3.59) imply

$$\varphi\left(t = 0\right) = \arcsin\left(\frac{\langle \omega \rangle}{S\mu} \sin 2\theta\right). \tag{3.67}$$

so that φ is a small angle. The potential energy for a simple pendulum is

$$V\left(\varphi\right) = k^2 \left[1 - \cos\left(\varphi + 2\theta\right)\right] \approx k^2 \left(\varphi + 2\theta\right)^2. \tag{3.68}$$

If $k^2 > 0$, which is true for the normal hierarchy $\Delta m^2 > 0$, we expect small oscillations around the initial position since the system begins in a stable position of the potential. The magnitude of flavour conversions is of the order $\sim \langle \omega \rangle / S\mu \ll 1$. We stress that normal hierarchy does not mean an absence of oscillations but rather *imperceptible* oscillations in P_z. No strong flavour oscillations are expected. On the contrary, for the inverted hierarchy $\Delta m^2 < 0$, $k^2 < 0$ and the initial φ indicates that the system begins in an unstable position and we expect very large anharmonic oscillations. P^z (as well as $\bar{\mathsf{P}}^z$) oscillates between two different maxima passing through a minimum $-\mathsf{P}^z$ ($-\bar{\mathsf{P}}^z$) several times. This implies total flavour conversion: all electronic neutrinos (anti-neutrinos) are converted into non-electronic neutrinos (anti-neutrinos) and vice-versa. This has been called bipolar oscillations in the literature [83]. If the initial condition are not symmetric as in Eq. (3.59), the asymmetry is measured by a constant $\varsigma = \bar{\mathsf{P}}^z / \mathsf{P}^z$ if $\bar{\mathsf{P}}^z < \mathsf{P}^z$ or $\varsigma = \mathsf{P}^z / \bar{\mathsf{P}}^z$ if $\bar{\mathsf{P}}^z > \mathsf{P}^z$ so that $0 < \varsigma < 1$. Bipolar oscillations are present in an asymmetric system as long as the relation

$$\frac{\mu}{|\langle \omega \rangle|} < 4 \frac{1 + \varsigma}{\left(1 - \varsigma\right)^2}. \tag{3.69}$$

is obeyed [125]. If this condition is not met, instead of bipolar oscillation we get synchronised oscillations. Since we are considering constant potentials, synchronised oscillations is equivalent to the normal hierarchy case. From Fig. 3.5 we can conclude that in the normal hierarchy case, neutrino oscillations have no effects on neutrino-cooled disks under the assumptions we have made. On the other hand, in the inverted hierarchy case, we expect extremely fast flavour conversions with periods of order $t_{\rm osc} \sim (10^{-9} - 10^{-5})$ s for high accretion rates and $t_{\rm osc} \sim (10^{-8} - 10^{-5})$ s for low accretion rates, between the respective $r_{\rm in}$ and $r_{\rm ign}$.

For the purpose of illustration we solve the equations of oscillations for the $\dot{M} = 0.1 M_\odot$ s^{-1} case at $r = 10 r_s$. The electronic (anti)-neutrino survival probability at this point is shown in Fig. 3.6 for inverted hierarchy and normal hierarchy,

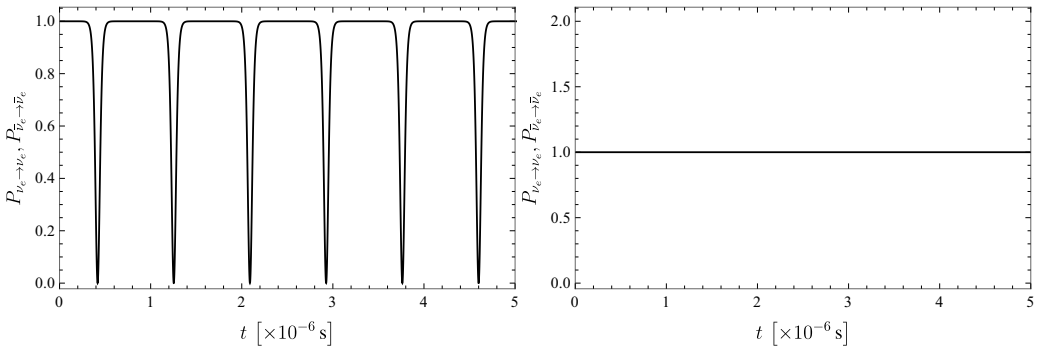

Figure 3.6. Survival provability for electron neutrinos and anti-neutrinos for the accretion disk with $\dot{M} = 0.1 M_\odot\ \mathrm{s}^{-1}$ at $r = 10 r_s$. The left plot corresponds to inverted hierarchy and the right plot corresponds to normal hierarchy.

respectively. On both plots, there is no difference between the neutrino and anti-neutrino survival probabilities. This should be expected since for this values of r the matter and self-interaction potentials are much larger than the vacuum potential, and there is virtually no difference between Eq. (3.46a) and Eq. (3.46b). Also, as mentioned before, note that the (anti)-neutrino flavour proportions remain virtually unchanged for normal hierarchy while the neutrino flavour proportions change drastically. The characteristic oscillation time of the survival probability in inverted hierarchy found on the plot is

$$t_{\mathrm{osc}} \approx 8.4 \times 10^{-7}\,\mathrm{s}, \tag{3.70}$$

which agree with the ones given by Eq. (3.66) up to a factor of order one. Such a small value suggests extremely quick $\nu_e\bar{\nu}_e \to \nu_x\bar{\nu}_x$ oscillations. A similar effect occurs for regions of the disk inside the ignition radius for all three accretion rates. In this example, the time average of the survival probabilities yield the values $\langle P_{\nu_e\to\nu_e}\rangle = \langle P_{\bar{\nu}_e\to\bar{\nu}_e}\rangle = 0.92$. With this number, Eq. (3.58), and Eq. (3.53), the (anti)-neutrino spectrum for both flavours can be constructed. But, more importantly, this means that the local observer at that point in the disk measures, on average, an electron (anti)-neutrino loss of around 8% which is represented by an excess of non-electronic (anti)-neutrinos.

In Sec. 3.3.1 we proposed to calculate neutrino oscillations assuming that small neighbouring regions of the disk are independent and that neutrinos can be viewed as isotropic gases in those regions. However, this cannot be considered a steady-state of the disk. To see this consider Fig. 3.4. The maximum value of the neutrino optical depth is of the order of 10^3 for the highest accretion rate, meaning that the time that takes neutrinos to travel a distance of one Schwarzschild inside the disk radius obeys

$$t_{r_s} \ll \mathrm{Max}\,(\tau_\nu)\, r_s \approx 10^{-2}\,\mathrm{s}. \tag{3.71}$$

which is lower than the accretion time of the disk as discussed in Sec. 3.2 but higher than the oscillation time. Different sections of the disk are not independent since they, very quickly, share (anti)-neutrinos created with a non-vanishing momentum along the radial direction. Furthermore, the oscillation pattern between neighbouring regions of the disk is not identical. In Fig. 3.7 we show the survival probability

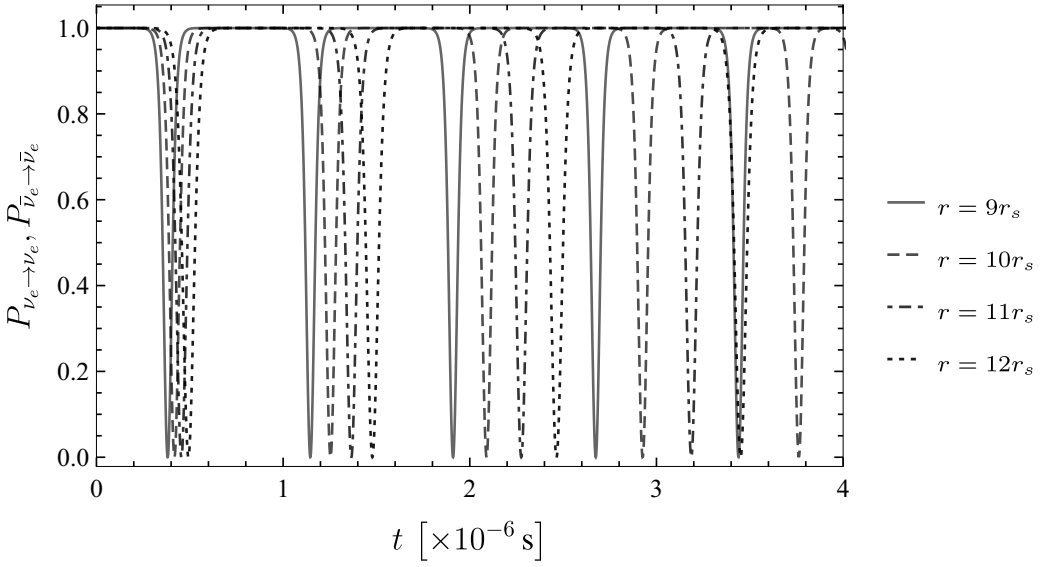

Figure 3.7. Survival provability for electron neutrinos and anti-neutrinos for the accretion disk with $\dot{M} = 0.1M_\odot\ \mathrm{s}^{-1}$ at $r = 9r_s, 10r_s, 11r_s, 12r_s$.

as a function of time for different (but close) values of r for $\dot{M} = 0.1M_\odot\ \mathrm{s}^{-1}$. The superposition between neutrinos with different oscillation histories has several consequences: (1) It breaks the isotropy of the gas because close to the BH, neutrinos are more energetic and their density is higher producing a radially directed net flux, meaning that the factor $\mathbf{v}_{\mathbf{q},t} \cdot \mathbf{v}_{\mathbf{p},t}$ does not average to zero. This implies that realistic equations of oscillations include a multi-angle term and a radially decaying neutrino flux similar to the situation in SN neutrinos. (2) It constantly changes the neutrino content ant any value of r independently of the neutrino collective evolution given by the values of the oscillation potentials at that point. This picture plus the asymmetry that electron and non-electron neutrinos experience through the matter environment (electron (anti)-neutrinos can interact through $n + \nu_e \to p + e^-$ and $p + \bar{\nu}_e \to n + e^+$), suggests that the disk achieves complete flavour equipartition (decoherence). We can identify two competing causes, namely, quantum decoherence and kinematic decoherence.

Quantum decoherence is the product of collisions among the neutrinos or with a thermal background medium can be understood as follows [236]. From Appx. D.2 we know that different (anti)-neutrino flavours posses different cross-sections and scattering rates $\Gamma_{\nu_i,\bar{\nu}_i}$. In particular, we have $\Gamma_{\nu_x} \approx \Gamma_{\bar{\nu}_x} < \Gamma_{\bar{\nu}_e} < \Gamma_{\nu_e}$. An initial electron (anti)-neutrino created at a point r will begin to oscillate into $\nu_x(\bar{\nu}_x)$. The probability of finding it in one of the two flavours evolves as previously discussed. However, in each interaction $n + \nu_e \to p + e^-$, the electron neutrino component of the superposition is absorbed, while the ν_x component remains unaffected. Thus, after the interaction the two flavours can no longer interfere. This allows the remaining ν_x oscillate and develop a new coherent ν_e component which is made incoherent in the next interaction. The process will come into equilibrium only when there are equal numbers of electronic and non-electronic neutrinos. That is, the continuous emission and absorption of electronic (anti)-neutrinos generates a non-electronic

(anti)-neutrinos with an average probability of $\langle P_{\nu_e \to \nu_e} \rangle$ in each interaction and once the densities of flavours are equal, the oscillation dynamic stops. An initial system composed of $\nu_e, \bar{\nu}_e$ turns into an equal mixture of $\nu_e, \bar{\nu}_e$ and $\nu_x, \bar{\nu}_x$, reflected as an exponential damping of oscillations. For the particular case in which non-electronic neutrinos can be considered as sterile (do not interact with the medium), the relaxation time of this process can be approximated as [126, 289]

$$t_Q = \frac{1}{2 l_{\nu\bar{\nu}} \langle \omega \rangle^2 \sin^2 2\theta} + \frac{2 l_{\nu\bar{\nu}} \lambda^2}{\langle \omega \rangle^2 \sin^2 2\theta} \tag{3.72}$$

where $l_{\nu\bar{\nu}}$ represents the (anti)-neutrino mean free path.

Kinematic decoherence is the result of a non-vanishing flux term such that at any point, (anti)-neutrinos travelling in different directions, do not experience the same SIP due to the multi-angle term in the integral of Eq. (1.21). Different trajectories do not oscillate in the same way, leading to a de-phasing and a decay of the average $\langle P_{\nu \to \nu} \rangle$ and thus to the equipartition of the overall flavour content. The phenomenon is similar to an ensemble of spins in an inhomogeneous magnetic field. In [237] it is shown that for asymmetric $\nu\bar{\nu}$ gas, even an infinitesimal anisotropy triggers an exponential evolution towards equipartition, and in [88] it was shown that if the symmetry between neutrinos and anti-neutrinos is not broken beyond the limit of 25%, kinematic decoherence is still the main effect of neutrino oscillations. As a direct consequence of the $\nu\bar{\nu}$ symmetry present within the ignition radius of accretion disks (see Fig. 3.3), equipartition among different neutrino flavours is expected. This multi-angle term keeps the order of the characteristic time $t_{\rm osc}$ of Eq. (3.66), unchanged and kinematic decoherence happens within a few oscillation cycles. The oscillation time gets smaller closer to the BH due to the $1/\mu^{1/2}$ dependence. Therefore, we expect that neutrinos emitted within the ignition radius will be equally distributed among both flavours in about few microseconds. Once the neutrinos reach this maximally mixed state, no further changes are expected. We emphasize that kinematic decoherence does not mean quantum decoherence. Figs. 3.6 and Fig. 3.7 clearly show the typical oscillation pattern which happens only if quantum coherence is still acting on the neutrino system. Kinematics decoherence, differently to quantum decoherence, is just the result of averaging over the neutrino intensities resulting from quick flavour conversion. Therefore, neutrinos are yet able to quantum oscillate if appropriate conditions are satisfied.

Simple inspection of Eq. (3.66) and Eq. (3.72) with Fig. 3.4 yields $t_{\rm osc} \ll t_Q$. Clearly the equipartition time is dominated by kinematic decoherence. These two effects are independent of the neutrino mass hierarchy and neutrino flavour equipartition is achieved for both hierarchies. Within the disk dynamic, this is equivalent to imposing the condition $\langle P_{\nu_e \to \nu_e} \rangle = \langle P_{\bar{\nu}_e \to \bar{\nu}_e} \rangle = 0.5$.

Fig. 3.8 shows a comparison between disks with and without neutrino flavour equipartition for the three accretion rates considered. The role of equipartition is to increase the disk's density, reduce the temperature and electron fraction, and further stabilize the electron degeneracy for regions inside the ignition radius. The effect is mild for low accretion rates and very pronounced for high accretion rates. This result is in agreement with our understanding of the dynamics of the disk and can be explained in the following way. In low accretion systems the neutrino optical depth for all flavours is $\tau_{\nu\bar{\nu}} \lesssim 1$ and the differences between the cooling fluxes, as

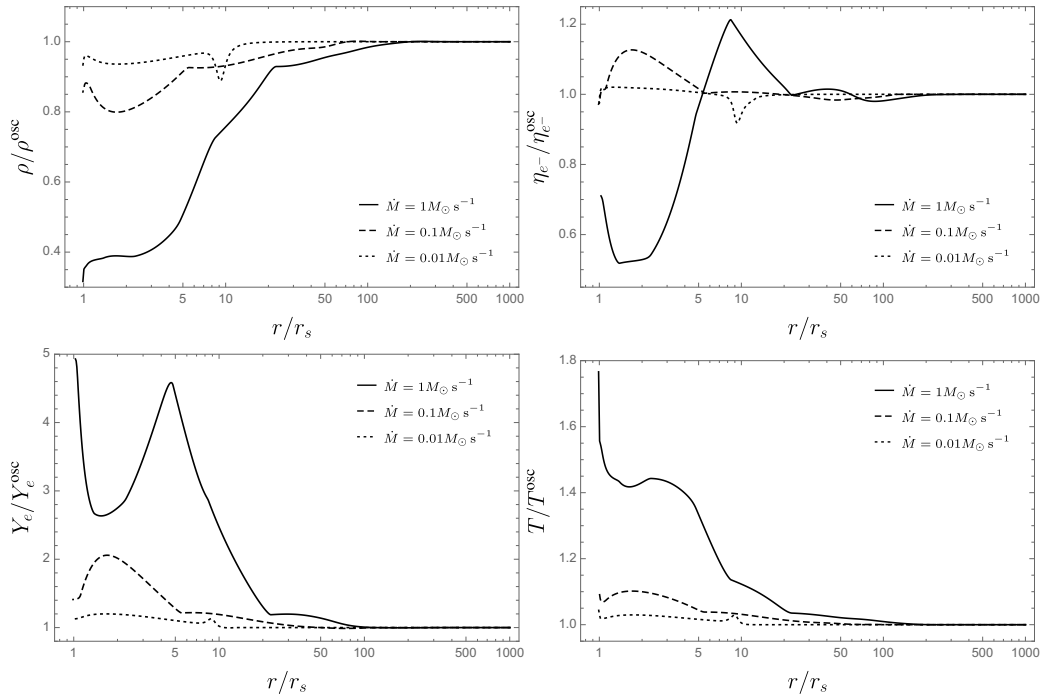

Figure 3.8. Comparison between the main variables describing thin disks with and without neutrino flavour equipartition for each accretion rate considered. Together with Fig. 3.3, these plots completely describe the profile of a disk under flavour equipartition.

given by Eq. (3.31) are small. Hence, when the initial (mainly electron flavour) is redistributed among both flavours, the total neutrino cooling remains virtually unchanged and the disk evolves as if equipartition had never occurred save the new emission flavour content. On the other hand, when accretion rates are high, the optical depth obeys $\tau_{\nu_x} \approx \tau_{\bar{\nu}_x} \lesssim \tau_{\bar{\nu}_e} < \tau_\nu \sim 10^3$. The ν_e cooling is heavily suppressed while the others are less so. When flavours are redistributed, the *new* ν_x particles a free to escape, enhancing the total cooling and reducing the temperature. As the temperature decreases, so do the electron and positron densities leading to a lower electron fraction. The net impact of flavour equipartition is to make the disk evolution less sensitive to ν_e opacity and, thus, increase the total cooling efficiency. As a consequence, once the fluid reaches a balance between F^+ and F_ν, this state is kept without being affected by high optical depths and η_{e^-} stays at a constant value until the fluid reaches the zero torque condition close to $r_{\rm in}$. Note that for every case, inside the ignition radius, we have $\tau_{\bar{\nu}_e} \approx \tau_{\nu_x} = \tau_{\bar{\nu}_x}$ so that equipartition enhances, mainly, neutrino cooling F_ν (and not anti-neutrino cooling $F_{\bar{\nu}}$). The quotient between neutrino cooling with and without equipartition can be estimated with

$$\frac{F_\nu^{\rm eq}}{F_\nu} \approx \frac{1}{2}\left(1 + \frac{\langle E_{\nu_x}\rangle}{\langle E_{\nu_e}\rangle}\frac{1+\tau_{\nu_e}}{1+\tau_{\nu_x}}\right). \tag{3.73}$$

This relation exhibits the right limits. From Fig. 3.3 we see that $\langle E_{\nu_e}\rangle \approx \langle E_{\nu_x}\rangle$. Hence, If $1 \gg \tau_{\nu_e} > \tau_{\nu_x}$, then $F_\nu^{\rm eq} = F_\nu$ and the equipartition is unnoticeable. But if $1 < \tau_{\nu_x} < \tau_{\nu_e}$ then $F_\nu^{\rm eq}/F_\nu > 1$. In our simulations, this fraction reaches values of 1.9 for $\dot{M} = 1M_\odot\ {\rm s}^{-1}$ to 2.5 for $\dot{M} = 0.01M_\odot\ {\rm s}^{-1}$.

The disk variables at each point do not change beyond a factor of order 5 in the most obvious case. However, these changes can be important for cumulative quantities, e.g. the total neutrino luminosity and the total energy deposition rate into electron-positron pairs due to neutrino anti-neutrino annihilation. To see this we perform a Newtonian calculation of these luminosities following [136, 253, 228, 244, 141, 316, 169], and references therein. The neutrino luminosity is calculated by integrating the neutrino cooling flux throughout both faces of the disk

$$L_{\nu_i} = 4\pi \int_{r_{\rm in}}^{r_{\rm out}} C_{\rm cap} F_{\nu_i} r dr. \tag{3.74}$$

Table 3.1. Comparison of total neutrino luminosities L_ν and annihilation luminosities $L_{\nu\bar{\nu}}$ between disk with and without flavour equipartition.

	Without oscillations						With oscillations (flavour equipartition)					
$\left[\frac{\text{MeV}}{M_\odot\ \text{s}^{-1}}\right]$ \ $\left[\text{MeV}\ \text{s}^{-1}\right]$	L_{ν_e}	$L_{\bar{\nu}_e}$	L_{ν_x}	$L_{\bar{\nu}_x}$	$L_{\nu_e\bar{\nu}_e}$	$L_{\nu_x\bar{\nu}_x}$	L_{ν_e}	$L_{\bar{\nu}_e}$	L_{ν_x}	$L_{\bar{\nu}_x}$	$L_{\nu_e\bar{\nu}_e}$	$L_{\nu_x\bar{\nu}_x}$
1	6.46×10^{58}	7.33×10^{58}	1.17×10^{58}	1.17×10^{58}	1.25×10^{57}	1.05×10^{55}	1.87×10^{58}	4.37×10^{58}	7.55×10^{58}	5.44×10^{58}	1.85×10^{56}	2.31×10^{56}
0.1	9.19×10^{57}	1.08×10^{58}	8.06×10^{55}	8.06×10^{55}	1.62×10^{55}	1.27×10^{50}	2.47×10^{57}	4.89×10^{57}	7.75×10^{57}	5.27×10^{57}	1.78×10^{54}	1.64×10^{54}
0.01	1.05×10^{57}	1.12×10^{57}	2.43×10^{55}	2.43×10^{55}	1.78×10^{53}	8.68×10^{48}	4.29×10^{56}	5.48×10^{56}	6.71×10^{56}	5.70×10^{56}	3.53×10^{52}	1.23×10^{52}

The factor $0 < C_{\rm cap} < 1$ is a function of the radius (called *capture function* in [298]) that accounts for the proportion of neutrinos that are re-captured by the BH and, thus, do not contribute to the total luminosity. For a BH with $M = 3M_\odot$ and $a = 0.95$, the numerical value of the capture function as a function of the dimensionless distance $x = r/r_s$ is well fitted by

$$C_{\rm cap}\,(x) = \left(1 + \frac{0.3348}{x^{3/2}}\right)^{-1}, \tag{3.75}$$

with a relative error smaller than 0.02%. To calculate the energy deposition rate, the disk is modeled as a grid of cells in the equatorial plane. Each cell k has a specific value of differential neutrino luminosity $\Delta\ell^k_{\nu_i} = F^k_{\nu_i} r_k \Delta r_k \Delta\phi_k$ and average neutrino energy $\langle E_{\nu_i}\rangle^k$. If a neutrino of flavour i is emitted from the cell k and an anti-neutrino is emitted from the cell k', and, before interacting at a point $\mathbf{r}$ above the disk, each travels a distance r_k and $r_{k'}$, then, their contribution to the energy deposition rate at $\mathbf{r}$ is (see Appx. D.3 for details)

$$\begin{aligned}\Delta Q_{\nu_i\bar\nu_i kk'} = {} & A_{1,i}\frac{\Delta\ell^k_{\nu_i}}{r_k^2}\frac{\Delta\ell^{k'}_{\bar\nu_i}}{r_{k'}^2}\left(\langle E_{\nu_i}\rangle^k + \langle E_{\bar\nu_i}\rangle^{k'}\right)\left(1 - \frac{\mathbf{r}_k\cdot\mathbf{r}_{k'}}{r_k r_{k'}}\right)^2 \\ & + A_{2,i}\frac{\Delta\ell^k_{\nu_i}}{r_k^2}\frac{\Delta\ell^{k'}_{\bar\nu_i}}{r_{k'}^2}\left(\frac{\langle E_{\nu_i}\rangle^k + \langle E_{\bar\nu_i}\rangle^{k'}}{\langle E_{\nu_i}\rangle^k\langle E_{\bar\nu_i}\rangle^{k'}}\right)\left(1 - \frac{\mathbf{r}_k\cdot\mathbf{r}_{k'}}{r_k r_{k'}}\right).\end{aligned} \tag{3.76}$$

The total neutrino annihilation luminosity is simply the sum over all pairs of cells integrated in space

$$L_{\nu_i\bar\nu_i} = 4\pi\int_{\mathcal{A}}\sum_{k,k'}\Delta Q_{\nu_i\bar\nu_i kk'}\,d^3\mathbf{r}, \tag{3.77}$$

where $\mathcal{A}$ is the entire space above (or below) the disk.

In Table 3.1 we show the neutrino luminosities and the neutrino annihilation luminosities for disks with and without neutrino collective effects. In each case, flavour equipartition induces a loss in L_{ν_e} by a factor of $\sim$3, and a loss in $L_{\bar\nu_e}$ luminosity by a factor of $\sim$2. At the same time, L_{ν_x} and $L_{\bar\nu_e}$ are increased by a factor $\sim$10. This translates into a reduction of the energy deposition rate due to electron neutrino annihilation by a factor of $\sim$7 while the energy deposition rate due to non-electronic neutrinos goes from being negligible to be of the same order of the electronic energy deposition rate. The net effect is to reduce the total energy deposition rate of neutrino annihilation by a factor of $\sim (3-5)$ for the accretion rates considered. In particular we obtain a for a factor 3.03 and 3.66 for $\dot M = 1\ M_\odot\ {\rm s}^{-1}$ and $\dot M = 0.01\ M_\odot\ {\rm s}^{-1}$, respectively and a factor 4.73 for $\dot M = 0.1\ M_\odot\ {\rm s}^{-1}$. The highest value correspond to and intermediate value of the accretion rate because, for this case, there is a ν_e cooling suppression ($\tau_{\nu_e} > 1$) and the quotient $\tau_{\nu_e}/\tau_{\nu_x}$ is maximal. By Eq. (3.73), the difference between the respective cooling terms is also maximal. In Fig. 3.9 we show the energy deposition rate per unit volume around the BH for each flavour with accretion rates $\dot M = 1\ M_\odot\ {\rm s}^{-1}$ and $\dot M = 0.1\ M_\odot\ {\rm s}^{-1}$. There we can see the drastic enhancement of the non-electronic neutrino energy deposition rate and the reduction of the electronic deposition rate. Due to the double

peak in the neutrino density for $\dot{M} = 0.01\ M_\odot\ \mathrm{s}^{-1}$ case (see Fig. 3.3), the deposition rate per unit volume also shows two peaks. One at $r_s < r < 2r_s$ and the other at $10\,r_s < r < 11\,r_s$. Even so, the behaviour is similar to the other cases.

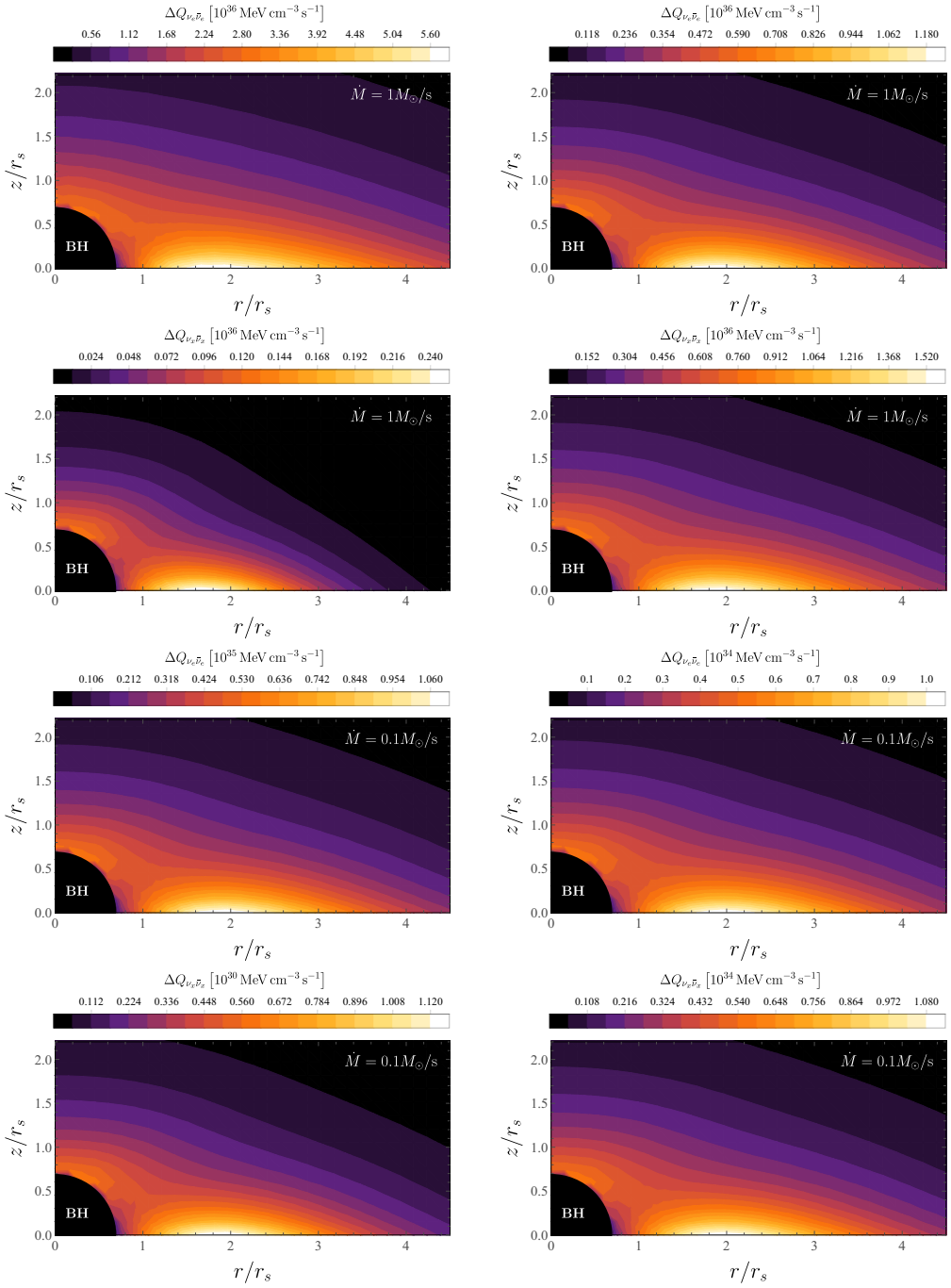

Figure 3.9. Comparison of the neutrino annihilation luminosity per unit volume $\Delta Q_{\nu_i\bar{\nu}_i} = \sum_{k,k'} \Delta Q_{\nu_i\bar{\nu}_i kk'}$ between disk without (*left column*) and with (*right column*) flavour equipartition.

3.6 Concluding Remarks and Perspectives

The generation of a seed, energetic e^-e^+ plasma seems to be a general prerequisite of GRB theoretical models for the explanation of the prompt gamma-ray emission. The e^-e^+ pair annihilation produce photons leading to an opaque pair-photon plasma that self-accelerates, expanding to ultra-relativistic Lorentz factors of the order of 10^2–10^3 (see, e.g., [231, 259, 260]). The reaching of transparency of MeV-photons at large Lorentz factor and corresponding large radii is requested to solve the so-called *compactness problem* posed by the observed non-thermal spectrum in the prompt emission [283, 223, 188]. There is a vast literature on this subject and we refer the reader to [221, 222, 186, 187, 29, 162], and references therein, for further details.

Neutrino-cooled accretion disks onto rotating BHs have been proposed as a possible way of producing the above-mentioned e^-e^+ plasma. The reason is that such disks emit a large amount of neutrino and antineutrinos that can undergo pair annihilation near the BH [228, 203, 154, 70, 155, 167, 123, 51, 142, 135, 143, 172, 316]. The viability of this scenario clearly depends on the energy deposition rate of neutrino-antineutrinos into e^-e^+ and so on the local (anti)-neutrino density and energy.

We have here shown that, inside these hyperaccreting disks, a rich neutrino oscillations phenomenology is present due to the high neutrino density. Consequently, the neutrino/antineutrino emission and the corresponding pair annihilation process around the BH leading to electron-positron pairs, are affected by neutrino flavour conversion. Using the thin disk and α-viscosity approximations, we have built a simple stationary model of general relativistic neutrino-cooled accretion disks around a Kerr BH, that takes into account not only a wide range of neutrino emission processes and nucleosynthesis but also the dynamics of flavour oscillations. The main assumption relies on considering the neutrino oscillation behaviour within small neighbouring regions of the disk as independent from each other. This, albeit being a first approximation to a more detailed picture, has allowed us to set the main framework to analyse the neutrino oscillations phenomenology in inside neutrino-cooled disks.

In the absence of oscillations, a variety of neutrino-cooled accretion disks onto Kerr BHs, without neutrino flavour oscillations, have been modelled in the literature (see, e.g., [114, 228, 51, 316] and [169] for a recent review). The physical setting of our disk model follows closely the ones considered in [51], but with some extensions and differences in some aspects:

(i) The equation of vertical hydrostatic equilibrium, Eq. (3.16), can be derived in several ways [207, 114, 7]. We followed a particular approach consistent with the assumptions in [207], in which we took the vertical average of a hydrostatic Euler equation in polar coordinates. The result is a an equation that leads to smaller values of the disk pressure when compared with other models. It is expected that the pressure at the centre of the disk is smaller than the average density multiplied by the local tidal acceleration at the equatorial plane. Still, the choice between the assortment of pressure relations is tantamount to a fine-tuning of the model. Within the thin disk approximation, all these approaches are equivalent since they all assume vertical equilibrium and neglect self-gravity.

(ii) Following the BdHN scenario for the explanation of GRBs associated with Type Ic SNe (see Sec. 3.1), we considered a gas composed of ^{16}O at the outermost

radius of the disk and followed the evolution of the ion content using the Saha equation to fix the local NSE. In [51], only ^{4}He is present and, in [316], ions up to ^{56}Fe are introduced. The affinity between these cases implies that this particular model of disk accretion is insensible to the initial mass fraction distribution. This is explained by the fact that the average binding energy for most ions is very similar, hence any cooling or heating due to a redistribution of nucleons, given by the NSE, is negligible when compared to the energy consumed by direct photodisintegration of alpha particles. Additionally, once most ions are dissociated, the main cooling mechanism is neutrino emission that is similar for all models, modulo the supplementary neutrino emission processes included in addition to electron and positron capture. However, during our numerical calculations, we noticed that the inclusion of non-electron neutrino emission processes can reduce the electron fraction by up to $\sim 8\%$. This effect is observed again during the simulation of flavour equipartition alluding to the need for detailed calculations of neutrino emissivities when establishing NSE state. We obtain similar results to [51] (see Fig. 3.3), but by varying the accretion rate and fixing the viscosity parameter. This suggests that a more natural differentiating set of variables in the hydrodynamic equations of an α-viscosity disk is the combination of the quotient $\dot{M}/\alpha$ and either $\dot{M}$ or α. This result is already evident in, for example, Fig. 11 and Fig. 12 of [51], but was not mentioned there.

Concerning neutrino oscillations, we showed that the conditions inside the ignition radius, the oscillation potentials follow the relation $\langle\omega\rangle \ll \mu \ll \lambda$, as it is illustrated by Fig. 3.5. We also showed that the within this region the number densities of electron neutrinos and anti-neutrinos are very similar. As a consequence of this particular environment very fast pair conversions $\nu_e\bar{\nu}_e \rightleftharpoons \nu_x\bar{\nu}_x$, induced by bipolar oscillations, are obtained for the inverted mass hierarchy case with oscillation frequencies between 10^9 s^{-1} and 10^5 s^{-1}. For the normal hierarchy case no flavour changes are observed (see Fig. 3.6 and Fig. 3.7). Bearing in mind the magnitude of these frequencies and the low neutrino travel times through the disk, we conclude that an accretion disk under our main assumption cannot represent a steady state. However, using numerical and algebraic results obtained in [237, 90, 88], and references therein, we were able to generalize our model to a more realistic picture of neutrino oscillations. The main consequence of the interaction between neighbouring regions of the disk is the onset of kinematic decoherence in a timescale of the order of the oscillation times. Kinematic decoherence induces fast flavour equipartition among electronic and non-electronic neutrinos throughout the disk. Therefore, the neutrino content emerging from the disk is very different from the one that is usually assumed (see, e.g., [175, 170]). The comparison between disks with and without flavour equipartition is summarized in Fig. 3.8 and Table 3.1. We found that flavour equipartition, while leaving anti-neutrino cooling practically unchanged, it enhances neutrino cooling by allowing the energy contained (and partially trapped inside the disk due to high opacity) within the ν_e gas to escape in the form of ν_x, rendering the disk insensible to the electron neutrino opacity. We give in Eq. (3.73) a relation to estimate the change in F_ν as a function of $\tau_{\nu_e}\tau_{\nu_x}$ that describes correctly the behaviour of the disk under flavour equipartition. The variation of the flavour content in the emission flux implies a loss in L_{ν_e} and an increase in L_{ν_x} and $L_{\bar{\nu}_e}$. As a consequence, the total energy deposition rate of the process $\nu + \bar{\nu} \to e^- + e^+$ is reduced. We showed that this reduction can be as high 80% and is maximal

whenever the quotient $\tau_{\nu_e}/\tau_{\nu_x}$ is also maximal and the condition $\tau_{\nu_e} > 1$ is obtained.

At this point we can identify several issues which have still to be investigated:

(1) Throughout the accretion disk literature, several fits to calculate the neutrino and neutrino annihilation luminosity can be found (see, e.g., [169] and references therein). However, all these fits were calculated without taking into account neutrino oscillations. Since we have shown that oscillations directly impact luminosity, these results need to be extended.

(2) Additionally, the calculations of the neutrino and neutrino annihilation luminosities we have performed, ignore general relativistic effects and the possible neutrino oscillations from the disk surface to the annihilation point. In [274], it has been shown that general relativistic effects can enhance the neutrino annihilation luminosity in a neutron star binary merger by a factor of 10. In [228], however, it is argued that in BHs this effect has to be mild since the energy gained by falling into the gravitational potential is lost by the electron-positron pairs when they climb back up. Nonetheless, this argument ignores the bending of neutrino trajectories and neutrino capture by te BH which can be significant for $r \lesssim 10r_s$. In [35], the increment is calculated to be no more than a factor of 2 and can be less depending on the geometry of the emitting surface. But, as before, they assume a purely $\nu_e\bar{\nu}_e$ emission and ignore oscillations after the emission. Simultaneously, the literature on neutrino oscillation above accretion disks (see, e.g., [175]) do not take int account oscillations inside the disk and assume only $\nu_e\bar{\nu}_e$ emission. A similar situation occurs in works studying the effect of neutrino emission on r-process nucleosynthesis in hot outflows (wind) ejected from the disk (see, e.g., [44]). It is still unclear how the complete picture (oscillations inside the disk $\rightarrow$ oscillations above the disk + relativistic effects) affect the final energy deposition. We are currently working on the numerical calculation of the annihilation energy deposition rate using a ray tracing code and including neutrino oscillations both inside the disk and after their emission from the disk surface. These results will be the subject of a future publication.

This chapter serves as a primer that has allowed us to identify key theoretical and numerical features involved in the study of neutrino oscillations in neutrino-cooled accretion disks. The unique conditions inside the disk and its geometry lend themselves to varied neutrino oscillations that can have an impact on a wide range of astrophysical phenomena: from e^-e^+ plasma production above BHs in GRB models, to r-process nucleosynthesis in disk winds and possible MeV neutrino detectability. As such, this topic deserves appropriate attention since it paves the way for new astrophysical scenarios for testing neutrino physics.

Appendix

Appendix A

Transformations and Christoffel Symbols

For the sake of completeness, here we give the explicitly the transformation used in Eq. (3.6) and the Christoffel symbols used during calculations. The coordinate transformation matrices between the CF and the LNRF on the tangent vector space is [21]

$$e_{\hat{\nu}}{}^{\mu} = \begin{pmatrix} \frac{1}{\sqrt{\omega^2 g_{\phi\phi} - g_{tt}}} & 0 & 0 & 0 \\ 0 & \frac{1}{\sqrt{g_{rr}}} & 0 & 0 \\ 0 & 0 & \frac{1}{\sqrt{g_{\theta\theta}}} & 0 \\ \frac{\omega}{\sqrt{\omega^2 g_{\phi\phi} - g_{tt}}} & 0 & 0 & \frac{1}{\sqrt{g_{\phi\phi}}} \end{pmatrix} \tag{A.1a}$$

$$e^{\hat{\nu}}{}_{\mu} = \begin{pmatrix} \sqrt{\omega^2 g_{\phi\phi} - g_{tt}} & 0 & 0 & 0 \\ 0 & \sqrt{g_{rr}} & 0 & 0 \\ 0 & 0 & \sqrt{g_{\theta\theta}} & 0 \\ -\omega\sqrt{g_{\phi\phi}} & 0 & 0 & \sqrt{g_{\phi\phi}} \end{pmatrix} \tag{A.1b}$$

so that the basis vectors transform as $\boldsymbol{\partial}_{\hat{\nu}} = e^{\mu}{}_{\hat{\nu}}\boldsymbol{\partial}_{\mu}$, that is, with $\boldsymbol{e}^T$. For clarity, coordinates on the LNRF have a caret ($x^{\hat{\mu}}$), coordinates on the CRF have a tilde ($x^{\tilde{\mu}}$) and coordinates on the LRF have two ($x^{\tilde{\hat{\mu}}}$). An observer on the LNRF sees the fluid elements move with an azimuthal velocity $\beta^{\hat{\phi}}$. This observer then can perform a Lorentz boost $L_{\beta^{\hat{\phi}}}$ to a new frame. On this new frame an observer sees the fluid elements falling radially with velocity $\beta^{\tilde{r}}$, so it can perform another Lorentz boost $L_{\beta^{\tilde{r}}}$ to the LRF. Finally, the transformation between the the LRF and the CF coordinates $x^{\mu} = e_{\hat{\rho}}{}^{\mu}(L_{\beta^{\hat{\phi}}})_{\tilde{\alpha}}{}^{\hat{\rho}}(L_{\beta^{\tilde{r}}})_{\tilde{\tilde{\nu}}}{}^{\tilde{\alpha}}x^{\tilde{\tilde{\nu}}} = A_{\tilde{\tilde{\nu}}}{}^{\mu}x^{\tilde{\tilde{\nu}}}$, where the components of $\boldsymbol{A}$ and

$\boldsymbol{A}^{-1}$ are

$$A_{\tilde{\nu}}{}^{\mu} = \begin{pmatrix} \frac{\gamma_{\tilde{r}}\gamma_{\hat{\phi}}}{\sqrt{\omega^2 g_{\phi\phi}-g_{tt}}} & \frac{\gamma_{\hat{\phi}}\gamma_{\tilde{r}}\beta^{\tilde{r}}}{\sqrt{\omega^2 g_{\phi\phi}-g_{tt}}} & 0 & \frac{\gamma_{\hat{\phi}}\beta^{\hat{\phi}}}{\sqrt{\omega^2 g_{\phi\phi}-g_{tt}}} \\ \frac{\gamma_{\tilde{r}}\beta^{\tilde{r}}}{\sqrt{g_{rr}}} & \frac{\gamma_{\tilde{r}}}{\sqrt{g_{rr}}} & 0 & 0 \\ 0 & 0 & \frac{1}{\sqrt{g_{\theta\theta}}} & 0 \\ \gamma_{\tilde{r}}\left(\frac{\omega\gamma_{\hat{\phi}}}{\sqrt{\omega^2 g_{\phi\phi}-g_{tt}}}+\frac{\gamma_{\hat{\phi}}\beta^{\hat{\phi}}}{\sqrt{g_{\phi\phi}}}\right) & \gamma_{\tilde{r}}\beta^{\tilde{r}}\left(\frac{\omega\gamma_{\hat{\phi}}}{\sqrt{\omega^2 g_{\phi\phi}-g_{tt}}}+\frac{\gamma_{\hat{\phi}}\beta^{\hat{\phi}}}{\sqrt{g_{\phi\phi}}}\right) & 0 & \frac{\gamma_{\hat{\phi}}}{\sqrt{g_{\phi\phi}}}+\frac{\omega\gamma_{\hat{\phi}}\beta^{\hat{\phi}}}{\sqrt{\omega^2 g_{\phi\phi}-g_{tt}}} \end{pmatrix} \tag{A.2a}$$

$$A^{\tilde{\nu}}{}_{\mu} = \begin{pmatrix} \gamma_{\tilde{r}}\gamma_{\hat{\phi}}\left(\sqrt{\omega^2 g_{\phi\phi}-g_{tt}}+\beta^{\hat{\phi}}\omega\sqrt{g_{\phi\phi}}\right) & -\gamma_{\tilde{r}}\beta^{\tilde{r}}\sqrt{g_{rr}} & 0 & -\gamma_{\tilde{r}}\gamma_{\hat{\phi}}\beta^{\hat{\phi}}\sqrt{g_{\phi\phi}} \\ -\gamma_{\hat{\phi}}\gamma_{\tilde{r}}\beta^{\tilde{r}}\left(\sqrt{\omega^2 g_{\phi\phi}-g_{tt}}+\beta^{\hat{\phi}}\omega\sqrt{g_{\phi\phi}}\right) & \gamma_{\tilde{r}}\sqrt{g_{rr}} & 0 & \gamma_{\tilde{r}}\gamma_{\hat{\phi}}\beta^{\tilde{r}}\beta^{\hat{\phi}}\sqrt{g_{\phi\phi}} \\ 0 & 0 & \sqrt{g_{\theta\theta}} & 0 \\ -\gamma_{\hat{\phi}}\left(\beta^{\hat{\phi}}\sqrt{\omega^2 g_{\phi\phi}-g_{tt}}+\omega\sqrt{g_{\phi\phi}}\right) & 0 & 0 & \gamma_{\hat{\phi}}\sqrt{g_{\phi\phi}} \end{pmatrix} \tag{A.2b}$$

Since Lorentz transformations do not commute, the transformation $\boldsymbol{A}$ raises the question: what happens if we invert the order? In this case, we would not consider a corotating frame but a *cofalling* frame on which observers see fluid elements, not falling, but rotating. The new transformation velocities $\beta^{r'}$, $\beta^{\phi'}$ are subject to the conditions $\beta^{\phi'} = \gamma_{r'}\beta^{\hat{\phi}}$, $\beta^{r'} = \beta^{\tilde{r}}/\gamma_{\hat{\phi}}$ and $\gamma_{r'}\gamma_{\phi'} = \gamma_{\tilde{r}}\gamma_{\hat{\phi}}$. Although both approaches are valid, considering that the radial velocity is an unknown, the first approach is clearly cleaner. To obtain the coordinate transformation between the CF and the CRF $A_{\tilde{\nu}}{}^{\mu}$ and $A^{\tilde{\nu}}{}_{\mu}$ we can simply set $\beta^{\tilde{r}} = 0$ in Eqs. (A.2). With this we can calculate

$$\frac{d\hat{\phi}}{d\hat{t}} = \beta^{\hat{\phi}} = \frac{u^{\mu}e^{\hat{\phi}}{}_{\mu}}{u^{\nu}e^{\hat{t}}{}_{\nu}} = \sqrt{\frac{g_{\phi\phi}}{\omega^2 g_{\phi\phi}-g_{tt}}}\,(\Omega-\omega)\,, \tag{A.3}$$

$$d\tilde{r} = \sqrt{g_{rr}}dr,\;\; d\tilde{t} = \frac{\gamma_{\hat{\phi}}}{\sqrt{\omega^2 g_{\phi\phi}-g_{tt}}}dt = \frac{1}{\sqrt{-g_{tt}-2\Omega g_{t\phi}-\Omega^2 g_{\phi\phi}}}dt,\;\; d\tilde{\theta} = \sqrt{g_{\theta\theta}}d\theta. \tag{A.4}$$

The non-vanishing Christoffel symbols are

$$\begin{aligned}
&\Gamma^{t}{}_{tr} = \frac{M\left(r^2-M^2a^2\cos^2\theta\right)\left(r^2+M^2a^2\right)}{\Sigma^2\Delta},\;\; \Gamma^{t}{}_{t\theta} = -\frac{M^3a^2r\sin 2\theta}{\Sigma^2},\\
&\Gamma^{t}{}_{r\phi} = -\frac{M^2a\left(3r^4+M^2a^2r^2+M^2a^2\cos^2\theta\left(r^2-M^2a^2\right)\right)\sin^2\theta}{\Sigma^2\Delta},\\
&\Gamma^{t}{}_{\theta\phi} = \frac{2M^4a^3r\cos\theta\sin^3\theta}{\Sigma^2},\;\; \Gamma^{r}{}_{tt} = \frac{M\Delta\left(r^2-M^2a^2\cos^2\theta\right)}{\Sigma^3},\\
&\Gamma^{r}{}_{t\phi} = -\frac{M^2a\Delta\left(r^2-M^2a^2\cos^2\theta\right)\sin^2\theta}{\Sigma^3},\;\; \Gamma^{r}{}_{rr} = \frac{r}{\Sigma}+\frac{M-r}{\Delta},\\
&\Gamma^{r}{}_{r\theta} = -\frac{M^2a^2\sin\theta}{M^2a^2\cos\theta+r^2\tan\theta},\;\; \Gamma^{r}{}_{\theta\theta} = -\frac{r\Delta}{\Sigma},\;\; \Gamma^{r}{}_{\phi\phi} = \left(Ma\Gamma^{r}{}_{t\phi}-\Gamma^{r}{}_{\theta\theta}\right)\sin^2\theta,\\
&\Gamma^{\theta}{}_{tt} = -\Gamma^{t}{}_{\theta\phi}\frac{\csc^2\theta}{Ma\Sigma},\;\; \Gamma^{\theta}{}_{t\phi} = \frac{M^2ar\left(r^2+M^2a^2\right)\sin 2\theta}{\Sigma^3},\;\; \Gamma^{\theta}{}_{rr} = \frac{M^2a^2\sin\theta\cos\theta}{\Sigma\Delta},\;\; \Gamma^{\theta}{}_{t\theta} = \frac{r}{\Sigma},\\
&\Gamma^{\theta}{}_{\theta\theta} = \Gamma^{r}{}_{r\theta},\;\; \Gamma^{\theta}{}_{\phi\phi} = \left(\frac{\Delta}{\Sigma}+\frac{2Mr\left(r^2+M^2a^2\right)^2}{\Sigma^3}\right)\sin\theta\cos\theta,\;\; \Gamma^{\phi}{}_{tr} = -\frac{M^2a\left(r^2-M^2a^2\cos^2\theta\right)}{\Sigma^2\Delta},\\
&\Gamma^{\phi}{}_{t\theta} = -\frac{2M^2ar\cot\theta}{\Sigma^2},\;\; \Gamma^{\phi}{}_{r\phi} = \frac{r\left(\Sigma-2Mr\right)}{\Sigma\Delta}+\frac{Ma\Sigma}{\Delta^2}\Gamma^{r}{}_{t\phi},\;\; \Gamma^{\phi}{}_{\theta\phi} = \cot\theta-\Gamma^{t}{}_{t\theta}.
\end{aligned} \tag{A.5}$$

Using the connection coefficients and the metric, both evaluated at the equatorial plane we can collect several equations for averaged quantities. The expansion of the fluid world lines is

$$\boldsymbol{\theta} = \nabla_{\mu}u^{\mu} = \frac{2}{r}u^{r}+\partial_{r}u^{r}. \tag{A.6}$$

There are several ways to obtain an approximate version of the shear tensor (see, e.g., [114, 198, 197]) but by far the simplest one is proposed by [207]. On the CRF the fluid four-velocity can be approximated by $u^{\tilde{\mu}} = (1, 0, 0, 0)$ by Eq. (3.7). Both the fluid four-acceleration $a_\nu = u^\mu \nabla_\mu u_\nu$ and expansion parameter, Eq. (A.6), vanish so that the shear tensor reduces to $2\sigma_{\tilde{\mu}\tilde{\nu}} = \nabla_{\tilde{\mu}} u_{\tilde{\nu}} + \nabla_{\tilde{\nu}} u_{\tilde{\mu}}$. In particular, the r-ϕ component is

$$\sigma_{\tilde{r}\tilde{\phi}} = -\frac{1}{2}\left(\Gamma^{\tilde{t}}_{\tilde{\phi}\tilde{r}} + \Gamma^{\tilde{t}}_{\tilde{r}\tilde{\phi}}\right) = -\frac{1}{4}\left(2c_{\tilde{t}\tilde{\phi}}{}^{\tilde{r}} + 2c_{\tilde{t}\tilde{r}}{}^{\tilde{\phi}}\right) = \frac{1}{2}c_{\tilde{r}\tilde{t}}{}^{\tilde{\phi}} = \frac{\gamma_{\hat{\phi}}^2}{2}\frac{\sqrt{g_{\phi\phi}}}{\sqrt{\omega^2 g_{\phi\phi} - g_{tt}}\sqrt{g_{rr}}}\partial_r\Omega \tag{A.7}$$

where $c_{\tilde{\mu}\tilde{\nu}}{}^{\tilde{\alpha}}$ are the commutation coefficients for the CRF. Finally, of particular interest is the $\tilde{\theta}$ component of the Riemann curvature tensor

$$R^{\tilde{\theta}}{}_{\tilde{t}\tilde{\theta}\tilde{t}}\Big|_{\theta=\pi/2} = \frac{M}{r^3}\frac{r^2 - 4aM^{3/2}r^{1/2} + 3M^2a^2}{r^2 - 3Mr + 2aM^{3/2}r^{1/2}}, \tag{A.8}$$

which gives a measurement of the relative acceleration in the $\tilde{\theta}$ direction of nearly equatorial geodesics.

Appendix B

Stress-Energy Tensor

Here we present some equations related to the stress-energy that we used in this paper. Eq. (3.10) for a zero bulk viscosity fluid in components is

$$T^{\mu}_{\nu} = \Pi u^{\mu} u_{\nu} + P\delta^{\mu}_{\nu} - 2\eta\sigma^{\mu}_{\nu} + q^{\mu}u_{\nu} + q_{\nu}u^{\mu}. \tag{B.1}$$

It's covariant derivative is

$$\begin{aligned} 0 = \nabla_{\mu} T^{\mu}_{\nu} &= u^{\mu}u_{\nu}\partial_{\mu}\Pi + \Pi\boldsymbol{\theta}u_{\nu} + \Pi a_{\nu} + \partial_{\nu}P - 2\eta\nabla_{\mu}\sigma^{\mu}_{\nu} \\ &\quad + q^{\mu}\nabla_{\mu}u_{\nu} + u_{\nu}\nabla_{\mu}q^{\mu} + q_{\nu}\boldsymbol{\theta} + u^{\mu}\nabla_{\mu}q_{\nu} \\ &= u^{\mu}\left[u_{\nu}\left(\partial_{\mu}\Pi - \frac{\Pi}{\rho}\partial_{\mu}\rho\right) - \frac{q_{\nu}}{\rho}\partial_{\mu}\rho\right] + \Pi a_{\nu} + \partial_{\nu}P - 2\eta\nabla_{\mu}\sigma^{\mu}_{\nu} \\ &\quad + q^{\mu}\nabla_{\mu}u_{\nu} + u_{\nu}\nabla_{\mu}q^{\mu} + u^{\mu}\nabla_{\mu}q_{\nu}, \end{aligned} \tag{B.2}$$

where baryon conservation is used $\rho\boldsymbol{\theta} = -u^{\mu}\partial_{\mu}\rho$. To get an equation of motion for the fluid, we project perpendicular to u_{ν}

$$\begin{aligned} 0 = P^{\nu}_{\beta}\nabla_{\mu}T^{\mu}_{\nu} &= u^{\mu}\left[u_{\beta}\left(\partial_{\mu}\Pi - \frac{\Pi}{\rho}\partial_{\mu}\rho\right) - \frac{q_{\beta}}{\rho}\partial_{\mu}\rho\right] + \Pi a_{\beta} + \partial_{\beta}P - 2\eta\nabla_{\mu}\sigma^{\mu}_{\beta} \\ &\quad + q^{\mu}\nabla_{\mu}u_{\beta} + u_{\beta}\nabla_{\mu}q^{\mu} + u^{\mu}\nabla_{\mu}q_{\beta} - u^{\mu}u_{\beta}\left[\partial_{\mu}\Pi - \frac{\Pi}{\rho}\partial_{\mu}\rho\right] \\ &\quad + u^{\nu}u_{\beta}\partial_{\nu}P - 2\eta u^{\nu}u_{\beta}\nabla_{\mu}\sigma^{\mu}_{\nu} - u_{\beta}\nabla_{\mu}q^{\mu} + u^{\nu}u_{\beta}u^{\mu}\nabla_{\mu}q_{\nu} \\ &= -\frac{q_{\beta}}{\rho}u^{\mu}\partial_{\mu}\rho + \Pi a_{\beta} + \partial_{\beta}P - 2\eta\nabla_{\mu}\sigma^{\mu}_{\beta} + q^{\mu}\nabla_{\mu}u_{\beta} + u^{\mu}\nabla_{\mu}q_{\beta} \\ &\quad + u_{\beta}u^{\nu}\partial_{\nu}P - 2\eta u^{\nu}u_{\beta}\nabla_{\mu}\sigma^{\mu}_{\nu} + u^{\nu}u_{\beta}u^{\mu}\nabla_{\mu}q_{\nu} \\ &= -\frac{q_{\beta}}{\rho}u^{\mu}\partial_{\mu}\rho + \Pi a_{\beta} + \partial_{\beta}P - 2\eta\nabla_{\mu}\sigma^{\mu}_{\beta} + q^{\mu}\nabla_{\mu}u_{\beta} + u^{\mu}\nabla_{\mu}q_{\beta} \\ &\quad + u_{\beta}\left(u^{\nu}\partial_{\nu}P + 2\eta\sigma^{\mu\nu}\sigma_{\mu\nu} - q_{\nu}a^{\nu}\right), \end{aligned} \tag{B.3}$$

where the identities $q_{\mu}u^{\mu} = u^{\mu}a_{\mu} = \sigma^{\mu\nu}u_{\nu} = 0$, $u_{\mu}u^{\nu} = -1$, $\sigma^{\mu\nu}\sigma_{\mu\nu} = \sigma^{\mu\nu}\nabla_{\mu}u_{\nu}$ are used. Combining the Eq. (B.2) and Eq. (B.3) we get

$$u^{\mu}\left[\partial_{\mu}U - \frac{U+P}{\rho}\partial_{\mu}\rho\right] = 2\eta\sigma^{\mu\nu}\sigma_{\mu\nu} - q_{\mu}a^{\mu} - \nabla_{\mu}q^{\mu}. \tag{B.4}$$

With Eq. (A.6) we can obtain an equation for mass conservation

$$\begin{aligned} 0 =& \nabla_\mu \left(\rho u^\mu\right) = u^\mu \partial_\mu \rho + \rho \boldsymbol{\theta} = u^\mu \partial_\mu \rho + \rho \left(\frac{2}{r} u^r + \partial_r u^r\right) \\ & \Rightarrow \partial_r \left(r^2 \rho u^r\right) + r^2 u^j \partial_j \rho = 0, \quad \text{for } j \in \{t, \theta, \phi\}\,. \end{aligned} \tag{B.5}$$

Finally, we reproduce the *zero torque at the innermost stable circular orbit* condition that appears in [211]. Using the killing vector fields $\boldsymbol{\partial}_\phi$, $\boldsymbol{\partial}_t$ we can calculate

$$\begin{aligned} 0 = \boldsymbol{\nabla} \cdot (\boldsymbol{T} \cdot \boldsymbol{\partial}_\phi) = \nabla_\mu T^\mu_\phi &= \frac{1}{\sqrt{-g}} \partial_\mu \left(\sqrt{-g} T^\mu_\phi\right) \\ &\approx \frac{1}{r^2} \partial_r \left(\rho u^r u_\phi r^2 - 2\eta \sigma^r_\phi r^2\right) + u_\phi \partial_\theta q^\theta \quad \text{with } \Pi \approx \rho \\ \Rightarrow \partial_r \left(\rho u^r u_\phi r^2 - 2\eta \sigma^r_\phi r^2\right) &= -r^2 u_\phi \partial_\theta q^\theta \\ \Rightarrow \partial_r \left(\frac{\dot{M}}{2\pi} u_\phi + 4 r H \eta \sigma^r_\phi\right) &= 2 H u_\phi \epsilon \quad \text{after integrating} \\ & \qquad\qquad\qquad\qquad \text{vertically and using Eq. (3.17)} \\ \text{Analogously for } \boldsymbol{\partial}_t,\ \partial_r \left(\frac{\dot{M}}{2\pi} u_t - 4 r H \Omega \eta \sigma^r_\phi\right) &= 2 H u_t \epsilon \quad \text{after integrating} \\ & \qquad\qquad\qquad\qquad \text{vertically and using Eq. (3.12)} \end{aligned} \tag{B.6}$$

The vertical integration of the divergence of the heat flux is as follows: Since, on average, $\boldsymbol{q} = q^\theta \boldsymbol{\partial}_\theta$, we have $\nabla_\mu q^\mu = \partial_\theta q^\theta$ and by Eq. (A.2), $q^\theta = r q^{\hat{\hat{\theta}}}$. Vertically integrating yields

$$\int_{\theta_{\min}}^{\theta_{\max}} \partial_\theta q^\theta r d\theta = r\, q^\theta \Big|_{\theta_{\min}}^{\theta_{\max}} = 2 q^{\tilde{\tilde{\theta}}} = 2 H \epsilon, \tag{B.7}$$

where $q^{\tilde{\tilde{\theta}}}$ is the averaged energy flux radiating out of a face of the disk, as measured by an observer on the LRF, which we approximate as the half-thickness of the disk H times the average energy density per unit proper time ϵ lost by the disk. With the variable change $z = 8\pi r H \eta \sigma^r_\phi / \dot{M}$ and $y = 4\pi H \epsilon / \dot{M}$ the equations reduce to

$$\partial_r \left(u_\phi + z\right) = y u_\phi, \tag{B.8a}$$

$$\partial_r \left(u_t - \Omega z\right) = y u_t. \tag{B.8b}$$

Using the relation $\partial_r u_t = -\Omega \partial_r u_\phi$ [323, Eq. (10.7.29)] and $\partial_r \left(u_t + \Omega u_\phi\right) = u_\phi \partial_r \Omega$ we can combine the previous equations to obtain

$$z = -\frac{y \left(u_t + \Omega u_\phi\right)}{\partial_r \Omega}, \tag{B.9a}$$

$$\partial_r \left(A B^2\right) = B \partial_r u_\phi, \tag{B.9b}$$

with $A = y/\partial_r\Omega$ and $B = u_t + \Omega u_\phi$. To integrate these equations we use the zero torque condition $z(r = r^*) = 0$ where r^* is the radius of the innermost stable circular orbit, which gives the relation

$$y = \frac{\partial_r\Omega}{(u_t + \Omega u_\phi)^2}\int_{r^*}^{r}(u_t + \Omega u_\phi)\,\partial_r u_\phi dr = \frac{\partial_r\Omega}{(u_t + \Omega u_\phi)^2}\left(u_t u_\phi|_{r^*}^{r} - 2\int_{r^*}^{r} u_\phi \partial_r u_t dr\right), \tag{B.10}$$

or, equivalently,

$$8\pi H r\rho\nu_{\rm turb}\sigma_\phi^r \approx 8\pi H r\Pi\nu_{\rm turb}\sigma_\phi^r = -\frac{\dot{M}}{(u_t + \Omega u_\phi)}\left(u_t u_\phi|_{r^*}^{r} - 2\int_{r^*}^{r} u_\phi \partial_r u_t dr\right). \tag{B.11}$$

Using Eq. (3.6), the approximation $\gamma_{\tilde{r}} \approx 1$ and the variable change $r = xM^2$ the integral can be easily evaluated by partial fractions

$$8\pi H r\rho\nu_{\rm turb}\sigma_\phi^r = \dot{M}M f\,(x, x^*)\,, \tag{B.12a}$$

$$f\,(x, x^*) = \frac{x^3 + a}{x^{3/2}\sqrt{x^3 - 3x + 2a}}\left(x - x^* - \frac{3}{2}a\ln\left(\frac{x}{x^*}\right) + \frac{1}{2}\sum_{i=1}^{3}\frac{ax_i^2 - 2x_i + a}{x_i^2 - 1}\ln\left(\frac{x - x_i}{x^* - x_i}\right)\right), \tag{B.12b}$$

where x_1, x_2, x_3 are the roots of the polynomial $x^3 - 3x + 2a$.

Appendix C

Nuclear Statistical Equilibrium

The results in this section appear in [230]. We include them here since they are necessary to solve Eq. (3.20). Neutrino dominated accretion disks reach densities above $\sim 10^7$ g cm^{-3} and temperatures above $\sim 5 \times 10^9$ K. For these temperatures, forward and reverse nuclear reactions are balanced and the abundances in the plasma are determined by the condition $\mu_i = Z_i\mu_p + N_i\mu_n$, that is, the Nuclear Statistical Equilibrium. However, for densities above 10^6 g cm^{-3}, the electron screening of charged particle reactions can affect the nuclear reaction rates. For this reason, to obtain an accurate NSE state it is necessary to include Coulomb corrections to the ion chemical potential. The Coulomb correction to the i-th chemical potential is given by

$$\frac{\mu_i^C}{T} = K_1\left[\Gamma_i\sqrt{\Gamma_i + K_2} - K_2\ln\left(\sqrt{\frac{\Gamma_i}{K_2}} + \sqrt{1+\frac{\Gamma_i}{K_2}}\right)\right] + 2K_3\left[\sqrt{\Gamma_i} - \arctan\sqrt{\Gamma_i}\right] + Z_1\left[\Gamma_i - Z_2\ln\left(1+\frac{\Gamma_i}{Z_1}\right)\right] + \frac{Z_3}{2}\ln\left(1+\frac{\Gamma_i^2}{Z_4}\right) \tag{C.1}$$

The ion coupling parameter is written in terms of the electron coupling parameter as $\Gamma_i = \Gamma_e Z_i^{5/3}$ with

$$\Gamma_e = \frac{e^2}{T}\left(\frac{4\pi Y_e n_B}{3}\right)^{1/3}. \tag{C.2}$$

where e is the electron charge. The parameters K_i, C_i are given in Table (C.1).

Table C.1. Fitting constants in Eq. (C.1) [230].

K_1	K_2	K_3	Z_1	Z_2	Z_3	Z_4
-0.907347	0.62849	0.278497	4.50×10^{-3}	170.0	-8.4×10^{-5}	3.70×10^{-3}

Appendix D

Neutrino Interactions and Cross-Sections

In this appendix we include the neutrino emission rates and neutrino cross-sections used in the accretion disk model. These expressions have been covered in [71, 301, 39, 252, 317, 42, 41]. We also include the expression energy emission rate for $\nu\bar{\nu}$ annihilation into electron-positron pairs. Whenever possible we write the rates in terms of generalized Fermi functions

$$\mathcal{F}_{k,\ell}\left(y,\eta\right)=\int_{\ell}^{\infty}\frac{x^{k}\sqrt{1+xy/2}}{\exp\left(x-\eta\right)+1}dx. \tag{D.1}$$

since some numerical calculations were done following [12]. Before proceeding we list some useful expressions and constants in Planck units that will be used. The numerical values can be found in [292].

$M_w \approx 6.584\times10^{-18}$ ..... W boson mass (D.2a)

$g_w \approx 0.653$ ..... Weak coupling constant (D.2b)

$g_a \approx 1.26$ ..... Axial-vector coupling constant (D.2c)

$\alpha^* \approx \dfrac{1}{137}$ ..... Fine structure constant (D.2d)

$\sin^2\theta_{\mathrm{W}} \approx 0.231$ ..... Weinberg angle (D.2e)

$\cos^2\theta_c \approx 0.947$ ..... Cabibbo angle (D.2f)

$G_F=\dfrac{\sqrt{2}g_w^2}{8M_w^2}\approx 1.738\times10^{33}$ ..... Fermi coupling constant (D.2g)

$C_{v,e}=2\sin^2\theta_{\mathrm{W}}+1/2$ ..... Weak interaction vector constant for ν_e (D.2h)

$C_{a,e}=1/2$ ..... Weak interaction axial-vector constant for ν_e (D.2i)

$C_{v,x}=C_{V,e}-1$ ..... Weak interaction vector constant for ν_x (D.2j)

$C_{a,x}=C_{A,e}-1$ ..... Weak interaction axial-vector constant for ν_x (D.2k)

$\sigma_0=\dfrac{4G_F^2m_e^2}{\pi}\approx 6.546\times10^{21}$ ..... Weak interaction cross-section (D.2l)

D.1 Neutrino Emissivities

- Pair annihilation $e^- + e^+ \to \nu + \bar{\nu}$

This process generates neutrinos of all flavours but around 70% are electron neutrinos [27]. This is due to the fact that the only charged leptons in the accretion systems we study are electrons and positrons, so creation of electron neutrinos occurs via either charged or neutral electroweak currents while creation of non-electronic neutrinos can only occur through neutral currents. Using the electron or positron four-momentum $p = (E, \boldsymbol{p})$, the Dicus' cross-section for a particular flavour i is [71]

$$\sigma_{D,i} = \frac{G_F^2}{12\pi E_{e^-} E_{e^+}} \Big[C_{+,i} \left(m_e^4 + 3m_e^2 p_{e^-} \cdot p_{e^+} + 2 \left(p_{e^-} \cdot p_{e^+} \right)^2 \right) + 3C_{-,i} \left(m_e^4 + m_e^2 p_{e^-} \cdot p_{e^+} \right) \Big] . \tag{D.3}$$

The factors $C_{\pm,i}$, are written in terms of the weak interaction vector and axial-vector constants: $C_{\pm,i} = C_{v,i}^2 \pm C_{a,i}^2$ [217]. Representing the Fermi-Dirac distribution for electrons (positrons) as $f_{e^-}(f_{e^+})$ with $\eta_{e^\mp}$ the electron (positron) degeneracy parameter including its rest mass. The number and energy emission rates can be calculated by replacing $\Lambda = 2$ and $\Lambda = E_{e^-} + E_{e^+}$ in the integral [317]:

$$\frac{4}{(2\pi)^6} \int \Lambda \sigma_D f_{e^-} f_{e^+} d^3\boldsymbol{p}_{e^-} d^3\boldsymbol{p}_{e^+}, \tag{D.4}$$

giving the expressions

$$\begin{aligned} R_{\nu_i+\bar{\nu}_i} = \frac{G_F^2 m_e^8}{18\pi} \big[& C_{+,i} \left(8\mathbb{U}_1\mathbb{V}_1 + 5\mathbb{U}_{-1}\mathbb{V}_{-1} + 9\mathbb{U}_0\mathbb{V}_0 - 2\mathbb{U}_{-1}\mathbb{V}_1 - 2\mathbb{U}_1\mathbb{V}_{-1} \right) \\ & + 9C_{-,i} \left(\mathbb{U}_{-1}\mathbb{V}_{-1} + \mathbb{U}_0\mathbb{V}_0 \right) \big] , \end{aligned} \tag{D.5a}$$

$$\begin{aligned} Q_{\nu_i+\bar{\nu}_i} = \frac{G_F^2 m_e^9}{36\pi} \big[& C_{+,i} \left(8 \left(\mathbb{U}_2\mathbb{V}_1 + \mathbb{U}_1\mathbb{V}_2 \right) + 7 \left(\mathbb{U}_1\mathbb{V}_0 + \mathbb{U}_0\mathbb{V}_1 \right) + 5 \left(\mathbb{U}_{-1}\mathbb{V}_0 + \mathbb{U}_0\mathbb{V}_{-1} \right) \right. \\ & \left. - 2 \left(\mathbb{U}_2\mathbb{V}_{-1} + \mathbb{U}_{-1}\mathbb{V}_2 \right) \right) + 9C_{-,i} \left(\mathbb{U}_0 \left(\mathbb{V}_1 + \mathbb{V}_{-1} \right) + \mathbb{V}_0 \left(\mathbb{U}_1 + \mathbb{U}_{-1} \right) \right) \big] . \end{aligned} \tag{D.5b}$$

The functions $\mathbb{U}, \mathbb{V}$ can be written in terms of generalized Fermi functions

$$\mathbb{U}_j = \sqrt{2}\xi^{3/2} \sum_{k=0}^{j+1} \binom{j+1}{k} \xi^k \mathcal{F}_{k+1/2,0} \left(\xi, \eta_{e^-} \right) , \tag{D.6a}$$

$$\mathbb{V}_j = \sqrt{2}\xi^{3/2} \sum_{k=0}^{j+1} \binom{j+1}{k} \xi^k \mathcal{F}_{k+1/2,0} \left(\xi, \eta_{e^+} \right) . \tag{D.6b}$$

It is often useful to define the functions

$$\varepsilon_i^m = \frac{2G_F^2 \left(m_e \right)^4}{3 \left(2\pi \right)^7} \int f_{e^-} f_{e^+} \left(E_{e^-}^m + E_{e^+}^m \right) \sigma_{D,i} \, d^3\mathbf{p}_{e^-} d^3\mathbf{p}_{e^+} \tag{D.7}$$

For $m = 0$ and $m = 1$ Eq. (D.7) gives the neutrino and anti-neutrino number emissivity (neutrino production rate), and the neutrino and anti-neutrino energy emissivity (energy per unit volume per unit time) for a certain flavour i, respectively (that is, Eq. (D.5)). Hence, not only we are able to calculate the total number and energy emissivity, but we can also calculate the neutrino or anti-neutrino energy moments with

$$\langle E^m_{\nu_i(\bar{\nu}_i)} \rangle = \frac{\varepsilon^m_i}{\varepsilon^0_i}, \text{ for } m \geq 1. \tag{D.8}$$

- Electron capture and positron capture $p + e^- \to n + \nu_e$, $n + e^+ \to p + \bar{\nu}_e$ and $A + e^- \to A' + \nu_e$

Due to lepton number conservation this process generated only electron (anti)-neutrinos. The number and energy emission rates for electron and positron capture by nucleons are

$$\begin{aligned}
R_{\nu_e} = {} & \frac{m_e^5 G_F^2 \cos^2\theta_c}{\sqrt{2}\pi^3}\left(1+3g_A^2\right)\Delta_{np}\xi^{3/2}\left[\xi^3\mathcal{F}_{7/2,\chi}(\xi,\eta_{e^-})\right. \\
& + (3-2\mathbb{Q})\,\xi^2\mathcal{F}_{5/2,\chi}(\xi,\eta_{e^-}) + (1-\mathbb{Q})(3-\mathbb{Q})\,\xi\mathcal{F}_{3/2,\chi}(\xi,\eta_{e^-}) \\
& \left. + (1-\mathbb{Q})^2\mathcal{F}_{1/2,\chi}(\xi,\eta_{e^-})\right], \qquad \text{(D.9a)} \\
Q_{\nu_e} = {} & \frac{m_e^6 G_F^2 \cos^2\theta_c}{\sqrt{2}\pi^3}\left(1+3g_A^2\right)\Delta_{np}\xi^{3/2}\left[\xi^4\mathcal{F}_{9/2,\chi}(\xi,\eta_{e^-})\right. \\
& + \xi^3(4-3\mathbb{Q})\,\mathcal{F}_{7/2,\chi}(\xi,\eta_{e^-}) + 3(\mathbb{Q}-1)(\mathbb{Q}-2)\,\xi^2\mathcal{F}_{5/2,\chi}(\xi,\eta_{e^-}) \\
& \left. + (1-\mathbb{Q})^2(4-\mathbb{Q})\,\xi\mathcal{F}_{3/2,\chi}(\xi,\eta_{e^-}) + (1-\mathbb{Q})^3\mathcal{F}_{1/2,\chi}(\xi,\eta_{e^-})\right], \qquad \text{(D.9b)} \\
R_{\bar{\nu}_e} = {} & \frac{m_e^5 G_F^2 \cos^2\theta_c}{\sqrt{2}\pi^3}\left(1+3g_A^2\right)\Delta_{pn}\xi^{3/2}\left[\xi^3\mathcal{F}_{7/2,0}(\xi,\eta_{e^+})\right. \\
& + (3+2\mathbb{Q})\,\xi^2\mathcal{F}_{5/2,0}(\xi,\eta_{e^+}) + (1+\mathbb{Q})(3+\mathbb{Q})\,\xi\mathcal{F}_{3/2,0}(\xi,\eta_{e^+}) \\
& \left. + (1+\mathbb{Q})^2\mathcal{F}_{1/2,0}(\xi,\eta_{e^+})\right], \qquad \text{(D.9c)} \\
Q_{\bar{\nu}_e} = {} & \frac{m_e^6 G_F^2 \cos^2\theta_c}{\sqrt{2}\pi^3}\left(1+3g_A^2\right)\Delta_{np}\xi^{3/2}\left[\xi^4\mathcal{F}_{9/2,0}(\xi,\eta_{e^+})\right. \\
& + \xi^3(4+3\mathbb{Q})\,\mathcal{F}_{7/2,0}(\xi,\eta_{e^+}) + 3(\mathbb{Q}+1)(\mathbb{Q}+2)\,\xi^2\mathcal{F}_{5/2,0}(\xi,\eta_{e^+}) \\
& \left. + (1+\mathbb{Q})^2(4+\mathbb{Q})\,\xi\mathcal{F}_{3/2,0}(\xi,\eta_{e^+}) + (1+\mathbb{Q})^3\mathcal{F}_{1/2,0}(\xi,\eta_{e^+})\right]. \qquad \text{(D.9d)}
\end{aligned}$$

where $\Delta_{ij} = (n_i - n_j)\,/\,(\exp(\eta_i - \eta_j) - 1)\,,\ i,j \in \{p,n\}$ are the Fermion blocking factors in the nucleon phase spaces and $\mathbb{Q} = (m_n - m_p)m_e \approx 2.531$ is the nucleon mass difference. The number and energy emission rates for electron capture by an

ion i are

$$R_{\nu_e,i} = \frac{\sqrt{2}m_e^5 G_F^2 \cos^2\theta_c}{7\pi^3} g_A^2 n_i \kappa_{Z_i} \kappa_{N_i} \xi^{3/2} \Big[\xi^3 \mathcal{F}_{7/2,\bar{\chi}}(\xi,\eta_{e^-}) + (3-2\mathbb{Q})\,\xi^2 \mathcal{F}_{5/2,\bar{\chi}}(\xi,\eta_{e^-}) + (1-\mathbb{Q})(3-\mathbb{Q})\,\xi \mathcal{F}_{3/2,\bar{\chi}}(\xi,\eta_{e^-}) + (1-\mathbb{Q})^2 \mathcal{F}_{1/2,\bar{\chi}}(\xi,\eta_{e^-})\Big], \tag{D.10a}$$

$$Q_{\nu_e,i} = \frac{\sqrt{2}m_e^6 G_F^2 \cos^2\theta_c}{7\pi^3} g_A^2 n_i \kappa_{Z_i} \kappa_{N_i} \xi^{3/2} \Big[\xi^4 \mathcal{F}_{9/2,\bar{\chi}}(\xi,\eta_{e^-}) + \xi^3 (4-3\mathbb{Q}) \mathcal{F}_{7/2,\bar{\chi}}(\xi,\eta_{e^-}) + 3(\mathbb{Q}-1)(\mathbb{Q}-2)\,\xi^2 \mathcal{F}_{5/2,\bar{\chi}}(\xi,\eta_{e^-}) + (1-\mathbb{Q})^2 (4-\mathbb{Q})\,\xi \mathcal{F}_{3/2,\bar{\chi}}(\xi,\eta_{e^-}) + (1-\mathbb{Q})^3 \mathcal{F}_{1/2,\bar{\chi}}(\xi,\eta_{e^-})\Big], \tag{D.10b}$$

The low limits of integration in these expressions are given by $\chi = (\mathbb{Q}-1)/\xi$ and $\bar{\chi} = (\mu_n - \mu_p + \Delta)/T - 1/\xi$ where $\Delta \approx 2.457 \times 10^{-22}$ is the energy of the neutron $1f_{5/2}$ state above the ground state. The functions $\kappa_{Z_i}, \kappa_{N_i}$ are

$$\kappa_{Z_i} = \begin{cases} 0 & \text{if } Z_i \leq 20. \\ Z_i - 20 & \text{if } 20 < Z_i \leq 28. \\ 8 & \text{if } Z_i > 28. \end{cases}, \quad \kappa_{N_i} = \begin{cases} 6 & \text{if } N_i \leq 34. \\ 40 - N_i & \text{if } 34 < N_i \leq 40. \\ 0 & \text{if } N_i > 40. \end{cases} \tag{D.11}$$

- Plasmon decay $\tilde{\gamma} \to \nu + \bar{\nu}$

$$R_{\nu_e+\bar{\nu}_e} = \frac{C_{v,e}\sigma_0 T^8}{96\pi^3 m_e^2 \alpha^*} \tilde{\gamma}^6 (\tilde{\gamma}+1) \exp(-\tilde{\gamma}), \tag{D.12a}$$

$$Q_{\nu_e+\bar{\nu}_e} = \frac{C_{v,e}\sigma_0 T^9}{192\pi^3 m_e^2 \alpha^*} \tilde{\gamma}^6 \left(\tilde{\gamma}^2 + 2\tilde{\gamma} + 2\right) \exp(-\tilde{\gamma}), \tag{D.12b}$$

$$R_{\nu_x+\bar{\nu}_x} = \frac{C_{v,x}\sigma_0 T^8}{48\pi^3 m_e^2 \alpha^*} \tilde{\gamma}^6 (\tilde{\gamma}+1) \exp(-\tilde{\gamma}), \tag{D.12c}$$

$$Q_{\nu_x+\bar{\nu}_x} = \frac{C_{v,x}\sigma_0 T^9}{96\pi^3 m_e^2 \alpha^*} \tilde{\gamma}^6 \left(\tilde{\gamma}^2 + 2\tilde{\gamma} + 2\right) \exp(-\tilde{\gamma}), \tag{D.12d}$$

where $\tilde{\gamma} = \tilde{\gamma}_0 \sqrt{\left(\pi^2 + 3(\eta_{e^-} + 1/\xi)^2\right)/3}$ and $\tilde{\gamma}_0 = 2\sqrt{\frac{\alpha^*}{3\pi}} \approx 5.565 \times 10^{-2}$.

- Nucleon-nucleon bremsstrahlung $n_1 + n_2 \to n_3 + n_4 + \nu + \bar{\nu}$

The nucleon-nucleon bremsstrahlung produces the same amount of neutrinos of all three flavours. The number and energy emission rates can be approximated by (see, e.g., [41])

$$R_{\nu_i+\bar{\nu}_i} = \left(2.59 \times 10^{13}\right) \left(X_p^2 + X_n^2 + \frac{28}{3} X_p X_n\right) n_B^2 \xi^{9/2}, \tag{D.13a}$$

$$Q_{\nu_i+\bar{\nu}_i} = \left(4.71 \times 10^{-9}\right) \left(X_p^2 + X_n^2 + \frac{28}{3} X_p X_n\right) n_B^2 \xi^{10/2}, \tag{D.13b}$$

D.2 Cross-Sections

We consider four interactions to describe the (anti)-neutrino total cross-section.

- Neutrino annihilation ($\nu + \bar{\nu} \to e^- + e^+$).

$$\sigma_{\nu_e\bar{\nu}_e} = \frac{4}{3} K_{\nu_e\bar{\nu}_e} \sigma_0 \frac{\langle E_{\nu_e}\rangle \langle E_{\bar{\nu}_e}\rangle}{m_e^2} \quad \text{with} \quad K_{\nu_e\bar{\nu}_e} = \frac{1 + 4\sin^2\theta_{\mathrm{W}} + 8\sin^4\theta_{\mathrm{W}}}{12}, \tag{D.14a}$$

$$\sigma_{\nu_x\bar{\nu}_x} = \frac{4}{3} K_{\nu_x\bar{\nu}_x} \sigma_0 \frac{\langle E_{\nu_x}\rangle \langle E_{\bar{\nu}_x}\rangle}{m_e^2} \quad \text{with} \quad K_{\nu_x\bar{\nu}_x} = \frac{1 - 4\sin^2\theta_{\mathrm{W}} + 8\sin^4\theta_{\mathrm{W}}}{12}, \tag{D.14b}$$

- Electron (anti)-neutrino absorption by nucleons ($\nu_e + n \to e^- + p$ and $\bar{\nu}_e + p \to e^+ + n$).

$$\sigma_{\nu_e n} = \sigma_0 \left(\frac{1 + 3g_a^2}{4}\right) \left(\frac{\langle E_{\nu_e}\rangle}{m_e} + \mathbb{Q}\right)^2 \sqrt{1 - \frac{1}{\left(\frac{\langle E_{\nu_e}\rangle}{m_e} + \mathbb{Q}\right)^2}}. \tag{D.15a}$$

$$\sigma_{\bar{\nu}_e p} = 3.83 \times 10^{22} \left(\frac{\wp\langle E_{\bar{\nu}_e}\rangle}{m_e} - \mathbb{Q}\right)^2 \sqrt{1 - \frac{1}{\left(\frac{\wp\langle E_{\bar{\nu}_e}\rangle}{m_e} - \mathbb{Q}\right)^2}} \left(\frac{\wp\langle E_{\bar{\nu}_e}\rangle}{m_e}\right)^{g(E_{\bar{\nu}_e})}, \tag{D.15b}$$

$$g(E_{\bar{\nu}_e}) = -0.07056 + 0.02018 \ln\left(\frac{\wp\langle E_{\bar{\nu}_e}\rangle}{m_e}\right) - 0.001953 \ln^3\left(\frac{\wp\langle E_{\bar{\nu}_e}\rangle}{m_e}\right). \tag{D.15c}$$

where $\wp = 0.511$.

- (Anti)-neutrino scattering by baryons ($\nu + A_i \to \nu + A_i$ and $\bar{\nu} + A_i \to \bar{\nu} + A_i$).

$$\sigma_p = \frac{\sigma_0 \langle E\rangle^2}{4m_e^2} \left(4\sin^4\theta_W - 2\sin^2\theta_W + \frac{1 + 3g_a^2}{4}\right) \tag{D.16a}$$

$$\sigma_n = \frac{\sigma_0 \langle E\rangle^2}{4m_e^2} \frac{1 + 3g_a^2}{4}. \tag{D.16b}$$

$$\sigma_{A_i} = \frac{\sigma_0 A_i^2 \langle E\rangle^2}{16m_e^2} \left[\left(4\sin^2\theta_W - 1\right) \frac{Z_i}{A_i} + 1 - \frac{Z_i}{A_i}\right]. \tag{D.16c}$$

- (Anti)-neutrino scattering by electrons or positrons ($\nu + e^\pm \to \nu + e^\pm$ and $\bar{\nu} + e^\pm \to \bar{\nu} + e^\pm$).

$$\sigma_e = \frac{3}{8} \sigma_0 \xi \frac{\langle E\rangle}{m_e} \left(1 + \frac{\eta_e + 1/\xi}{4}\right) \left[\left(C_{v,i} + n_\ell C_{a,i}\right)^2 + \frac{1}{3}\left(C_{v,i} - n_\ell C_{a,i}\right)^2\right]. \tag{D.17}$$

Here, n_ℓ is the (anti)-neutrino lepton number (that is, 1 for neutrinos and -1 for anti-neutrinos, depending on the cross-section to be calculated), and, in the

last four expressions, $\langle E \rangle$ is replaced by the average (anti)-neutrino energy of the corresponding flavour. With these expressions, the total opacity for neutrinos or anti-neutrinos is

$$\kappa_{\nu_i(\bar{\nu}_i)} = \frac{\sum_i \sigma_i n_i}{\rho}, \tag{D.18}$$

where n_i is the number density of the target particle associated with the process corresponding to the cross-section σ_i. The (anti)-neutrino optical depth appearing in Eq. (3.31) can then be approximated as

$$\tau_{\nu_i(\bar{\nu}_i)} = \int \kappa_{\nu_i(\bar{\nu}_i)} \rho d\theta \approx \kappa_{\nu_i(\bar{\nu}_i)} \rho H. \tag{D.19}$$

D.3 Neutrino–Anti-neutrino Pair Annihilation

Since the main interaction between $\nu\bar{\nu}$ is the annihilation into $e^- e^+$, this process above neutrino-cooled disks has been proposed as the origin of the energetic plasma involved in the production of GRBs. Once the (anti)-neutrino energy emissivity and average energies are calculated it is possible to calculate the energy deposition rate of the process $\nu_i + \bar{\nu}_i \rightarrow e^- + e^+$ for each flavour i. Ignoring Pauli blocking effects in the phase spaces of electron and positrons, the local energy deposition rate at a position $\mathbf{r}$ by $\nu\bar{\nu}$ annihilation can be written in terms of the neutrino and anti-neutrino distributions $f_{\nu_i} = f_{\nu_i}(\mathbf{r}, E_\nu)$, $f_{\bar{\nu}_i} = f_{\bar{\nu}_i}(\mathbf{r}, E_{\bar{\nu}})$ as [136]

$$\begin{aligned} Q_{\nu_i\bar{\nu}_i} = {} & A_{1,i} \int_0^\infty dE_{\nu_i} \int_0^\infty dE_{\bar{\nu}_i} E_{\nu_i}^3 E_{\bar{\nu}_i}^3 \left(E_{\nu_i} + E_{\bar{\nu}_i}\right) \int_{S_2} d\Omega_{\nu_i} \int_{S_2} d\Omega_{\bar{\nu}_i} f_{\nu_i} f_{\bar{\nu}_i} (1 - \cos\theta)^2 \\ & + A_{2,i} \int_0^\infty dE_{\nu_i} \int_0^\infty dE_{\bar{\nu}_i} E_{\nu_i}^2 E_{\bar{\nu}_i}^2 \left(E_{\nu_i} + E_{\bar{\nu}_i}\right) \int_{S_2} d\Omega_{\nu_i} \int_{S_2} d\Omega_{\bar{\nu}_i} f_{\nu_i} f_{\bar{\nu}_i} (1 - \cos\theta) \end{aligned} \tag{D.20}$$

where we have introduced the constants appearing in Eq. (3.76)

$$\begin{aligned} A_{1,i} &= \frac{\sigma_0 \left[(C_{v,i} - C_{a,i})^2 + (C_{v,i} + C_{a,i})^2\right]}{12\pi^2 m_e^2} \\ A_{2,i} &= \frac{\sigma_0 \left[2C_{v,i}^2 - C_{a,i}^2\right]}{6\pi^2 m_e^2} \end{aligned} \tag{D.21}$$

In Eq. (D.20), θ is the angle between the neutrino and anti-neutrino momentum and $d\Omega$ is the differential solid angle of the incident (anti)-neutrino at $\mathbf{r}$. The integral can be re-written in terms of the total intensity (energy integrated intensity) $I_\nu = \int E_\nu^3 f_\nu dE_\nu$ as [253]

$$\begin{aligned} Q_{\nu_i\bar{\nu}_i} = {} & A_{1,i} \int_{S_2} d\Omega_{\nu_i} I_{\nu_i} \int_{S_2} d\Omega_{\bar{\nu}_i} I_{\bar{\nu}_i} \left(\langle E_{\nu_i} \rangle + \langle E_{\bar{\nu}_i} \rangle\right) (1 - \cos\theta)^2 \\ & + A_{2,i} \int_{S_2} d\Omega_{\nu_i} I_{\nu_i} \int_{S_2} d\Omega_{\bar{\nu}_i} I_{\bar{\nu}_i} \frac{\langle E_{\nu_i} \rangle + \langle E_{\bar{\nu}_i} \rangle}{\langle E_{\nu_i} \rangle \langle E_{\bar{\nu}_i} \rangle} (1 - \cos\theta) \end{aligned} \tag{D.22}$$

The incident radiation intensity passing through the solid differential angle $d\Omega$ at $\mathbf{r}$ is the intensity $I_{\mathbf{r}_d,\nu}$ emitted from the point on the disk $\mathbf{r}_d$ diluted by the inverse

square distance $r_k = |\mathbf{r} - \mathbf{r}_d|$ between both points. Finally, assuming that each point $\mathbf{r}_d$ on the disk's surface acts as a half-isotropic radiator of (anti)-neutrinos, the total flux emitted at $\mathbf{r}_d$ is $F_{\mathbf{r}_d,\nu} = \int_0^{\pi/2} \int_0^{2\pi} I_{\mathbf{r}_d,\nu} \cos\theta' \sin\theta' d\theta' d\phi' = \pi I_{\mathbf{r}_d,\nu}$, with θ', ϕ' the direction angles at $\mathbf{r}_d$. Collecting all obtains

$$\begin{aligned} Q_{\nu_i\bar{\nu}_i} = A_{1,i} \int\limits_{\mathbf{r}_{d,\nu_i}\in\text{disk}} d\mathbf{r}_{d,\nu_i} \int\limits_{\mathbf{r}_{d,\bar{\nu}_i}\in\text{disk}} d\mathbf{r}_{d,\bar{\nu}_i} \; \frac{F_{\mathbf{r}_d,\nu_i}}{r_{k,\nu_i}^2} \frac{F_{\mathbf{r}_d,\bar{\nu}_i}}{r_{k,\bar{\nu}_i}^2} \left(\langle E_{\nu_i}\rangle + \langle E_{\bar{\nu}_i}\rangle\right) (1-\cos\theta)^2 \\ + A_{2,i} \int\limits_{\mathbf{r}_{d,\nu_i}\in\text{disk}} d\mathbf{r}_{d,\nu_i} \int\limits_{\mathbf{r}_{d,\bar{\nu}_i}\in\text{disk}} d\mathbf{r}_{d,\bar{\nu}_i} \; \frac{F_{\mathbf{r}_d,\nu_i}}{r_{k,\nu_i}^2} \frac{F_{\mathbf{r}_d,\bar{\nu}_i}}{r_{k,\bar{\nu}_i}^2} \frac{\langle E_{\nu_i}\rangle + \langle E_{\bar{\nu}_i}\rangle}{\langle E_{\nu_i}\rangle\langle E_{\bar{\nu}_i}\rangle} (1-\cos\theta) \end{aligned} \tag{D.23}$$

Bibliography

[1] Aartsen, M. G., et al. First Observation of PeV-Energy Neutrinos with IceCube. *Physical Review Letters*, **111** (2013), 021103. arXiv:1304.5356, doi:10.1103/PhysRevLett.111.021103.

[2] Abazajian, K. N., Beacom, J. F., and Bell, N. F. Stringent constraints on cosmological neutrino-antineutrino asymmetries from synchronized flavor transformation. Phys. Rev. D, **66** (2002), 013008. arXiv:astro-ph/0203442, doi:10.1103/PhysRevD.66.013008.

[3] Abe, K., et al. Letter of Intent: The Hyper-Kamiokande Experiment — Detector Design and Physics Potential —. *ArXiv e-prints*, (2011). arXiv:1109.3262.

[4] Abramowicz, M. A., Björnsson, G., and Pringle, J. E. *Theory of Black Hole Accretion Discs*. Cambridge University Press (1999).

[5] Abramowicz, M. A., Chen, X.-M., Granath, M., and Lasota, J.-P. Advection-dominated accretion flows around kerr black holes. *The Astrophysical Journal*, **471** (1996), 762. Available from: https://doi.org/10.1086%2F178004, doi:10.1086/178004.

[6] Abramowicz, M. A. and Fragile, P. C. Foundations of Black Hole Accretion Disk Theory. *Living Rev. Rel.*, **16** (2013), 1. arXiv:1104.5499, doi:10.12942/lrr-2013-1.

[7] Abramowicz, M. A., Lanza, A., and Percival, M. J. Accretion disks around kerr black holes: Vertical equilibrium revisited. *The Astrophysical Journal*, **479** (1997), 179. Available from: https://doi.org/10.1086%2F303869, doi:10.1086/303869.

[8] Agostini, M., et al. Borexino's search for low-energy neutrino and antineutrino signals correlated with gamma-ray bursts. *Astroparticle Physics*, **86** (2017), 11. arXiv:1607.05649, doi:10.1016/j.astropartphys.2016.10.004.

[9] Ahmad, Q. R., et al. Direct evidence for neutrino flavor transformation from neutral-current interactions in the sudbury neutrino observatory. *Phys. Rev. Lett.*, **89** (2002), 011301. Available from: https://link.aps.org/doi/10.1103/PhysRevLett.89.011301, doi:10.1103/PhysRevLett.89.011301.

[10] Aimuratov, Y., Ruffini, R., Muccino, M., Bianco, C. L., Penacchioni, A. V., Pisani, G. B., Primorac, D., Rueda, J. A., and Wang, Y. GRB 081024B and GRB 140402A: Two Additional Short GRBs from Binary Neutron Star Mergers. ApJ, **844** (2017), 83. arXiv:1704.08179, doi:10.3847/1538-4357/aa7a9f.

[11] Akhmedov, E. K. and Smirnov, A. Y. Paradoxes of neutrino oscillations. *Physics of Atomic Nuclei*, **72** (2009), 1363. arXiv:0905.1903, doi:10.1134/S1063778809080122.

[12] Aparicio, J. M. A Simple and Accurate Method for the Calculation of Generalized Fermi Functions. ApJS, **117** (1998), 627. doi:10.1086/313121.

[13] Bahcall, J. N., Concepcion Gonzalez-Garcia, M., and na-Garay, C. P. Solar Neutrinos Before and After KamLAND. *Journal of High Energy Physics*, **2003** (2003), 009. arXiv:hep-ph/0212147, doi:10.1088/1126-6708/2003/02/009.

[14] Balantekin, A. B. and Yuksel, H. Global Analysis of Solar Neutrino and KamLAND Data. *arXiv e-prints*, (2003), hep-ph/0301072. arXiv:hep-ph/0301072.

[15] Balbus, S. A. Enhanced Angular Momentum Transport in Accretion Disks. ARA&A, **41** (2003), 555. arXiv:astro-ph/0306208, doi:10.1146/annurev.astro.41.081401.155207.

[16] Balbus, S. A. and Hawley, J. F. A powerful local shear instability in weakly magnetized disks. I - Linear analysis. II - Nonlinear evolution. ApJ, **376** (1991), 214. doi:10.1086/170270.

[17] Balbus, S. A. and Hawley, J. F. Instability, turbulence, and enhanced transport in accretion disks. *Reviews of Modern Physics*, **70** (1998), 1. doi:10.1103/RevModPhys.70.1.

[18] Barbieri, R. and Dolgov, A. Neutrino oscillations in the early universe. *Nuclear Physics B*, **349** (1991), 743 . Available from: http://www.sciencedirect.com/science/article/pii/055032139190396F, doi:https://doi.org/10.1016/0550-3213(91)90396-F.

[19] Bardeen, J. M. A Variational Principle for Rotating Stars in General Relativity. ApJ, **162** (1970), 71. doi:10.1086/150635.

[20] Bardeen, J. M. Kerr Metric Black Holes. Nature, **226** (1970), 64. doi:10.1038/226064a0.

[21] Bardeen, J. M., Press, W. H., and Teukolsky, S. A. Rotating Black Holes: Locally Nonrotating Frames, Energy Extraction, and Scalar Synchrotron Radiation. ApJ, **178** (1972), 347. doi:10.1086/151796.

[22] Batta, A., Ramirez-Ruiz, E., and Fryer, C. The Formation of Rapidly Rotating Black Holes in High-mass X-Ray Binaries. ApJ, **846** (2017), L15. arXiv:1708.00570, doi:10.3847/2041-8213/aa8506.

[23] Bayless, A. J., Even, W., Frey, L. H., Fryer, C. L., Roming, P. W. A., and Young, P. A. The Effects on Supernova Shock Breakout and Swift Light Curves Due to the Mass of the Hydrogen-rich Envelope. ApJ, **805** (2015), 98. arXiv:1401.4449, doi:10.1088/0004-637X/805/2/98.

[24] Becerra, L., Bianco, C. L., Fryer, C. L., Rueda, J. A., and Ruffini, R. On the Induced Gravitational Collapse Scenario of Gamma-ray Bursts Associated with Supernovae. ApJ, **833** (2016), 107. arXiv:1606.02523, doi:10.3847/1538-4357/833/1/107.

[25] Becerra, L., Cipolletta, F., Fryer, C. L., Rueda, J. A., and Ruffini, R. Angular Momentum Role in the Hypercritical Accretion of Binary-driven Hypernovae. ApJ, **812** (2015), 100. arXiv:1505.07580, doi:10.1088/0004-637X/812/2/100.

[26] Becerra, L., Ellinger, C. L., Fryer, C. L., Rueda, J. A., and Ruffini, R. SPH Simulations of the Induced Gravitational Collapse Scenario of Long Gamma-Ray Bursts Associated with Supernovae. ApJ, **871** (2019), 14. arXiv:1803.04356, doi:10.3847/1538-4357/aaf6b3.

[27] Becerra, L., Guzzo, M. M., Rossi-Torres, F., Rueda, J. A., Ruffini, R., and Uribe, J. D. Neutrino Oscillations within the Induced Gravitational Collapse Paradigm of Long Gamma-Ray Bursts. ApJ, **852** (2018), 120. arXiv:1712.07210, doi:10.3847/1538-4357/aaa296.

[28] Belczynski, K., Bulik, T., and Bailyn, C. The Fate of Cyg X-1: An Empirical Lower Limit on Black-hole-Neutron-star Merger Rate. ApJ, **742** (2011), L2. arXiv:1107.4106, doi:10.1088/2041-8205/742/1/L2.

[29] Berger, E. Short-Duration Gamma-Ray Bursts. ARA&A, **52** (2014), 43. arXiv:1311.2603, doi:10.1146/annurev-astro-081913-035926.

[30] Berger, E., Fong, W., and Chornock, R. An r-process Kilonova Associated with the Short-hard GRB 130603B. ApJ, **774** (2013), L23. arXiv:1306.3960, doi:10.1088/2041-8205/774/2/L23.

[31] Bethe, H. A. Possible explanation of the solar-neutrino puzzle. *Phys. Rev. Lett.*, **56** (1986), 1305. Available from: https://link.aps.org/doi/10.1103/PhysRevLett.56.1305, doi:10.1103/PhysRevLett.56.1305.

[32] Bildsten, L. and Cutler, C. Tidal interactions of inspiraling compact binaries. ApJ, **400** (1992), 175. doi:10.1086/171983.

[33] Bilenky, S. M. Neutrino oscillations: brief history and present status. *ArXiv e-prints*, (2014). arXiv:1408.2864.

[34] Bilenky, S. M. and Pontecorvo, B. Again on Neutrino Oscillations. *Lett. Nuovo Cim.*, **17** (1976), 569. doi:10.1007/BF02746567.

[35] Birkl, R., Aloy, M. A., Janka, H. T., and Müller, E. Neutrino pair annihilation near accreting, stellar-mass black holes. A&A, **463** (2007), 51. arXiv:astro-ph/0608543, doi:10.1051/0004-6361:20066293.

[36] Blaes, O. General Overview of Black Hole Accretion Theory. Space Sci. Rev., **183** (2014), 21. arXiv:1304.4879, doi:10.1007/s11214-013-9985-6.

[37] Blaes, O. M. Course 3: Physics Fundamentals of Luminous Accretion Disks around Black Holes. In *Accretion Discs, Jets and High Energy Phenomena in Astrophysics* (edited by V. Beskin, G. Henri, F. Menard, and et al.), pp. 137–185 (2004). arXiv:astro-ph/0211368.

[38] Blandford, R. D. and McKee, C. F. Fluid dynamics of relativistic blast waves. *Physics of Fluids*, **19** (1976), 1130. doi:10.1063/1.861619.

[39] Bruenn, S. W. Stellar core collapse - Numerical model and infall epoch. ApJS, **58** (1985), 771. doi:10.1086/191056.

[40] Buresti, G. A note on stokes' hypothesis. *Acta Mechanica*, **226** (2015), 3555. Available from: https://doi.org/10.1007/s00707-015-1380-9, doi:10.1007/s00707-015-1380-9.

[41] Burrows, A., Reddy, S., and Thompson, T. A. Neutrino opacities in nuclear matter. *Nuclear Physics A*, **777** (2006), 356 . Special Issue on Nuclear Astrophysics. Available from: http://www.sciencedirect.com/science/article/pii/S0375947404007730, doi:https://doi.org/10.1016/j.nuclphysa.2004.06.012.

[42] Burrows, A. and Thompson, T. A. Neutrino-matter interaction rates in supernovae. In *Stellar Collapse* (edited by C. L. Fryer), pp. 133–174. Springer Netherlands, Dordrecht (2004). ISBN 978-0-306-48599-2. Available from: https://doi.org/10.1007/978-0-306-48599-2_5, doi:10.1007/978-0-306-48599-2_5.

[43] Burrows, D., Garmire, G., Ricker, G., Bautz, M., Nousek, J., Grupe, D., and Racusin, J. Chandra Searches for Late-Time Jet Breaks in GRB X-ray Afterglows. In *Chandra's First Decade of Discovery* (edited by S. Wolk, A. Fruscione, and D. Swartz) (2009).

[44] Caballero, O. L., McLaughlin, G. C., and Surman, R. NEUTRINO SPECTRA FROM ACCRETION DISKS: NEUTRINO GENERAL RELATIVISTIC EFFECTS AND THE CONSEQUENCES FOR NUCLEOSYNTHESIS. *The Astrophysical Journal*, **745** (2012), 170. Available from: https://doi.org/10.1088%2F0004-637x%2F745%2F2%2F170, doi:10.1088/0004-637x/745/2/170.

[45] Cadelano, M., Pallanca, C., Ferraro, F. R., Salaris, M., Dalessandro, E., Lanzoni, B., and Freire, P. C. C. Optical Identification of He White Dwarfs Orbiting Four Millisecond Pulsars in the Globular Cluster 47 Tucanae. ApJ, **812** (2015), 63. arXiv:1509.01397, doi:10.1088/0004-637X/812/1/63.

[46] Caito, L., Bernardini, M. G., Bianco, C. L., Dainotti, M. G., Guida, R., and Ruffini, R. GRB060614: a "fake" short GRB from a merging binary

system. A&A, **498** (2009), 501. arXiv:0810.4855, doi:10.1051/0004-6361/200810676.

[47] Calder, A. C., Townsley, D. M., Seitenzahl, I. R., Peng, F., Messer, O. E. B., Vladimirova, N., Brown, E. F., Truran, J. W., and Lamb, D. Q. Capturing the Fire: Flame Energetics and Neutronization for Type Ia Supernova Simulations. ApJ, **656** (2007), 313. arXiv:astro-ph/0611009, doi:10.1086/510709.

[48] Cano, Z., Wang, S.-Q., Dai, Z.-G., and Wu, X.-F. The Observer's Guide to the Gamma-Ray Burst Supernova Connection. *Advances in Astronomy*, **2017** (2017), 8929054. arXiv:1604.03549, doi:10.1155/2017/8929054.

[49] Cardall, C. Y. Liouville equations for neutrino distribution matrices. *Phys. Rev.*, **D78** (2008), 085017. arXiv:0712.1188, doi:10.1103/PhysRevD.78.085017.

[50] Chakraborty, S., Choubey, S., Dasgupta, B., and Kar, K. Effect of Collective Flavor Oscillations on the Diffuse Supernova Neutrino Background. *JCAP*, **0809** (2008), 013. arXiv:0805.3131, doi:10.1088/1475-7516/2008/09/013.

[51] Chen, W.-X. and Beloborodov, A. M. Neutrino-cooled Accretion Disks around Spinning Black Holes. ApJ, **657** (2007), 383. arXiv:astro-ph/0607145, doi:10.1086/508923.

[52] Chevalier, R. A. Neutron star accretion in a supernova. ApJ, **346** (1989), 847. doi:10.1086/168066.

[53] Cipolletta, F., Cherubini, C., Filippi, S., Rueda, J. A., and Ruffini, R. Fast rotating neutron stars with realistic nuclear matter equation of state. Phys. Rev. D, **92** (2015), 023007. arXiv:1506.05926, doi:10.1103/PhysRevD.92.023007.

[54] Cipolletta, F., Cherubini, C., Filippi, S., Rueda, J. A., and Ruffini, R. Last stable orbit around rapidly rotating neutron stars. Phys. Rev. D, **96** (2017), 024046. arXiv:1612.02207, doi:10.1103/PhysRevD.96.024046.

[55] Clifford, F. E. and Tayler, R. J. The equilibrium distribution of nuclides in matter at high temperatures. MmRAS, **69** (1965), 21.

[56] Covino, S., Malesani, D., Tagliaferri, G., Vergani, S. D., Chincarini, G., Kann, D. A., Moretti, A., Stella, L., and Mistici Collaboration. Achromatic breaks for Swift GRBs: Any evidence? *Nuovo Cimento B Serie*, **121** (2006), 1171. arXiv:astro-ph/0612643, doi:10.1393/ncb/i2007-10239-4.

[57] Cowan, C. L., Reines, F., Harrison, F. B., Kruse, H. W., and McGuire, A. D. Detection of the free neutrino: a confirmation. *Science*, **124** (1956), 103. Available from: https://science.sciencemag.org/content/124/3212/103, arXiv:

https://science.sciencemag.org/content/124/3212/103.full.pdf, doi:10.1126/science.124.3212.103.

[58] Danby, G., Gaillard, J.-M., Goulianos, K., Lederman, L. M., Mistry, N., Schwartz, M., and Steinberger, J. Observation of high-energy neutrino reactions and the existence of two kinds of neutrinos. *Phys. Rev. Lett.*, **9** (1962), 36. Available from: https://link.aps.org/doi/10.1103/PhysRevLett.9.36, doi:10.1103/PhysRevLett.9.36.

[59] Dasgupta, B. and Dighe, A. Collective three-flavor oscillations of supernova neutrinos. *Phys. Rev.*, **D77** (2008), 113002. arXiv:0712.3798, doi:10.1103/PhysRevD.77.113002.

[60] Dasgupta, B., Dighe, A., and Mirizzi, A. Identifying neutrino mass hierarchy at extremely small theta(13) through Earth matter effects in a supernova signal. *Phys. Rev. Lett.*, **101** (2008), 171801. arXiv:0802.1481, doi:10.1103/PhysRevLett.101.171801.

[61] Dasgupta, B., Dighe, A., Mirizzi, A., and Raffelt, G. G. Collective neutrino oscillations in non-spherical geometry. *Phys. Rev.*, **D78** (2008), 033014. arXiv:0805.3300, doi:10.1103/PhysRevD.78.033014.

[62] Davis, R., Harmer, D. S., and Hoffman, K. C. Search for neutrinos from the sun. *Phys. Rev. Lett.*, **20** (1968), 1205. Available from: https://link.aps.org/doi/10.1103/PhysRevLett.20.1205, doi:10.1103/PhysRevLett.20.1205.

[63] de Gouvêa, A., Kayser, B., and Mohapatra, R. N. Manifest cp violation from majorana phases. *Phys. Rev. D*, **67** (2003), 053004. Available from: https://link.aps.org/doi/10.1103/PhysRevD.67.053004, doi:10.1103/PhysRevD.67.053004.

[64] de Holanda, P. C. and Smirnov, A. Y. Solar neutrinos: the SNO salt phase results and physics of conversion. *Astroparticle Physics*, **21** (2004), 287. arXiv:hep-ph/0309299, doi:10.1016/j.astropartphys.2004.01.007.

[65] de Salas, P. F., Forero, D. V., Ternes, C. A., Tortola, M., and Valle, J. W. F. Status of neutrino oscillations 2018: 3σ hint for normal mass ordering and improved CP sensitivity. *Phys. Lett.*, **B782** (2018), 633. arXiv:1708.01186, doi:10.1016/j.physletb.2018.06.019.

[66] Della Valle, M. Supernovae and Gamma-Ray Bursts: A Decade of Observations. *International Journal of Modern Physics D*, **20** (2011), 1745. doi:10.1142/S0218271811019827.

[67] Della Valle, M., et al. An enigmatic long-lasting γ-ray burst not accompanied by a bright supernova. Nature, **444** (2006), 1050. arXiv:arXiv:astro-ph/0608322, doi:10.1038/nature05374.

[68] DeWitt, B. S. The global approach to quantum field theory. Vol. 1, 2. *Int. Ser. Monogr. Phys.*, **114** (2003), 1.

[69] Dezalay, J.-P., Barat, C., Talon, R., Syunyaev, R., Terekhov, O., and Kuznetsov, A. Short cosmic events - A subset of classical GRBs? In *American Institute of Physics Conference Series* (edited by W. S. Paciesas and G. J. Fishman), vol. 265 of *American Institute of Physics Conference Series*, pp. 304–309 (1992).

[70] Di Matteo, T., Perna, R., and Narayan, R. Neutrino Trapping and Accretion Models for Gamma-Ray Bursts. ApJ, **579** (2002), 706. arXiv:astro-ph/0207319, doi:10.1086/342832.

[71] Dicus, D. A. Stellar energy-loss rates in a convergent theory of weak and electromagnetic interactions. *Phys. Rev.*, **D6** (1972), 941. doi:10.1103/PhysRevD.6.941.

[72] Diehl, S., Fryer, C., and Herwig, F. The Formation of Hydrogen Deficient Stars through Common Envelope Evolution. In *Hydrogen-Deficient Stars* (edited by A. Werner and T. Rauch), vol. 391 of *Astronomical Society of the Pacific Conference Series*, p. 221 (2008). arXiv:0711.0322.

[73] Dighe, A. Supernova neutrino oscillations: What do we understand? In *Journal of Physics Conference Series*, vol. 203 of *Journal of Physics Conference Series*, p. 012015 (2010). arXiv:0912.4167, doi:10.1088/1742-6596/203/1/012015.

[74] Dolgov, A. D. Neutrinos in the Early Universe. *Sov. J. Nucl. Phys.*, **33** (1981), 700. [Yad. Fiz.33,1309(1981)].

[75] Dolgov, A. D., Hansen, S. H., Pastor, S., Petcov, S. T., Raffelt, G. G., and Semikoz, D. V. Cosmological bounds on neutrino degeneracy improved by flavor oscillations. *Nuclear Physics B*, **632** (2002), 363. arXiv:hep-ph/0201287, doi:10.1016/S0550-3213(02)00274-2.

[76] Dominik, M., Belczynski, K., Fryer, C., Holz, D. E., Berti, E., Bulik, T., Mandel, I., and O'Shaughnessy, R. Double Compact Objects. I. The Significance of the Common Envelope on Merger Rates. ApJ, **759** (2012), 52. arXiv:1202.4901, doi:10.1088/0004-637X/759/1/52.

[77] Duan, H., Fuller, G. M., and Carlson, J. Simulating nonlinear neutrino flavor evolution. *Comput. Sci. Dis.*, **1** (2008), 015007. arXiv:0803.3650, doi:10.1088/1749-4699/1/1/015007.

[78] Duan, H., Fuller, G. M., Carlson, J., and Qian, Y.-Z. Coherent Development of Neutrino Flavor in the Supernova Environment. *Physical Review Letters*, **97** (2006), 241101. arXiv:astro-ph/0608050, doi:10.1103/PhysRevLett.97.241101.

[79] Duan, H., Fuller, G. M., Carlson, J., and Qian, Y.-Z. Simulation of Coherent Non-Linear Neutrino Flavor Transformation in the Supernova Environment. 1. Correlated Neutrino Trajectories. *Phys. Rev.*, **D74** (2006), 105014. arXiv:astro-ph/0606616, doi:10.1103/PhysRevD.74.105014.

[80] Duan, H., Fuller, G. M., Carlson, J., and Qian, Y.-Z. Flavor Evolution of the Neutronization Neutrino Burst from an O-Ne-Mg Core-Collapse Supernova. *Phys. Rev. Lett.*, **100** (2008), 021101. arXiv:0710.1271, doi:10.1103/PhysRevLett.100.021101.

[81] Duan, H., Fuller, G. M., and Qian, Y.-Z. Collective neutrino flavor transformation in supernovae. Phys. Rev. D, **74** (2006), 123004. arXiv:astro-ph/0511275, doi:10.1103/PhysRevD.74.123004.

[82] Duan, H., Fuller, G. M., and Qian, Y.-Z. A Simple Picture for Neutrino Flavor Transformation in Supernovae. *Phys. Rev.*, **D76** (2007), 085013. arXiv:0706.4293, doi:10.1103/PhysRevD.76.085013.

[83] Duan, H., Fuller, G. M., and Qian, Y.-Z. Collective Neutrino Oscillations. *Ann. Rev. Nucl. Part. Sci.*, **60** (2010), 569. arXiv:1001.2799, doi:10.1146/annurev.nucl.012809.104524.

[84] Eguchi, K., et al. First results from kamland: Evidence for reactor antineutrino disappearance. *Phys. Rev. Lett.*, **90** (2003), 021802. Available from: https://link.aps.org/doi/10.1103/PhysRevLett.90.021802, doi:10.1103/PhysRevLett.90.021802.

[85] Eichler, D., Livio, M., Piran, T., and Schramm, D. N. Nucleosynthesis, neutrino bursts and gamma-rays from coalescing neutron stars. *Nature*, **340** (1989), 126. doi:10.1038/340126a0.

[86] Eliezer, S. and Swift, A. R. Experimental Consequences of electron Neutrino-Muon-neutrino Mixing in Neutrino Beams. *Nucl. Phys.*, **B105** (1976), 45. doi:10.1016/0550-3213(76)90059-6.

[87] Enqvist, K., Kainulainen, K., and Maalampi, J. Refraction and Oscillations of Neutrinos in the Early Universe. *Nucl. Phys.*, **B349** (1991), 754. doi:10.1016/0550-3213(91)90397-G.

[88] Esteban-Pretel, A., Pastor, S., Tomas, R., Raffelt, G. G., and Sigl, G. Decoherence in supernova neutrino transformations suppressed by deleptonization. *Phys. Rev.*, **D76** (2007), 125018. arXiv:0706.2498, doi:10.1103/PhysRevD.76.125018.

[89] Esteban-Pretel, A., Pastor, S., Tomas, R., Raffelt, G. G., and Sigl, G. Mu-tau neutrino refraction and collective three-flavor transformations in supernovae. *Phys. Rev.*, **D77** (2008), 065024. arXiv:0712.1137, doi:10.1103/PhysRevD.77.065024.

[90] Fogli, G. L., Lisi, E., Marrone, A., and Mirizzi, A. Collective neutrino flavor transitions in supernovae and the role of trajectory averaging. *JCAP*, **0712** (2007), 010. arXiv:0707.1998, doi:10.1088/1475-7516/2007/12/010.

[91] Fogli, G. L., Lisi, E., Marrone, A., Montanino, D., Palazzo, A., and Rotunno, A. M. Neutrino Oscillations: A Global Analysis. *arXiv e-prints*, (2003), hep-ph/0310012. arXiv:hep-ph/0310012.

[92] Fogli, G. L., Lisi, E., Marrone, A., and Palazzo, A. Global analysis of three-flavor neutrino masses and mixings. *Progress in Particle and Nuclear Physics*, **57** (2006), 742. arXiv:hep-ph/0506083, doi:10.1016/j.ppnp.2005.08.002.

[93] Fogli, G. L., Lisi, E., Mirizzi, A., and Montanino, D. Probing supernova shock waves and neutrino flavor transitions in next-generation water-Cerenkov detectors. *JCAP*, **0504** (2005), 002. arXiv:hep-ph/0412046, doi:10.1088/1475-7516/2005/04/002.

[94] Fogli, G. L., Lisi, E., Montanino, D., and Mirizzi, A. Analysis of energy and time dependence of supernova shock effects on neutrino crossing probabilities. *Phys. Rev.*, **D68** (2003), 033005. arXiv:hep-ph/0304056, doi:10.1103/PhysRevD.68.033005.

[95] Frail, D. A., et al. Beaming in Gamma-Ray Bursts: Evidence for a Standard Energy Reservoir. ApJ, **562** (2001), L55. arXiv:astro-ph/0102282, doi:10.1086/338119.

[96] Frank, J., King, A., and Raine, D. J. *Accretion Power in Astrophysics: Third Edition*. Cambridge University Press (2002).

[97] Frensel, M., Wu, M.-R., Volpe, C., and Perego, A. Neutrino flavor evolution in binary neutron star merger remnants. Phys. Rev. D, **95** (2017), 023011. arXiv:1607.05938, doi:10.1103/PhysRevD.95.023011.

[98] Fritzsch, H. and Minkowski, P. Vector-Like Weak Currents, Massive Neutrinos, and Neutrino Beam Oscillations. *Phys. Lett.*, **62B** (1976), 72. doi:10.1016/0370-2693(76)90051-4.

[99] Fryer, C., Benz, W., Herant, M., and Colgate, S. A. What Can the Accretion-induced Collapse of White Dwarfs Really Explain? ApJ, **516** (1999), 892. arXiv:astro-ph/9812058, doi:10.1086/307119.

[100] Fryer, C. L. Neutrinos from Fallback onto Newly Formed Neutron Stars. ApJ, **699** (2009), 409. arXiv:0711.0551, doi:10.1088/0004-637X/699/1/409.

[101] Fryer, C. L., Benz, W., and Herant, M. The Dynamics and Outcomes of Rapid Infall onto Neutron Stars. ApJ, **460** (1996), 801. arXiv:astro-ph/9509144, doi:10.1086/177011.

[102] Fryer, C. L., Herwig, F., Hungerford, A., and Timmes, F. X. Supernova Fallback: A Possible Site for the r-Process. ApJ, **646** (2006), L131. arXiv:astro-ph/0606450, doi:10.1086/507071.

[103] Fryer, C. L., Oliveira, F. G., Rueda, J. A., and Ruffini, R. Neutron-Star-Black-Hole Binaries Produced by Binary-Driven Hypernovae. *Physical Review Letters*, **115** (2015), 231102. arXiv:1505.02809, doi:10.1103/PhysRevLett.115.231102.

[104] Fryer, C. L., Rockefeller, G., and Warren, M. S. SNSPH: A Parallel Three-dimensional Smoothed Particle Radiation Hydrodynamics Code. ApJ, **643** (2006), 292. arXiv:astro-ph/0512532, doi:10.1086/501493.

[105] Fryer, C. L., Rueda, J. A., and Ruffini, R. Hypercritical Accretion, Induced Gravitational Collapse, and Binary-Driven Hypernovae. *Astrophys. J.*, **793** (2014), L36. arXiv:1409.1473, doi:10.1088/2041-8205/793/2/L36.

[106] Fryer, C. L. and Warren, M. S. Modeling Core-Collapse Supernovae in Three Dimensions. ApJ, **574** (2002), L65. arXiv:astro-ph/0206017, doi:10.1086/342258.

[107] Fryer, C. L., Woosley, S. E., and Hartmann, D. H. Formation Rates of Black Hole Accretion Disk Gamma-Ray Bursts. ApJ, **526** (1999), 152. arXiv:astro-ph/9904122, doi:10.1086/307992.

[108] Fryer, C. L., Woosley, S. E., Herant, M., and Davies, M. B. Merging White Dwarf/Black Hole Binaries and Gamma-Ray Bursts. ApJ, **520** (1999), 650. arXiv:astro-ph/9808094, doi:10.1086/307467.

[109] Fryer, C. L., et al. Constraints on Type Ib/c Supernovae and Gamma-Ray Burst Progenitors. PASP, **119** (2007), 1211. arXiv:astro-ph/0702338, doi:10.1086/523768.

[110] Fukuda, Y., et al. Measurement of the flux and zenith-angle distribution of upward throughgoing muons by super-kamiokande. *Phys. Rev. Lett.*, **82** (1999), 2644. Available from: https://link.aps.org/doi/10.1103/PhysRevLett.82.2644, doi:10.1103/PhysRevLett.82.2644.

[111] Fuller, G. M., Mayle, R. W., Wilson, J. R., and Schramm, D. N. Resonant neutrino oscillations and stellar collapse. ApJ, **322** (1987), 795. doi:10.1086/165772.

[112] Fuller, G. M. and Qian, Y.-Z. Simultaneous flavor transformation of neutrinos and antineutrinos with dominant potentials from neutrino-neutrino forward scattering. *Phys. Rev.*, **D73** (2006), 023004. arXiv:astro-ph/0505240, doi:10.1103/PhysRevD.73.023004.

[113] Galama, T. J., et al. An unusual supernova in the error box of the γ-ray burst of 25 April 1998. Nature, **395** (1998), 670. arXiv:astro-ph/9806175, doi:10.1038/27150.

[114] Gammie, C. F. and Popham, R. Advection-dominated Accretion Flows in the Kerr Metric. I. Basic Equations. ApJ, **498** (1998), 313. arXiv:astro-ph/9705117, doi:10.1086/305521.

[115] Gell-Mann, M. and Pais, A. Behavior of neutral particles under charge conjugation. *Phys. Rev.*, **97** (1955), 1387. Available from: https://link.aps.org/doi/10.1103/PhysRev.97.1387, doi:10.1103/PhysRev.97.1387.

[116] Giacconi, R. and Ruffini, R. (eds.). *Physics and astrophysics of neutron stars and black holes* (1978).

[117] Giunti, C. Status of neutrino masses and mixing. *European Physical Journal C*, **33** (2004), 852. arXiv:hep-ph/0309024, doi:10.1140/epjcd/s2003-03-917-2.

[118] Giunti, C. and Chung, W. K. *Fundamentals of Neutrino Physics and Astrophysics*. Oxford University Press (2007).

[119] Giunti, C., Kim, C. W., and Lee, U. W. When do neutrinos really oscillate? quantum mechanics of neutrino oscillations. *Phys. Rev. D*, **44** (1991), 3635. Available from: https://link.aps.org/doi/10.1103/PhysRevD.44.3635, doi:10.1103/PhysRevD.44.3635.

[120] Gonzalez-Garcia, M. C., Maltoni, M., and Schwetz, T. Updated fit to three neutrino mixing: status of leptonic CP violation. *Journal of High Energy Physics*, **2014** (2014), 52. arXiv:1409.5439, doi:10.1007/JHEP11(2014)052.

[121] Goodman, J. Are gamma-ray bursts optically thick? ApJ, **308** (1986), L47. doi:10.1086/184741.

[122] Gribov, V. and Pontecorvo, B. Neutrino astronomy and lepton charge. *Physics Letters B*, **28** (1969), 493 . Available from: http://www.sciencedirect.com/science/article/pii/0370269369905255, doi:https://doi.org/10.1016/0370-2693(69)90525-5.

[123] Gu, W.-M., Liu, T., and Lu, J.-F. Neutrino-dominated Accretion Models for Gamma-Ray Bursts: Effects of General Relativity and Neutrino Opacity. ApJ, **643** (2006), L87. arXiv:astro-ph/0604370, doi:10.1086/505140.

[124] Guetta, D. and Della Valle, M. On the Rates of Gamma-Ray Bursts and Type Ib/c Supernovae. ApJ, **657** (2007), L73. arXiv:astro-ph/0612194, doi:10.1086/511417.

[125] Hannestad, S., Raffelt, G. G., Sigl, G., and Wong, Y. Y. Y. Self-induced conversion in dense neutrino gases: Pendulum in flavour space. *Phys. Rev.*, **D74** (2006), 105010. [Erratum: Phys. Rev.D76,029901(2007)]. arXiv:astro-ph/0608695, doi:10.1103/PhysRevD.74.105010,10.1103/PhysRevD.76.029901.

[126] Harris, R. A. and Stodolsky, L. Two state systems in media and "Turing's paradox". *Physics Letters B*, **116** (1982), 464. doi:10.1016/0370-2693(82)90169-1.

[127] Hawley, J. F. and Balbus, S. A. A Powerful Local Shear Instability in Weakly Magnetized Disks. II. Nonlinear Evolution. ApJ, **376** (1991), 223. doi:10.1086/170271.

[128] Haxton, W. C., Hamish Robertson, R. G., and Serenelli, A. M. Solar Neutrinos: Status and Prospects. ARA&A, **51** (2013), 21. arXiv:1208.5723, doi:10.1146/annurev-astro-081811-125539.

[129] Haxton, W. C. and Holstein, B. R. Neutrino physics. *American Journal of Physics*, **68** (2000), 15. Available from: https://doi.org/10.1119/1.19368, arXiv:https://doi.org/10.1119/1.19368, doi:10.1119/1.19368.

[130] Hills, J. G. The effects of sudden mass loss and a random kick velocity produced in a supernova explosion on the dynamics of a binary star of arbitrary orbital eccentricity - Applications to X-ray binaries and to the binary pulsars. ApJ, **267** (1983), 322. doi:10.1086/160871.

[131] Horiuchi, S. and Kneller, J. P. What can be learned from a future supernova neutrino detection? *Journal of Physics G Nuclear Physics*, **45** (2018), 043002. arXiv:1709.01515, doi:10.1088/1361-6471/aaa90a.

[132] Iwamoto, K., Nomoto, K., Höflich, P., Yamaoka, H., Kumagai, S., and Shigeyama, T. Theoretical light curves for the type IC supernova SN 1994I. ApJ, **437** (1994), L115. doi:10.1086/187696.

[133] Izzo, L., Rueda, J. A., and Ruffini, R. GRB 090618: a candidate for a neutron star gravitational collapse onto a black hole induced by a type Ib/c supernova. A&A, **548** (2012), L5. arXiv:1206.2887, doi:10.1051/0004-6361/201219813.

[134] Izzo, L., Ruffini, R., Penacchioni, A. V., Bianco, C. L., Caito, L., Chakrabarti, S. K., Rueda, J. A., Nandi, A., and Patricelli, B. A double component in GRB 090618: a proto-black hole and a genuinely long gamma-ray burst. A&A, **543** (2012), A10. arXiv:1202.4374, doi:10.1051/0004-6361/201117436.

[135] Janiuk, A. and Yuan, Y.-F. The role of black hole spin and magnetic field threading the unstable neutrino disk in gamma ray bursts. A&A, **509** (2010), A55. arXiv:0911.0395, doi:10.1051/0004-6361/200912725.

[136] Janka, H.-T. Implications of detailed neutrino transport for the heating by neutrino-antineutrino annihilation in supernova explosions. A&A, **244** (1991), 378.

[137] Janka, H.-T. and Hillebrandt, W. Monte Carlo simulations of neutrino transport in type II supernovae. A&AS, **78** (1989), 375.

[138] Janka, H.-T. and Hillebrandt, W. Neutrino emission from type II supernovae - an analysis of the spectra. A&A, **224** (1989), 49.

[139] Kalitzin, N. S. On the âĂIJNagoya ModelâĂİ of the Elementary Particles: . *Progress of Theoretical Physics*, **25** (1961), 719. Available from: https://doi.org/10.1143/PTP.25.719, arXiv:http://oup.prod.sis.lan/ptp/article-pdf/25/4/719/5299056/25-4-719.pdf, doi:10.1143/PTP.25.719.

[140] Kato, S., Fukue, J., and Mineshige, S. *Black-Hole Accretion Disks — Towards a New Paradigm —*. Kyoto University Press (2008).

[141] Kawanaka, N. and Kohri, K. A possible origin of the rapid variability of gamma-ray bursts due to convective energy transfer in hyperaccretion discs. MNRAS, **419** (2012), 713. arXiv:1103.4713, doi:10.1111/j.1365-2966.2011.19733.x.

[142] Kawanaka, N. and Mineshige, S. Neutrino-cooled Accretion Disk and Its Stability. ApJ, **662** (2007), 1156. arXiv:astro-ph/0702630, doi:10.1086/517985.

[143] Kawanaka, N., Piran, T., and Krolik, J. H. Jet Luminosity from Neutrino-dominated Accretion Flows in Gamma-Ray Bursts. ApJ, **766** (2013), 31. arXiv:1211.5110, doi:10.1088/0004-637X/766/1/31.

[144] Kayser, B. Neutrino physics. *eConf*, **C040802** (2004), L004. arXiv:hep-ph/0506165.

[145] Keil, M. T., Raffelt, G. G., and Janka, H.-T. Monte Carlo study of supernova neutrino spectra formation. *Astrophys. J.*, **590** (2003), 971. arXiv:astro-ph/0208035, doi:10.1086/375130.

[146] King, A. Accretion disc theory since Shakura and Sunyaev. Mem. Soc. Astron. Italiana, **83** (2012), 466. arXiv:1201.2060.

[147] King, A. R., Pringle, J. E., and Livio, M. Accretion disc viscosity: how big is alpha? MNRAS, **376** (2007), 1740. arXiv:astro-ph/0701803, doi:10.1111/j.1365-2966.2007.11556.x.

[148] Kirilova, D. P. Neutrino oscillations and the early universe. *Central European Journal of Physics*, **2** (2004), 467. arXiv:astro-ph/0312569, doi:10.2478/BF02476426.

[149] Klebesadel, R. W. The durations of gamma-ray bursts. In *Gamma-Ray Bursts - Observations, Analyses and Theories* (edited by C. Ho, R. I. Epstein, and E. E. Fenimore), pp. 161–168. Cambridge University Press (1992).

[150] Klein, O. On the statistical derivation of the laws of chemical equilibrium. *Il Nuovo Cimento (1943-1954)*, **6** (1949), 171. Available from: https://doi.org/10.1007/BF02780980, doi:10.1007/BF02780980.

[151] Klein, O. On the thermodynamical equilibrium of fluids in gravitational fields. *Rev. Mod. Phys.*, **21** (1949), 531. Available from: https://link.aps.org/doi/10.1103/RevModPhys.21.531, doi:10.1103/RevModPhys.21.531.

[152] Kneller, J. P. The Physics Of Supernova Neutrino Oscillations. *ArXiv e-prints*, (2015). arXiv:1507.01434.

[153] Kneller, J. P. and McLaughlin, G. C. Monte Carlo neutrino oscillations. *Phys. Rev.*, **D73** (2006), 056003. arXiv:hep-ph/0509356, doi:10.1103/PhysRevD.73.056003.

[154] Kohri, K. and Mineshige, S. Can Neutrino-cooled Accretion Disks Be an Origin of Gamma-Ray Bursts? ApJ, **577** (2002), 311. arXiv:astro-ph/0203177, doi:10.1086/342166.

[155] Kohri, K., Narayan, R., and Piran, T. Neutrino-dominated Accretion and Supernovae. ApJ, **629** (2005), 341. arXiv:astro-ph/0502470, doi:10.1086/431354.

[156] Kostelecky, V., Pantaleone, J., and Samuel, S. Neutrino oscillations in the early universe. *Physics Letters B*, **315** (1993), 46 . Available from: http://www.sciencedirect.com/science/article/pii/037026939390156C, doi:https://doi.org/10.1016/0370-2693(93)90156-C.

[157] Kostelecky, V. A. and Samuel, S. Neutrino oscillations in the early universe with an inverted neutrino mass hierarchy. *Phys. Lett.*, **B318** (1993), 127. doi:10.1016/0370-2693(93)91795-O.

[158] Kostelecky, V. A. and Samuel, S. Nonlinear neutrino oscillations in the expanding universe. *Phys. Rev.*, **D49** (1994), 1740. doi:10.1103/PhysRevD.49.1740.

[159] Kotko, I. and Lasota, J.-P. The viscosity parameter α and the properties of accretion disc outbursts in close binaries. A&A, **545** (2012), A115. arXiv:1209.0017, doi:10.1051/0004-6361/201219618.

[160] Kouveliotou, C., Meegan, C. A., Fishman, G. J., Bhat, N. P., Briggs, M. S., Koshut, T. M., Paciesas, W. S., and Pendleton, G. N. Identification of two classes of gamma-ray bursts. ApJ, **413** (1993), L101. doi:10.1086/186969.

[161] Krolik, J. H. *Active galactic nuclei : from the central black hole to the galactic environment*. Princeton University Press (1999).

[162] Kumar, P. and Zhang, B. The physics of gamma-ray bursts and relativistic jets. Phys. Rep., **561** (2015), 1. arXiv:1410.0679, doi:10.1016/j.physrep.2014.09.008.

[163] Landau, L. D. and Lifshitz, E. M. *Fluid mechanics*. Oxford: Pergamon Press, 1959 (1959).

[164] Lasota, J.-P. Black Hole Accretion Discs. In *Astrophysics of Black Holes: From Fundamental Aspects to Latest Developments* (edited by C. Bambi), vol. 440 of *Astrophysics and Space Science Library*, p. 1 (2016). arXiv:1505.02172, doi:10.1007/978-3-662-52859-4_1.

[165] Lazarus, P., et al. Timing of a young mildly recycled pulsar with a massive white dwarf companion. MNRAS, **437** (2014), 1485. arXiv:1310.5857, doi:10.1093/mnras/stt1996.

[166] Lee, W. H., Ramirez-Ruiz, E., and Page, D. Opaque or Transparent? A Link between Neutrino Optical Depths and the Characteristic Duration of Short Gamma-Ray Bursts. ApJ, **608** (2004), L5. doi:10.1086/422217.

[167] Lee, W. H., Ramirez-Ruiz, E., and Page, D. Dynamical Evolution of Neutrino-cooled Accretion Disks: Detailed Microphysics, Lepton-driven Convection, and Global Energetics. ApJ, **632** (2005), 421. arXiv:astro-ph/0506121, doi:10.1086/432373.

[168] Li, L.-X. and Paczyński, B. Transient Events from Neutron Star Mergers. ApJ, **507** (1998), L59. arXiv:astro-ph/9807272, doi:10.1086/311680.

[169] Liu, T., Gu, W.-M., and Zhang, B. Neutrino-dominated accretion flows as the central engine of gamma-ray bursts. *New Astronomy Reviews*, **79** (2017), 1 . Available from: http://www.sciencedirect.com/science/article/pii/S1387647316300756, doi:https://doi.org/10.1016/j.newar.2017.07.001.

[170] Liu, T., Zhang, B., Li, Y., Ma, R.-Y., and Xue, L. Detectable MeV neutrinos from black hole neutrino-dominated accretion flows. Phys. Rev. D, **93** (2016), 123004. arXiv:1512.07203, doi:10.1103/PhysRevD.93.123004.

[171] Lunardini, C. and Smirnov, A. Y. High-energy neutrino conversion and the lepton asymmetry in the universe. Phys. Rev. D, **64** (2001), 073006. arXiv:hep-ph/0012056, doi:10.1103/PhysRevD.64.073006.

[172] Luo, S. and Yuan, F. Global neutrino heating in hyperaccretion flows. MNRAS, **431** (2013), 2362. arXiv:1301.1102, doi:10.1093/mnras/stt337.

[173] MacFadyen, A. I. and Woosley, S. E. Collapsars: Gamma-Ray Bursts and Explosions in "Failed Supernovae". ApJ, **524** (1999), 262. arXiv:astro-ph/9810274, doi:10.1086/307790.

[174] Maki, Z., Nakagawa, M., and Sakata, S. Remarks on the Unified Model of Elementary Particles. *Progress of Theoretical Physics*, **28** (1962), 870. Available from: https://doi.org/10.1143/PTP.28.870, arXiv:http://oup.prod.sis.lan/ptp/article-pdf/28/5/870/5258750/28-5-870.pdf, doi:10.1143/PTP.28.870.

[175] Malkus, A., Kneller, J. P., McLaughlin, G. C., and Surman, R. Neutrino oscillations above black hole accretion disks: Disks with electron-flavor emission. Phys. Rev. D, **86** (2012), 085015. arXiv:1207.6648, doi:10.1103/PhysRevD.86.085015.

[176] Malkus, A., McLaughlin, G. C., and Surman, R. Symmetric and standard matter neutrino resonances above merging compact objects. Phys. Rev. D, **93** (2016), 045021. arXiv:1507.00946, doi:10.1103/PhysRevD.93.045021.

[177] Maltoni, M., Schwetz, T., Tórtola, M. A., and Valle, J. W. Status of three-neutrino oscillations after the SNO-salt data. Phys. Rev. D, **68** (2003), 113010. arXiv:hep-ph/0309130, doi:10.1103/PhysRevD.68.113010.

[178] Manmoto, T. Advection-dominated Accretion Flow around a Kerr Black Hole. ApJ, **534** (2000), 734. doi:10.1086/308768.

[179] Mao, S. and Yi, I. Relativistic beaming and gamma-ray bursts. ApJ, **424** (1994), L131. doi:10.1086/187292.

[180] Maoz, D. and Hallakoun, N. The binary fraction, separation distribution, and merger rate of white dwarfs from SPY. MNRAS, **467** (2017), 1414. arXiv:1609.02156, doi:10.1093/mnras/stx102.

[181] Maoz, D., Hallakoun, N., and Badenes, C. The separation distribution and merger rate of double white dwarfs: improved constraints. MNRAS, **476** (2018), 2584. arXiv:1801.04275, doi:10.1093/mnras/sty339.

[182] Mavrodiev, S. C. and Deliyergiyev, M. A. Modification of the nuclear landscape in the inverse problem framework using the generalized Bethe-Weizsäcker mass formula. *International Journal of Modern Physics E*, **27** (2018), 1850015-708. doi:10.1142/S0218301318500155.

[183] Mazets, E. P., et al. Catalog of cosmic gamma-ray bursts from the KONUS experiment data. I. Ap&SS, **80** (1981), 3. doi:10.1007/BF00649140.

[184] McKellar, B. H. J. and Thomson, M. J. Oscillating doublet neutrinos in the early universe. *Phys. Rev.*, **D49** (1994), 2710. doi:10.1103/PhysRevD.49.2710.

[185] Mertens, S. Direct Neutrino Mass Experiments. In *Journal of Physics Conference Series*, vol. 718 of *Journal of Physics Conference Series*, p. 022013 (2016). arXiv:1605.01579, doi:10.1088/1742-6596/718/2/022013.

[186] Mészáros, P. Theories of Gamma-Ray Bursts. ARA&A, **40** (2002), 137. arXiv:arXiv:astro-ph/0111170, doi:10.1146/annurev.astro.40.060401.093821.

[187] Mészáros, P. Gamma-ray bursts. *Reports on Progress in Physics*, **69** (2006), 2259. arXiv:astro-ph/0605208, doi:10.1088/0034-4885/69/8/R01.

[188] Meszaros, P., Laguna, P., and Rees, M. J. Gasdynamics of relativistically expanding gamma-ray burst sources - Kinematics, energetics, magnetic fields, and efficiency. ApJ, **415** (1993), 181. arXiv:astro-ph/9301007, doi:10.1086/173154.

[189] Meszaros, P. and Rees, M. J. Poynting Jets from Black Holes and Cosmological Gamma-Ray Bursts. ApJ, **482** (1997), L29. doi:10.1086/310692.

[190] Metzger, B. D., et al. Electromagnetic counterparts of compact object mergers powered by the radioactive decay of r-process nuclei. MNRAS, **406** (2010), 2650. arXiv:1001.5029, doi:10.1111/j.1365-2966.2010.16864.x.

[191] Mihalas, D. and Mihalas, B. W. *Foundations of radiation hydrodynamics*. Oxford University Press (1984).

[192] Mikheyev, S. P. and Smirnov, A. Y. Resonant amplification of ν oscillations in matter and solar-neutrino spectroscopy. *Il Nuovo Cimento C*, **9** (1986), 17. Available from: https://doi.org/10.1007/BF02508049, doi:10.1007/BF02508049.

[193] Mirabel, I. F. and Rodríguez, L. F. Microquasars in our Galaxy. Nature, **392** (1998), 673. doi:10.1038/33603.

[194] Mirizzi, A., Tamborra, I., Janka, H. T., Saviano, N., Scholberg, K., Bollig, R., Hüdepohl, L., and Chakraborty, S. Supernova neutrinos: production, oscillations and detection. *Nuovo Cimento Rivista Serie*, **39** (2016), 1. arXiv:1508.00785, doi:10.1393/ncr/i2016-10120-8.

[195] Misiaszek, M., Odrzywołek, A., and Kutschera, M. Neutrino spectrum from the pair-annihilation process in the hot stellar plasma. *Phys. Rev. D*, **74** (2006), 043006. Available from: http://link.aps.org/doi/10.1103/PhysRevD.74.043006, doi:10.1103/PhysRevD.74.043006.

[196] Misner, C. W., Thorne, K. S., and Wheeler, J. A. *Gravitation*. Princeton University Press (1973).

[197] Moeen Moghaddas, M. Calculation of the relativistic Bulk Viscosity, Shear Viscosity and Shear-Stress Viscosity of Accretion Disks around the Rotating Black Holes. *arXiv e-prints*, (2017), arXiv:1712.02493. arXiv:1712.02493.

[198] Moeen Moghaddas, M., Ghanbari, J., and Ghodsi, A. Shear tensor and dynamics of relativistic accretion disks around rotating black holes. *arXiv e-prints*, (2012), arXiv:1207.6455. arXiv:1207.6455.

[199] Montesinos, M. Review: Accretion Disk Theory. *ArXiv e-prints*, (2012). arXiv:1203.6851.

[200] Muccino, M., Ruffini, R., Bianco, C. L., Izzo, L., and Penacchioni, A. V. GRB 090227B: The Missing Link between the Genuine Short and Long Gamma-Ray Bursts. ApJ, **763** (2013), 125. arXiv:1205.6600, doi:10.1088/0004-637X/763/2/125.

[201] Narayan, R. and McClintock, J. E. Advection-dominated accretion and the black hole event horizon. *New Astronomy Reviews*, **51** (2008), 733 . Jean-Pierre Lasota, X-ray Binaries, Accretion Disks and Compact Stars. Available from: http://www.sciencedirect.com/science/article/pii/S1387647308000043, doi:https://doi.org/10.1016/j.newar.2008.03.002.

[202] Narayan, R., Paczynski, B., and Piran, T. Gamma-ray bursts as the death throes of massive binary stars. ApJ, **395** (1992), L83. arXiv:astro-ph/9204001, doi:10.1086/186493.

[203] Narayan, R., Piran, T., and Kumar, P. Accretion Models of Gamma-Ray Bursts. ApJ, **557** (2001), 949. arXiv:astro-ph/0103360, doi:10.1086/322267.

[204] Narayan, R., Piran, T., and Shemi, A. Neutron star and black hole binaries in the Galaxy. ApJ, **379** (1991), L17. doi:10.1086/186143.

[205] Nomoto, K. and Hashimoto, M. Presupernova evolution of massive stars. Phys. Rep., **163** (1988), 13. doi:10.1016/0370-1573(88)90032-4.

[206] Notzold, D. and Raffelt, G. Neutrino Dispersion at Finite Temperature and Density. *Nucl. Phys.*, **B307** (1988), 924. doi:10.1016/0550-3213(88)90113-7.

[207] Novikov, I. D. and Thorne, K. S. Astrophysics of black holes. In *Black Holes (Les Astres Occlus)* (edited by C. Dewitt and B. S. Dewitt), pp. 343–450 (1973).

[208] Paczynski, B. A model of selfgravitating accretion disk. Acta Astron., **28** (1978), 91.

[209] Paczynski, B. Gamma-ray bursters at cosmological distances. ApJ, **308** (1986), L43. doi:10.1086/184740.

[210] Paczyński, B. Are Gamma-Ray Bursts in Star-Forming Regions? *The Astrophysical Journal Letters*, **494** (1998), L45.

[211] Page, D. N. and Thorne, K. S. Disk-Accretion onto a Black Hole. Time-Averaged Structure of Accretion Disk. ApJ, **191** (1974), 499. doi:10.1086/152990.

[212] Pal, P. B. Particle Physics Confronts the Solar Neutrino Problem. *International Journal of Modern Physics A*, **7** (1992), 5387. doi:10.1142/S0217751X92002465.

[213] Pantaleone, J. Dirac neutrinos in dense matter. *Phys. Rev. D*, **46** (1992), 510. Available from: https://link.aps.org/doi/10.1103/PhysRevD.46.510, doi:10.1103/PhysRevD.46.510.

[214] Pantaleone, J. Neutrino oscillations at high densities. *Physics Letters B*, **287** (1992), 128 . Available from: http://www.sciencedirect.com/science/article/pii/037026939291887F, doi:https://doi.org/10.1016/0370-2693(92)91887-F.

[215] Pantaleone, J. Neutrino oscillations at high densities. *Physics Letters B*, **287** (1992), 128. doi:10.1016/0370-2693(92)91887-F.

[216] Pastor, S. and Raffelt, G. Flavor oscillations in the supernova hot bubble region: Nonlinear effects of neutrino background. *Phys. Rev. Lett.*, **89** (2002), 191101. arXiv:astro-ph/0207281, doi:10.1103/PhysRevLett.89.191101.

[217] Patrignani, C. et al. Review of Particle Physics. *Chin. Phys.*, **C40** (2016), 100001. doi:10.1088/1674-1137/40/10/100001.

[218] Pessah, M. E., Chan, C.-K., and Psaltis, D. The fundamental difference between shear alpha viscosity and turbulent magnetorotational stresses. MNRAS, **383** (2008), 683. arXiv:astro-ph/0612404, doi:10.1111/j.1365-2966.2007.12574.x.

[219] Petcov, S. T. On the Nonadiabatic Neutrino Oscillations in Matter. *Phys. Lett.*, **B191** (1987), 299. [,427(1987)]. doi:10.1016/0370-2693(87)90259-0.

[220] Pian, E., et al. BEPPOSAX Observations of GRB 980425: Detection of the Prompt Event and Monitoring of the Error Box. ApJ, **536** (2000), 778. arXiv:astro-ph/9910235, doi:10.1086/308978.

[221] Piran, T. Gamma-ray bursts and the fireball model. Phys. Rep., **314** (1999), 575. arXiv:arXiv:astro-ph/9810256, doi:10.1016/S0370-1573(98)00127-6.

[222] Piran, T. The physics of gamma-ray bursts. *Reviews of Modern Physics*, **76** (2004), 1143. arXiv:astro-ph/0405503, doi:10.1103/RevModPhys.76.1143.

[223] Piran, T., Shemi, A., and Narayan, R. Hydrodynamics of Relativistic Fireballs. MNRAS, **263** (1993), 861. arXiv:astro-ph/9301004, doi:10.1093/mnras/263.4.861.

[224] Pontecorvo, B. Mesonium and anti-mesonium. *Sov. Phys. JETP*, **6** (1957), 429. [Zh. Eksp. Teor. Fiz.33,549(1957)].

[225] Pontecorvo, B. Inverse beta processes and nonconservation of lepton charge. *Sov. Phys. JETP*, **7** (1958), 172. [Zh. Eksp. Teor. Fiz.34,247(1957)].

[226] Pontecorvo, B. Neutrino Experiments and the Problem of Conservation of Leptonic Charge. *Sov. Phys. JETP*, **26** (1968), 984. [Zh. Eksp. Teor. Fiz.53,1717(1967)].

[227] Pontecorvo, B. Neutrino Experiments and the Problem of Conservation of Leptonic Charge. *Soviet Journal of Experimental and Theoretical Physics*, **26** (1968), 984.

[228] Popham, R., Woosley, S. E., and Fryer, C. Hyperaccreting Black Holes and Gamma-Ray Bursts. ApJ, **518** (1999), 356. arXiv:astro-ph/9807028, doi:10.1086/307259.

[229] Postnov, K. A. and Yungelson, L. R. The Evolution of Compact Binary Star Systems. *Living Reviews in Relativity*, **17** (2014), 3. arXiv:1403.4754, doi:10.12942/lrr-2014-3.

[230] Potekhin, A. Y. and Chabrier, G. Equation of state of fully ionized electron-ion plasmas. ii. extension to relativistic densities and to the solid phase. *Phys. Rev. E*, **62** (2000), 8554. Available from: https://link.aps.org/doi/10.1103/PhysRevE.62.8554, doi:10.1103/PhysRevE.62.8554.

[231] Preparata, G., Ruffini, R., and Xue, S.-S. The dyadosphere of black holes and gamma-ray bursts. A&A, **338** (1998), L87. arXiv:astro-ph/9810182.

[232] Pringle, J. E. Accretion discs in astrophysics. ARA&A, **19** (1981), 137. doi:10.1146/annurev.aa.19.090181.001033.

[233] Qian, L., Abramowicz, M. A., Fragile, P. C., Horák, J., Machida, M., and Straub, O. The Polish doughnuts revisited. I. The angular momentum distribution and equipressure surfaces. A&A, **498** (2009), 471. arXiv:0812.2467, doi:10.1051/0004-6361/200811518.

[234] Qian, Y. Z. and Fuller, G. M. Neutrino-neutrino scattering and matter enhanced neutrino flavor transformation in Supernovae. *Phys. Rev.*, **D51** (1995), 1479. arXiv:astro-ph/9406073, doi:10.1103/PhysRevD.51.1479.

[235] Raffelt, G., Sigl, G., and Stodolsky, L. Non-abelian boltzmann equation for mixing and decoherence. *Phys. Rev. Lett.*, **70** (1993), 2363. Available from: https://link.aps.org/doi/10.1103/PhysRevLett.70.2363, doi:10.1103/PhysRevLett.70.2363.

[236] Raffelt, G. G. *Stars as laboratories for fundamental physics : the astrophysics of neutrinos, axions, and other weakly interacting particles*. University of Chicago Press (1996).

[237] Raffelt, G. G. and Sigl, G. Self-induced decoherence in dense neutrino gases. *Phys. Rev.*, **D75** (2007), 083002. arXiv:hep-ph/0701182, doi:10.1103/PhysRevD.75.083002.

[238] Raffelt, G. G. and Smirnov, A. Yu. Adiabaticity and spectral splits in collective neutrino transformations. *Phys. Rev.*, **D76** (2007), 125008. arXiv:0709.4641, doi:10.1103/PhysRevD.76.125008.

[239] Raffelt, G. G. and Smirnov, A. Yu. Self-induced spectral splits in supernova neutrino fluxes. *Phys. Rev.*, **D76** (2007), 081301. [Erratum: Phys. Rev.D77,029903(2008)]. arXiv:0705.1830, doi:10.1103/PhysRevD.76.081301,10.1103/PhysRevD.77.029903.

[240] Rauscher, T. Nuclear Partition Functions at Temperatures Exceeding 10^{10} K. ApJS, **147** (2003), 403. http://nucastro.org/tables.html#partf. arXiv:astro-ph/0304047, doi:10.1086/375733.

[241] Rauscher, T. and Thielemann, F. K. Astrophysical Reaction Rates From Statistical Model Calculations. *Atomic Data and Nuclear Data Tables*, **75** (2000), 1. http://nucastro.org/tables.html#partf. arXiv:astro-ph/0004059, doi:10.1006/adnd.2000.0834.

[242] Rees, M. J. and Meszaros, P. Relativistic fireballs - Energy conversion and time-scales. MNRAS, **258** (1992), 41P. doi:10.1093/mnras/258.1.41P.

[243] Rees, M. J. and Meszaros, P. Unsteady outflow models for cosmological gamma-ray bursts. ApJ, **430** (1994), L93. arXiv:astro-ph/9404038, doi:10.1086/187446.

[244] Rosswog, S., Ramirez-Ruiz, E., and Davies, M. B. High-resolution calculations of merging neutron stars - III. Gamma-ray bursts. MNRAS, **345** (2003), 1077. doi:10.1046/j.1365-2966.2003.07032.x.

[245] Rudzskii, M. A. Kinetic equations for neutrino spin- and type-oscillations in a medium. Ap&SS, **165** (1990), 65. doi:10.1007/BF00653658.

[246] Rueda, J. A. and Ruffini, R. On the Induced Gravitational Collapse of a Neutron Star to a Black Hole by a Type Ib/c Supernova. ApJ, **758** (2012), L7. arXiv:1206.1684, doi:10.1088/2041-8205/758/1/L7.

[247] Rueda, J. A., Ruffini, R., Becerra, L. M., and Fryer, C. L. Simulating the induced gravitational collapse scenario of long gamma-ray bursts. *International Journal of Modern Physics A*, **33** (2018), 1844031. doi:10.1142/S0217751X18440311.

[248] Rueda, J. A., Ruffini, R., and Wang, Y. Induced Gravitational Collapse, Binary-Driven Hypernovae, Long Gramma-ray Bursts and Their Connection with Short Gamma-ray Bursts. *Universe*, **5** (2019), 110. arXiv:1905.06050, doi:10.3390/universe5050110.

[249] Rueda, J. A., Ruffini, R., Wang, Y., Bianco, C. L., Blanco-Iglesias, J. M., Karlica, M., Lorén-Aguilar, P., Moradi, R., and Sahakyan, N. Electromagnetic emission of white dwarf binary mergers. J. Cosmology Astropart. Phys., **3** (2019), 044. arXiv:1807.07905, doi:10.1088/1475-7516/2019/03/044.

[250] Rueda, J. A., et al. The binary systems associated with short and long gamma-ray bursts and their detectability. *International Journal of Modern Physics D*, **26** (2017), 1730016-309. doi:10.1142/S0218271817300166.

[251] Rueda, J. A., et al. GRB 170817A-GW170817-AT 2017gfo and the observations of NS-NS, NS-WD and WD-WD mergers. J. Cosmology Astropart. Phys., **10** (2018), 006. arXiv:1802.10027, doi:10.1088/1475-7516/2018/10/006.

[252] Ruffert, M., Janka, H.-T., and Schaefer, G. Coalescing neutron stars - a step towards physical models. I. Hydrodynamic evolution and gravitational-wave emission. A&A, **311** (1996), 532. arXiv:astro-ph/9509006.

[253] Ruffert, M., Janka, H.-T., Takahashi, K., and Schaefer, G. Coalescing neutron stars - a step towards physical models. II. Neutrino emission, neutron tori, and gamma-ray bursts. A&A, **319** (1997), 122. arXiv:astro-ph/9606181.

[254] Ruffini, R. Fundamental Physics from Black Holes, Neutron Stars and Gamma-Ray Bursts. *International Journal of Modern Physics D*, **20** (2011), 1797. arXiv:1107.0862, doi:10.1142/S0218271811019876.

[255] Ruffini, R., Bernardini, M. G., Bianco, C. L., Vitagliano, L., Xue, S.-S., Chardonnet, P., Fraschetti, F., and Gurzadyan, V. Black

Hole Physics and Astrophysics: The GRB-Supernova Connection and URCA-1 - URCA-2. In *The Tenth Marcel Grossmann Meeting. Proceedings of the MG10 Meeting held at Brazilian Center for Research in Physics (CBPF), Rio de Janeiro, Brazil, 20-26 July 2003, Eds.: Mário Novello; Santiago Perez Bergliaffa; Remo Ruffini. Singapore: World Scientific Publishing, in 3 volumes, ISBN 981-256-667-8 (set), ISBN 981-256-980-4 (Part A), ISBN 981-256-979-0 (Part B), ISBN 981-256-978-2 (Part C), 2006, XLVIII + 2492 pp.: 2006, p.369* (edited by M. Novello, S. Perez Bergliaffa, and R. Ruffini), p. 369 (2006). arXiv:astro-ph/0503475, doi:10.1142/9789812704030_0026.

[256] Ruffini, R., Bianco, C. L., Fraschetti, F., Xue, S.-S., and Chardonnet, P. On a Possible Gamma-Ray Burst-Supernova Time Sequence. ApJ, **555** (2001), L117. arXiv:astro-ph/0106534, doi:10.1086/323177.

[257] Ruffini, R., Karlica, M., Sahakyan, N., Rueda, J. A., Wang, Y., Mathews, G. J., Bianco, C. L., and Muccino, M. A GRB Afterglow Model Consistent with Hypernova Observations. ApJ, **869** (2018), 101. arXiv:1712.05000, doi:10.3847/1538-4357/aaeac8.

[258] Ruffini, R., Melon Fuksman, J. D., and Vereshchagin, G. V. On the role of a cavity in the hypernova ejecta of GRB190114C. *arXiv e-prints*, (2019). arXiv:1904.03163.

[259] Ruffini, R., Salmonson, J. D., Wilson, J. R., and Xue, S.-S. On evolution of the pair-electromagnetic pulse of a charged black hole. *Astronomy and Astrophysics Supplement*, **138** (1999), 511.

[260] Ruffini, R., Salmonson, J. D., Wilson, J. R., and Xue, S.-S. On the pair-electromagnetic pulse from an electromagnetic black hole surrounded by a baryonic remnant. A&A, **359** (2000), 855. arXiv:astro-ph/0004257.

[261] Ruffini, R., Wang, Y., Enderli, M., Muccino, M., Kovacevic, M., Bianco, C. L., Penacchioni, A. V., Pisani, G. B., and Rueda, J. A. GRB 130427A and SN 2013cq: A Multi-wavelength Analysis of An Induced Gravitational Collapse Event. ApJ, **798** (2015), 10. arXiv:1405.5723, doi:10.1088/0004-637X/798/1/10.

[262] Ruffini, R. and Wilson, J. Possibility of Neutrino Emission from Matter Accreting into a Neutron Star. *Physical Review Letters*, **31** (1973), 1362. doi:10.1103/PhysRevLett.31.1362.

[263] Ruffini, R., et al. On Gamma-Ray Bursts. In *The Eleventh Marcel Grossmann Meeting On Recent Developments in Theoretical and Experimental General Relativity, Gravitation and Relativistic Field Theories* (edited by H. Kleinert, R. T. Jantzen, and R. Ruffini), pp. 368–505 (2008). arXiv:0804.2837, doi:10.1142/9789812834300_0019.

[264] Ruffini, R., et al. GRB 140619B: a short GRB from a binary neutron star merger leading to black hole formation. ApJ, **808** (2015), 190. arXiv:1412.1018, doi:10.1088/0004-637X/808/2/190.

[265] Ruffini, R., et al. GRB 090510: A Genuine Short GRB from a Binary Neutron Star Coalescing into a Kerr-Newman Black Hole. ApJ, **831** (2016), 178. arXiv:1607.02400, doi:10.3847/0004-637X/831/2/178.

[266] Ruffini, R., et al. On the Classification of GRBs and Their Occurrence Rates. ApJ, **832** (2016), 136. arXiv:1602.02732, doi:10.3847/0004-637X/832/2/136.

[267] Ruffini, R., et al. Early X-Ray Flares in GRBs. ApJ, **852** (2018), 53. arXiv:1704.03821, doi:10.3847/1538-4357/aa9e8b.

[268] Ruffini, R., et al. On the GeV emission of the type I BdHN GRB 130427A. *arXiv e-prints*, (2018). arXiv:1812.00354.

[269] Ruffini, R., et al. On the Rate and on the Gravitational Wave Emission of Short and Long GRBs. ApJ, **859** (2018), 30. doi:10.3847/1538-4357/aabee4.

[270] Ruffini, R., et al. On the Ultra-relativistic Prompt Emission, the Hard and Soft X-Ray Flares, and the Extended Thermal Emission in GRB 151027A. ApJ, **869** (2018), 151. arXiv:1712.05001, doi:10.3847/1538-4357/aaee68.

[271] Ruffini, R., et al. On the universal GeV emission in binary-driven hypernovae and their inferred morphological structure. *ArXiv e-prints*, (2018). arXiv:1803.05476.

[272] Ruffini, R., et al. The inner engine of GeV-radiation-emitting gamma-ray bursts. *arXiv e-prints*, (2018). arXiv:1811.01839.

[273] Ruffini, R., et al. Self-similarity and power-laws in GRB 190114C. *arXiv e-prints*, (2019). arXiv:1904.04162.

[274] Salmonson, J. D. and Wilson, J. R. General Relativistic Augmentation of Neutrino Pair Annihilation Energy Deposition near Neutron Stars. ApJ, **517** (1999), 859. arXiv:astro-ph/9908017, doi:10.1086/307232.

[275] Salmonson, J. D. and Wilson, J. R. A Model of Short Gamma-Ray Bursts: Heated Neutron Stars in Close Binary Systems. ApJ, **578** (2002), 310. arXiv:astro-ph/0203349, doi:10.1086/342311.

[276] Sana, H., et al. Binary Interaction Dominates the Evolution of Massive Stars. *Science*, **337** (2012), 444. arXiv:1207.6397, doi:10.1126/science.1223344.

[277] Sato, G., et al. Swift Discovery of Gamma-Ray Bursts without a Jet Break Feature in Their X-Ray Afterglows. ApJ, **657** (2007), 359. arXiv:astro-ph/0611148, doi:10.1086/510610.

[278] Savage, M. J., Malaney, R. A., and Fuller, G. M. Neutrino Oscillations and the Leptonic Charge of the Universe. *Astrophys. J.*, **368** (1991), 1. doi:10.1086/169665.

[279] Sawyer, R. F. Speed-up of neutrino transformations in a supernova environment. *Physical Review D*, **72** (2005), 045003. arXiv:hep-ph/0503013, doi:10.1103/PhysRevD.72.045003.

[280] Sawyer, R. F. The multi-angle instability in dense neutrino systems. *Phys. Rev.*, **D79** (2009), 105003. arXiv:0803.4319, doi:10.1103/PhysRevD.79.105003.

[281] Schechter, J. and Valle, J. W. F. Neutrino masses in su(2) $\otimes$ u(1) theories. *Phys. Rev. D*, **22** (1980), 2227. Available from: https://link.aps.org/doi/10.1103/PhysRevD.22.2227, doi:10.1103/PhysRevD.22.2227.

[282] Shakura, N. I. and Sunyaev, R. A. Black holes in binary systems. Observational appearance. A&A, **24** (1973), 337.

[283] Shemi, A. and Piran, T. The appearance of cosmic fireballs. ApJ, **365** (1990), L55. doi:10.1086/185887.

[284] Sigl, G. and Raffelt, G. General kinetic description of relativistic mixed neutrinos. *Nucl. Phys.*, **B406** (1993), 423. doi:10.1016/0550-3213(93)90175-O.

[285] Smartt, S. J. Progenitors of Core-Collapse Supernovae. ARA&A, **47** (2009), 63. arXiv:0908.0700, doi:10.1146/annurev-astro-082708-101737.

[286] Smartt, S. J. Observational Constraints on the Progenitors of Core-Collapse Supernovae: The Case for Missing High-Mass Stars. PASA, **32** (2015), e016. arXiv:1504.02635, doi:10.1017/pasa.2015.17.

[287] Smith, N. Mass Loss: Its Effect on the Evolution and Fate of High-Mass Stars. ARA&A, **52** (2014), 487. arXiv:1402.1237, doi:10.1146/annurev-astro-081913-040025.

[288] Smith, N., Li, W., Silverman, J. M., Ganeshalingam, M., and Filippenko, A. V. Luminous blue variable eruptions and related transients: diversity of progenitors and outburst properties. MNRAS, **415** (2011), 773. arXiv:1010.3718, doi:10.1111/j.1365-2966.2011.18763.x.

[289] Stodolsky, L. Treatment of neutrino oscillations in a thermal environment. *Phys. Rev. D*, **36** (1987), 2273. Available from: https://link.aps.org/doi/10.1103/PhysRevD.36.2273, doi:10.1103/PhysRevD.36.2273.

[290] Strack, P. and Burrows, A. Generalized Boltzmann formalism for oscillating neutrinos. *Phys. Rev.*, **D71** (2005), 093004. arXiv:hep-ph/0504035, doi:10.1103/PhysRevD.71.093004.

[291] Sun, H., Zhang, B., and Li, Z. Extragalactic High-energy Transients: Event Rate Densities and Luminosity Functions. ApJ, **812** (2015), 33. arXiv:1509.01592, doi:10.1088/0004-637X/812/1/33.

[292] Tanabashi, M., et al. Review of particle physics. *Phys. Rev. D*, **98** (2018), 030001. Available from: https://link.aps.org/doi/10.1103/PhysRevD.98.030001, doi:10.1103/PhysRevD.98.030001.

[293] Tanvir, N. R., Levan, A. J., Fruchter, A. S., Hjorth, J., Hounsell, R. A., Wiersema, K., and Tunnicliffe, R. L. A 'kilonova' associated with the short-duration γ-ray burst GRB 130603B. Nature, **500** (2013), 547. arXiv:1306.4971, doi:10.1038/nature12505.

[294] Tauris, T. M., Langer, N., Moriya, T. J., Podsiadlowski, P., Yoon, S.-C., and Blinnikov, S. I. Ultra-stripped Type Ic Supernovae from Close Binary Evolution. ApJ, **778** (2013), L23. arXiv:1310.6356, doi:10.1088/2041-8205/778/2/L23.

[295] Tauris, T. M., Langer, N., and Podsiadlowski, P. Ultra-stripped supernovae: progenitors and fate. MNRAS, **451** (2015), 2123. arXiv:1505.00270, doi:10.1093/mnras/stv990.

[296] Tauris, T. M., van den Heuvel, E. P. J., and Savonije, G. J. Formation of Millisecond Pulsars with Heavy White Dwarf Companions:Extreme Mass Transfer on Subthermal Timescales. ApJ, **530** (2000), L93. arXiv:astro-ph/0001013, doi:10.1086/312496.

[297] Tavani, M. Euclidean versus Non-Euclidean Gamma-Ray Bursts. ApJ, **497** (1998), L21. arXiv:astro-ph/9802192, doi:10.1086/311276.

[298] Thorne, K. S. Disk-Accretion onto a Black Hole. II. Evolution of the Hole. ApJ, **191** (1974), 507. doi:10.1086/152991.

[299] Tian, J. Y., Patwardhan, A. V., and Fuller, G. M. Neutrino flavor evolution in neutron star mergers. Phys. Rev. D, **96** (2017), 043001. arXiv:1703.03039, doi:10.1103/PhysRevD.96.043001.

[300] Tolman, R. C. *Relativity, Thermodynamics, and Cosmology*. Clarendon Press (1934).

[301] Tubbs, D. L. and Schramm, D. N. Neutrino Opacities at High Temperatures and Densities. ApJ, **201** (1975), 467. doi:10.1086/153909.

[302] Uribe Suárez, J. D. and Rueda Hernandez, J. A. Neutrino oscillations in a neutrino-dominated accretion disk around a Kerr BH. *arXiv e-prints*, (2019). arXiv:1909.01841.

[303] Vincenti, W. G. and Kruger, C. H. *Introduction to physical gas dynamics*. Krieger Pub Co (June 1, 1975) (1965).

[304] Vissani, F. Solar neutrino physics on the beginning of 2017. *ArXiv e-prints*, (2017). arXiv:1706.05435.

[305] Volpe, C. Theoretical developments in supernova neutrino physics: mass corrections and pairing correlators. In *Journal of Physics Conference Series*,

vol. 718 of *Journal of Physics Conference Series*, p. 062068 (2016). arXiv:1601.05018, doi:10.1088/1742-6596/718/6/062068.

[306] Wald, R. M. Black hole in a uniform magnetic field. Phys. Rev. D, **10** (1974), 1680. doi:10.1103/PhysRevD.10.1680.

[307] Wang, Y., Rueda, J. A., Ruffini, R., Becerra, L., Bianco, C., Becerra, L., Li, L., and Karlica, M. Two Predictions of Supernova: GRB 130427A/SN 2013cq and GRB 180728A/SN 2018fip. ApJ, **874** (2019), 39. arXiv:1811.05433, doi:10.3847/1538-4357/ab04f8.

[308] Wolfenstein, L. Neutrino Oscillations in Matter. *Phys. Rev.*, **D17** (1978), 2369. doi:10.1103/PhysRevD.17.2369.

[309] Wong, Y. Y. Analytical treatment of neutrino asymmetry equilibration from flavor oscillations in the early universe. Phys. Rev. D, **66** (2002), 025015. arXiv:hep-ph/0203180, doi:10.1103/PhysRevD.66.025015.

[310] Woosley, S. E. Gamma-ray bursts from stellar mass accretion disks around black holes. ApJ, **405** (1993), 273. doi:10.1086/172359.

[311] Woosley, S. E. and Bloom, J. S. The Supernova Gamma-Ray Burst Connection. ARA&A, **44** (2006), 507. arXiv:astro-ph/0609142, doi:10.1146/annurev.astro.43.072103.150558.

[312] Wu, M.-R. and Qian, Y.-Z. Resonances Driven by a Neutrino Gyroscope and Collective Neutrino Oscillations in Supernovae. *Phys. Rev.*, **D84** (2011), 045009. arXiv:1105.2068, doi:10.1103/PhysRevD.84.045009.

[313] Wu, M.-R. and Tamborra, I. Fast neutrino conversions: Ubiquitous in compact binary merger remnants. *Phys. Rev. D*, **95** (2017), 103007. Available from: https://link.aps.org/doi/10.1103/PhysRevD.95.103007, doi:10.1103/PhysRevD.95.103007.

[314] Xing, Z.-z. Properties of CP Violation in Neutrino-Antineutrino Oscillations. *Phys. Rev.*, **D87** (2013), 053019. arXiv:1301.7654, doi:10.1103/PhysRevD.87.053019.

[315] Xing, Z.-z. and Zhou, S. *Neutrinos in particle physics, astronomy and cosmology*. Zhejiang University Press, Hangzhou (2011) (2011). ISBN 9783642175596, 9787308080248.

[316] Xue, L., Liu, T., Gu, W.-M., and Lu, J.-F. Relativistic Global Solutions of Neutrino-dominated Accretion Flows. ApJS, **207** (2013), 23. arXiv:1306.0655, doi:10.1088/0067-0049/207/2/23.

[317] Yakovlev, D. G., Kaminker, A. D., Gnedin, O. Y., and Haensel, P. Neutrino emission from neutron stars. Phys. Rep., **354** (2001), 1. arXiv:astro-ph/0012122, doi:10.1016/S0370-1573(00)00131-9.

[318] Yoon, S.-C., Woosley, S. E., and Langer, N. Type Ib/c Supernovae in Binary Systems. I. Evolution and Properties of the Progenitor Stars. ApJ, **725** (2010), 940. arXiv:1004.0843, doi:10.1088/0004-637X/725/1/940.

[319] Young, P. A., Fryer, C. L., Hungerford, A., Arnett, D., Rockefeller, G., Timmes, F. X., Voit, B., Meakin, C., and Eriksen, K. A. Constraints on the Progenitor of Cassiopeia A. ApJ, **640** (2006), 891. arXiv:astro-ph/0511806, doi:10.1086/500108.

[320] Yuan, F. and Narayan, R. Hot Accretion Flows Around Black Holes. ARA&A, **52** (2014), 529. arXiv:1401.0586, doi:10.1146/annurev-astro-082812-141003.

[321] Zaizen, M., Yoshida, T., Sumiyoshi, K., and Umeda, H. Collective neutrino oscillations and detectabilities in failed supernovae. Phys. Rev. D, **98** (2018), 103020. arXiv:1811.03320, doi:10.1103/PhysRevD.98.103020.

[322] Zel'dovich, Y. B., Ivanova, L. N., and Nadezhin, D. K. Nonstationary Hydrodynamical Accretion onto a Neutron Star. *Soviet Astronomy*, **16** (1972), 209.

[323] Zeldovich, Y. B. and Novikov, I. D. *Relativistic astrophysics. Vol.1: Stars and relativity.* University of Chicago Press (1971).

[324] Zhang, D. and Dai, Z. G. Hyperaccretion Disks around Neutron Stars. *Astrophys. J.*, **683** (2008), 329. arXiv:0712.0423, doi:10.1086/589820.

[325] Zhang, D. and Dai, Z. G. Hyperaccreting Neutron Star Disks and Neutrino Annihilation. ApJ, **703** (2009), 461. arXiv:0901.0431, doi:10.1088/0004-637X/703/1/461.

[326] Zhu, Y.-L., Perego, A., and McLaughlin, G. C. Matter Neutrino Resonance Transitions above a Neutron Star Merger Remnant. *ArXiv e-prints*, (2016). arXiv:1607.04671.